Localization-Based
Fluorescence Correlation Spectroscopy

Johannes M. Stein

SIGILL·UNIVERSITAT·LUDOVIC·MAXIM

München 2020

Localization-Based Fluorescence Correlation Spectroscopy

Johannes M. Stein

Dissertation

durchgeführt an der

Fakultät für Physik
der
Ludwig-Maximilians-Universität München
vorgelegt von
Johannes M. Stein
geb. am 19.02.1990 in Köln

München, den 24.09.2020

Dissertation eingereicht am: 24.09.2020

Erstgutachter: Prof. Dr. Petra Schwille
Zweitgutachter: Prof. Dr. Ralf Jungmann

Tag der mündlichen Prüfung: 11.11.2020

Für Dr. Peter Speich

ZUSAMMENFASSUNG

Die Fluoreszenzmikroskopie ist ein zentraler Baustein der heutigen Lebenswissenschaften. Eine bedeutende Weiterentwicklung auf diesem Feld stellt die superauflösende Fluoreszenzmikroskopie dar, die es erlaubt, spezifische Strukturen im Nanometerbereich auf der Ebene einzelner Biomoleküle zu visualisieren. Eine dieser superauflösenden Methoden ist ein Verfahren namens DNA-PAINT (Points Accumulation for Imaging in Nanoscale Topography), das mittels DNA-Nanotechnologie höchste räumliche Auflösung ermöglicht. Die Fluoreszenzkorrelationspektroskopie (FCS) ist ein extrem empfindliches optisches Verfahren, das zeitliche Fluoreszenzfluktuationen auf der Ebene einzelner Moleküle erfasst und Zugang zu den molekularen Dynamiken erschließt, die diesen Fluktuationen zugrunde liegen. In dieser Arbeit wurden die Konzepte von DNA-PAINT und kamerabasierter FCS zu einer neuen Methode namens lokalisationsbasierte FCS (lbFCS) vereint. Die lbFCS ermöglicht einerseits, reversible bimolekulare Interaktionen vom Typ Rezeptor-Ligand hochparallelisiert und mit Einzelmolekülauflösung zu vermessen. Andererseits ist es mit der lbFCS im Falle von Rezeptoransammlungen oder multimerischen Komplexen im Nanometerbereich möglich, die jeweilige Anzahl von Untereinheiten zu bestimmen. In Kombination mit DNA-PAINT wird die lbFCS so zu einem quantitativen Werkzeug, um potentiell ungeklärte strukturbiologische Fragestellungen zu bearbeiten. In dieser Arbeit konnten mithilfe der lbFCS sowohl die zugrundeliegenden Raten der reversiblen DNA-PAINT Hybridisierungreaktion, als auch die Anzahl der auf DNA-Nanostrukturen angebrachten Einzelstränge bestimmt werden. Durch diesen engen Bezug wurde die lbFCS auch von Weiterentwicklungen der Methode DNA-PAINT begünstigt, die ebenfalls im Rahmen dieser Arbeit mitentwickelt wurden. Diese beinhalten die Konstruktion eines Fluoreszenzmikroskops mit verbesserter Ausleuchtung, eine Studie zur Untersuchung von photoinduziertem Schaden der DNA-Moleküle während der Bildaufnahme und eine durch Sequenz- und Pufferoptimierung ermöglichte Beschleunigung des Aufnahmevorgangs. Außerdem umfasst diese Arbeit eine Anwendung von DNA-PAINT im Zusammenspiel mit der *in-vitro*-Rekonstitution von selbstorganisierenden Proteinen und zeigt das aussichtsreiche Entwicklungspotential diesbezüglich auf. Ein zusätzlicher Abschnitt unveröffentlichter Ergebnisse beschreibt die erstmalige Anwendung der lbFCS in Kombination mit DNA-PAINT zum Zählen von Proteinen in fixierten Zellen. Neben einer Vielzahl positiver Beobachtungen offenbarten sich dabei auch Einschränkungen in der Anwendbarkeit der bisherigen Implementierung. Zahlreiche einfach zu realisierende Ideen zur Weiterentwicklung lassen die lbFCS dennoch als vielversprechendes Werkzeug erscheinen um zukünftig möglicherweise auch zu strukturbiologischen Entdeckungen beizutragen.

Abstract

Fluorescence microscopy is a fundamental tool within the life sciences. An important development in this field was marked by the advent of super-resolution fluorescence microscopy, which allows to specifically visualize biological structures on the nanometer scale. One of these super-resolution methods is termed DNA-PAINT (Points Accumulation for Imaging in Nanoscale Topography), which achieves highest spatial resolution using DNA nanotechnology. Fluorescence Correlation Spectroscopy (FCS) is an extremely sensitive optical method, detecting fluorescence fluctuations on the level of individual molecules and providing access to the molecular dynamics, on which these fluctuations are based. In this thesis, the underlying concepts of DNA-PAINT and camera-based FCS were combined into a new method termed localization-based FCS (lbFCS). In the first place, lbFCS allows to measure reversible bimolecular reaction rates of receptor-ligand binding in a highly-parallelized manner and with single-molecule resolution. Secondly, in the case of receptor assemblies or multimeric complexes, lbFCS enables molecular counting with respect to the number of subunits on the nanometer scale. In combination with DNA-PAINT, lbFCS can become a quantitative tool for unraveling unresolved structural biological questions. Within this thesis, both abilities of lbFCS were demonstrated based on the reversible hybridization reaction of fluorescently-labeled oligonucleotides used in DNA-PAINT and the counting of the complementary strands attached to DNA nanostructures. Due to this close entanglement, the development of lbFCS was also favored by further advancements of DNA-PAINT as an imaging approach, which are also included within this thesis. These comprise the construction of a fluorescence microscope with an improved illumination profile, a systematic study of photo-induced damage to DNA molecules during image acquisition and accelerated imaging due to optimization of oligonucleotide sequence design and buffer optimization. In addition, this work includes the an application of DNA-PAINT imaging in conjunction with *in vitro* reconstitution of self-organizing proteins, highlighting an auspicious potential in this regard. In a further section of unpublished results, lbFCS in combination with DNA-PAINT was applied for the first time to count proteins in fixed cells. Besides several positive observations, cellular experiments also revealed limitations of the current implementation. Numerous ideas offering easy-to-implement modifications yet make lbFCS a promising tool, potentially contributing to structural biological discoveries in the future.

PUBLICATIONS AND MANUSCRIPTS

PUBLICATIONS RELATED TO THIS THESIS

Blumhardt P, **Stein J**, Mücksch J, Stehr F, Bauer J, Jungmann R, Schwille P (2018) Photo-Induced Depletion of Binding Sites in DNA-PAINT Microscopy. ***Molecules*** 23(12):3165

Stehr F*, **Stein J***, Schueder F, Schwille P, Jungmann R (2019) Flat-top TIRF illumination boosts DNA-PAINT imaging and quantification. ***Nature Communications*** 10(1):1268

Stein J*, Stehr F*, Schueler P, Blumhardt P, Schueder F, Mücksch J, Jungmann R, Schwille P (2019) Towards absolute molecular numbers in DNA-PAINT. ***Nano Letters*** 19(11):8182

Schueder F, **Stein J**, Stehr F, Auer A, Sperl B, Strauss MT, Schwille P, Jungmann R (2019) An order of magnitude faster DNA-PAINT imaging by optimized sequence design and buffer conditions. ***Nature Methods*** 16(11):1101

ADDITIONAL PUBLICATIONS AND MANUSCRIPTS

Wade OK, Woehrstein JB, Nickels PC, Strauss S, Stehr F, **Stein J**, Schueder F, Strauss MT, Ganji M, Schnitzbauer J, Grabmeyer H, Yin P, Schwille P, Jungmann R (2019) 124-Color Super-resolution Imaging by Engineering DNA-PAINT Blinking Kinetics. ***Nano Letters*** 19(4):2641

Stein J*, Stehr F*, Bauer J, Niederauer C, Jungmann R, Ganzinger K, Schwille P (2020) Tracking Single Particles for Hours via continuous DNA-mediated Fluorophore Exchange. ***BioRxiv***

---

* These authors contributed equally to this work

Contents

ZUSAMMENFASSUNG iv

ABSTRACT v

PUBLICATIONS vi

CONTENTS vii

I Scientific Context 1

1 INTRODUCTION AND OUTLINE 3
1.1 Fluorescence in the Life Sciences 3
1.2 DNA Nanotechnology 4
1.3 Content of This Thesis 5

2 THEORETICAL BASIS 7
2.1 Fluorescence Microscopy and Fluorescence Spectroscopy 7
2.1.1 Fluorescence 7
2.1.2 The Diffraction Limit and Super-Resolution Microscopy 8
2.1.3 Single Molecule Localization Microscopy 9
2.1.4 Total Internal Reflection Fluorescence Microscopy 9
2.1.5 Fluorescence Correlation Spectroscopy 11
2.1.6 Confocal FCS 11
2.1.7 Surface-Integrated FCS 12
2.2 DNA Nanotechnology 13
2.2.1 Repurposing DNA with Novel Functions 13
2.2.2 DNA-PAINT 15
2.2.3 DNA-PAINT Kinetics: Receptor-Ligand Binding 16
2.3 Localization-Based FCS 18
2.3.1 Introduction to the Concept 18
2.3.2 Derivation of the Fit-Function in lbFCS 20

II Peer-Reviewed Research Articles 25

3 PHOTO-INDUCED DEPLETION OF DOCKING STRANDS IN DNA-PAINT 27
3.1 Motivation and Summary 27
3.2 PUBLICATION P1: Photo-Induced Depletion of Binding Sites in DNA-PAINT Microscopy 28

4 Homogeneous TIRF Illumination **59**
- 4.1 Motivation and Summary . . . 59
- 4.2 Publication P2: Flat-top TIRF illumination boosts DNA-PAINT imaging and quantification . . . 60

5 Accelerating DNA-PAINT Imaging **87**
- 5.1 Motivation and Summary . . . 87
- 5.2 Publication P3: An order of magnitude faster DNA-PAINT imaging by optimized sequence design and buffer conditions . . . 88

6 Localization-Based Fluorescence Correlation Spectroscopy **113**
- 6.1 Motivation and Summary . . . 113
- 6.2 Publication P4: Toward Absolute Molecular Numbers in DNA-PAINT 114

III Additional Results and Discussion 139

7 Advancing Localization-Based Fluorescence Correlation Spectroscopy **141**
- 7.1 Introduction . . . 141
- 7.2 Measuring Bimolecular Binding Rates at the Single Molecule Level . . 142
  - 7.2.1 The Current lbFCS Workflow . . . 143
  - 7.2.2 Two-Point Concentration Series . . . 145
  - 7.2.3 Faster Image Acquisition . . . 146
  - 7.2.4 Fast Acquisition of Two-Point Concentration Series . . . 150
  - 7.2.5 Conclusion . . . 151
- 7.3 Counting Single Molecules . . . 152
  - 7.3.1 From Two Concentration Measurements to a Revised Counting Approach . . . 152
  - 7.3.2 Concentration Series by Imager Exchange . . . 156
  - 7.3.3 First Application to Cellular Targets . . . 159
  - 7.3.4 Conclusion . . . 164

8 *In Vitro* Reconstitution at Super-Resolution **167**
- 8.1 Introduction . . . 167
  - 8.1.1 The MinCDE System . . . 167
  - 8.1.2 Studying MinDE Pattern Formation *In Vitro* - Beyond FtsZ Positioning . . . 168
- 8.2 Results . . . 170
  - 8.2.1 DNA-PAINT Imaging of DNA Origami Positioned by MinDE . 170
  - 8.2.2 Crosslinking DNA Origami Prior to MinDE Reconstitution . . . 172
- 8.3 Summary and Outlook . . . 172

9 Future Perspectives **177**

IV Appendix **179**
A.1 Appendix to Chapter 7 181
A.1.1 Sample Preparation and Imaging Conditions 181
A.1.2 Filtering and Counting DNA origami Exchange Series 182
A.1.3 Filtering and Counting Fixed U2OS Cells 183
A.2 Appendix to Chapter 8 184
A.2.1 Sample Preparation and Imaging Conditions 184

LIST OF FIGURES **187**

LIST OF TABLES **189**

LIST OF ABBREVIATIONS **191**

BIBLIOGRAPHY **193**

ACKNOWLEDGEMENTS **211**

Part I

Scientific Context

1

Introduction and Outline

1.1 Fluorescence in the Life Sciences

The physical phenomenon of fluorescence is nowadays pivotal to a broad range of technical and diagnostic applications within the life sciences. In the context of biological research, fluorescence microscopy has become an indispensible tool due to its ability to provide images at superior contrast, discriminating "what is interesting (signal) from what is not (background)" [1]. This is achieved via specific attachement of fluorescent labels allowing to record images of labeled targets above an otherwise black background. Due to the large spectral range of available fluorophores, fluorescence microscopy provides multiplexing capabilities by simultaneously imaging different cellular or molecular structures and components [1]. The so-far unmet power of specificity is highlighted by the beautiful image depicted in Fig. 1.1, showing COS cells labeled for actin (grey) and mitochondria (orange).

Since the first report of a fluorescence microscope in 1911 [2], fluorescence microscopy has been repeatedly revolutionized by significant technical advances, often paired with ingenious ideas over the past century. It is impossible to exhaustively review and give credit to all contributions that have led to the vast range of present fluorescence microscopy variants within this introduction. To name a few, important hallmarks constitute, e.g., the significant background reduction enabled by confocal microscopy [3–5] and Total Internal Reflection Fluorescence (TIRF) microscopy [6] or the ability to image larger three-dimensional volumes and tissues introduced by two-photon microscopy [7] and light-sheet microscopy [8, 9]. Genetic tagging by fluorescent proteins - with Green Fluorescent Protein (GFP) at the forefront - enabled researchers to image and monitor virtually any protein of interest in living organisms [10–12]. Besides providing valuable structural insights, fluorescence microscopy has been exploited to report on molecular dynamics via Fluorescence Recovery After Photobleaching (FRAP) [13, 14] and Fluorescence Correlation Spectroscopy (FCS) [15–17]. Finally, fluorescence microscopy was revolutionized once more by the recent advent of super-resolution microscopy, providing specific access to the nanometer scale which was previously obscured by the diffraction limit of standard microscopes [18–21].

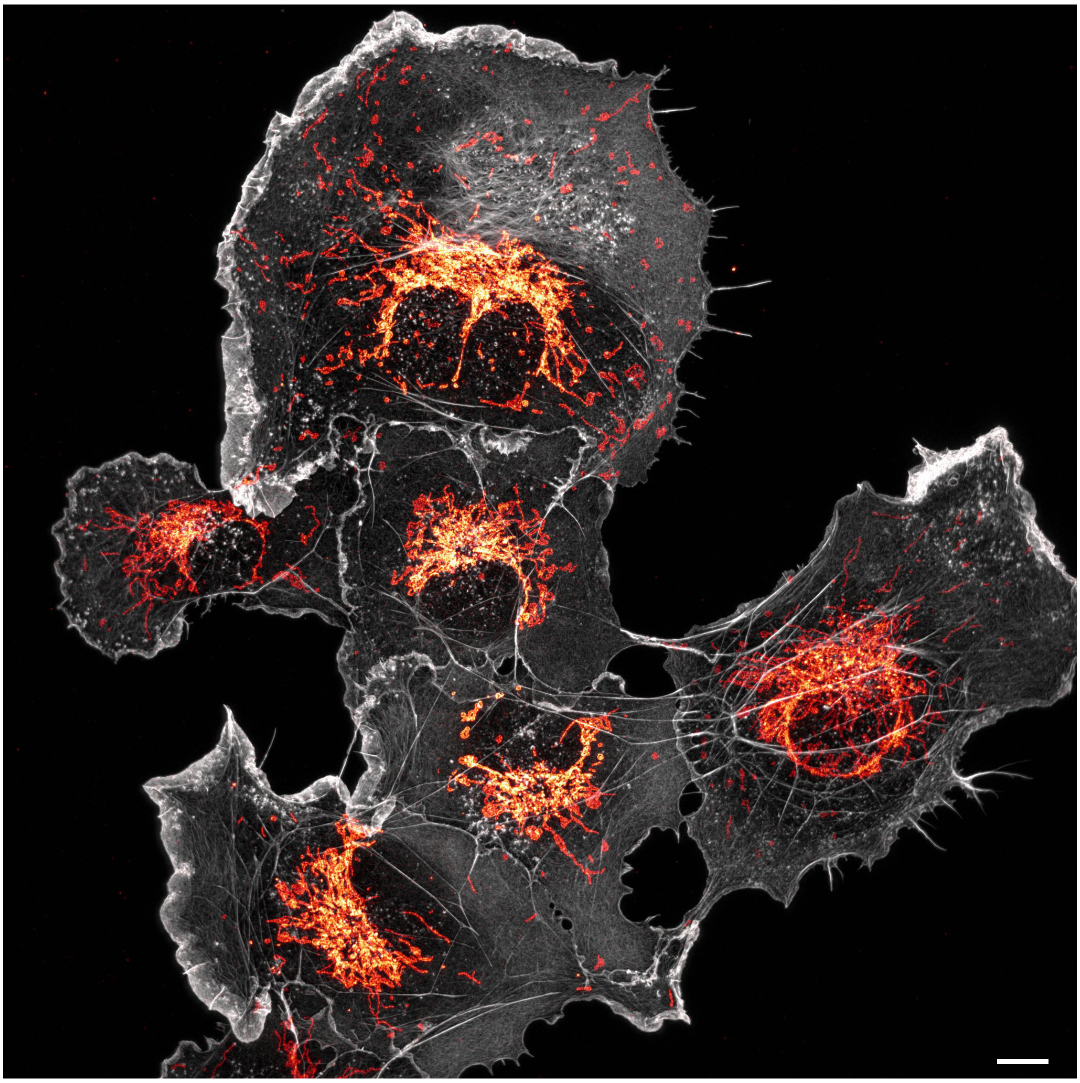

Figure 1.1. Specificity in Fluorescence Microscopy. Fluorescence image of COS cells labeled for actin (grey, phalloidin labeling) and mitochondria (orange, anti-TOM20 labeling). Scale bar 10 μm. Image and permission by Christophe Leterrier, NeuroCyto, INP CNRS-Aix Marseille Université.

1.2 DNA Nanotechnology

Deciphering the structure of DNA and the principles underlying its hybridization has enabled scientists to utilize this remarkable molecule for purposes far beyond its biological function of encoding genetic information. Already in 1982 Nadrian Seeman envisioned that the mechanism behind single DNA strands self-assembling into double helices via complementary Watson-Crick base pairing could be exploited to use DNA as a construction material for threedimensional structures [22]. As a pioneer of DNA nanotechnology, this field of research has experienced remarkable developments over the past 40 years and is nowadays widely established in leading life science institutions around the globe [23, 24]. A major breakthrough in the field was marked by the development of the DNA origami method by Paul Rothemund, who employed viral DNA as a scaffold material to design nanostructures of arbitrary 2D shapes [25], which was soon extended to 3D shapes [26]. Applications in DNA nanotechnology nowadays comprise DNA computation [27] such as logic circuits [28] and neural networks [29, 30], nanomechanical devices [31], DNA walkers [32] and robots [33].

Notably, Watson-Crick base pairing has also been exploited for molecular recognition in the context of fluorescence microscopy. In an approach termed Fluorescence In-Situ Hybridization (FISH), fluorescently-labeled DNA probes hybridize to complementary chromosomal regions within cells, allowing to specifically visualize and map genetic loci [34, 35]. Recently, a DNA-based super-resolution fluorescence microscopy approach termed DNA-PAINT (Points Accumulation for Imaging in Nanoscale Topography) has been developed, allowing to image specific targets labeled with short single stranded DNA, to which complementary and fluorescently-labeled oligonucleotides transiently hybridize [36, 37].

1.3 Content of This Thesis

The work presented in this thesis was enabled by recent advances in DNA-PAINT [37–39] and camera-based FCS [40]. Unifying the underlying concepts, we developed a method we termed localization-based FCS, driven by two motivations: i) measuring the reaction rates of transient binding interactions between immobile receptors and freely-diffusing ligands at the single molecule level and ii) molecular counting of receptor copy numbers in case of multimeric receptor complexes. We benchmarked the ability of lbFCS to measure reversible DNA hybridization to surface-immobilized DNA origami nanostructures and demonstrated the ability to efficiently monitor reaction changes induced by environmental variations, e.g., in temperature or ion concentrations. In combination with DNA-PAINT imaging, we showed that the measured binding rates enable lbFCS of absolute counting of copy numbers within dense accumulations of target molecules at the nanoscale. Due to this close entanglement, the development of lbFCS was also favored by further advances of DNA-PAINT as an imaging approach, to which we have also contributed whithin this thesis, both on the side of instrumentation and implementation. This included a systematic study of docking strand depletion in DNA-PAINT experiments (Chapter 3), construction of a custom fluorescence microscope with a refined excitation profile for high-throughput imaging (Chapter 4) and the optimization of sequence design and buffer composition, significantly accelerating image acquisition (Chapter 5). All these findings ultimately integrated into the proof-of-principle study of lbFCS in combination with DNA-PAINT and DNA origami nanostructures (Chapter 6). Furthermore, this thesis comprises new, unpublished results advancing both the framework of lbFCS focusing on measuring reaction rates and the framework for using lbFCS for molecular counting in combination with DNA-PAINT (Chapter 7). The latter includes the first application to cellular targets, aiming at counting copy numbers of nucleoporins in the nuclear pore complex of fixed U2OS cells. Additionaly, results of an imaging-based side project in combination with *in vitro* reconstitution of *E. coli*'s MinDE system are presented (Chapter 8), pointing towards promising applications of DNA-PAINT in conjunction of self-assembling proteins.

Throughout this thesis, the pronoun "we" includes this author and all contributors to a certain project, acknowledging the collaborative nature of this field of research. Individual contributions of this author are highlighted in case of peer-reviewed journal articles in Part II, and contributions from collaborators in the presentation of unpublished results are explicitly acknowledged in Part III.

2

Theoretical Basis

2.1 Fluorescence Microscopy and Fluorescence Spectroscopy

2.1.1 Fluorescence

The physical principle behind fluorescence is based on the interaction between electromagnetic radiation and a fluorescent molecule (so-called fluorophore). The established simplified scheme of the involved processes is illustrated in a Jablonski diagram (see Fig. 2.6). Exposing a fluorophore to light of a suitable wavelength, absorption of a photon can lead to its transition from an electronic singlet ground state to an excited singlet state ($S_0 \longrightarrow S_1$). Fluorescence refers the process of radiative relaxation from the excited state back to the ground state ($S_1 \longrightarrow S_0$). Due to non-radiative energy dissipation such as internal conversion or vibrational relaxation, the emitted photon usually has a longer wavelength than the absorpted photon, which is termed Stokes shift. The Stokes shift allows spectral separation of excitation light

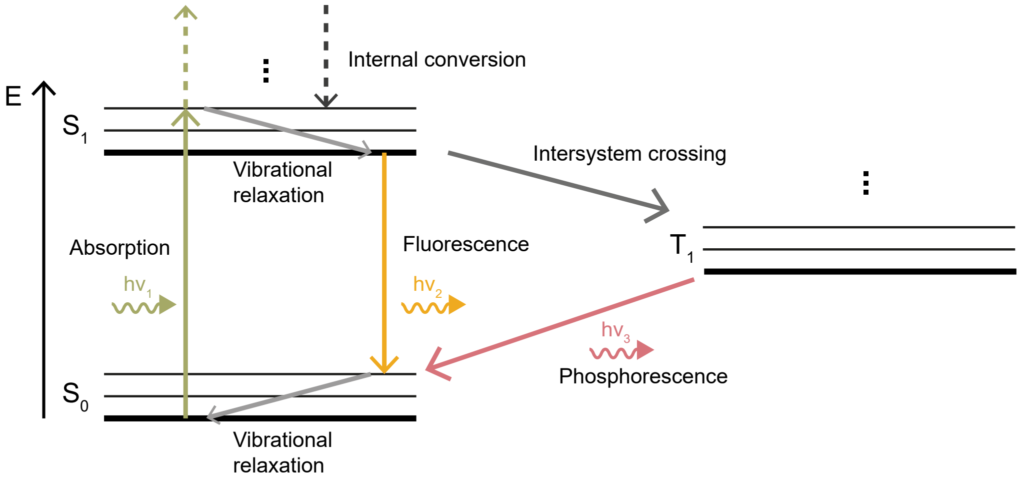
Internal conversion
E
S_1
Vibrational relaxation
Intersystem crossing
T_1
Absorption
hv_1
Fluorescence
hv_2
hv_3
Phosphorescence
S_0
Vibrational relaxation

Figure 2.1. Jablonski Diagram. A simplified schematic of the reaction pathways involved in fluorophore excitation-relaxation. Radiative processes (colored arrows) include absorption, fluorescence and phosphorescence and non-radiative processes comprise vibrational relaxation, internal conversion and intersystem crossing.

and fluorescence emission by means of optical filters, and thus formation of images from emitted fluorescence alone. An additional non-radiative transition is termed intersystem crossing from the excited singlet state to a long-lived excited triplet state ($S_1 \rightarrow T_1$). The radiative relaxation $T_1 \rightarrow S_0$ is called phosphorescence.

Importantly, a fluorophore cannot undergo unlimited excitation-relaxation cycles, but eventually enters a permanently dark state, which is referred to as 'photobleaching'. Conventional fluorescence microscopy is hence limited by the photon budget (number of emitted photons before bleaching) of the fluorescent labels. The underlying principle of photobleaching and further implications are discussed in Chapter 3.

2.1.2 The Diffraction Limit and Super-Resolution Microscopy

In 1873, Ernst Abbe famously described that the achievable resolution of a light microscope follows the relation [41]:

$$d = \frac{\lambda}{2n\sin\alpha} = \frac{\lambda}{2NA} \tag{2.1}$$

where d is the smallest resolvable distance between to points, λ is the wavelength of the illuminating light source, n is the refractive index of the medium and α the half angle of the cone over which the objective can collect light from the sample. The term $n\sin\alpha$ is summarized as the numerical apperture NA.

For over a century this theorem was limiting the accessible resolution in far-field light microscopy to about 200 nm. Since the size of individual proteins is around ~1 nm, the structural details of molecular arrangements and information with respect to interaction partners on the nanoscale was obscured behind the diffraction limit. Access to the (sub-)molecular level in biological samples was over decades exclusively reserved to (cryogenic) electron microscopy - an immensely succesful alternative visualization approach which itself revolutionized structural biology [42]. Despite its superior resolution, however, rendered images in electron microscopy are grey scale, lacking the ability to distinguish molecular identities in the cellular context. The prevailing urge to gain specific access to the nanoscale by means of light microscopy eventually led to the invention of super-resolution microscopy, an achievement worth the Nobel Prize in Chemistry awarded to Eric Betzig, Stefan W. Hell and William E. Moerner in 2014.

While the first circumvention of the diffraction limit in an experiment was demonstrated by Klar *et al.* in 2000 [19], a broad variety of super-resolution approaches based on different principles were put forth over the past two decades [43–45]. These methods can in general be assigned to two groups of common working principles. The first group employs structural illumination pattern engineering and comprises methods such as Stimulated Emission Depletion (STED) [18, 46, 47] and Structured Illumination Microscopy (SIM) [48–50]. The second group is based on exploiting stochastic on-off switching of the fluorophores and includes Single-Molecule Localization Microscopy (SMLM) [20, 21] as well as Super-Resolution Optical Fluctuation Microscopy (SOFI) [51] and related techniques. A recent approach termed MINFLUX combines the concepts of structural illumination and stochastic activation demonstrating achievable resolutions of up to 1-3 nm in fixed and living cells [52, 53].

2.1.3 Single Molecule Localization Microscopy

Since all experimental work within this thesis is based on the super-resolution variant of SMLM, the working principle is briefly revisited within this section. Classically, in wide-field fluorescence microscopy a fluorescently-labeled specimen is excited by a laser, such that all excited fluorophores simultaneously emit fluorescence light, thereby producing a diffraction-limited image. In SMLM, the diffraction limit is circumvented by stochastically activating only a small subset of all fluorophores in a single camera frame during image acquisition (see Fig. 2.2). Recording thousands of camera frames ensures that every fluorescent emitter in the field of view is expected to have been captured at least once in its active state during the acquisition. The diffraction-limited image of a single emitter can be approximated by a 2D Gaussian function, allowing to pinpoint the center position (i.e., the position of the fluorophore itself) at nanometer precision. Localizing all center positions in all camera frames during post-processing yields a list of coordinates, which allows to render a super-resolved image. Various strategies for generating the characteristic 'blinking' required for data acquisition in SMLM have been devised. The most prominent implementations are techniques related to Photoactivated Localization Microscopy (PALM) [21, 54], Stochastic Optical Reconstruction Microscopy (STORM) [20, 55] and Points Accumulation for Imaging in Nanoscale Topography (PAINT) [56]. These include forcing most fluorophores into an inactive, non-fluorescent state, for instance, using laser-based inactivation and/or chemicals [20, 21, 55]. Alternatively, specific reversible binding interactions have been exploited to transiently immobilize freely-diffusing fluorophores at the target of interest [36, 56].

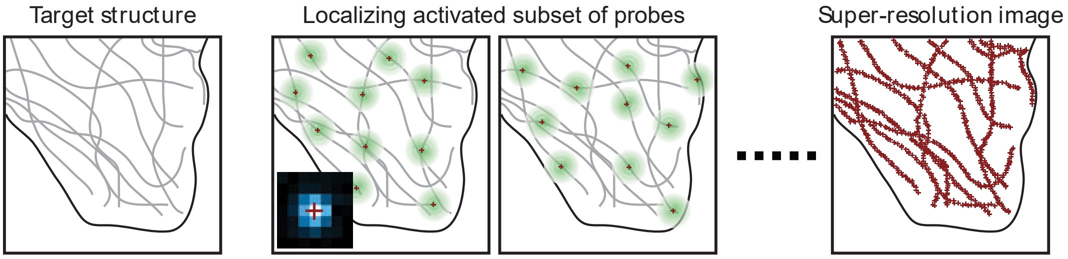

Figure 2.2. Principle of Single Molecule Localization Microscopy. In SMLM, only a small subset of all fluorophores is activated in a single camera frame, ensuring isolated emission form individual fluorophores (green circles). Acquiring image time series ensures registering emission events from ideally all fluorophores at the target structure. The diffraction-limited image of a single fluorophore (black inset) can be approximated by a 2D Gaussian fit, revealing the coordinate of the fluorophore at the center (red cross). Determination of all center coordinates allows rendering a super-resolved image. Reprinted from [45] with permission from Annual Reviews, Inc, copyright (2009).

2.1.4 Total Internal Reflection Fluorescence Microscopy

Total Internal Reflection Fluorescence (TIRF) microscopy is a popular fluorescence imaging modality providing selective surface illumination, thereby achieving exceptional contrast along the axial dimension. After its initial implementation based on

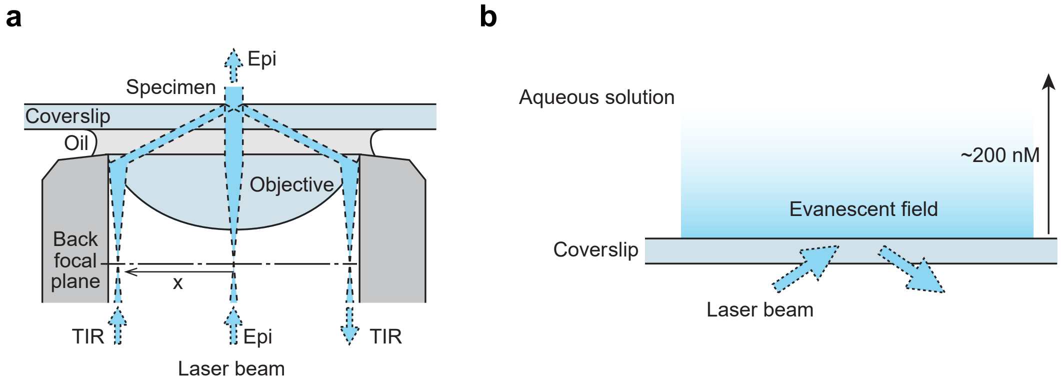

Figure 2.3. Principle of TIRF Microscopy. **a** In objective-type TIRF microscopy, a collimated laser beam is focussed into the back focal plane of the high *NA* objective similar to epi-fluorescence illumination. Laterally shifting the entry point at the back focal away from the optical axes (indicated by the distance x), results in an inclination of the laser beam leaving the objective. Immersion oil matching the refractive index of the coverslip ensures that the laser beam experiences a refractive index mismatch only at the interphase between coverslip and aqueous solution. At a given distance x, the critical angle for total internal reflection is reached. **b** Illustration of the evanescent field in the aqueous phase generated by total internal reflection. The intensity of the evanescent field decays exponentially along the axial direction confining excitation of fluorophores to an only ~200 nm deep volume close to the surface of the coverslip. (a) Reprinted and adapted with permission from Springer Nature Methods [57], Copyright (2008).

a prism [6], nowadays objective-type TIRF microscopy is the established variant. A custom TIRF microscope featuring an improved illumination scheme was designed and constructed within the work of this thesis jointly with Florian Stehr and is subject to Chapter 4.

The principle of TIRF microscopy exploits the phenomenon of refraction of light traversing two media of different refractive indices $n_1 > n_2$, as described by Snell's Law:

$$n_1 \sin\theta_1 = n_2 \sin\theta_2 \tag{2.2}$$

where θ_1 is the angle of the incident light beam and θ_2 the angle of the refracted light beam. If the incident angle exceeds a so-called critical angle $\theta_c = \arcsin n_2/n_1$, total internal reflection occurs and all light is reflected back to the first medium. However, the reflected light generates an evanescent electromagnetic field in the lower refractive index medium, which has the same frequency as the incident light, but whose intensity $I(z)$ decays exponentially along the axial dimension z:

$$I(z) = I_0 \exp(-z/z_0) \tag{2.3}$$

where I_0 is the intensity at the interface and z_0 the distance along z after which I_0 decayed to $1/e$. This axial decay constant at a given wavelength λ can be obtained via:

$$z_0 = \frac{\lambda}{4\pi\sqrt{n_1^2 \sin^2\theta_1 - n_2^2}} \tag{2.4}$$

Fig. 2.3 illustrates the working principle of objective-type TIRF microscopy in more detail. Using the refractive index of glass $n_1 = 1.52$ and of water $n_2 = 1.33$ yields a critical angle of $\theta_c = 61.05°$. Note that these large angles can only be achieved using objectives with a high numerical aperture such that typically objectives featuring $NA > 1.45$ are employed. The combination of a $\lambda = 561$ nm laser with an incident angle of $\theta_1 = 65°$ yields $z_0 = 124$ nm (using Eq. 2.4). This fast decay of the evanescent field on the order of ~200 nm results in an excellent axial resolution by only exciting fluorophores (and hence detecting fluorescence from) close to the glass surface.

2.1.5 Fluorescence Correlation Spectroscopy

As previously mentioned in the introduction, the phenomenon of fluorescence has been exploited in countless other ways than imaging a biological specimen for the purpose of structural visualization *in vivo* or *in situ*. One prominent alternative application of fluorophores is to serve as a reporter, allowing to monitor the dynamics of specific molecular species over time [58–60]. One such time-domain technique is Fluorescence Correlation Spectroscopy (FCS), which is based on the observation of fluctuations of the fluorescence signal collected from a microscopic detection volume. Typically, the fluctuations are governed by fluorescently-labeled target molecules entering and leaving the detection volume (or area) from which the signal is detected [61] or by brightness fluctuations of the fluorescent species [62]. Temporal correlation analysis of the recorded signal can lead to a quantitative description of the underlying dynamics at thermodynamic equilibrium, e.g., 3D diffusion or receptor-ligand interactions [62]. Since its first implementation nearly half a century ago, FCS underwent remarkable developments and nowadays marks one of the hallmarks of light microscopy. A large number of review articles relate the historic milestones of FCS and report on the plethora of its modifications and applications [63–67].

2.1.6 Confocal FCS

Despite the first experimental realization by Magde *et al.* in 1972 (including the theoretical foundation) [15], the major breakthrough of FCS is marked nearly 20 years later by an optical design allowing superior single molecule sensitiviy: the concept of confocal illumination and detection [16, 17]. Enabled by substantial developments in both laser stability and photodetection sensitivity [68], the confocal design allowed direct detection of individual fluorescently-labeled molecules diffusing freely in aqueous solutions [69]. A schematic of a confocal FCS setup is depicted in Fig. 2.4. Focusing a collimated laser beam (blue) into the sample using a high NA objective generates a diffraction-limited excitation volume in the focal plane. Inserting a pinhole in front of the photodetector eliminates any out-of-focus fluorescence, thereby generating a femtoliter detection volume (red ellipse in inset). The ability to sense the passage times and fluctuating numbers of single molecules in this strikingly small volume element and to obtain statistically-relevant information on the multitude of factors influencing the dynamics of these molecules marked the beginning of the huge success of confocal FCS [68]. An important generalization of FCS was introduced by FCCS, especially dual-color FCCS, allowing for the first time to directly characterize bimolecular interactions in aqueous solutions on the single molecule

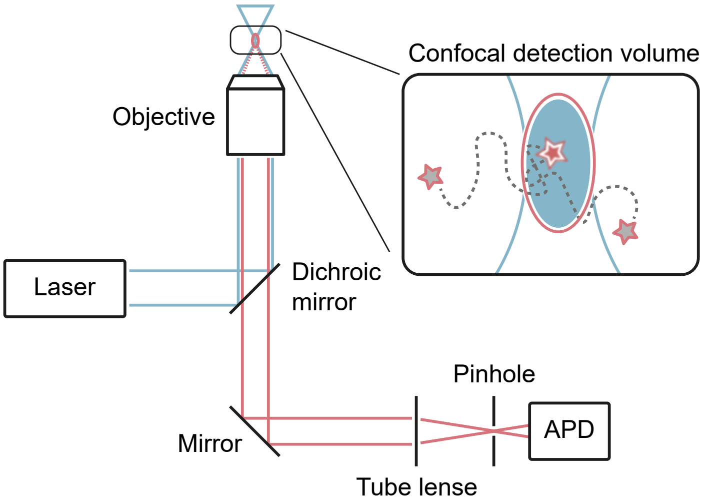

Figure 2.4. Schematic of confocal FCS setup. The excitation laser (blue) is focussed into an aqueous sample through the objective generating a diffraction-limited excitation volume in the focal plane. Fluorescence collected by the objective is spectrally separated from the excitation light using a dichroic mirror and focused on an avalanche photodiode detector. A pinhole is placed in front of the photodetector eliminating any out-of-focus fluorescence of excited molecules in the focused cone of laser light. Confining detection to a femtoliter-sized volume element allows sensing of single molecule passaging at high sensitivity.

level [70–73]. Eliminating out-of-focus fluorescence has made confocal scanning microscopes a widely-spread imaging modality, particularly for imaging in 3D, and they can nowadays be found as standard equipment in imaging-based life science institutions. Due to the similarity in the optical path, FCS modules are available for most commercial laser scanning microscopy solutions.

2.1.7 Surface-Integrated FCS

A recent camera-based FCS variant employing wide-field illumination jointly developed by our co-workers Jonas Mücksch and Philipp Blumhardt is termed Surface-Integrated FCS (SI-FCS) [40]. In contrast to confocal FCS, here the fluctuating fluorescence intensity recorded from a larger surface area using TIRF microscopy is temporally correlated. The idea of combining TIRF microscopy with FCS was already explored in the same year of the seminal TIRF publication in 1981 by the same group [6], when Thompson *et al.* quantified the nonspecific surface adsorption of fluorescently-labeled immunoglobulins on quartz [74]. This initial detection scheme of TIR-FCS featured a single photon-counting point detector, resulting in a confined xyz detection volume. The advent of the less intricate objective-type TIRF implementation in combination with high NA-objectives [75, 76] introduced TIR-FCS to a larger community, leading to several successful studies ranging from protein binding over membrane diffusion to dye photophysics [77–81]. The first use of camera-based detection in combination with TIR-FCS was demonstrated by the group of Thorsten Wohland, utilizing an EMCCD camera instead of a point detector [82]. The spatial component introduced by camera-based TIR-FCS has been exploited, e.g., to visualize

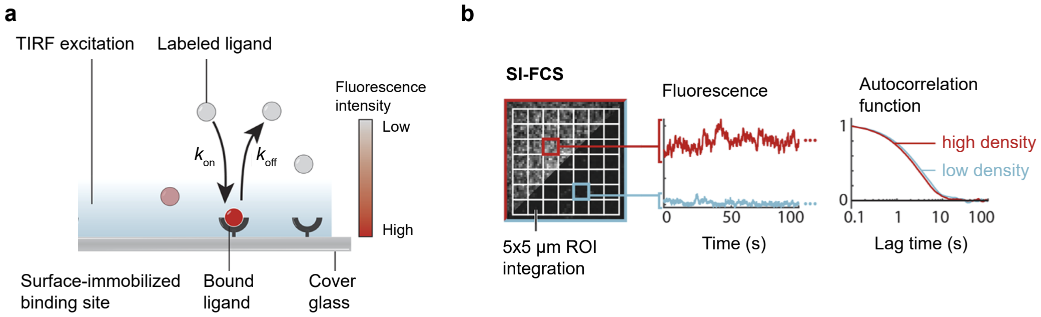

Figure 2.5. Principle of Surface-Integrated FCS. **a** Principle of quantifying bimolecular surface binding with SI-FCS. Fluorescently-labeled ligand reversibly bind to surface-immobilized receptors, following the reaction type described in Eq. 2.5 (see page 16). TIRF-excitation ensures surface-selective illumination in order to detect fluorescence of bound ligand at a high signal-to-noise ratio with respect to unbound ligand. **b** The signal of recorded image time series is integrated over a set of ROIs yielding one intensity trace per ROI. Autocorrelation analysis of the intensity traces can reveal the receptor-ligand binding rates. Reprinted and rearranged from [40] (CC BY-NC 4.0).

maps of 2D diffusion in the lipid membranes of live cells [82] or to circumvent the necessity of additional calibration measurements [83]. Furthermore, the parallelized read-out of thousands of camera pixels introduced unprecedented multiplexing capabilities to FCS, however, at the cost of temporal resolution [82]. A camera-based implementation termed k-space image correlation spectroscopy was developed by the group of Paul Wiseman, targeting receptor-ligand binding interactions [84].

Taking up the substantial work done in the field [74, 82–85], our co-workers recently developed SI-FCS, again highlighting the potential that lies within using camera-based TIR-FCS for quantitative studies of reversible receptor-ligand interactions [40]. By integrating the detected fluorescence signal over larger Region of Interests (ROIs), our co-workers successfully demonstrated that SI-FCS allows to precisely characterize interactions of ligands with surface receptor-immobilized receptors in combination with a standard TIRF microscope. In a proof-of-principle study, the method was validated based on reversible oligonucleotide hybridization (as in DNA-PAINT), with accessible binding times ranging from hundreds of milliseconds to tens of seconds [40]. The working principle, which is potentially also transferable to study live cell surface binding interactions, is illustrated in Fig. 2.5. SI-FCS is a versatile tool allowing to analyze bimolecular reactions at equilibrium and, importantly, over a wide range of receptor surface densities [40]. SI-FCS is used as a complementary method to assess the influence of photobleaching during DNA-PAINT imaging in Chapter 3.

2.2 DNA Nanotechnology

2.2.1 Repurposing DNA with Novel Functions

Deciphering the structure of DNA and the principles underlying its hybridization has enabled scientists to exploit this remarkable molecule for purposes far beyond its biological function of encoding genetic information. As described in Chapter 1, over the last 40 years DNA nanotechnology has become an extensive field of research [23,

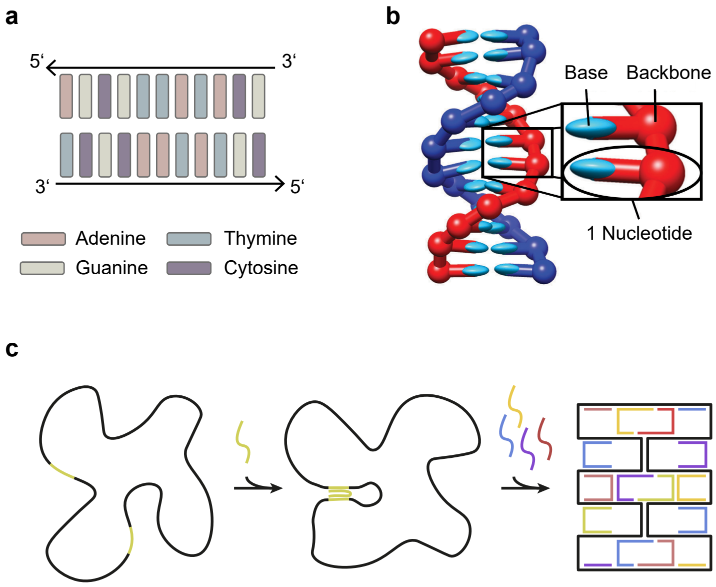

Figure 2.6. The Structural Basis of DNA Nanotechnology. **a** Schematic of Watson-Crick basepairing of two complementary DNA strands. **b** Structure of the double helix formed by two fully-complementary DNA strands. **c** Principle of the DNA origami method. (b) Reprinted from [86] (CC BY-NC 4.0).

24]. In fact, all presented work within this thesis relies on DNA nanotechnology, which is why it is worthwile to revisit the fundamentals about this fascinating molecule.

DNA - Deoxyribonucleic Acid - is a linear polymer built from its constituents termed nucleotides. A nucleotide is a chemical compound comprising one of four nitrogenous bases (Adenine, Thymine, Guanine and Cytosine; short A, T, G, C), a sugar (deoxyribose) and a phosphate group. The chain of nucleotides is linked via covalent bonds in the sugar-phosphate backbone. A DNA strand has a chemical directionality since in the backbone the 3′ oxygen atom of one deoxyribose molecule is linked to the 5′ oxygen atom of the following one via a phosphodiester bond and, therefore, has a 3′- and a 5′ end. Fig. 2.6a schematically illustrates Watson-Crick [87] base pairing of DNA in its double stranded form. Despite the fact that bases can pair with each others in all possible combinations [24], including itself [88], the preferred interaction is A-T via two hydrogen bonds and G-C via three hydrogen bonds. For the double helix to form, both DNA strands need to be fully complementary, i.e., following the A-T, G-C pattern and of opposing directionality. Fig. 2.6b shows a coarse-grained rendering [86] of the double helix, highlighting the backbones of the two strands (red and blue) and the bases facing each others on the inside (cyan). The stability of the helical structure arises not only from the lateral hydrogen bonding, but also substantially from axial ′base-stacking′ via π-electron interactions of the overlying bases.

As previously mentioned in the introduction, the method DNA origami exploits the structural basis of helix formation in order to use DNA as a building material on the nanoscale [24]. In this thesis, DNA origami were prepared using the viral DNA of the m13mp18 bacteriophage as a scaffold material. Fig. 2.6c illustrates the principle of folding this DNA scaffold (black) into a desired and pre-designed shape. The m13mp18 genome consists of a single-stranded loop of ~7,000 bases of known sequence. Upon addition of an oligonucleotide (green) designed to be partially complementary to two highlighted regions on the scaffold strand, this so-called ’staple’ strand will eventually hybridize to both regions, thereby clamping together the two spatially-separated segments. Smart design of many staples (colored) allows to shape the scaffold into desired geometries [25], here indicated by a rectangular shape. Besides making DNA accessible as building material for almost arbitrary 2D and 3D nanoscale structures [24–26], the base complementarity of DNA has also led to its use for specific targeting in fluorescence microscopy in approaches such as Fluorescence In-Situ Hybridization (FISH) [89, 90] or DNA-PAINT [36, 37].

2.2.2 DNA-PAINT

As a Single-Molecule Localization Microscopy method, DNA-PAINT is based on the principle of stochastic on-off switching of single target molecules for downstream localization and super-resolution rendering [36, 37] (see Section 2.1.3). In contrast to PALM and STORM, where the fluorescent label resides permanently attached to its target, the PAINT approach relies on reversible and sparse binding of a fluorescent species to the target of interest [56]. In DNA-PAINT, the target molecules are labeled with short single-stranded oligonucleotides (so-called ’docking strands’). The stochastic blinking is mediated via reversible DNA hybridization of complementary ’imager’ oligonucleotides, which carry a fluorescent dye as a label and are added to the imaging solution (see Fig. 2.7a). Once an imager binds to a docking strand, the immobilized dye molecule emits a local fluorescence burst, which appears as a bright spot on the camera image above the background of fast-diffusing unbound imagers, as depicted in Fig.2.7b. Looking at a single docking strand over time, each time a bright spot appears on the camera, a localization is produced during post-processing. Thus, each docking strand contributes a cluster of localizations to the final super-resolved image. The spatial distribution of a localization cluster is governed by the localization precision [91], typically on the order of a few nanometers in DNA-PAINT [37]. In addition to the spatial information, a localization cluster features a time domain, because the camera frame in which each localization happened is known. This is illustrated schematically in the instensity vs. time trace which can be plotted for each localization cluster.

The repetitive nature of imager binding offers various advantages compared to permanently-attached fluorescent labels. For instance, it decouples the number of localizations achieved per target molecule from the photon budget of a single dye, since even if the dye of an imager bleaches, it can in theory be replenished in an infinite cycle by fresh imagers. A limiting case of docking strand depletion and a corresponding alleviation strategy are discussed in Chapter 3. Furthermore, the imaging solution can be repeatedly exchanged with orthogonal imagers to achieve multiplexed imaging of different targets even in a single color channel [38]. However, the concept of diffusing imagers is not compatible with live cell imaging of intracellular targets, but only applies to fixed cells. Moreover, imaging experiments require some sort of optical sectioning in DNA-PAINT [92, 93] due to the non-fluorogenic nature of imagers causing a high background (i.e., also unbound imagers fluoresce). For

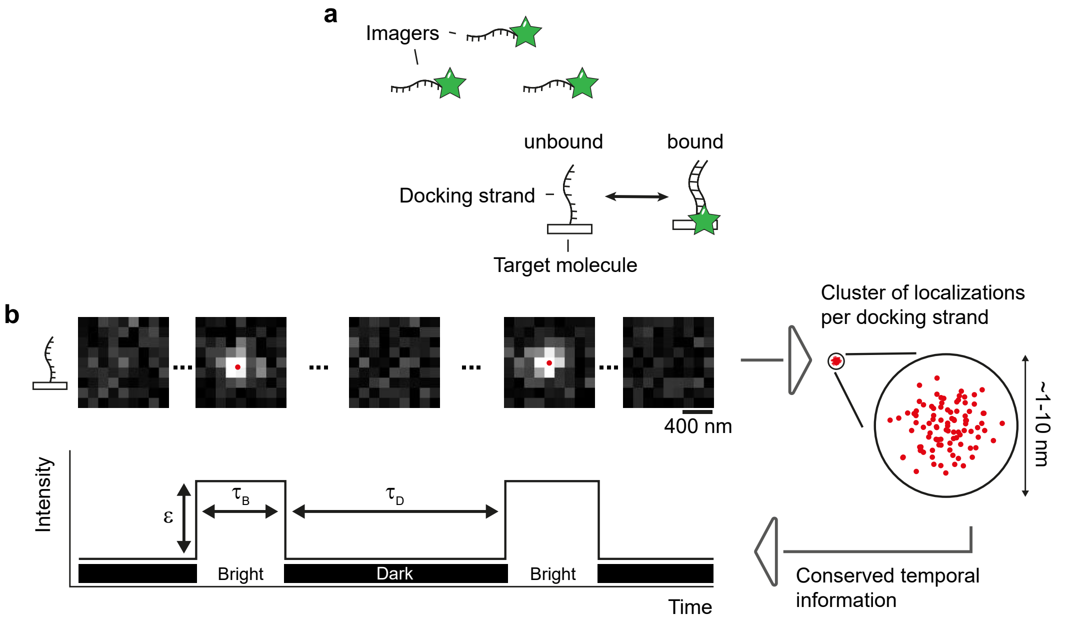

Figure 2.7. Principle of DNA-PAINT. **a** Fluorescently-labeled and freely-diffusing imagers reversibly bind to complementary docking strands, which are attached as label to the target molecule of interest. **b** Exemplary blinking as observed from a single docking strand. Imager binding results in a bright spot on the camera image allowing to localize the target molecule (red point) during post-processing. Each docking strands contributes a cluster of localizations to the final DNA-PAINT image. In these clusters the temporal information of imager binding events is conserved.

this reason, TIRF microscopy is one of the most popular imaging modalities for DNA-PAINT, as further discussed in Chapter 4. In addition, DNA origami is a versatile technology in combination with DNA-PAINT, since patterns of docking strands at defined distances and stoichiometries (i.e., number of docking strands per origami) can easily be implemented on DNA nanostructures for benchmarking and reference experiments [36, 37, 93, 94].

However, the strength of DNA-PAINT that is most central to this thesis is the programmability of the imager binding reaction, enabling advanced quantitative experimental and analysis applications.

2.2.3 DNA-PAINT Kinetics: Receptor-Ligand Binding

In analogy to receptor-ligand interactions, the binding of imagers to docking strands in DNA-PAINT is well-described by a reversible bimolecular chemical reaction:

$$A + B \underset{k_{\mathrm{off}}}{\overset{k_{\mathrm{on}}}{\rightleftharpoons}} C \tag{2.5}$$

Here, A denotes the concentration of freely-diffusing imagers, B the concentration of unbound docking strands and C the concentration of hybridized imager-docking strand complexes (note that for historic reasons the imager concentration will abbreviated as $'c'$ throughout the results part of this thesis). The imager association rate is given by k_{on} and the dissociation rate is given by k_{off}. Accordingly, the fluctuations observed in the intensity vs. time trace of a localization cluster (see Fig. 2.7) due to imager binding events are governed by Eq. 2.5. It has been previously demonstrated that the underlying reaction rates can be calculated from the dwell times in the bound state ('bright time' or τ_{B}) and in the unbound state ('dark time' or τ_{D}) [36, 37]. Cumulative analysis of all τ_{B} and τ_{D} yields k_{on} and k_{off} via the following relations [36]:

$$\tau_{\mathrm{B}} = \frac{1}{k_{\mathrm{off}}} \tag{2.6}$$

and

$$\tau_{\mathrm{D}} = \frac{1}{k_{\mathrm{on}}A} \left(= \frac{1}{k_{\mathrm{on}}c} \right) \tag{2.7}$$

where τ_{B} is the mean bright time and τ_{D} the mean dark time. When considered at equilibrium, the concentration of bound complexes C remains constant over time:

$$\frac{\mathrm{d}}{\mathrm{d}t}C = k_{\mathrm{on}}AB - k_{\mathrm{off}}C = 0 \tag{2.8}$$

It should be noted that k_{on} is a second-order reaction rate (acting on both reactants A and B) and has units (1/Ms). In contrast, k_{off} acting solely on a single reactant C is a first-order reaction rate with units (1/s). Eq. 2.8 can be rewritten as:

$$\frac{AB}{C} = \frac{k_{\mathrm{off}}}{k_{\mathrm{on}}} = K_{\mathrm{D}} \tag{2.9}$$

Here, the dissociation constant K_{D} was introduced as the ratio between k_{off} and k_{on}. K_{D} is a concentration with units (M) and has become the established parameter for characterizing bimolecular chemical reactions with respect to their affinity (the lower K_{D}, the higher the affinity, i.e., the more stable the bound complex).
The binding free energy ΔG of the reaction can be calculated from K_{D} via:

$$\Delta G = -RT \ln \frac{K_{\mathrm{D}}}{K_0} \tag{2.10}$$

where R is the gas constant, T is the temperature and K_0 is a reference concentration of 1 M to ensure that the argument of the logarithm is dimensionless.

In general, for DNA hybridization both k_{on} and k_{off} depend on various factors, such as the olignucleotide sequence design, the temperature or the buffer ion composition [36, 86, 95–97]. Full control over the latter parameters offer a unique programmability to adjust the hybridization reaction according to the desired range. Remarkably, once the experimental parameters are fixed, the hybridization rates can be treated as global constants [97]. This strength has so far been exploited for pseudo-color assignment using kinetic DNA-PAINT barcodes [98] and for molecular counting with DNA-PAINT [39], as further discussed in Chapter 6.

In DNA-PAINT it is favorable to aim for a high k_{on} in order to accelerate imaging, while operating at a moderate imager concentration (see Chapter 5). Typical values that can be reached for k_{on} are on the order of 10^6/Ms at room temperature, e.g., by minimizing secondary structure formation of the imager sequence design [99] or by optimizing the buffer conditions [100].

In contrast, k_{off} should be adjusted according to the expected time it takes for the dye molecule to bleach, which should be longer than the imager dwell time in the bound state τ_B (see Eq. 2.6) in order to prohibit unnecessary occupation of docking strands by bleached imagers [101]. This 'bleaching time' is a function of applied laser excitation irradiance and depends on the experimental requirements. For instance, in Chapter 6 we operated with τ_B on the order of seconds in contrast to a τ_B on the order hundreds of milliseconds in Chapter 5.

The strand design of imagers and docking strands for this thesis was aided by the Nucleic Acid Package (NUPACK) [102]. This useful web-based software suite allows to predict the thermodynamic properties of oligonucleotides based on their sequence, such as the self-interaction probability for single strands or the ΔG of imager-docking strand duplex.

2.3 Localization-Based FCS

2.3.1 Introduction to the Concept

Within the work presented in this thesis, we developed localization-based Fluorescence Correlation Spectroscopy as a novel imaging-based FCS variant. Our motivation was to use lbFCS in combination with DNA-PAINT by precisely measuring the imager binding reaction rates and using the rates as a self-calibraion for molecular counting of docking strands. However, the theoretical working principle of lbFCS derived within this section applies to any reversible bimolecular reaction following Eq. 2.5, for instance protein-nucleic acid and protein-protein interactions. The development was carried out jointly with Florian Stehr in an equally-contributing collaboration and its proof-of-princple demonstration [97] using DNA origami and oligonucleotide hybridization is subject to Chapter 6.

As a starting point, similar to SI-FCS, essentially lbFCS is a camera-based approach allowing to analyze binding interactions between immobilized receptors and fluorescently-labeled ligands. However, instead of integrating the detected fluorescence signal over larger surface areas, individual binding events are localized during post-processing, as in DNA-PAINT (see Fig. 2.8 for a schematic of the working principle). In the rendered PAINT image, given a sparse surface density, thousands of immobilized receptors can each be identified by a cluster of localizations produced by reversible binding interactions with their fluorescently-labeled partner molecules. As described for DNA-PAINT in Section 2.2.2, the temporal binding information is conserved within these localization clusters. Temporal autocorrelation of the localization-based intensity fluctuations, performed for each cluster, provides access to the kinetic rates as well as the number of receptors per localization cluster (in case of multimeric complexes).

Since Chapter 6 comprises a detailed introduction on molecular counting with lbFCS and the motivation of relating localization clusters in SMLM to absolute copy numbers of target molecules, here the concept is only briefly related to its akin FCS variants SI-FCS and confocal FCS with respect to the ability of measuring binding rates. First and foremost, lbFCS is a direct offspring of SI-FCS essentially applying a very similar type of analysis to the examined intensity fluctuations. However,

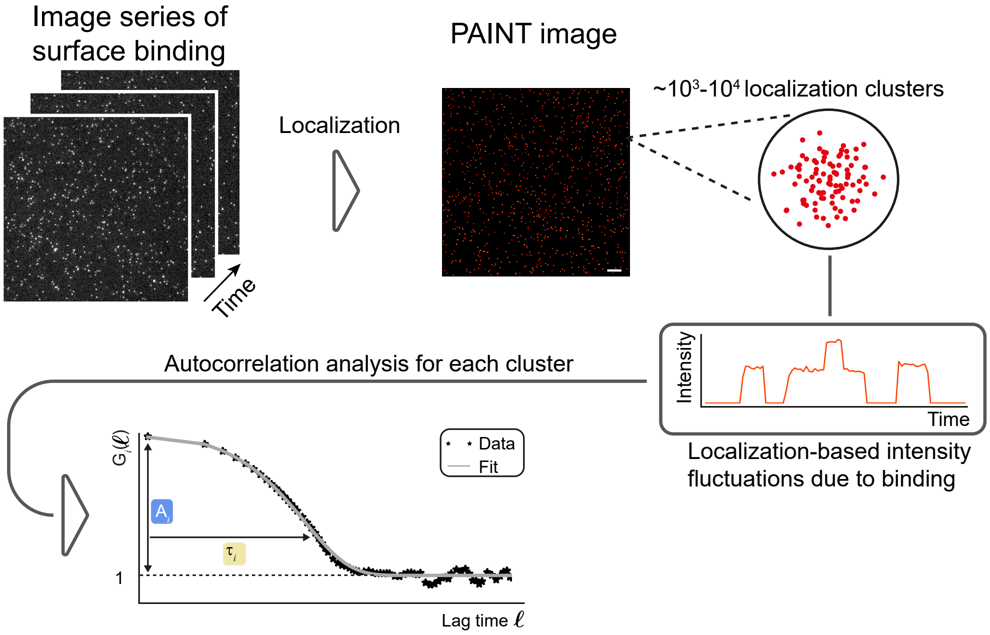
Image series of surface binding
Time
Localization
PAINT image
~10³-10⁴ localization clusters
Intensity
Time
Localization-based intensity fluctuations due to binding
Autocorrelation analysis for each cluster
G(ℓ)
A
τ
1
Data
Fit
Lag time ℓ

Figure 2.8. Principle of Localization-Based FCS. Image series of sparse single molecule binding of a fluorescently-labeled ligand to its surface-immobilized receptor are acquired using TIRF microscopy and subsequently localized as in DNA-PAINT. Localization clusters in the resulting super-resolved PAINT image are subject to temporal autocorrelation analysis providing access to k_{on}, k_{off} and the number of receptors N per localization cluster. Reprinted in parts from [97] (CC BY-NC 4.0).

the obvious differences originate from the intermediate steps of applying a single molecule localization algorithm, rendering a super-resolved image and applying the autocorrelation analysis in parallel to thousands of sub-diffraction-sized 'detection areas' of registered localization clusters. This spatial-selectivity largely eliminates nonspecific surface adsorbtion from lbFCS analysis. Furthermore, the 'all-or-nothing' principle of binding (i.e., the detection of localizations) largely excludes additional dynamics potentially contributing to the autocorrelation function, e.g., 3D diffusion of the fluorescently-labeled ligand close to the glass surface. However, robust localization of single fluorophores requires high signal-to-noise ratios, potentially limiting the working range of lbFCS in its current form compared to SI-FCS and confocal FCS with respect to fast interactions. Additionally, lbFCS allows the continuous observation of thousands of single molecules in parallel while maintaining molecular identity of the immobilized species. Molecular identity denotes the ability to attribute all local ligand binding events observed over time to a single receptor (or a single receptor complex). While in confocal FCS the femtoliter detection volume similarly senses passages of single diffusing or binding molecular species, the molecular identity after each passage or binding event is lost. Similarly, in SI-FCS intrinsically an ensemble of receptors is monitored over a larger surface area. This can become potentially limiting in case of heterogeneous interactions, which might be obscured behind the ensemble mean. Of course, the molecular identity of the diffusing ligands is equally lost in lbFCS, but potential heterogeneities in surface immobilized receptor species can be explicitly sampled at the single molecule level.

2.3.2 Derivation of the Fit-Function in lbFCS

In this section, an analytical expression for the autocorrelation function in lbFCS is derived. The derived framework is in general valid for any bimolecular receptor-ligand interaction (see Eq. 2.5 on page 16) and aims at measuring the reaction rates (k_{on}, k_{off}) as well as at counting the receptor copy number in case of multimeric targets. However, within the work of this thesis, lbFCS was exclusively used to study DNA hybridization dynamics as well as for counting the copy numbers of DNA-PAINT docking strands. Therefore, this derivation is intended to provide a didactic introduction to how the lbFCS obersvables relate to the experimental quantities in DNA-PAINT imaging experiments.

Starting point of our considerations is a single DNA origami structure carrying N independent docking strands, which is immobilized on the glass slide of a closed sample with imagers present at a given concentration c. The reactions of imager binding and unbinding are at equilibirium (i.e., governed by Eq. 2.5), implying that all independent docking strands are subject to globally-valid k_{on}, k_{off} and c during imaging. Furthermore, we assume that this is an ergodic system, i.e., the ensemble average and the time average are equivalent. The excitation laser power is assumed to be adjusted such that influence of photobleaching on k_{off} can be neglegted. After image acquisition and post-processing, the localization cluster obtained from that DNA origami contains the temporal information on all detected imager binding events to the N docking strands in form of a fluctuating intensity signal $I(t)$ at a given point in time t (compare Fig. 2.8). The normalized autocorrelation function of this signal is defined as:

$$G(\ell) = \frac{\langle I(t)I(t+\ell)\rangle}{\langle I(t)\rangle^2} \tag{2.11}$$

where ℓ is the lag time at which the autocorrelation function is evaluated and the angle brackets denote the time average over measurement time T (e.g., $\langle I(t)\rangle = \frac{1}{T}\int_0^T I(t)dt$). Due to the system being at equilibrium, the intensity signal in Eq. 2.11 can be expressed in terms of its mean $\langle I(t)\rangle$ and the fluctuations $\delta I(t)$ around its mean:

$$G(\ell) = \frac{\langle(\langle I(t)\rangle + \delta I(t))(\langle I(t)\rangle + \delta I(t+\ell))\rangle}{\langle I(t)\rangle^2} = \frac{\langle \delta I(t)\delta I(t+\ell)\rangle}{\langle I(t)\rangle^2} + 1 \tag{2.12}$$

Adapting earlier considerations for TIRF-based FCS with respect to surface-immobilized receptor-ligand binding [40, 74, 103], the intensity fluctuations $\delta I(t)$ are equivalent to fluctuations of the number of bound imager-docking strand complexes $\delta C(t)$. Thus, the autocorrelation function can be expressed as:

$$G(\ell) = \frac{\langle \delta C(t)\delta C(t+\ell)\rangle}{\langle C(t)\rangle^2} + 1 = \frac{g_{CC}(\ell)}{\langle C(t)\rangle^2} + 1 \tag{2.13}$$

where $g_{CC}(\ell)$ was introduced as the non-normalized concentration correlation function. Note that in $g_{CC}(\ell)$, t is arbitrary and we can simply set $t = 0$:

$$g_{CC}(\ell) = \langle \delta C(0)\delta C(\ell)\rangle \tag{2.14}$$

As stated in Section 2.2.3, the fluctuations $\delta C(t)$ are governed by:

$$\frac{\mathrm{d}}{\mathrm{d}t}\delta C(t) = k_{\mathrm{on}}c\delta B(t) - k_{\mathrm{off}}\delta C(t) \tag{2.15}$$

where $\delta B(t)$ is the fluctuations of the number of unbound docking strands. Note that the total number of docking strands on the DNA origami is conserved, i.e., $N = B + C$. An increase in C directly implies a decrease in B:

$$\delta C(t) = -\delta B(t) \tag{2.16}$$

This relation allows to transform Eq. 2.15 into a differential equation for $g_{CC}(\ell)$:

$$\begin{aligned} &\frac{\mathrm{d}}{\mathrm{d}\ell}g_{CC}(\ell) = \frac{\mathrm{d}}{\mathrm{d}\ell}\langle\delta C(0)\delta C(\ell)\rangle = \langle\delta C(0)\frac{\mathrm{d}}{\mathrm{d}\ell}\delta C(\ell)\rangle \\ &= \langle\delta C(0)(-k_{\mathrm{on}}c - k_{\mathrm{off}})\delta C(\ell)\rangle = -(k_{\mathrm{on}}c + k_{\mathrm{off}})\langle\delta C(0)\delta C(\ell)\rangle \\ &\Rightarrow \frac{\mathrm{d}}{\mathrm{d}\ell}g_{CC}(\ell) = -(k_{\mathrm{on}}c + k_{\mathrm{off}})g_{CC}(\ell) \end{aligned} \tag{2.17}$$

With the simple solution of an exponential function to this type of differential equation, we obtain our preliminary fit model:

$$G_{model}(\ell) = G_0 e^{-\ell/(k_{\mathrm{on}}c+k_{\mathrm{off}})} \tag{2.18}$$

G_0 is the amplitude of the exponential decay at the boundary condition $\ell = 0$, which will be derived analytically for $G(\ell)$ in the following, starting from the non-normalized autocorrelation function:

$$g(\ell) = \langle I(t)I(t+\ell)\rangle \tag{2.19}$$

The localization-based fluctuating intensity signal $I(t)$ at a given time point t is the sum over the individual signals $I_n(t)$ arising from the N docking strands on the DNA origami:

$$I(t) = \sum_{n=1}^{N} I_n(t) \tag{2.20}$$

Inserting Eq. 2.20 into Eq. 2.19 yields:

$$g(\ell) = \langle\sum_{n=1}^{N} I_n(t)\sum_{m=1}^{N} I_m(t+\ell)\rangle \tag{2.21}$$

Linearity of the average allows to seperate the autocorrelation term from the cross-correlation terms:

$$g(\ell) = \sum_{n=1}^{N}\langle I_n(t)I_n(t+\ell)\rangle + \sum_{m\neq n}^{N}\langle I_n(t)I_m(t+\ell)\rangle \tag{2.22}$$

Note that for independent docking strands the right sum in Eq. 2.22 is constant for all ℓ:

$$\langle I_n(t)I_m(t+\ell)\rangle = \langle I_n(t)I_m(t)\rangle = \langle I_n(t)\rangle\langle I_m(t)\rangle = \langle I_n(t)\rangle^2 \tag{2.23}$$

where we have assumed that i) the signal of two different docking strands is not correlated (independent on ℓ), ii) the average of the product of uncorrelated signals equals the product of the averages and iii) that all docking strands have equal average signals. Inserting Eq. 2.23 into Eq. 2.22 yields:

$$g(\ell) = N\langle I_n(t)I_n(t+\ell)\rangle + N(N-1)\langle I_n(t)\rangle^2 \tag{2.24}$$

In order to normalize $g(\ell)$ we derive an expression of the mean intensity of the signal:

$$\langle I(t)\rangle = \langle\sum_{n=1}^{N} I_n(t)\rangle = \sum_{n=1}^{N}\langle I_n(t)\rangle = N\langle I_n(t)\rangle \tag{2.25}$$

Dividing Eq. 2.24 by the mean intensity squared yields the normalized autocorrelation function $G(\ell)$:

$$G(\ell) = \frac{g(\ell)}{\langle I(t)\rangle^2} = \frac{1}{N}\frac{\langle I_n(t)I_n(t+\ell)\rangle - \langle I_n(t)\rangle^2}{\langle I_n(t)\rangle^2} + 1 \tag{2.26}$$

For the boundary coundition $\ell = 0$, we evaluate $G(\ell = 0)$ in order to find an expression for G_0 (see Eq. 2.18):

$$G(\ell = 0) = G_0 = \frac{1}{N}\frac{\langle I_n(t)^2\rangle - \langle I_n(t)\rangle^2}{\langle I_n(t)\rangle^2} + 1 \tag{2.27}$$

Next we can derive analytical expressions for both $\langle I_n(t)\rangle$ and $\langle I_n^2(t)\rangle$:

$$\langle I_n(t)\rangle = \frac{1}{T}\int_0^T I_n(t)dt \tag{2.28}$$

$$\langle I_n^2(t)\rangle = \frac{1}{T}\int_0^T I_n^2(t)dt \tag{2.29}$$

where T is the total measurement time. Revisiting the schematic intensity trace of a single docking strand depicted in Fig. 2.7, the integral in Eq. 2.28 equals the integrated area over all bright times, which can be expressed as:

$$\int_0^T I_n(t)dt = k \times \tau_{\mathrm{B}}\epsilon \tag{2.30}$$

with k as the total number of binding events , τ_{B} as the mean bright time and ϵ as the mean number of photons detected per localization. Following the same reasoning for $\int_0^T I_n^2(t)dt$:

$$\int_0^T I_n^2(t)dt = k \times \tau_{\mathrm{B}}\epsilon^2 \tag{2.31}$$

For sufficiently long measurement times, T can be expressed in terms of the total number of binding cycles:

$$T = k \times (\tau_{\mathrm{B}} + \tau_{\mathrm{D}}) \tag{2.32}$$

Inserting Eq. 2.30 and Eq. 2.32 into 2.28 and Eq. 2.31 and Eq. 2.32 into 2.29 yields:

$$\langle I_n(t)\rangle = \frac{1}{k(\tau_{\mathrm{B}} + \tau_{\mathrm{B}})} k\tau_{\mathrm{B}}\epsilon = \epsilon \frac{\tau_{\mathrm{B}}}{\tau_{\mathrm{B}} + \tau_{\mathrm{d}}} \tag{2.33}$$

and

$$\langle I_n^2(t)\rangle = \epsilon^2 \frac{\tau_{\mathrm{B}}}{\tau_{\mathrm{B}} + \tau_{\mathrm{d}}} = \epsilon\langle I_n(t)\rangle \tag{2.34}$$

With these two expressions Eq. 2.27 becomes:

$$\begin{aligned} G_0 &= \frac{1}{N}\frac{\epsilon\langle I_n(t)\rangle - \langle I_n(t)\rangle^2}{\langle I_n(t)\rangle^2} + 1 \\ &= \frac{1}{N}\frac{\epsilon - \epsilon\frac{\tau_{\mathrm{B}}}{\tau_{\mathrm{B}}+\tau_{\mathrm{d}}}}{\epsilon\frac{\tau_{\mathrm{B}}}{\tau_{\mathrm{B}}+\tau_{\mathrm{d}}}} + 1 = \frac{1}{N}\frac{\tau_{\mathrm{D}}}{\tau_{\mathrm{B}}} + 1 \end{aligned} \tag{2.35}$$

With the known relations in Eq. 2.6 and Eq. 2.7, G_0 is brought into its final form:

$$G_0 = \frac{1}{N}\frac{k_{\mathrm{off}}}{k_{\mathrm{on}}c} + 1 \tag{2.36}$$

Finally, we arrive at our analytical autocorrelation fit function:

$$G_{model}(\ell) = Ae^{-\ell/\tau} + 1 \tag{2.37}$$

with τ as the characteristic decay constant:

$$\tau = (k_{\mathrm{on}}c + k_{\mathrm{off}})^{-1} \tag{2.38}$$

and the amplitude A:

$$A = \frac{1}{N}\frac{k_{\mathrm{off}}}{k_{\mathrm{on}}c} \tag{2.39}$$

This model function $G_{model}(\ell)$ is fitted to the computed autocorrelation curve of the experimental signal. Closing the loop of the didactic example of a DNA origami in the beginning, we assume now that the DNA-PAINT image contains thousands of (well-separated) localization clusters originating from thousands of DNA origami. Applying lbFCS analysis to each individiual cluster i yields a set of observables (A_i, τ_i), reporting on the targeted quantities of interest (k_{on}, k_{off}, N) at excellent statistics.

Part II

Peer-Reviewed Research Articles

3

Photo-Induced Depletion of Docking Strands in DNA-PAINT

3.1 Motivation and Summary

Theoretically, the bimolecular binding reaction of imagers to their targeted docking strands in DNA-PAINT experiments is perpetual. As a consequence, the number of localizations obtained per individual docking strand should scale linearly with image acquisition time, assuming an infinite reservoir of imagers at a constant concentration. Experimentally, however, a loss of docking strands can be observed for long acquisition times violating this linearity. This is of particular relevance for quantitative DNA-PAINT approaches such as qPAINT [39] and lbFCS [97], when the copy numbers of the target molecule are inferred from the number of detected docking strands within localization clusters. Here, we systematically assay this loss of docking strands in DNA-PAINT and support our observations with complementary SI-FCS measurements of the imager binding kinetics. Our results clearly show a photo-induced depletion of docking strands, which is a consequence of the generation of reactive oxygen species by the dye molecules of bound imagers. We show that the depletion can be effectively surpressed by addition of oxygen scavenging systems, making these ingredients essential for using DNA hybridization as a quantitative tool.

3.2 Publication P1: Photo-Induced Depletion of Binding Sites in DNA-PAINT Microscopy

Photo-Induced Depletion of Binding Sites in DNA-PAINT Microscopy

Philipp Blumhardt, Johannes Stein, Jonas Mücksch, Florian Stehr,
Julian Bauer, Ralf Jungmann and Petra Schwille

Author contributions:

Conceptualization, P.B. and J.M.; Formal analysis, P.B., **J.S.**, F.S. and J.B.; Funding acquisition, R.J. and P.S.; Investigation, P.B. and **J.S.**; Methodology, P.B., **J.S.**, J.M. and F.S.; Project administration, P.B. and **J.S.**; Resources, P.B., **J.S.**, J.M. and F.S.; Software, P.B., **J.S.**, J.M. and F.S.; Supervision, R.J. and P.S.; Validation, P.B., **J.S.** and F.S.; Visualization, P.B., **J.S.**, F.S. and J.B.; Writing—original draft, P.B.; Writing—review & editing, P.B., **J.S.**, J.M., F.S., R.J. and P.S.

published in

Molecules (2018), 23, 12, 3165

Reprinted from [104] under the CC BY-NC 4.0 license.

molecules

MDPI

Article

Photo-Induced Depletion of Binding Sites in DNA-PAINT Microscopy

Philipp Blumhardt [1], Johannes Stein [1], Jonas Mücksch [1], Florian Stehr [1], Julian Bauer [1], Ralf Jungmann [2,3] and Petra Schwille [1,*]

[1] Cellular and Molecular Biophysics, Max Planck Institute of Biochemistry, Am Klopferspitz 18, 82152 Martinsried, Germany; blumhardt@biochem.mpg.de (P.B.); jstein@biochem.mpg.de (J.S.); muecksch@biochem.mpg.de (J.M.); stehr@biochem.mpg.de (F.S.); jubauer@biochem.mpg.de (J.B.)
[2] Molecular Imaging and Bionanotechnology, Max Planck Institute of Biochemistry, Am Klopferspitz 18, 82152 Martinsried, Germany; jungmann@biochem.mpg.de
[3] Department of Physics and Center for Nanoscience, Ludwig Maximilian University, Geschwister-Scholl-Platz 1, 80539 Munich, Germany
* Correspondence: schwille@biochem.mpg.de; Tel.: +49-89-8578-2901

Academic Editor: Jörg Fitter
Received: 31 October 2018; Accepted: 29 November 2018; Published: 30 November 2018

Abstract: The limited photon budget of fluorescent dyes is the main limitation for localization precision in localization-based super-resolution microscopy. Points accumulation for imaging in nanoscale topography (PAINT)-based techniques use the reversible binding of fluorophores and can sample a single binding site multiple times, thus elegantly circumventing the photon budget limitation. With DNA-based PAINT (DNA-PAINT), resolutions down to a few nanometers have been reached on DNA-origami nanostructures. However, for long acquisition times, we find a photo-induced depletion of binding sites in DNA-PAINT microscopy that ultimately limits the quality of the rendered images. Here we systematically investigate the loss of binding sites in DNA-PAINT imaging and support the observations with measurements of DNA hybridization kinetics via surface-integrated fluorescence correlation spectroscopy (SI-FCS). We do not only show that the depletion of binding sites is clearly photo-induced, but also provide evidence that it is mainly caused by dye-induced generation of reactive oxygen species (ROS). We evaluate two possible strategies to reduce the depletion of binding sites: By addition of oxygen scavenging reagents, and by the positioning of the fluorescent dye at a larger distance from the binding site.

Keywords: DNA-PAINT; surface-integrated fluorescence correlation spectroscopy (SI-FCS); reactive oxygen species; photo-induced DNA damage; super-resolution microscopy

1. Introduction

Super-resolution microscopy has greatly contributed to the study of biological specimens with resolutions down to few nanometers while retaining the high specificity of fluorescent labels [1–3]. The stochastic blinking of individual fluorophores enables the precise localization of molecules in various single molecule localization microscopy (SMLM) methods. In many variants of SMLM, in particular the prominent PALM [4,5] and (d)STORM [6,7], the number of photons available from permanently bound, individual fluorophores determines the achievable localization precision [8,9]. In particular, the spatial information from non-functional or immediately photo-bleached labels is entirely lost. In contrast, points accumulation for imaging in nanoscale topography (PAINT) [10] generates the blinking of fluorophores by reversible binding reactions. While an individual binding event is still limited by the photon-budget of the fluorescent dye, binding sites can be revisited by fresh probes and thus contribute to higher resolved images [11]. In DNA-based PAINT (DNA-

PAINT) [11,12] the structure of interest is labeled with a short DNA single strand (docking strand), serving as binding site for fluorescently labeled complementary single (imager) strands. The formed duplex immobilizes the imager for the time of binding and creates a bright, localized spot on the detector, usually a sensitive camera, while freely diffusing imager strands remain blurred as a constant background intensity.

Transient binding reactions not only enable super-resolution microscopy, but their kinetics also reflect on the nature of the binding process. Under appropriate imaging conditions, the kinetics of the transient binding can be directly extracted from time traces of the localization data [12,13]. In samples with high densities of binding events, where localization fails, fluorescence correlation spectroscopy (FCS) can reliably extract binding kinetics [14–16]. We recently showed that surface-integrated fluorescence correlation spectroscopy (SI-FCS) can determine the kinetic rates of transient DNA hybridization [15].

However, the advantage of DNA-PAINT in that individual binding sites are revisited is limited for long acquisitions, due to photo-induced damages, effectively creating an upper limit for the image quality. In addition, SI-FCS experiments suffer from the depletion of bindings sites, complicating the correct extraction of kinetic rates. Unwanted photo-induced effects are intrinsic to fluorescence microscopy [17,18]. Excited states of fluorescent molecules in general, but in particular long-lived triplet states, are prone to oxidation or reduction and the subsequent generation of highly reactive molecules [18–22]. Triplet states have been found to play a role in photo-bleaching pathways and to promote the generation of reactive oxygen species (ROS) [19,22–28]. ROS are not only known to bleach fluorescent dyes [18,29] and have phototoxic effects on biological samples [30,31], but also to damage DNA [32,33].

The damage induced by ROS is significantly reduced by the use of oxygen scavenging buffers that remove molecular oxygen from solution and thereby lower the amount of reactive oxygen species. The popular enzymatic oxygen scavenging system glucose oxidase, catalase and glucose (GO+C) [34,35] produces gluconic acid, consequently acidifying the sample. GO + C is thus not suited for long acquisitions or pH dependent systems [36–38]. An alternative systems is the combination of protocatechuate-dioxygenase and 3,4-protocatechuic acid (PCD+PCA) [39,40]. The oxidation of PCA produces muconic acid, but at the same time has a buffering effect around pH 8, leading to improved pH stability compared to GO+C [41]. More recently, pyranose oxidase, catalase and glucose (PO+C) have been reported as effective oxygen scavengers with no acidifying effect over the time span of hours [41]. In particular, when studying the DNA duplex formation above the melting temperature, prerequisite for DNA-PAINT imaging, the reaction kinetics are sensitive to the pH of the solution and salt concentrations [12].

Since molecular oxygen acts as triplet quencher, its removal increases the triplet lifetime, leading to long-lived dark states and decreased fluorescence [18,22,42]. The vitamin E analog Trolox has been found to serve as effective triplet quencher in combination with oxygen scavenging systems, resulting in comparably bright and photostable fluorescence imaging conditions [43,44]. In this study, we systematically investigate the stability for long acquisition time series in DNA-PAINT microscopy and SI-FCS kinetic measurements. We provide two practical solutions to the inherent problem of phototoxicity, by comparing two oxygen scavenging reagents, and by presenting a modified imager that utilizes a higher distance of fluorescent dye to docking site.

2. Results

To systematically investigate the effect of the photo-induced depletion of binding sites, we compared DNA-PAINT super-resolution microscopy and SI-FCS kinetic measurements from samples in the presence and absence of oxygen scavenging systems. If the depletion of binding sites is caused by ROS, oxygen scavenging buffers will lead to a longer lifetime of binding sites. Additionally, we probed whether the distance of fluorescent dye to the docking strand influences the rate of depletion. To achieve optimal resolution in SMLM, the fluorescent dye is conventionally placed in closest possible proximity to the labeling site. In DNA-PAINT, this is easily achieved by design. In many cases, including this study, the DNA origami scaffold and the fluorescent probe on the imager strand are upon binding only separated by a short spacer [11,12,45]. This arrangement, however, also creates ROS close to the docking strand, and is therefore prone to damaging of DNA bases resulting in an increased depletion rate of binding sites. Assuming an isotropic diffusion of ROS, an increase in the distance between fluorescent dye and the docking strand ought to decrease the probability for interaction. We investigated the depletion of docking sites in the following five conditions (Figure 1):

1. Conventional: we used standard conditions as commonly found in DNA-PAINT super-resolution microscopy and SI-FCS measurements [11,15];
2. Oxygen scavengers:
   a) PO+C: we added PO+C as oxygen scavenging system and Trolox as triplet quencher to samples otherwise identical to (1);
   b) PCD+PCA: as in (2a), but with PCD+PCA as oxygen scavenging system and Trolox added;
3. 18-mer spacer:
   a) we extended the 10-nucleotide (nt) imager by an additional 18-mer double stranded spacer sequence to attach the dye at greater distance from the hybridizing docking strand, maintaining otherwise conditions as in (1);
   b) we added PO+C as in (2a) to samples otherwise identical to (3a).

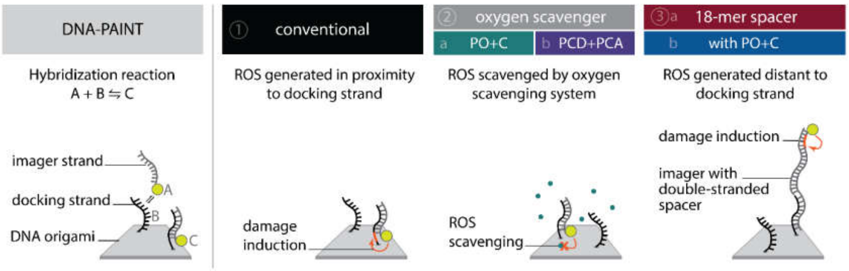
DNA-PAINT
Hybridization reaction
A + B ⇆ C
imager strand
A
docking strand
B
DNA origami
C
① conventional
ROS generated in proximity to docking strand
damage induction
② oxygen scavenger
a PO+C
b PCD+PCA
ROS scavenged by oxygen scavenging system
ROS scavenging
③a 18-mer spacer
b with PO+C
ROS generated distant to docking strand
damage induction
imager with double-stranded spacer

Figure 1. Schematic of DNA-PAINT with the binding of imager strands (A) to docking strands (B) forming the hybridized duplex (C) (left panel). Overview of the conditions to explore the photo-induced depletion of binding sites in DNA-PAINT microscopy and kinetic measurement with SI-FCS (right panel): (**1**) conventional 9 nt overlapping imager, (**2**) identical imager as in (1) but in presence of a oxygen scavenging system (2a: PO+C or 2b: PCD+PCA), (**3a**) a modified imager with identical binding sequence and buffer conditions as in (1) but extended by an double-stranded spacer, increasing the distance of dye and docking strand and (**3b**) the combination of 18-mer spacer and PO+C. ROS scavenging and an increased distance of the fluorescent dye to the docking strand are ought to decrease the rate of depletion of docking sites.

Depletion of binding sites in DNA-PAINT manifests itself in a decrease in the number of localizations with increasing measurement time (Figure A1, left panel, raw data is available as supplementary material). To study the underlying effect, two processes have to be disentangled: First, the bleaching of fluorescence imager strands in solution, and second, a depletion of docking sites. The effective concentration of fluorescent imager strands within the total internal reflection fluorescence (TIRF) excitation volume can be assumed equilibrated with the bulk solution concentration, as the exchange rate of imager strands from solution by diffusion is about four orders of magnitude faster than the exposure time or minimum correlation time (Figure A2). Bleaching of the bulk imager solution is usually negligible in DNA-PAINT, as the reservoir of fluorophores in solution is large enough so that the concentration of fluorescent dye is not affected by imaging a small volume via TIRF illumination. Accordingly, moving the sample laterally by more than the size of the illumination fully recovers the number of initial localizations (Figure A1, right panel). Thus, photo-bleaching does not significantly affect the bulk dye concentration. The second effect, the depletion of binding sites, however, affects the surface-immobilized sample, therefore dominates in the observation region and accumulates over time.

To observe the photo-induced depletion of docking sites under conventionally used imaging conditions, we rendered super-resolved DNA-PAINT images from five subsets of one 25,000 frame or 83-min-long acquisition at a peak irradiance of $I_0 = 0.2\ \mathrm{kW/cm^2}$, allowing for the localization of individual binding sites. Depending on the particular application, DNA-PAINT experiments are conventionally performed with peak irradiances up to $6\ \mathrm{kW/cm^2}$ [11], further enhancing the problem of photo-induced damages. The first subset, covering the first 17 min, renders a super-resolved image with the majority of docking sites visible. Due to the limited incorporation efficiency, not all docking sites are observable in the first subset [46]. Later subsets show a decreasing number of localized binding sites, indicating that less docking strands are available for hybridization of imager strands on the DNA origami scaffold (Figures 2a and A3). Time traces of localizations within circular areas enclosing the individual docking sites show frequent binding events in the beginning of the acquisition, but eventually turn dark during the measurement (Figure 2b).

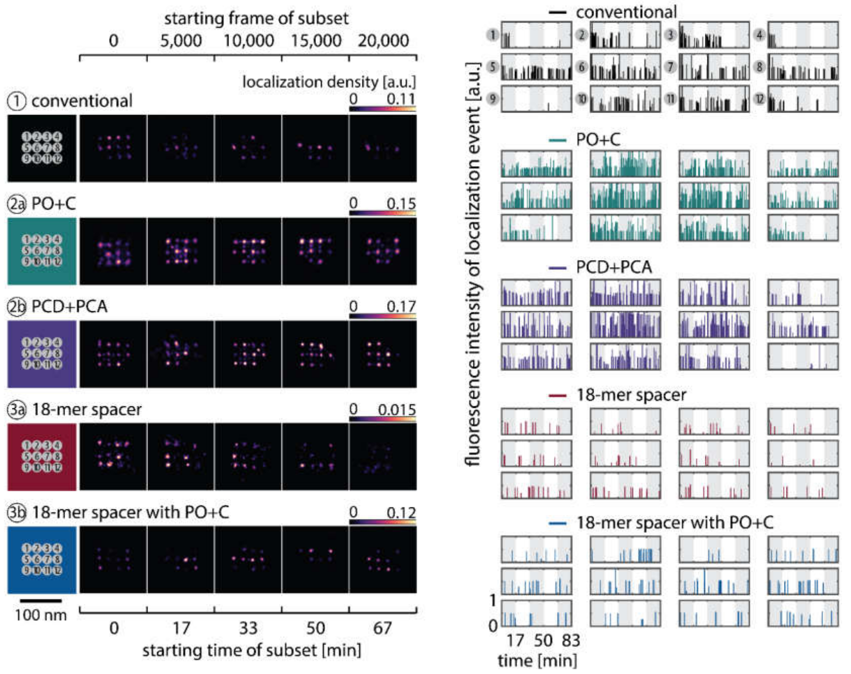

(**a**) (**b**)

Figure 2. Long DNA-PAINT acquisition of DNA origami nanostructures with 12 exposed docking strands arranged in a 3 × 4 grid with 20 nm spacing. Five conditions are displayed: conventional imager (1, black), conventional imager with oxygen scavenging system added (2a: PO+C, turquoise; 2b: PCD+PCA, purple), imager with 18-mer spacer between docking sequence and fluorescent dye (3a, red) and the 18-mer spacer with PO+C (3b, blue). **(a)** Time series of representative super-resolved DNA-PAINT images, reconstructed from five subsequent 5,000 frame long subsets of a 25,000 frame long acquisition (in total 83 min). Additional examples are listed in the appendix (Figure A3). Scale Bar: 100 nm. **(b)** Time traces of localizations within circular areas picked as individual bindings sites. The alternating shade of the background indicates the five subsets. DNA-PAINT raw data is available as supplementary material.

We further quantitatively investigated the depletion of binding sites in DNA-PAINT microscopy by automated alignment and averaging of the acquired DNA origami nanostructures (Figure A4), as published previously [11,46]. The drift correction, identification and averaging of nanostructures were performed on the complete time series prior to division into the subsets. Selected individual binding sites on the averaged image were then back-translated to individual nanostructures (Picasso: 'Unfold') to analyze the intensity trace of each docking site individually. To account for rare unspecific binding events, only traces with more than three localizations per subset were counted as active docking sites. This cutoff slightly changes the absolute numbers of active docking sites, but does not influence the qualitative shape of the observed decays. Following this analysis, roughly 10 docking sites are on average detected as active in the initial subset for the conventional imager in absence (1) and presence of oxygen scavenging buffers (2a,b) (Figure 3a, left panel), in agreement with previous investigations [46]. With increasing measurement time, increasing numbers of docking sites become inactive, leaving on average six binding sites per nanostructure active, with the conventional imager at the end of the time series. In stark contrast, less than one binding site is depleted on average during the entire measurement in presence of oxygen scavenging buffers. The depletion of binding sites is limited to the irradiated sample region, and non-irradiated areas are indistinguishable from a fresh sample (Figure 3a, right panel). In case of the 18-mer spacer (3a,b), we observe a decreased association rate, leading not only to a lower number of localizations, but also to docking sites not being visited frequently enough to classify docking sites reliably as active within one subset. Using the whole time series to identify docking sites, the total number of active docking sites is recovered to about 10, similar to the conventional imager (Figure A5). Irrespective of the low association rate, docking sites are also depleted for the imager carrying the 18-mer spacer ($I_0 = 0.2$ $\mathrm{kW/cm^2}$) (Figure 3a). For the combination of 18-mer spacer and oxygen scavenger PO+C (3b), we observe an increased error rate within the automated structure alignment and a slightly decreased number of active docking sites (Figure A5). As mentioned, the cut-off for unspecific binding events does not influence the qualitative shape of the decay.

Further, the depletion can also be analyzed based on the kinetics of the reoccurring binding events to individual DNA origami. We use the well-established analysis of the duration of individual binding events and the time span between two consecutive binding events, referred to as bright time τ_B and dark time τ_D, respectively [11–13]. For the conventional imager strand (1), we observe an increasing dark time for later subsets, which directly reflects on the depletion of binding sites (Figure 3b, top). For completely depleted binding sites, the dark time becomes theoretically infinite. In practice, noise misinterpreted as localization event limits the dark times and leads to a large scatter of the distribution of dark times for later subsets. With the addition of oxygen scavenging buffers (2a,b), the average dark time appears shorter and does not show any significant dependence on the measurement time, indicating a strong reduction in the depletion of binding sites. The two oxygen scavenging systems PO+C and PCD+PCA seem to perform similarly well in reduction of the depletion. For the 18-mer spacer, dark times are higher as for the conventional imager, reproducing the apparent lower association rate (Figures 2b and 3b). Without oxygen scavengers (3a), an increase in dark times is observed, as depletion of binding sites is induced under the chosen irradiation conditions. Adding oxygen-scavenger to the 18-mer spacer (3b) stabilizes the dark times on the level observed in the first subset without oxygen scavengers (3a).

The bright time τ_B, in return, is stable or slightly decreases with time (Figure 3b, bottom). The conventional imager and the 18-mer spacer show similar bright times, shortened by the photobleaching of the fluorescent dye to less than 2 seconds. With the addition of oxygen scavenging buffers, the bright times increase to roughly 4 seconds, matching the values expected from SI-FCS measurements for a bleaching-free regime (Table 1 from SI-FCS results below). The observed slight decrease in bright time can be attributed to an artifact arising for two simultaneous binding events that are misinterpreted by the localization algorithm [11] as one longer binding event (Figure A6). The more binding sites are accessible, the higher is the probability for two imager strands to bind simultaneously. With increasing measurement time and according depletion of binding sites, the probability to bind two imager strands decreases, and thus the bright time approaches its true value in the later subsets. The dependencies of dark and bright time on the number of docking sites per nanostructure appear similarly in simulations (Figure A6b). Experimentally, the decreasing bright time can be avoided by lower imager concentrations at the cost of extended measurement times to maintain the total amount of localizations. The increasing dark time, however, is intrinsic to the depletion of docking sites and can particularly hinder quantitative analyses based on the association rate [13].

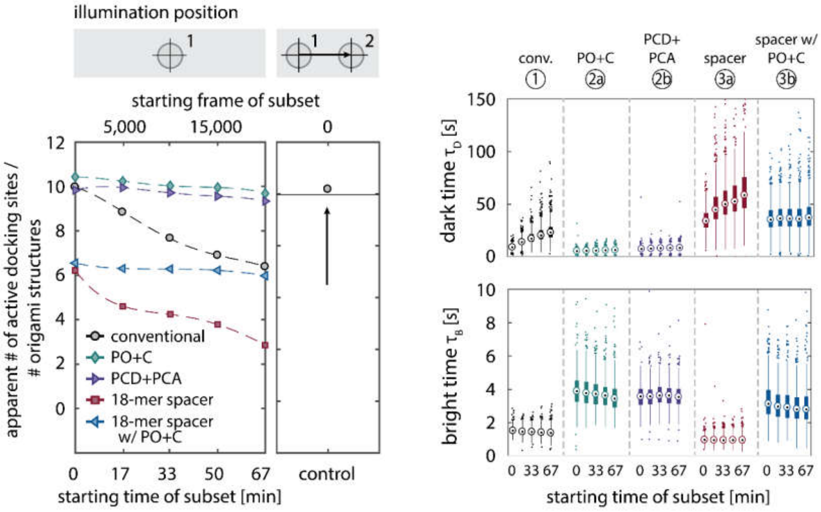

(a) (b)

Figure 3. Quantitative analysis of the depletion of docking strands in DNA-PAINT super-resolution microscopy. The five conditions displayed are identical to Figure 2. (**a**) Left panel: active docking sites are counted individually on DNA origami nanostructures, based on the back-translation of the position of docking sites picked on automatically averaged nanostructures (Figure A4) and divided by the total number of identified origami structures. The dashed line is a guide to the eye. Right panel: a control of 5,000 frames, equivalent to the first subset, was measured in a previously not irradiated area on the same sample and compared to the initial number of active docking sites (solid horizontal line) for the conventional condition (right panel). The total numbers of identified DNA origami nanostructures for the five conditions are: (1) 786, (2a) 824, (2b) 566, (3a) 690, (3b) 580 and 690 for the control of condition (1). (**b**) Box plots of the bright times τ_B and dark times τ_D for the subsets shown in (a). Circles indicate the median; bottom and top edges of the box (bold vertical lines) indicate the 25 th and 75 th percentiles, respectively. The whiskers extend to the data points not considered outliers (thin vertical lines); outliers are plotted individually as dots.

The high irradiances necessary for precise localization of fluorophores in super-resolution microscopy lead to a high probability of photo-bleaching fluorophores while still being attached to the docking strand [15], thus adding an additional layer of complexity. To further separate the effect of photo-bleaching from the depletion of individual binding sites, we analyzed the hybridization kinetics in a low irradiance regime ($I_0 = 0.018\ \mathrm{kW/cm^2}$) with surface-integrated fluorescence correlation spectroscopy (SI-FCS) [15]. The fluctuations in fluorescence intensity of transiently hybridizing imager and docking strands are analyzed to extract the binding rates. This approach does not rely on any localization or discrimination of individual binding events and can thus be performed at orders of magnitude lower irradiances. Nonetheless, SI-FCS traces exhibit a decaying mean fluorescence intensity that is accounted for by a monoexponential detrending of the intensity trace before the autocorrelation [15]. The fluorescence intensity $I(t)$ of each integrated region is fitted and subsequently divided by:

$$I(t) = I_0 \exp(-\kappa\, t) + I_\infty, \tag{1}$$

with the effective depletion rate κ characterizing the loss in fluorescence intensity, the amplitude I_0 and the offset I_∞ (Figure A7). For a one-component reversible binding, the SI-FCS autocorrelation function $G_N(\tau)$, with the amplitude normalized to one, is an exponential function decaying with a characteristic decay time τ_c:

$$G_N(\tau) = \exp\left(-\frac{\tau}{\tau_c}\right), \tag{2}$$

A detailed derivation of the SI-FCS autocorrelation function is found in [15]. The monoexponential correction (Equation 1) allows the accurate quantification of kinetics via SI-FCS, when the characteristic decay time τ_c of the autocorrelation function (ACF) is much shorter than the characteristic time of detrending ($\tau_c \ll 1/\kappa$).

With higher average concentration of fluorescent imager in solution $\langle A \rangle$, the probability of docking sites to be occupied increases. In SI-FCS, an increase of imager concentration manifests itself as a decrease of the characteristic decay time τ_c, which can be expressed in terms of the association and dissociation rates k_a and k_d, respectively:

$$\tau_c(\langle A \rangle) = \frac{1}{k_a \langle A \rangle + k_d} \tag{3}$$

We performed five titration series of the imager concentration $\langle A \rangle$ with otherwise identical conditions as described above: with conventional imager in absence of oxygen scavenging buffers (1), with PO+C added (2a), PCD+PCA added (2b), with the 18-mer spacer (3a), and the combination of 18-mer spacer and PO+C (3b). We obtained similar hybridization rates for conventional imager with and without oxygen scavenger system (Figure 4a). Comparing the conventional to the oxygen-scavenged buffer, the dissociation rate is slightly lowered ($(0.303 \pm 0.010)\ \mathrm{s}^{-1}$ compared to $(0.268 \pm 0.017)\ \mathrm{s}^{-1}$, and $(0.25 \pm 0.02)\ \mathrm{s}^{-1}$ for conditions (1), (2a), and (2b) respectively). This decrease is potentially caused by residual photo-bleaching of bound fluorophores, which was previously not observed when determining a bleaching-free regime by variation of the excitation power [15]. The imager with 18-mer spacer (3a,b) shows a decreased association rate (Figure 4b), in agreement with the lower binding frequency observed in DNA-PAINT traces (Figure 2b) and the higher dark times (Figure 3b). A lower association rate can be caused by different steric features of the imager, which are reflected by a larger hydrodynamic radius. We determined the translational diffusion coefficient as $(120 \pm 20)\ \mu\mathrm{m}^2/\mathrm{s}$ for the 18-mer spacer, being by a factor 1.7 smaller than the diffusion coefficient of the conventional imager (Figure A2c). We observe a difference for the association rate in absence (3a) and presence (3b) of PO+C only slightly larger than the estimated error of the measurement. The dissociation rate is similar to the conditions in presence of oxygen scavenging buffer (Table 1).

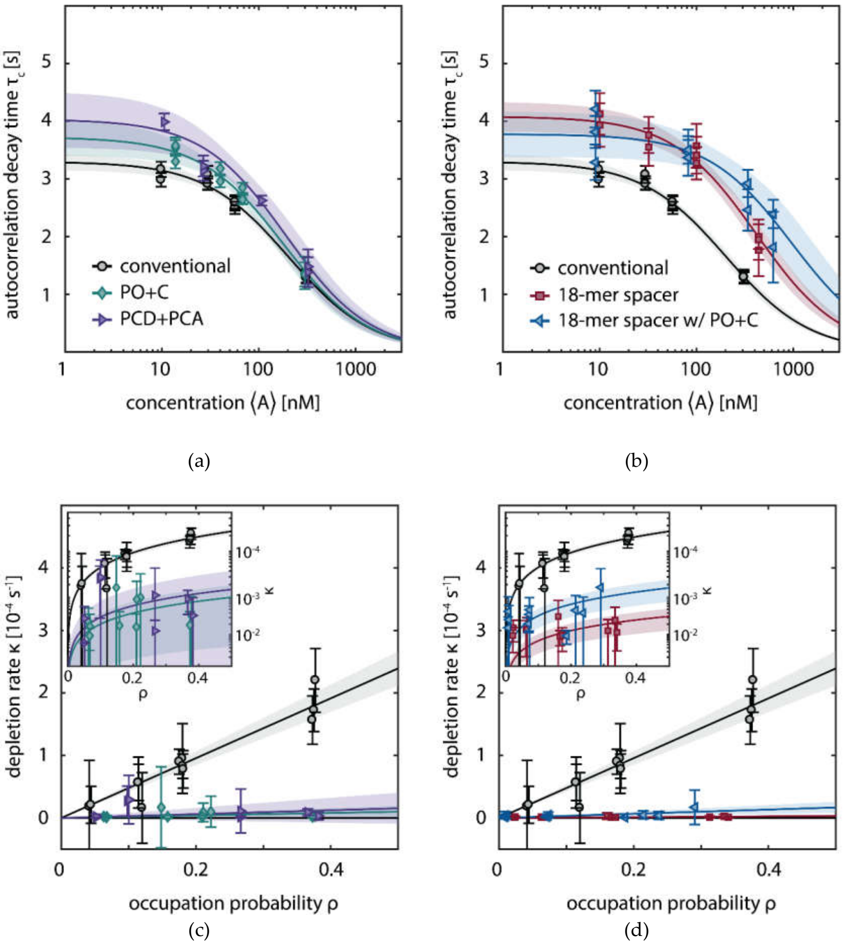

(a) (b)

(c) (d)

Figure 4. Depletion of docking sites investigated by SI-FCS at low irradiance (0.018 kW/cm^2). (**a**) Titration series of the imager concentration $\langle A\rangle$ with 9 nt overlap for conventional imager strands (black), addition of oxygen scavenging system PO+C (turquoise) and PCD+PCA (purple). Data points and error bars represent mean and standard deviation from 64 regions of interest (5.1 × 5.1 µm), respectively. Solid lines show the fit to equation (2). The 95% functional error bounds are displayed as shaded areas. (**b**) As (a) but comparing the conventional imager to the 18-mer spacer (red) and 18-mer spacer with PO+C (blue). **(c)** The effective depletion rate κ (Equation 1) of docking strands depends linearly on the occupation probability ρ, which is calculated from the concentration and the kinetic rate constants according to equation (6). Solid lines show the fit to equation (4). Data points and errors are displayed as described in (a). The inset shows the depletion rate κ on a logarithmic scale. (**d**) Samples as in (b) displayed as in (c). SI-FCS raw data is available as supplementary material.

Table 1. Binding kinetics as measured by SI-FCS titrations of the imager concentrations $\langle A \rangle$. Hybridization rates and affinity as obtained from the titrations in Figure 4. The errors represent the 95% confidence bounds of the fit.

Imaging Condition	k_a **[$10^6 \cdot$ Ms^{-1}]**	k_d **[s^{-1}]**	K_d **[nM]**
conventional	1.49 ± 0.17	0.303 ± 0.010	200 ± 30
PO+C	1.5 ± 0.4	0.268 ± 0.017	180 ± 60
PCD+PCA	1.3 ± 0.4	0.25 ± 0.02	190 ± 70
18-mer spacer	0.59 ± 0.11	0.245 ± 0.012	420 ± 100
18-mer spacer with PO+C	0.28 ± 0.12	0.26 ± 0.02	1000 ± 500

To investigate the effect of depletion of binding sites in SI-FCS, we compared the rate of the detrending κ (Equation 1 and Figure A7a) in absence and presence of oxygen scavenging buffers and the 18-mer spacer. If the process of depletion of docking sites is mediated by the fluorescent dye, only hybridized duplexes create damages. Therefore, κ represents an effective depletion rate, which is given by a depletion rate constant δ specific to the investigated system, lowered by multiplication with the occupation probability $\rho(\langle A \rangle)$ of docking sites:

$$\kappa(\rho) = \delta \cdot \rho(\langle A \rangle), \tag{4}$$

The occupation probability ρ is intuitively accessible as the fraction of the bright time τ_B to the duration of one binding cycle, represented by the sum of bright and dark time $(\tau_B + \tau_D)$:

$$\rho = \frac{\tau_B}{\tau_B + \tau_D} \tag{5}$$

Bright and dark times are principally accessible from low irradiance PAINT measurements, allowing for the individual detection of docking sites. High irradiances, however, as required to resolve multiple narrow spaced binding sites on one DNA origami nanostructure, reduce the bright time and hinder the direct determination of the occupation probability. Without the need for localization, ρ can be expressed in variables accessible from SI-FCS titrations, in particular the association rate $k_a = 1/(\tau_D \langle A \rangle)$ and the dissociation rate $k_d = 1/\tau_B$, as:

$$\rho = \frac{1}{1 + k_d (k_a \langle A \rangle)^{-1}} \tag{6}$$

Experimentally, we determine the specific depletion rate constant δ by varying the concentration $\langle A \rangle$ of fluorescent imager in solution (Equation (4)). For the conventional imager (1), we confirm the linear dependence of $\kappa(\rho)$ with a slope of $\delta_{\mathrm{conv}} = (470 \pm 40) \cdot 10^{-6}\ \mathrm{s}^{-1}$. Strikingly, the slope δ decreases by two orders of magnitude when oxygen scavenger is added (Figure 4c), thus nearly eliminating the depletion of binding sites ($(20 \pm 19) \cdot 10^{-6}\ \mathrm{s}^{-1}$ and $(30 \pm 50) \cdot 10^{-6}\ \mathrm{s}^{-1}$, for PO+C and PCD+PCA, respectively). Similarly, the 18-mer spacer reduces the depletion rate to $(7 \pm 4) \cdot 10^{-6}\ \mathrm{s}^{-1}$ and $(33 \pm 18) \cdot 10^{-6}\ \mathrm{s}^{-1}$ in absence and presence of PO+C, respectively (Figure 4d). For the low irradiances ($I_0 = 0.018\ \mathrm{kW/cm^2}$), employed in SI-FCS, the effect of depletion of binding sites approaches zero for both oxygen scavenging systems and the 18-mer spacer. As apparent from the estimated errors of the individual measurements, the differences observed for the close to zero depletion rates are indistinguishable within the precision of the measurement. The depletion is only distinguishable from zero at high imager concentrations (Figure 4b and Table 2).

Table 2. Slope of the linear fit of equation (4) to the depletion rate $\kappa(\rho)$ in Figure 2. The errors represent the 95% confidence bounds of the fit.

Imaging Condition	$\delta\ [\mathbf{10^{-6} \cdot s^{-1}}]$
conventional	480 ± 55
PO+C	20 ± 19
PCD+PCA	30 ± 50
18-mer spacer	7 ± 4
18-mer spacer with PO+C	33 ± 18

3. Discussion

To summarize, we have confirmed that docking strands in DNA-PAINT microscopy are depleted by irradiation with visible light in an indirect process mediated by the excitation of fluorescent dyes. DNA-PAINT microscopy with long acquisition series showed that individual docking sites get irreversibly lost in irradiated areas (Figure 2 and 3). In the majority of SMLM methods, the resolution and signal-to-noise ratio (SNR) of super-resolved images are limited by the photon-budget of fluorophores irreversibly bound to labeled sites [8,9]. Making use of the reoccurring binding and a large reservoir of fluorescent imager, DNA-PAINT is less limited by the photo-bleaching of fluorophores to precisely localize binding sites [11]. In this work, we showed that DNA-PAINT is ultimately limited by the eventual damage of docking sites.

We showed evidence that the depletion of docking strands of DNA origami nanostructures is caused by damages of DNA handles and can thus be distinguished from photo-bleaching of fluorophores (Figure 3). In our SI-FCS experiments, we find a linear dependence of the effective depletion rate on the presence of fluorescently labeled imager (Figure 4c,d). This does not only show that the depletion process is mediated by bound fluorophores, but it also indicates that direct photo-damage of DNA is negligible compared to fluorophore-mediated damages. Our experiments in oxygen scavenging buffers strongly indicate the involvement of ROS in the depletion of available docking strands. Not only do we see a significantly reduced depletion in high irradiance DNA-PAINT microscopy ($I_0 = 0.2\ \mathrm{kW/cm^2}$) (Figures 2 and 3), but also in low irradiance SI-FCS measurements ($I_0 = 0.018\ \mathrm{kW/cm^2}$), we observed a close to zero depletion rate (Figures 4c,d and Table 2). The importance of ROS for photo-induced damages following fluorescence excitation has been studied not only in the context of fluorescence photo-bleaching [18,19,22,27–29], but also phototoxicity [30,31] and in particular DNA damage [32,33,47]. ROS have also been shown to contribute to photo-induced unbinding of proteins [48,49]. Generally, ROS are one of the main sources for DNA damage and have been intensively investigated in relation to several kinds of cancer [50–53]. Our results show the cause for the depletion to be ROS generated downstream of the fluorescence excitation, diffusing to the DNA origami nanostructures and finally damaging the exposed docking stands. From our experiments, it is not possible to identify the type of created ROS, the type of induced DNA damage or the affected DNA bases. Different ROS, most prominently singlet oxygen and superoxide radicals, are supposedly formed from excited fluorescent states [29,54]. The likelihood and type of induced damage is reported to be sequence dependent and enriched at duplex ends [33]. Previous studies suggest that guanine is preferentially damaged, due to its lowest redox potential among the DNA bases [55–57]. Not only were oxidation products frequently found in guanine repeats [33,55], but also electron hole diffusion along the DNA leads to guanine oxidation distant from the site of single electron transfer [58–60]. On the other hand, adenine and thymine are the predominant bases on the docking strand that are closest to the fluorescent dye upon imager binding. Thus, most likely, a variety of damage types is induced simultaneously.

The probability of a ROS to reach a docking site by 3D diffusion scales with the squared distance between both, assuming a much longer free path length of the ROS [61,62]. Accordingly, a larger spacing between docking strands and fluorophores reduced the depletion of binding sites (Figure 4b) at low irradiances ($0.018\ \mathrm{kW/cm^2}$). Oxygen scavenging buffers and the 18-mer spacer show similar depletion rate constants ($(20 \pm 19) \cdot 10^{-6}\ \mathrm{s^{-1}}$, $(30 \pm 50) \cdot 10^{-6}\ \mathrm{s^{-1}}$ and $(7 \pm 4) \cdot 10^{-6}\ \mathrm{s^{-1}}$, for PO+C, PCD+PCA and 18-mer spacer, respectively), suggesting that both are similarly effective in eliminating photo-toxic effects (Figures 4c,d and Table 2). Addition of PO+C to the 18-mer spacer did not show any further improvement for SI-FCS measurements. The given error of the close to zero depletion rates potentially underestimates the measurement uncertainty, as slow exponential decays (up to 10^6 s) are fitted only with limited accuracy based on 5-h measurements. Based on our results, we regard them indistinguishable. At the high irradiances ($0.2\ \mathrm{kW/cm^2}$) used for super-resolution microscopy, the 18-mer spacer is significantly less efficient in lowering the depletion (Figure 3). In contrast, the depletion seems to occur at a rate similar to the conventional (1) imager and does not show a significant improvement in the stability of docking sites. Adding PO+C to the 18-mer spacer (3b) eliminates the depletion of docking sites as effectively, as for the short imager (2a). We hypothesize that this difference is caused by the different irradiances intrinsic to the two applied methods. Photo-reactions from excited states are known to depend non-linearly on the excitation irradiance [19,21,22]. Comparing the feasibility for kinetic investigations compared to localization precision, a large spacer is expected to decrease the accuracy in SMLM, due to the larger accessible space for the fluorophore upon DNA hybridization [9]. On averaged DNA-PAINT images of several hundred origami nanostructures, the 18-mer spacer imager resolves binding sites with overall precision and accuracy (Figure A4) comparable to the imager with the fluorescent dye attached in close proximity to the docking strand. Individually localized origami nanostructures exhibit a significant loss in image quality that is additionally reduced by the lower association rate of the 18-mer spaced imager (Table 1). Interestingly, adding PO+C to the 18-mer spacer (3b) improves the achievable resolution, reaching results similar to the conventional imager strands (2a). We attribute the reduced blur of the 18-mer spacer with PO+C on the averages to the lower association rate and thus fewer simultaneous binding events (Figure A4). The effect is alternatively achieved in DNA-PAINT acquisitions by a lower imager concentration. A reduced association rate of the 18-mer spaced imager compared to the conventional imager can be partially attributed to a larger hydrodynamic radius, as experimentally confirmed by diffusion measurements in confocal FCS (Figure A2c). For applications based on the kinetics of binding, in particular SI-FCS [15] and qPAINT [13], adding a spacer sequence improves the photo-stability at low-irradiance conditions, while being free from chemical modifications and not requiring specialized buffers. Generally, we expect the positioning of the fluorescent dye with respect to the binding sequence to offer unexplored optimization potential for reducing photo-toxicity in applications without the need for maximally precise localization.

In SI-FCS, a second component to the autocorrelation function can be observed at lag times larger than 10 seconds with concentrations of conventional imager strands higher than 30 to 100 nM (Figure A7b). We previously speculated that unspecific binding might be the main cause for this second component [15]. In the light of the results presented in this work, we now assume the photo-induced depletion of binding sites to be the primary cause (Figure A7b). While at low concentrations the applied detrending is sufficient to eliminate additional contributions in the correlation curve, with increasing concentration, the depletion and therefore the second component becomes more pronounced. The oxygen scavenging system PO+C massively reduces the depletion of docking strands even at the highest employed concentrations (300 nM, Figure A7a) and therefore removes the second contribution from the autocorrelation curves (Figure A7b). The second employed oxygen scavenging system (PCD+PCA) exhibits fluctuating intensity traces that are not fully described by a monoexponential detrending. In particular, we observe periods with increasing average fluorescence intensities that are not observed in any other experimental condition. In our hands, PCD+PCA causes less stable experimental conditions, which manifest themselves as fluctuating fluorescence intensities over time. This effect is particularly pronounced for sample life spans exceeding hours or days. The observed instabilities may potentially be attributed to a nuclease contamination of PCD [63]. In case of PO+C, we did not find any hint on alterations of the sample and therefore conclude PO+C to be favorable for long lasting acquisitions. The 18-mer spacer exhibits a second component of the autocorrelation, which is becoming further pronounced by adding PO+C. We speculate that the 18-mer spacer exhibits additional dynamics on the time scale of tens of seconds, which are independent of the concentration and thus different from previously observed additional components in SI-FCS. Under all conditions, we observe at concentrations above 30 to 100 nM, depending on the condition, that the correlation curves do not decay to zero, irrespective of the addition of oxygen scavenging buffers or the extension with the 18-mer spacer. We therefore assume that a non-perfect focus stabilization, fluctuating laser intensities or temperature changes during a 5-h measurement may account for the multiple components on the time scale of min. However, those contributions separate well in time from the decay of interest of the autocorrelation function and therefore do not hinder the quantitative analysis of autocorrelation curves.

In summary, we have shown that in DNA-PAINT super-resolution microscopy, binding sites are damaged by ROS, which are generated from excited fluorescent dyes on hybridized imager strands. Not only does this effect limit the achievable acquisition time of DNA-PAINT, but it also hinders quantitative analysis based on the kinetics of the hybridization reaction. Similarly, long acquisition series in SI-FCS show artifacts generated by the loss of binding sites even though performed at low irradiances to avoid photo-bleaching. DNA-PAINT super-resolution microscopy and SI-FCS measurements benefit from the use of oxygen scavenging buffers, of which PO+C showed best long-term stability. Further, we presented an extended imager strand with an 18-mer spacer that drastically reduces the depletion of binding sites at low irradiances without additives to the sample. In particular for applications exploiting the kinetics of DNA hybridization, not only the addition of oxygen scavenging systems, but also a design placing the dye at larger distance from the docking site, will improve quantitative analysis. We believe that these results will be of general interest for the future design of fluorescence-based, minimally invasive applications of DNA nanotechnology. To our knowledge, this is the first time that the PO+C oxygen scavenging system has been applied to enhance the performance of DNA-PAINT super-resolution microscopy and we believe this system to be of use also in the context of three-dimensional cellular imaging of fixed specimen, which requires extended acquisition times.

4. Materials and Methods

4.1. Origami Purification

DNA origami nanostructures were synthesized as described previously [11] and subsequently PEG purified. Folded DNA origami structures were mixed 1:1 (*v*/*v*) with 2× PEG purification buffer (PEG-8000 15% (*w*/*v*), 500 mM NaCl, 1× TE buffer), centrifuged for 30 min at 17,900 rcf and 4 °C. The supernatant was removed and the DNA origami resuspended in folding buffer (12.5 mM $MgCl_2$, 10 mM Tris, 1 mM EDTA at pH 8.0) by shaking and heating for 5 min at 600 rpm and 30 °C. Previously described steps were repeated two times to increase the purification. Finally, DNA origami nanostructures were stored at −20 °C until use. The assembly of DNA origami nanostructures was confirmed using DNA-PAINT microscopy (Figures 2 and A3). Origami structures exposed the docking sequence 5′-TTATACATCTA-3′, consisting of a TT-spacer followed by nine nucleotides complementary to the imager sequence.

4.2. Buffers

For simplicity, we name the used buffers A+ and B+. Buffer A+ contains 10 mM Tris-HCl, 100 mM NaCl, 0.05% (*v*/*v*) Tween20. Buffer B+ contains 5 mM Tris-HCl, 10 mM MgCl2, 1 mM EDTA, 0.05% (*v*/*v*) Tween20. Enyme buffer for the PO+C oxygen scavenging systems consists of 10 mM Tris pH 7.5, 50 mM KCl and 20% glycerol for better stability of the stock solutions.

4.3. Fluorescent Imager Solutions

Labeled imager strand solutions were used in varying target concentrations (10, 30, 100, 300 or 600 nM) in five conditions:

1. 'Conventional', as employed previously [11,15] with the sequence 5′-CTAGATGTAT-3′-Cy3B (Eurofins SAM, Ebersberg, Germany) [64];
2. 'Oxygen scavenger'

   a) PO+C, as (1) but incubated for 1 hour prior to measurement with the PO+C oxygen scavenger system (1× PO, 1× C, 0.8 % Glucose as described in [65]), with 1× Trolox added. Stock solutions: 100× PO solution consists of 26 mg of PO (P4234-250UN, Sigma-Aldrich Chemie GmbH, Taufkirchen, Germany), 684 μL of enzyme buffer; 100× C solution consists of 2 mg Catalase in 1 ml enzyme buffer. Both were centrifuge filtered (Ultrafree MC-GV, Merck KGaA, Darmstadt, Germany; 0.22 μm), flash frozen in liquid nitrogen and stored at −80 °C; 100× Trolox solution consists of 100 mg of Trolox (Sigma-Aldrich 238813-1G), 430 μL of methanol and 345 μL of NaOH (1 M) in 3.2 mL of H_2O, stored at −20 °C);
   b) PCD+PCA, as (1) but incubated for 1 hour prior to measurement with the PCD+PCA oxygen scavenger system (1× PCD, 1× PCA, 1× Trolox), as described in [11]. Stock solutions: 40× PCA solution consists of 154 mg of PCA (37580-25G-F, Sigma-Aldrich) in 10 mL of water, adjusted to pH 9.0 with NaOH; 100× PCD solution consists of 9.3 mg of PCD (P8279-25UN, Sigma-Aldrich) and 13.3 mL of buffer (50% glycerol stock in 50 mM KCl, 1 mM EDTA and 100 mM Tris–HCl, pH 8.0), Trolox as above, all stored at −20 °C;

3. ’18-mer spacer’,
   a) with the sequence Cy3B-5′-GTT ATG GGT GGT TTG GGG-CTAGATGTAT-3′ (Eurofins SAM), where the hybridizing nucleotide sequence is identical to (1). Incubation 1:1 at identical concentration with 5′-CCC CAA ACC ACC CAT AAC-3′ complementary unlabeled strands forms a stable duplex, increasing the persistence length of the 18-mer spacer. The fluorescent dye is attached at 5′ to maximize the distance of dye and hybridizing nucleotides. The sequence was checked to not form a secondary structure using the Nucleic Acid Package (NUPACK) [66];
   b) as in (3a) but with PO+C added as in (2a).

4.4. Sample Preparation

Sealed sample chambers were prepared as described previously [11,15]. In brief, high precision #1.5 coverslips (Paul Marienfeld GmbH, Lauda Königshofen, Germany) were sonicated in acetone (chemical grade, Merck KGaA, Germany) for 10 min and then rinsed twice with ethanol (chemical grade, Merck Millipore, Germany) and water (milli-Q, Merck KGaA, Darmstadt, Germany) and gently dried with pressurized nitrogen. The cleaning of the coverslip was completed by putting a drop of 2-propanol on it (Uvasol, Merck KGaA, Darmstadt, Germany) and wiping with a paper tissue (Kimtech Science, Sigma Aldrich). The same procedure was performed on microscope slides (76 × 26 mm^2, Menzel, Thermo Fisher Scientific, Waltham, MA, USA). The high precision coverslip and the microscope slide were assembled into a flow chamber by gluing them together with double-sided sticky-tape (Scotch, Conrad Electronic SE, Hirschau, Germany), yielding a roughly 5 × 22 × 0.08 mm^3 large chamber. For DNA-PAINT unspecific binding between origami structures is easily detected in the final image and thus glass surfaces were used without prior cleaning. In a series of volume exchanges, the flow chamber was first incubated with 20 μL of 1 mg/mL albumin, biotin-labeled bovine (Sigma-Aldrich) in buffer A+ for two min, washed with 40 μL buffer A+, incubated with 20 μL of 0.5 mg/mL streptavidin (Thermo Fisher Scientific) in buffer A+ for two min, washed with 40 μL buffer A+ and washed with 40 μL buffer B+.

For DNA-PAINT imaging, 20 μL folded DNA origami solution, diluted 1:200 from PEG purified solution in B+ buffer, were incubated for five min. For SI-FCS, 20 μl folded DNA origami solution, diluted 1:20 from PEG purified solution in B+ buffer, were incubated for ten min. Chambers were washed with 40 μl buffer B+ and finally loaded with 20 μL of imager solution in the required condition (10 μM for DNA-PAINT imaging). In a final step, the chamber was sealed using two-component epoxy glue (Toolcraft, Conrad Electronic SE) or picodent twinsil 22 two component glue (picodent, Wipperfuerth, Germany). We verified the final concentration of fluorescently labeled ssDNA by confocal FCS measurements.

4.5. DNA-PAINT Microscopy Setup

DNA-PAINT imaging was carried out on an inverted custom-built microscope in an objective-type TIRF configuration with an oil-immersion objective (UAPON, 100×, NA 1.49, Olympus Europe, Hamburg, Germany). Fluorophores were excited with a DPSS laser with a wavelength of 561nm (output power 1W, DPSS-system, MPB Communications Inc., Montreal, QC, Canada). Laser power was adjusted by polarization rotation with a half-wave plate (WPH05M-561, Thorlabs, Dachau, Germany) before passing a polarizing beam-splitter cube (PBS101, Thorlabs). To spatially clean the beam-profile the laser light was coupled into a single-mode polarization-maintaining fiber (P3-488PM-FC-2, Thorlabs) using an aspheric lens (C610TME-A, Thorlabs). The coupling polarization into the fiber was adjusted using a zero-order half wave plate (WPH05M-561, Thorlabs). The laser light was collimated after the fiber using an achromatic doublet lens (AC254-050-A-ML, Thorlabs) resulting in a collimated beam of ~6 mm full-width at half-maximum (FWHM). The laser beam was magnified by a factor of 2.5 using a telescope custom-built from two achromatic doublets (AC254-030-A-ML and AC508-075-A-ML, both Thorlabs). The excitation light was finally focused in the objective's back focal plane using an achromatic doublet lens (AC508-180-A-ML, Thorlabs). Fluorescence light was separated from the excitation by a dichroic beam splitter (F68-785, AHF Analysentechnik, Tübingen, Germany) directly below the objective, spectrally filtered with an emission filter (605/64, AHF Analysentechnik). The signal from the sample was finally imaged on a sCMOS camera (Zyla 4.2, Andor Technologies, Belfast, UK) without further magnification (TTL180-A, Thorlabs) resulting in an effective pixel size of 130 nm (after 2 × 2 binning). Microscopy samples were mounted on an x-y-z stage (S31121010FT and FTP2050, both Advanced Scientific Instrumentation, Eugene, OR, USA) used for focusing and laterally moving the sample with the microscope objective fixed in position.

4.6. DNA-PAINT Image Acquisition

DNA-PAINT super-resolution data was acquired with a sCMOS camera using μManager [67]. Acquisition parameters were: full chip 2 × 2 pixel binning, read out rate 200 MHz and dynamic range 16-bit. The exposure time was set to 200 ms, resulting in a camera frame rate of 5 Hz and in ~83 min of total measurement time. The excitation power was set to 22 mW behind the objective with a Gaussian shaped illumination with a $1/e^2$-width of 84 μm, resulting in a peak irradiance of $0.2\ \mathrm{kW/cm^2}$.

4.7. DNA-PAINT Data Analysis

Super-resolved DNA-PAINT images were computed with Picasso according to [11]. Binding events were localized by Gaussian least-square fitting with a net gradient chosen to suppress localizations of noise. Localizations were drift corrected in a three-step process, first by redundant cross-correlation (RCC) [11,68], subsequently based on picked DNA origami and finally based on picked individual docking sites. To generate subsets, the drift corrected localizations were split in subsets of 5,000 frames each with a custom-written Python script and finally rendered individually. Super-resolved images were rendered blurring individual spots based on the global localization precision. To analyze bright and dark times, origami structures were picked (Picasso: 'pick similar') and further analyzed by a custom-written Python script (https://github.com/DerGoldeneReiter/qPAINT) acting on Picasso's 'Picked localization' files. Dark times of one frame were ignored to reduce artifacts caused by single missed localizations. For docking site analysis picked origami structures were averaged (translation and rotation) to a designed model structure using the 'average3' module of Picasso with a pixel oversampling of 40, setting a custom symmetry of 180 degrees [46]. All individual docking sites were picked on the average image (Figure A4) in the render module of Picasso. 'Unfold' translates the picks of the average back to the individually picked structures and thus, picks of the individual docking sites on every origami structure are obtained. After counting the localizations of each picked single docking site, a lower cut-off value (three localizations) was used to identify active individual docking sites. Dividing the number of the active dockings sites by the number of the originally picked origami structures used for averaging yields the average number of docking sites per origami.

4.8. SI-FCS TIRF Microscope

DNA-PAINT and SI-FCS time series were recorded on a custom-built TIRF microscope, constructed around a Nikon Eclipse Ti-S body as described previously [15]. Fluorescence was excited by 561 nm diode-pumped solid state (DPSS) laser (Cobolt Jive, 50 mW nominal, Hübner GmbH & Co. KG, Kassel Germany), spatially filtered by a single-mode fiber (kineFLEX-P-3-S-405.640-0.7-FCS-P0 and kineMATIX, Qioptiq, Hamble, UK), collimated (f = 25 mm, all standard achromats, Edmund Optics, Karlsruhe, Germany), linearly polarized (CCM1-PBS251/M, Thorlabs) and three-fold magnified (f = −25, 75 mm). The TIRF angle was controlled by translating the focus (f = 225 mm) of the excitation beam by means of a piezo-electric stage (Q545, Physikalische Instrumente, Karlsruhe, Germany) in the back focal plane of the objective (Nikon SR Apo TIRF, 100× magnification, 1.49 numerical aperture (NA), Nikon, Düsseldorf, Germany).

Fluorescence emission was separated from the excitation (zt405/488/561/640rpc flat, AHF Analysentechnik, Tübingen, Germany) before entering the microscope body. The image on the camera-port was relayed on an electron-multiplying charge-coupled device (EMCCD) camera (iXon Ultra 897, Andor Technologies) by an additional 4f telescope (f = 200 mm, AC254-200-A-ML, Thorlabs). Laser emission was attenuated and synchronized with the camera acquisition by an acousto-optical tunable filter (TF-525-250, Gooch & Housego, Torquay, UK), which was interfaced through a PCI Express card (PCIe-6323 and BNC-2110) and controlled with a custom LabView 2011 software (all National Instruments, Austin, TX, USA). The emission light was additionally band-pass filtered (593/46).

Drifting of the focus position was eliminated by a custom-built focus stabilization. A near-infrared laser (LP785-SF20, Thorlabs) was totally internally reflected from the glass-water interface of cover-slide and sample. The beam position was monitored on a CMOS camera (UI-3240CP-NIR-GL, Imaging Development Systems, Obersulm, Germany). A feedback control implemented in LabVIEW 2015 (National Instruments) maximized the cross-correlation of the images of the laser spot and a reference image, respectively. The axial sample position was adjusted every 200 ms accordingly (P737.2SL and E-709.SRG, Physikalische Instrumente). The sample and objective were temperature stabilized to 23 °C. (H101-CRYO-BL stabilization unit, with H101-MINI sample chamber and OKO-MOC objective stabilization, Okolab, Ottaviano, Italy).

4.9. SI-FCS Image Acquisition

Images were recorded using the Andor Solis software (Andor Technologies, Version 4.28) with 4x4 hardware binning as 64 × 64 pixel images for 1.5 million frames, as described previously [15], resulting in ~5 h total measurement time. The exposure time was 10 ms, resulting in a camera frame rate of 85 Hz. The excitation power was set to 0.75 mW behind the objective, with a Gaussian shaped illumination with $a\ 1/e^2$-width of 51 μm, resulting in a peak irradiance of 0.018 kJ/cm^2. The EMCCD camera was used with electron multiplying gain, adapted according to the brightness of the sample.

4.10. SI-FCS Data Analysis

The autocorrelation curves were computed and analyzed using a custom-written Matlab 2017a (The MathWorks, Natick, MA, USA) software, described previously [15]. Intensity traces were generated by additional 8x8 software binning, resulting in 5.12 μm effective integrated area size, representing 32 × 32 native camera pixel. The signal in each pixel was integrated, yielding 64 intensity traces, which were bleach and drift-corrected by a single exponential, and individually correlated using the multiple-τ algorithm [69], in which we doubled the bin width after every sixteenth point in the autocorrelation curve. The obtained autocorrelation curves were fitted individually by a single exponential decay with an offset, from which the amplitude and the characteristic decay time were obtained. Similar to [15], concentrations above 100 nM were fitted with a bi-exponential to account for the second component originating from depletion of docking sites.

4.11. Direct Measurement of the Concentration of Imager Strands with Confocal FCS

We measured the solution concentrations of imager strands with confocal FCS, as described previously [15]. In brief, we used a commercial LSM 780 ConfoCor3 system (Zeiss AG, Oberkochen, Germany) with the confocal volume positioned 40 µm above the cover slide. We calibrated the confocal volume using Alexa546NHS (Thermo Fisher) and its reported diffusion coefficient $D = 341\ \frac{\mu m^2}{s}$ at 22.5 °C [70]. We calculated the corresponding diffusion coefficient at the measurement temperature (26.5 °C to 27 °C) using the well-known relation $D \sim \frac{T}{\eta(T)}$ and an empirical expression for the temperature dependence of the viscosity η of water [71]. We applied a simple 3D diffusion model function:

$$G(\tau) = N^{-1}\left(1+\frac{\tau}{\tau_D}\right)^{-1}\left(1+\frac{\tau}{S^2\tau_D}\right)^{-\frac{1}{2}}, \tag{7}$$

as justified previously [15]. Here, N is the average number of particles in the detection volume, $\tau_D = \frac{w_{xy}^2}{4D}$ the diffusion time, with w_{xy} being the e^{-2}-value of the Gaussian detection volume and S the structure parameter. Concentrations are directly obtained from the amplitude of the correlation curves: $c = N\left(\pi^{\frac{3}{2}} w_{xy}^3 S\right)^{-1}$. As diffusion coefficient, we measured $D_{\mathrm{conv}} = (201 \pm 5)\frac{\mu m^2}{s}$ (n = 8), in agreement with previously reported results [15,72] and $D_{\text{18-mer spacer}} = (120 \pm 20)\frac{\mu m^2}{s}$ (n = 4) for the 18-mer spacer. The presented numbers correspond to mean and standard deviation of the indicated n measurements, each of them at least 20 min long.

4.12. Simulation of Bright and Dark Times

Simulations of the bright and dark time distributions were generated with COPASI [73]. Biochemical parameters for the simulation were: Mass action irreversible ($A + B \rightarrow C,\ C \rightarrow A + B$), $k_a = 1.5 \cdot 10^6 (\mathrm{Ms})^{-1}$, $k_d = 0.3\ \mathrm{s}^{-1}$ with varying number of initial species values (B=12,10,8,6,4) corresponding to single dockings sites and fixed imager concentration of $\langle A \rangle = 10$ nM. Time course simulations were performed with the same interval spacing (0.2s) and total acquisition time (17min per time segment) used in the DNA-PAINT image acquisitions. Obtained traces were analyzed analogous to experimental data using a custom-written Python script (https://github.com/DerGoldeneReiter/qPAINT).

Supplementary Materials: Raw data for DNA-PAINT, confocal FCS and SI-FCS experiments is available for download from: https://edmond.mpdl.mpg.de/imeji/collection/2FgPkBEehRCbXAZP

Author Contributions: Conceptualization, P.B. and J.M.; Formal analysis, P.B., J.S., F.S. and J.B.; Funding acquisition, R.J. and P.S.; Investigation, P.B. and J.S.; Methodology, P.B., J.S., J.M. and F.S.; Project administration, P.B. and J.S.; Resources, P.B., J.S., J.M. and F.S.; Software, P.B., J.S., J.M. and F.S.; Supervision, R.J. and P.S.; Validation, P.B., J.S. and F.S.; Visualization, P.B., J.S., F.S. and J.B.; Writing—original draft, P.B.; Writing—review & editing, P.B., J.S., J.M., F.S., R.J. and P.S.

Funding: P.S. acknowledges grant money from the Gottfried Wilhelm Leibniz Prize by the German Research foundation. This work was supported in part by the DFG through the Emmy Noether Program (DFG JU 2957/1-1), the SFB 1032 (Nanoagents for spatiotemporal control of molecular and cellular reactions, Project A11), the ERC through an ERC Starting Grant (MolMap, Grant agreement no. 680241), the Max Planck Society, the Max Planck Foundation, and the Center for Nanoscience (CeNS) to R.J. J.M. is grateful for financial support from the excellence cluster Nanosystems Initiative Munich. J.S. is grateful for financial support from the Graduate School of Quantitative Biosciences Munich (QBM).

Acknowledgments: We thank Sonal and Kristina A. Ganzinger for introducing us to the PO+C oxygen scavenging system and providing all necessary materials; Alena Khmelinskaia and Henri G. Franquelim for assistance in the design of the 18-mer spacer; all previous, and additionally Philipp Glock, Florian Schüder and

Maximilian T. Strauss for helpful discussion; Patrick Steiner and Sigrid Bauer for experimental assistance. P.B. and J.M. acknowledge support from the International Max Planck Research School for Molecular and Cellular Life Sciences (IMPRS-LS). P.B., J.M., J.S., F.S. acknowledge support from the Center for NanoScience (CeNS).

Conflicts of Interest: The authors declare no conflict of interest.

Appendix A

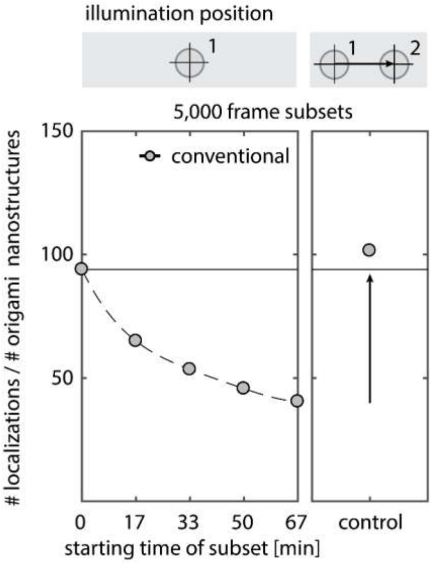

Figure A1. With increasing measurement time, the total number of localizations per DNA origami nanostructure decreases. One large time series of 25,000 frames (83 min) was drift corrected and subsequently divided into five subsets of 5,000 frames (17 min each). Acquiring an additional 5,000-frame-subset on the same sample in a previously not irradiated area recovers the initial number of localizations, indicating that bulk bleaching of fluorophores in solution is negligible compared to the locally observed decrease in the number of localizations.

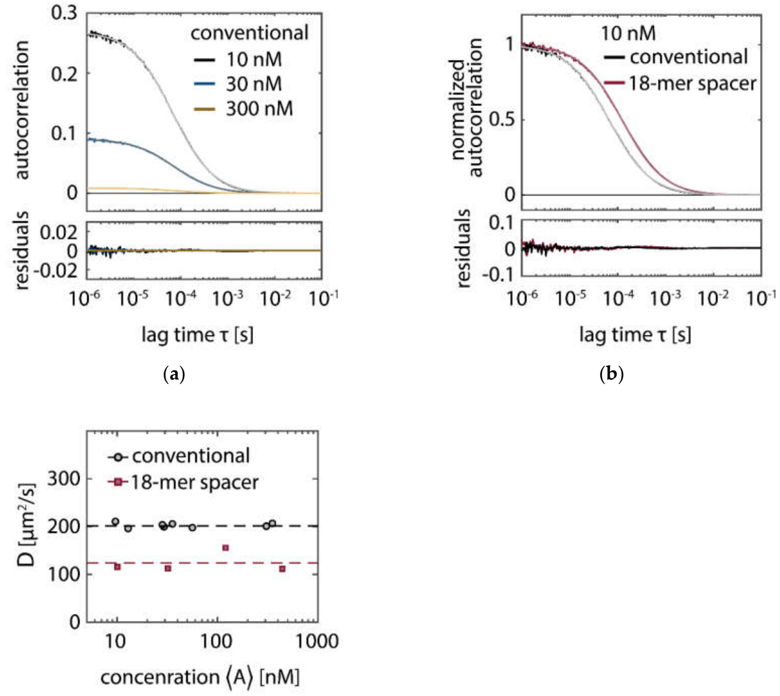

(**a**) (**b**)

(**c**)

Figure A2. Confocal FCS measurement of the imager concentration and diffusion coefficient. **(a)** Representative autocorrelation curves for the conventional imager with their respective fits to a simple 3D diffusion model (Equation 7) and residuals. The three displayed curves have the target concentrations 10 nM (black), 30 nM (blue) and 300 nM (brown) and the measured concentrations 9.8 nM, 29.7 nM and 310 nM, respectively. **(b)** Normalized autocorrelation curves at the target concentration 10 nM for the conventional condition (identical to (a)) and the 18-mer spacer, leading to a decrease in the diffusion time. **(c)** Diffusion coefficient D for the conventional and 18-mer spacer condition at different concentrations. The average diffusion coefficients (dashed lines) are determined as (mean ± std.): $(201 \pm 5)\ \mu\mathrm{m}^2/s$ (in good agreement with previously reported results [15,72]) and $(120 \pm 20)\ \mu\mathrm{m}^2/s$ for the conventional and the 18-mer spacer, respectively. Based on the determined diffusion coefficients, we conclude that bleached imager within the TIRF excitation volume is predominantly recovered from solution by diffusion along the direction of the evanescent excitation. The diffusion time can be estimated as $t_D \sim d_{\mathrm{ev}}^2/D$, with d_{ev} being the evanescent field of the TIRF illumination. Assuming the penetration depth as $d_{\mathrm{ev}} \sim 75\ \mathrm{nm}$ [74], we obtain $t_D \sim 50\ \mu\mathrm{s}$, three orders of magnitude faster than the PAINT exposure time (200 ms) or the minimal SI-FCS correlation time (100 ms). In the high irradiance regime ($I_0 = 0.2\ \mathrm{kW/cm^2}$), the rate of photo-bleaching within the TIRF illumination can be assumed four orders of magnitude slower than the recovery by diffusion, based on the bright times found for the conventional condition, which is shortened by photo-bleaching to $\tau_B \sim 2\ \mathrm{s}$ (Figure 3b). Raw data of confocal FCS measurements is available as supplementary material.

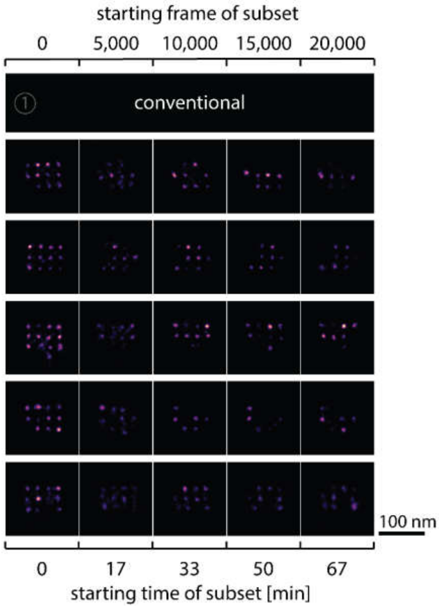
starting frame of subset
0
5,000
10,000
15,000
20,000
①
conventional
100 nm
0
17
33
50
67
starting time of subset [min]

(**a**)

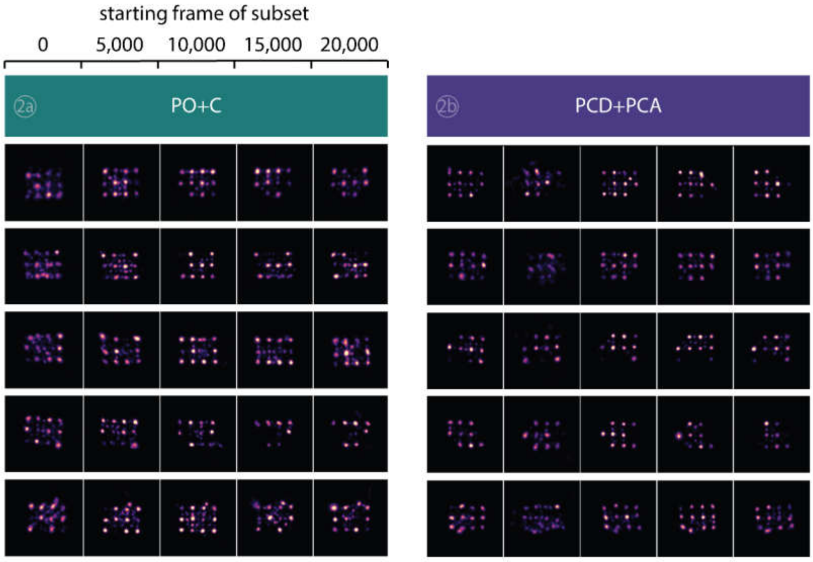
starting frame of subset
0
5,000
10,000
15,000
20,000
2a
PO+C
2b
PCD+PCA

Figure A3. *Cont.*

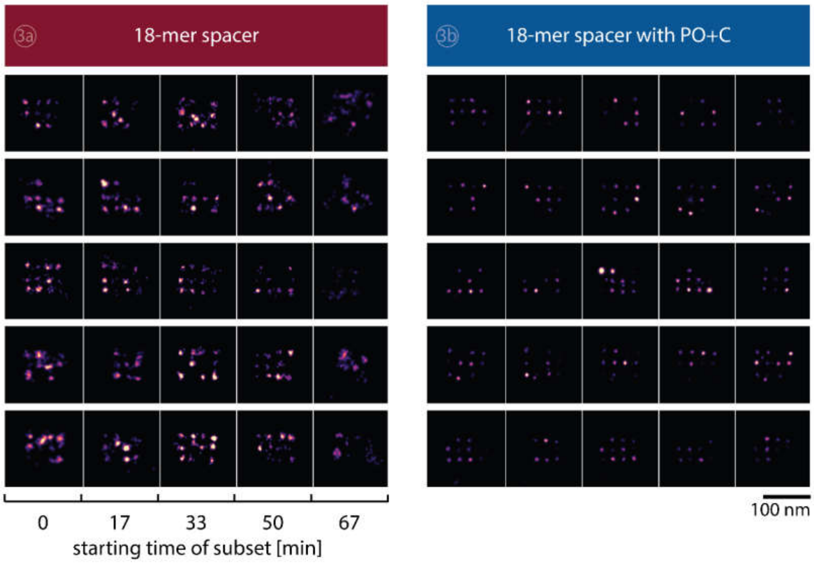
3a
18-mer spacer
3b
18-mer spacer with PO+C
0
17
33
50
67
starting time of subset [min]
100 nm

(**b**)

Figure A3. Selected DNA-PAINT super-resolved images of DNA nanostructures showing the depletion of binding sites in the five different conditions. **(a)** Images for the conventional imager (1). Five rows display different nanostructures that showed a high number of initially available docking sites. Images along the five columns represent the localizations within a subset of 5,000 frames from a 25,000 frame long measurement. Scale bar: 100 nm. **(b)** Images taken with addition of the oxygen scavenging buffer PO+C (2a), PCD+PCA (2b), extension with an 18-mer spacer (3a) and the combination of 18-mer spacer and PO+C (3b).

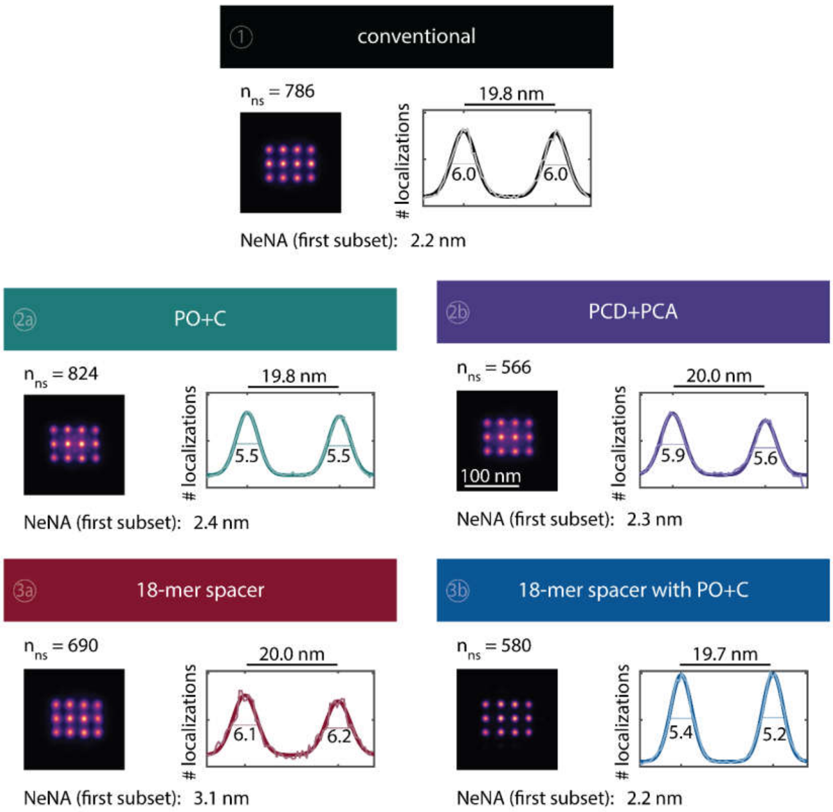

Figure A4. Averaged super-resolved DNA-PAINT images of DNA origami nanostructures for the whole time series of 83 min. The total numbers of identified DNA origami nanostructures n_{ns} employed for averaging are stated above the average images. Line profiles of total number of localizations through the two lower left points from each averaged image were fitted with a double Gaussian function $\left(f(x) = a_1 \exp\left[\frac{(x-b_1)^2}{2\sigma_1^2}\right] + a_2 \exp\left[\frac{(x-b_2)^2}{2\sigma_2^2}\right] + c\right)$. The number stated for each peak is the FWHM (in nm) and can be interpreted as a measure of the achievable resolution; the peak-to-peak distance is shown above the plot. Additionally, the value of the nearest neighbor analysis (NeNA) [11,75] is shown for the first subset.

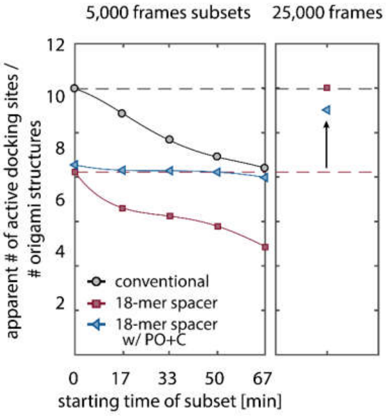

Figure A5. The observed lower number of active docking sites for the 18-mer spacer (conditions 3a and 3b) is caused by the lower association rate of the extended imager. Identifying active docking sites on the whole time series of 25,000 frames, recovers the number of initially active docking sites expected from the conventional imaging condition (condition 1).

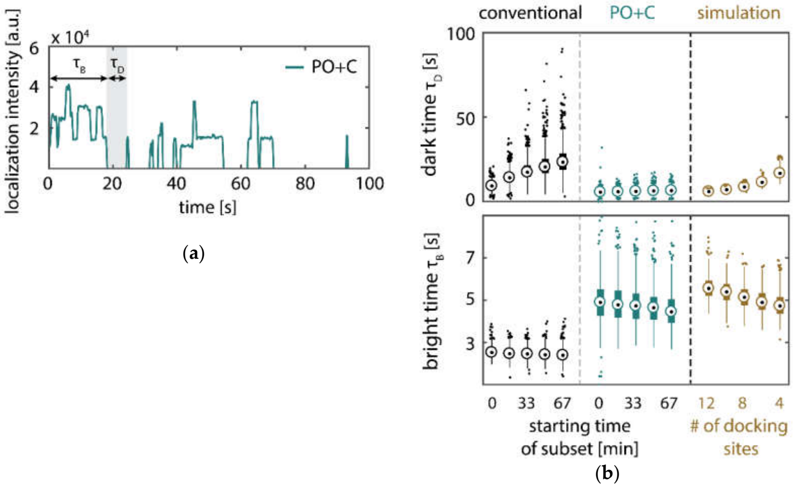

(**a**)

(**b**)

Figure A6. The number of available docking sites per origami structures influences the dark and bright times. **(a)** Intensity trace (representative section) of localizations assigned to the DNA origami presented in Figure 2 (PO+C) showing the effect of simultaneous binding. The step-wise increase corresponds to binding of imager strands, while the step-wise decrease indicates unbinding of an imager strand or photo-bleaching of individual fluorophores. **(b)** Comparison of experimentally obtained kinetics with simulations of origami nanostructures exposing a varying number of docking sites. On the one hand, a depletion of docking sites causes an increase in dark time τ_D, as individual hybridization events are as probable, but the number of possible binding partners is reduced. On the other hand, the localization algorithm counts temporally overlapping binding events within one diffraction-limited spot as one longer binding event. The probability for simultaneous binding increases with the number of binding sites in one diffraction limited spot. For the simulation, we made the following assumptions, based on the results from SI-FCS measurements (see Table 1): association rate $k_a = 1.5 \times 10^6\ (\text{mol·s})^{-1}$, $k_d = 0.3\ \text{s}^{-1}$, $c = 10\ \text{nM}$ and the number of binding sites decreasing step-wise with every subset from initially 12 to finally four binding sites. The simulated intensities from individual binding sites added up to obtain intensity traces for origami nanostructures

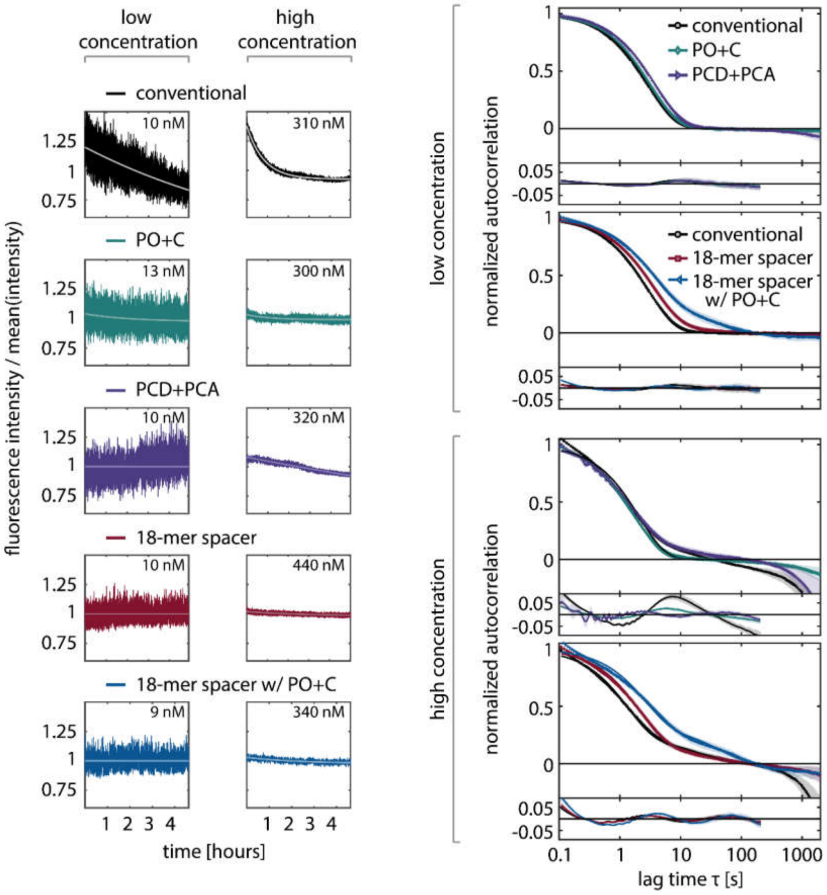

(**a**) (**b**)

Figure A7. Influence of the depletion of binding sites on the autocorrelation function: **(a)** Decays of the integrated fluorescence intensity within a representative region of interest (dark shade) and fit of the mono-exponential detrending function (equation 1, light shade). For all five conditions (conventional, addition of oxygen scavenging system (PO+C and PCD+PCA), 18-mer spacer and 18-mer spacer with PO+C) an example at low and high concentration is shown. The concentrations of individual samples were measured by confocal FCS. **(b)** Representative normalized autocorrelation functions and residuals with conditions as in (a) (solid lines). Shaded areas represent the standard deviation from 64 regions of interest.

1. Huang, B.; Bates, M.; Zhuang, X. Super-Resolution Fluorescence Microscopy. *Annu. Rev. Biochem.* **2009**, *78*, 993–1016, doi:10.1146/annurev.biochem.77.061906.092014.
2. Baddeley, D.; Bewersdorf, J. Biological Insight from Super-Resolution Microscopy: What We Can Learn from Localization-Based Images. *Annu. Rev. Biochem.* **2018**, *87*, 965–989, doi:10.1146/annurev-biochem-060815-014801.
3. Pertsinidis, A.; Zhang, Y.; Chu, S. Subnanometre single-molecule localization, registration and distance measurements. *Nature* **2010**, doi:10.1038/nature09163.
4. Betzig, E.; Patterson, G.H.; Sougrat, R.; Lindwasser, O.W.; Olenych, S.; Bonifacino, J.S.; Davidson, M.W.; Lippincott-Schwartz, J.; Hess, H.F. Imaging Intracellular Fluorescent Proteins at Nanometer Resolution.

Science **2006**, *313*, 1642 LP-1645.

5. Hess, S.T.; Girirajan, T.P.K.; Mason, M.D. Ultra-High Resolution Imaging by Fluorescence Photoactivation Localization Microscopy. *Biophys. J.* **2006**, *91*, 4258–4272, doi:10.1529/BIOPHYSJ.106.091116.
6. Rust, M.J.; Bates, M.; Zhuang, X. Sub-diffraction-limit imaging by stochastic optical reconstruction microscopy (STORM). *Nat. Methods* **2006**, *3*, 793, doi:10.1038/nmeth929.
7. Heilemann, M.; van de Linde, S.; Schüttpelz, M.; Kasper, R.; Seefeldt, B.; Mukherjee, A.; Tinnefeld, P.; Sauer, M. Subdiffraction-Resolution Fluorescence Imaging with Conventional Fluorescent Probes. *Angew. Chem. Int. Ed.* **2008**, *47*, 6172–6176, doi:10.1002/anie.200802376.
8. Thompson, R.E.; Larson, D.R.; Webb, W.W. Precise Nanometer Localization Analysis for Individual Fluorescent Probes. *Biophys. J.* **2002**, *82*, 2775–2783, doi:10.1016/S0006-3495(02)75618-X.
9. Deschout, H.; Zanacchi, F.C.; Mlodzianoski, M.; Diaspro, A.; Bewersdorf, J.; Hess, S.T.; Braeckmans, K. Precisely and accurately localizing single emitters in fluorescence microscopy. *Nat. Methods* **2014**, *11*, 253.
10. Sharonov, A.; Hochstrasser, R.M. Wide-field subdiffraction imaging by accumulated binding of diffusing probes. *Proc. Natl. Acad. Sci. USA* **2006**, *103*, 18911 LP-18916.
11. Schnitzbauer, J.; Strauss, M.T.; Schlichthaerle, T.; Schueder, F.; Jungmann, R. Super-resolution microscopy with DNA-PAINT. *Nat. Protoc.* **2017**, *12*, 1198–1228.
12. Jungmann, R.; Steinhauer, C.; Scheible, M.; Kuzyk, A.; Tinnefeld, P.; Simmel, F.C. Single-Molecule Kinetics and Super-Resolution Microscopy by Fluorescence Imaging of Transient Binding on DNA Origami. *Nano Lett.* **2010**, *10*, 4756–4761, doi:10.1021/nl103427w.
13. Jungmann, R.; Avendano, M.S.; Dai, M.; Woehrstein, J.B.; Agasti, S.S.; Feiger, Z.; Rodal, A.; Yin, P. Quantitative super-resolution imaging with qPAINT. *Nat. Method* **2016**, *13*, 439–442, doi:10.1038/nmeth.3804.
14. Lieto, A.M.; Cush, R.C.; Thompson, N.L. Ligand-Receptor Kinetics Measured by Total Internal Reflection with Fluorescence Correlation Spectroscopy. *Biophys. J.* **2003**, *85*, 3294–3302, doi:http://dx.doi.org/10.1016/S0006-3495(03)74748-1.
15. Mücksch, J.; Blumhardt, P.; Strauss, M.T.; Petrov, E.P.; Jungmann, R.; Schwille, P. Quantifying Reversible Surface Binding via Surface-Integrated Fluorescence Correlation Spectroscopy. *Nano Lett.* **2018**, *18*, 3185–3192, doi:10.1021/acs.nanolett.8b00875.
16. Peng, S.; Wang, W.; Chen, C. Surface Transient Binding-Based Fluorescence Correlation Spectroscopy (STB-FCS), a Simple and Easy-to-Implement Method to Extend the Upper Limit of the Time Window to Seconds. *J. Phys. Chem. B* **2018**, doi:10.1021/acs.jpcb.8b03476.
17. Diaspro, A.; Chirico, G.; Usai, C.; Ramoino, P.; Dobrucki, J. *Photobleaching BT—Handbook Of Biological Confocal Microscopy*; Springer: Boston, MA, USA, 2006; pp. 690–702, ISBN 978-0-387-45524-2.
18. Ha, T.; Tinnefeld, P. Photophysics of Fluorescent Probes for Single-Molecule Biophysics and Super-Resolution Imaging. *Annu. Rev. Phys. Chem.* **2012**, *63*, 595–617, doi:10.1146/annurev-physchem-032210-103340.
19. Eggeling, C.; Widengren, J.; Rigler, R.; Seidel, C.A.M. Photostability of Fluorescent Dyes for Single-Molecule Spectroscopy: Mechanisms and Experimental Methods for Estimating Photobleaching in Aqueous Solution BT—Applied Fluorescence in Chemistry, Biology and Medicine. In *Applied Fluorescence in Chemistry, Biology and Medicine*; Rettig, W., Strehmel, B., Schrader, S., Seifert, H., Eds.; Springer: Berlin/Heidelberg, Germany, 1999; pp. 193–240, ISBN 978-3-642-59903-3.
20. Eggeling, C.; Widengren, J.; Rigler, R.; Seidel, C.A.M. Photobleaching of Fluorescent Dyes under Conditions Used for Single-Molecule Detection: Evidence of Two-Step Photolysis. *Anal. Chem.* **1998**, *70*, 2651–2659, doi:10.1021/ac980027p.
21. Eggeling, C.; Volkmer, A.; Seidel, C.A.M. Molecular Photobleaching Kinetics of Rhodamine 6G by One- and Two-Photon Induced Confocal Fluorescence Microscopy. *ChemPhysChem* **2005**, *6*, 791–804, doi:10.1002/cphc.200400509.
22. Widengren, J.; Chmyrov, A.; Eggeling, C.; Löfdahl, P.-Å.; Seidel, C.A.M. Strategies to Improve Photostabilities in Ultrasensitive Fluorescence Spectroscopy. *J. Phys. Chem. A* **2007**, *111*, 429–440, doi:10.1021/jp0646325.
23. Wilkinson, F.; McGarvey, D.J.; Olea, A.F. Excited Triplet State Interactions with Molecular Oxygen: Influence of Charge Transfer on the Bimolecular Quenching Rate Constants and the Yields of Singlet Oxygen [O*2(1.DELTA.g)] for Substituted Naphthalenes in Various Solvents. *J. Phys. Chem.* **1994**, *98*, 3762–3769, doi:10.1021/j100065a035.

24. Davidson, R.S. Mechanisms of photo-oxidation reactions. *Pestic. Sci.* **1979**, *10*, 158–170, doi:10.1002/ps.2780100210.
25. Hoogenboom, J.P.; van Dijk, E.M.H.P.; Hernando, J.; van Hulst, N.F.; García-Parajó, M.F. Power-Law-Distributed Dark States are the Main Pathway for Photobleaching of Single Organic Molecules. *Phys. Rev. Lett.* **2005**, *95*, 97401, doi:10.1103/PhysRevLett.95.097401.
26. Vogelsang, J.; Kasper, R.; Steinhauer, C.; Person, B.; Heilemann, M.; Sauer, M.; Tinnefeld, P. A Reducing and Oxidizing System Minimizes Photobleaching and Blinking of Fluorescent Dyes. *Angew. Chem. Int. Ed.* **2008**, *47*, 5465–5469, doi:10.1002/anie.200801518.
27. Widengren, J.; Rigler, R. Mechanisms of photobleaching investigated by fluorescence correlation spectroscopy. *Bioimaging* **1996**, *4*, 149–157.
28. Eggeling, C.; Widengren, J.; Brand, L.; Schaffer, J.; Felekyan, S.; Seidel, C.A.M. Analysis of Photobleaching in Single-Molecule Multicolor Excitation and Förster Resonance Energy Transfer Measurements. *J. Phys. Chem. A* **2006**, *110*, 2979–2995, doi:10.1021/jp054581w.
29. Zheng, Q.; Jockusch, S.; Zhou, Z.; Blanchard, S.C. The contribution of reactive oxygen species to the photobleaching of organic fluorophores. *Photochem. Photobiol.* **2014**, *90*, 448–454, doi:10.1111/php.12204.
30. Dixit, R.; Cyr, R. Cell damage and reactive oxygen species production induced by fluorescence microscopy: Effect on mitosis and guidelines for non-invasive fluorescence microscopy. *Plant J.* **2003**, *36*, 280–290, doi:10.1046/j.1365-313X.2003.01868.x.
31. Schneckenburger, H.; Weber, P.; Wagner, M.; Schickinger, S.; Richter, V.; Bruns, T.; Strauss, W.S.L.; Wittig, R. Light exposure and cell viability in fluorescence microscopy. *J. Microsc.* **2012**, *245*, 311–318, doi:10.1111/j.1365-2818.2011.03576.x.
32. Sies, H.; Menck, C.F.M. Singlet oxygen induced DNA damage. *Mutat. Res.* **1992**, *275*, 367–375, doi:10.1016/0921-8734(92)90039-R.
33. Matter, B.; Seiler, C.L.; Murphy, K.; Ming, X.; Zhao, J.; Lindgren, B.; Jones, R.; Tretyakova, N. Mapping three guanine oxidation products along DNA following exposure to three types of reactive oxygen species. *Free Radic. Biol. Med.* **2018**, *121*, 180–189, doi:10.1016/j.freeradbiomed.2018.04.561.
34. Harada, Y.; Sakurada, K.; Aoki, T.; Thomas, D.D.; Yanagida, T. Mechanochemical coupling in actomyosin energy transduction studied by in vitro movement assay. *J. Mol. Biol.* **1990**, *216*, 49–68, doi:10.1016/S0022-2836(05)80060-9.
35. Benesch, R.E.; Benesch, R. Enzymatic Removal of Oxygen for Polarography and Related Methods. *Science* **1953**, *118*, 447 LP-448.
36. Shi, X.; Lim, J.; Ha, T. Acidification of the Oxygen Scavenging System in Single-Molecule Fluorescence Studies: In Situ Sensing with a Ratiometric Dual-Emission Probe. *Anal. Chem.* **2010**, *82*, 6132–6138, doi:10.1021/ac1008749.
37. Englander, S.W.; Calhoun, D.B.; Englander, J.J. Biochemistry without oxygen. *Anal. Biochem.* **1987**, *161*, 300–306, doi:10.1016/0003-2697(87)90454-4.
38. Kim, S.-E.; Lee, I.-B.; Hong, S.-C. The effect of the oxygen scavenging system on the pH of buffered sample solutions: In the context of single-molecule fluorescence measurements. *Bull. Korean Chem. Soc.* **2012**, *33*, 958–962.
39. Patil, P.V.; Ballou, D.P. The Use of Protocatechuate Dioxygenase for Maintaining Anaerobic Conditions in Biochemical Experiments. *Anal. Biochem.* **2000**, *286*, 187–192, doi:10.1006/ABIO.2000.4802.
40. Aitken, C.E.; Marshall, R.A.; Puglisi, J.D. An Oxygen Scavenging System for Improvement of Dye Stability in Single-Molecule Fluorescence Experiments. *Biophys. J.* **2008**, *94*, 1826–1835, doi:10.1529/BIOPHYSJ.107.117689.
41. Swoboda, M.; Henig, J.; Cheng, H.-M. M.; Brugger, D.; Haltrich, D.; Plumeré, N.; Schlierf, M. Enzymatic Oxygen Scavenging for Photostability without pH Drop in Single-Molecule Experiments. *ACS Nano* **2012**, *6*, 6364–6369, doi:10.1021/nn301895c.
42. Widengren, J.; Dapprich, J.; Rigler, R. Fast interactions between Rh6G and dGTP in water studied by fluorescence correlation spectroscopy. *Chem. Phys.* **1997**, *216*, 417–426, doi:10.1016/S0301-0104(97)00014-1.
43. Rasnik, I.; McKinney, S.A.; Ha, T. Nonblinking and long-lasting single-molecule fluorescence imaging. *Nat. Methods* **2006**, *3*, 891.
44. Dave, R.; Terry, D.S.; Munro, J.B.; Blanchard, S.C. Mitigating Unwanted Photophysical Processes for Improved Single-Molecule Fluorescence Imaging. *Biophys. J.* **2009**, *96*, 2371–2381, doi:10.1016/j.bpj.2008.11.061.

45. Jungmann, R.; Avendaño, M.S.; Woehrstein, J.B.; Dai, M.; Shih, W.M.; Yin, P. Multiplexed 3D cellular super-resolution imaging with DNA-PAINT and Exchange-PAINT. *Nat. Methods* **2014**, *11*, 313.
46. Strauss, M.T.; Schueder, F.; Haas, D.; Nickels, P.C.; Jungmann, R. Quantifying absolute addressability in DNA origami with molecular resolution. *Nat. Commun.* **2018**, *9*, 1600, doi:10.1038/s41467-018-04031-z.
47. Cadet, J.; Teoule, R. Comparative Study of Oxidation of Nucleic Acid Components by Hydroxyl Radicas, Singlet Oxygen and Superoxide Anion Radicals. *Photochem. Photobiol.* **1978**, *28*, 661–665, doi:10.1111/j.1751-1097.1978.tb06991.x.
48. Neumüller, K.G.; Elsayad, K.; Reisecker, J.M.; Waxham, M.N.; Heinze, K.G. Photounbinding of Calmodulin from a Family of CaM Binding Peptides. *PLoS ONE* **2010**, *5*, e14050.
49. Heinze, K.G.; Costantino, S.; De Koninck, P.; Wiseman, P.W. Beyond Photobleaching, Laser Illumination Unbinds Fluorescent Proteins. *J. Phys. Chem. B* **2009**, *113*, 5225–5233, doi:10.1021/jp8060152.
50. Marnett, L.J. Oxyradicals and DNA damage. *Carcinogenesis* **2000**, *21*, 361–370.
51. Malins, D.C.; Gunselman, S.J.; Holmes, E.H.; Polissar, N.L. The etiology of breast cancer characteristic alterations in hydroxyl radical-induced dna base lesions during oncogenesis with potential for evaluating incidence risk. *Cancer* **2018**, *71*, 3036–3043, doi:10.1002/1097-0142(19930515)71:10<3036::AID-CNCR2820711025>3.0.CO;2-P.
52. Paz-Elizur, T.; Krupsky, M.; Blumenstein, S.; Elinger, D.; Schechtman, E.; Livneh, Z. DNA Repair Activity for Oxidative Damage and Risk of Lung Cancer. *JNCI J. Natl. Cancer Inst.* **2003**, *95*, 1312–1319.
53. Liou, G.-Y.; Storz, P. Reactive oxygen species in cancer. *Free Radic. Res.* **2010**, *44*, 479–496, doi:10.3109/10715761003667554.
54. Bonnett, R.; Martínez, G. Photobleaching of sensitisers used in photodynamic therapy. *Tetrahedron* **2001**, *57*, 9513–9547, doi:10.1016/S0040-4020(01)00952-8.
55. Prat, F.; Houk, K.N.; Foote, C.S. Effect of Guanine Stacking on the Oxidation of 8-Oxoguanine in B-DNA. *J. Am. Chem. Soc.* **1998**, *120*, 845–846, doi:10.1021/ja972331q.
56. Neeley, W.L.; Essigmann, J.M. Mechanisms of Formation, Genotoxicity, and Mutation of Guanine Oxidation Products. *Chem. Res. Toxicol.* **2006**, *19*, 491–505, doi:10.1021/tx0600043.
57. Greenberg, M.M. In vitro and in vivo effects of oxidative damage to deoxyguanosine. *Biochem. Soc. Trans.* **2004**, *32*, 46–50.
58. Hirakawa, K.; Suzuki, H.; Oikawa, S.; Kawanishi, S. Sequence-specific DNA damage induced by ultraviolet A-irradiated folic acid via its photolysis product. *Arch. Biochem. Biophys.* **2003**, *410*, 261–268, doi:10.1016/S0003-9861(02)00722-1.
59. Colson, A.O.; Besler, B.; Close, D.M.; Sevilla, M.D. Ab initio molecular orbital calculations of DNA bases and their radical ions in various protonation states: Evidence for proton transfer in GC base pair radical anions. *J. Phys. Chem.* **1992**, doi:10.1021/j100181a028.
60. Yun, B.H.; Lee, Y.A.; Kim, S.K.; Kuzmin, V.; Kolbanovskiy, A.; Dedon, P.C.; Geacintov, N.E.; Shafirovich, V. Photosensitized oxidative DNA damage: From hole injection to chemical product formation and strand cleavage. *J. Am. Chem. Soc.* **2007**, doi:10.1021/ja066954s.
61. Ogilby, P.R. Singlet oxygen: There is indeed something new under the sun. *Chem. Soc. Rev.* **2010**, *39*, 3181, doi:10.1039/b926014p.
62. Redmond, R.W.; Kochevar, I.E. Symposium-in-Print: Singlet Oxygen Invited Review. *Photochem. Photobiol.* **2007**, *82*, 1178–1186, doi:10.1562/2006-04-14-IR-874.
63. Senavirathne, G.; Liu, J.; Lopez, M.A., Jr.; Hanne, J.; Martin-Lopez, J.; Lee, J.-B.; Yoder, K.E.; Fishel, R. Widespread nuclease contamination in commonly used oxygen-scavenging systems. *Nat. Methods* **2015**, *12*, 901.
64. Cooper, M.; Ebner, A.; Briggs, M.; Burrows, M.; Gardner, N.; Richardson, R.; West, R. Cy3B™: Improving the Performance of Cyanine Dyes. *J. Fluoresc.* **2004**, *14*, 145–150, doi:10.1023/B:JOFL.0000016286.62641.59.
65. Sonal; Ganzinger, K.A.; Vogel, S.K.; Mücksch, J.; Blumhardt, P.; Schwille, P. Myosin-II activity generates a dynamic steady state with continuous actin turnover in a minimal actin cortex. *J. Cell Sci.* **2018**. doi:10.1101/312512.
66. Zadeh, J.N.; Steenberg, C.D.; Bois, J.S.; Wolfe, B.R.; Pierce, M.B.; Khan, A.R.; Dirks, R.M.; Pierce, N.A. NUPACK: Analysis and design of nucleic acid systems. *J. Comput. Chem.* **2011**, *32*, 170–173, doi:10.1002/jcc.21596.
67. Edelstein, A.; Amodaj, N.; Hoover, K.; Vale, R.; Stuurman, N. Computer Control of Microscopes Using μManager. *Curr. Protoc. Mol. Biol.* **2010**, *92*, 14.20.1–14.20.17, doi:10.1002/0471142727.mb1420s92.

68. Wang, Y.; Schnitzbauer, J.; Hu, Z.; Li, X.; Cheng, Y.; Huang, Z.-L.; Huang, B. Localization events-based sample drift correction for localization microscopy with redundant cross-correlation algorithm. *Opt. Express* **2014**, *22*, 15982, doi:10.1364/OE.22.015982.
69. Schätzel, K. Correlation techniques in dynamic light scattering. *Appl. Phys. B* **1987**, *42*, 193–213, doi:10.1007/BF00693937.
70. Petrášek, Z.; Schwille, P. Precise Measurement of Diffusion Coefficients using Scanning Fluorescence Correlation Spectroscopy. *Biophys. J.* **2008**, *94*, 1437–1448, doi:http://dx.doi.org/10.1529/biophysj.107.108811.
71. Kestin, J.; Sokolov, M.; Wakeham, W.A. Viscosity of liquid water in the range -8 C to 150 C. *J. Phys. Chem. Ref. Data* **1978**, *7*, 941–948, doi:10.1063/1.555581.
72. Stellwagen, E.; Lu, Y.; Stellwagen, N.C. Unified Description of Electrophoresis and Diffusion for DNA and Other Polyions. *Biochemistry* **2003**, *42*, 11745–11750, doi:10.1021/bi035203p.
73. Hoops, S.; Sahle, S.; Gauges, R.; Lee, C.; Pahle, J.; Simus, N.; Singhal, M.; Xu, L.; Mendes, P.; Kummer, U. COPASI—A COmplex PAthway SImulator. *Bioinformatics* **2006**, *22*, 3067–3074.
74. Niederauer, C.; Blumhardt, P.; Mücksch, J.; Heymann, M.; Lambacher, A.; Schwille, P. Direct characterization of the evanescent field in objective-type total internal reflection fluorescence microscopy. *Opt. Express* **2018**, *26*, 20492–20506, doi:10.1364/OE.26.020492.
75. Endesfelder, U.; Malkusch, S.; Fricke, F.; Heilemann, M. A simple method to estimate the average localization precision of a single-molecule localization microscopy experiment. *Histochem. Cell Biol.* **2014**, *141*, 629–638, doi:10.1007/s00418-014-1192-3.

© 2018 by the authors. Licensee MDPI, Basel, Switzerland. This article is an open access article distributed under the terms and conditions of the Creative Commons Attribution (CC BY) license (http://creativecommons.org/licenses/by/4.0/).

4

Homogeneous TIRF Illumination

4.1 Motivation and Summary

Due to the excellent axial constraint of the excitation profile in TIRF microscopy down to 200 nm, it is the preferred choice for fluorescence imaging of specimens close to the coverslip surface. For surface-binding characterization approaches such as lbFCS and SI-FCS, TIRF microscopy is particularly useful for monitoring binding events at high signal-to-noise ratios with respect to the high fluorescence background of unbound ligand. Furthermore, TIRF microscopy is commonly used for DNA-PAINT imaging, where the signal-to-noise ratio translates into localization precisions on the order of a few nanometers. Typically, standard TIRF microscopes employ a Gaussian laser beam resulting in an inhomogeneous excitation profile, potentially biasing fluorescence-based surface binding assays. This inhomogeneous excitation can cause artifacts during DNA-PAINT imaging, leading to a non-truthful reconstruction of the image data. Within the work of this chapter, we constructed a custom TIRF microscope which features a homogeneous 'flat-top' excitation profile via refractive beam shaping. The flat-top TIRF microscope paves way for both high-throughput kinetic assays and DNA-PAINT imaging over large field of views (FOVs) without substantial trade-offs in image quality.

4.2 PUBLICATION P2: Flat-top TIRF illumination boosts DNA-PAINT imaging and quantification

Flat-top TIRF illumination boosts DNA-PAINT imaging and quantification

Florian Stehr, Johannes Stein, Florian Schueder
Petra Schwille and Ralf Jungmann

Author contributions:

F.St. and **J.S.** contributed equally. F.St. and **J.S.** built the microscope, designed and performed experiments, analyzed data, and wrote the manuscript. F.Sc. designed DNA origami structures, performed cell experiments and wrote the manuscript. F.St., **J.S.**, F.Sc., and R.J. conceived of the study. R.J. supervised the study, interpreted data, and wrote the manuscript. P.S. supervised the study and wrote the manuscript. **All authors** reviewed and approved the manuscript.

published in

Nature Communications (2019), 10, 1, 1268

Reprinted from [93] under the CC BY-NC 4.0 license.

nature COMMUNICATIONS

ARTICLE

https://doi.org/10.1038/s41467-019-09064-6 OPEN

Flat-top TIRF illumination boosts DNA-PAINT imaging and quantification

Florian Stehr[1], Johannes Stein[1], Florian Schueder[1,2], Petra Schwille[1] & Ralf Jungmann[1,2]

Super-resolution (SR) techniques have extended the optical resolution down to a few nanometers. However, quantitative treatment of SR data remains challenging due to its complex dependence on a manifold of experimental parameters. Among the different SR variants, DNA-PAINT is relatively straightforward to implement, since it achieves the necessary 'blinking' without the use of rather complex optical or chemical activation schemes. However, it still suffers from image and quantification artifacts caused by inhomogeneous optical excitation. Here we demonstrate that several experimental challenges can be alleviated by introducing a segment-wise analysis approach and ultimately overcome by implementing a flat-top illumination profile for TIRF microscopy using a commercially-available beam-shaping device. The improvements with regards to homogeneous spatial resolution and precise kinetic information over the whole field-of-view were quantitatively assayed using DNA origami and cell samples. Our findings open the door to high-throughput DNA-PAINT studies with thus far unprecedented accuracy for quantitative data interpretation.

---

[1] Max Planck Institute of Biochemistry, 82152 Martinsried, Munich, Germany. [2] Faculty of Physics and Center for Nanoscience, Ludwig Maximilian University, 80539 Munich, Germany. These authors contributed equally: Florian Stehr, Johannes Stein. Correspondence and requests for materials should be addressed to P.S. (email: schwille@biochem.mpg.de) or to R.J. (email: jungmann@biochem.mpg.de)

The advent of super-resolution microscopy has revolutionized life science research by providing access to molecular structures with light microscopy, which were previously hidden below the diffraction limit. One of the major branches in the field is referred to as single molecule localization microscopy (SMLM) and includes methods such as photo-activated localization microscopy[1] (PALM), Stochastic optical reconstruction microscopy[2] (STORM), point accumulation in nanoscale topology[3] (PAINT), and their descendants[4]. In STORM and PALM, the blinking required for super-resolution reconstruction is obtained by complex photo-physical switching and activation of target-bound fluorophores. In contrast, PAINT imaging is based on reversible binding of a fluorescent species to the target structure. DNA-PAINT[5] exploits the specificity of DNA by using single-stranded oligonucleotides as labels ("docking strands") to which fluorescently-labeled complementary "imager" strands bind. Due to the non-fluorogenic nature of imagers (i.e., dye-labeled imager strands do fluoresce if not bound to their respective target strands), DNA-PAINT experiments are typically performed using some sort of selective plane illumination and/or detection, such as total internal reflection fluorescence (TIRF) microscopy[6], oblique illumination[7], or spinning disk confocal microscopy[8]. Besides offering spectrally-unlimited multiplexing capabilities (Exchange-PAINT)[9] and quantitative imaging (qPAINT)[10], DNA-PAINT can achieve spatial resolutions down to ~5 nm using standard TIRF microscopy[5]. As it is the case for all SMLM methods, reconstructed images have to be carefully interpreted, as they can be prone to artifacts arising e.g., from inhomogeneous illumination caused by the Gaussian laser profile[11,12]. This becomes especially important if localization datasets are used to extract quantitative information such as blinking kinetics, absolute molecule numbers, and other parameters beyond "just" binning of localizations to render qualitative images. Furthermore, inhomogeneous illumination can lead to spot-detection and fitting artifacts, ultimately resulting in a non-truthful reconstruction of the image data. One prominent example are false localizations originating from multiple active single emitters in a diffraction-limited area. A manifold of rather sophisticated methods and algorithms have been developed to deal with these multi-emitter localizations in SMLM data[13–17]. However, they are often not straightforward to implement or computationally intense. Approaches for obtaining homogeneous illumination throughout the field-of-view should make it possible to use rather simple global thresholding algorithms to efficiently filter out these mislocalizations and omit them from downstream analysis.

While different solutions for uniform laser excitation have been proposed and applied to SMLM[18–20], these approaches negatively affect TIRF microscopy, due to their inherent reduction of spatial coherence[18,19]. Although coherent transformation of a Gaussian laser beam into a flat-top intensity profile by means of refractive beam-shaping has been pioneered decades ago[21,22], only very recently flat-top TIR illumination has been reported with the help of refractive beam-shaping elements, promising clear advantages regarding the interpretation of single molecule experiments[23] and their potential application to SMLM[24].

In this study, we identify imaging and quantification artifacts introduced by inhomogeneous sample illumination in DNA-PAINT. To achieve this, we present a novel processing metric based on analyzing radial image segments that allows us to quantitatively assess these artifacts and—at least to some extend—overcome the limitation of inhomogeneous sample illumination without the need for sophisticated post-processing of the data. In order to improve on that and to reduce the amount of post-processing necessary to achieve truthful representation of the data, we employ flat-top TIR illumination for DNA-PAINT microscopy and demonstrate an increased homogeneity of almost all experimental observables when compared to standard Gaussian illumination. This has several implications: first, we achieved the same spot detection efficiency throughout the whole FOV (important for truthful SMLM reconstruction), thus eliminating the necessity for advanced spot finding algorithms, which take non-uniform illumination into account. Second, the uniformity of the excitation field allowed us to obtain accurate and precise binding time distributions for DNA-PAINT, independent of the position in the FOV. We used this predictability to demonstrate improved kinetic analysis of binding durations over the whole FOV. Third, we achieved uniform localization precision allowing spatial resolution better than 10 nm. Lastly, we find that homogeneous TIR excitation enables us to robustly identify multi-emitter localizations simply according to the number of photons detected. By exploiting the advantage of DNA-PAINT that sufficient sampling of the target structure is provided due to reversible binding of new imagers, we can afford to exclude all of these multi-emitter localizations detected by straightforward thresholding and thereby largely improve image quality for artifact-free quantitative statements without sophisticated image post-processing. Combining all advantages, we performed cellular DNA-PAINT imaging of the microtubule network in fixed cells and achieved a significant reduction of artifacts in the periphery compared to Gaussian illumination while preserving the image quality in terms of spatial resolution.

Results

Robust spot detection and homogeneous blinking. To achieve flat-top illumination, we employed a refractive beam-shaping element called piShaper (AdlOptica GmbH, Berlin, Germany), which we placed in the excitation path of a custom-built TIRF microscope (a setup sketch can be found in Supplementary Figure 1). While transforming the profile of the excitation laser, refractive beam-shaping does preserve spatial coherence[23], which still enables efficient TIRF microscopy in contrast to previously reported flat-field super-resolution studies[18,19]. In order to quantitatively analyze the flat-top TIRF profile, we recorded a sequence of fluorescence images of a sample containing a high surface density of immobilized DNA origami structures, to which freely diffusing imager strands could bind. Figure 1a shows full-chip TIRF images obtained by averaging all acquisition frames for the Gaussian and flat-top profiles (left and right panel, respectively). Exemplary line profiles (Fig. 1b) show the fluorescence intensity variation along the specified axis for Gaussian (upper panel) and flat-top illumination (lower panel), yielding an intensity decrease by nearly a factor of three for Gaussian illumination vs. stable intensity for flat-top illumination.

In DNA-PAINT, blinking is achieved by the transient binding of short fluorescently-labeled DNA oligonucleotide "imager strands" to a DNA "docking" strand which is attached to the target of interest (Fig. 2a). The duration of blinking events is defined as bright time. We designed rectangular DNA origami nanostructures with a 20-nm-spaced pattern of 3 × 4 docking strands ("20-nm-grids", Fig. 2b) in order to quantitatively characterize the effect of inhomogeneous illumination on DNA-PAINT imaging. Super-resolution images of 20-nm-grids were acquired either using Gaussian or flat-top illumination and subsequently segmented into concentric rings such that each segment contained a similar number of structures (~800 per segment) for subsequent analysis (Fig. 2c).

First, we examined the detection efficiency of our spot finding and single-molecule fitting algorithm during SR reconstruction for a given threshold in the computed net gradient between adjacent pixels in the raw images[5]. Figure 2d compares exemplary

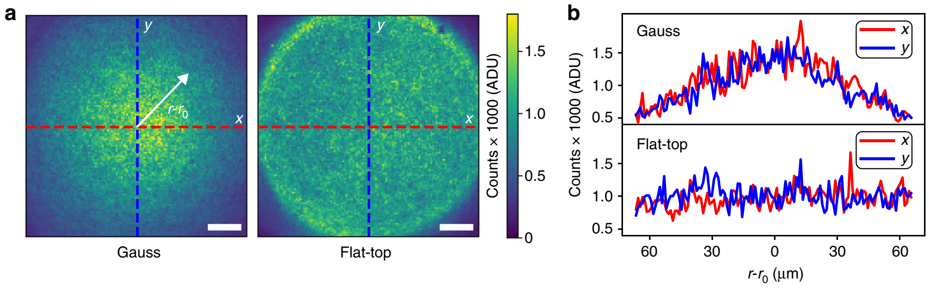

Fig. 1 Gauss vs. flat-top illumination profiles. **a** Traditional illumination profile for TIRF microscopy with a Gaussian laser beam (left) compared to a flat-top profile created by a refractive beam-shaping device in the excitation path (right). **b** Line plots of fluorescence intensity along *x* and *y* axes (red and blue, respectively) for both profiles in **a**. Scale bars, 20 µm in **a**

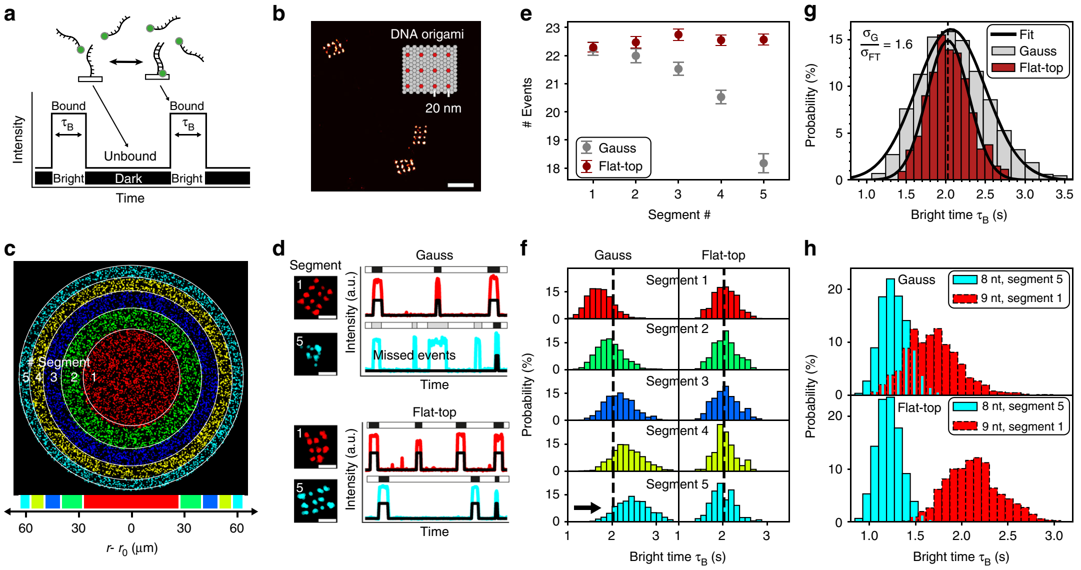

Fig. 2 Flat-top illumination improves single-molecule detection and enables precise binding time quantification. **a** Schematic of DNA-PAINT: dye-labeled imager strands reversibly bind to complementary docking sites that are attached to the target of interest. Binding events result in apparent target blinking required for single molecule localization microscopy (SMLM). **b** DNA-PAINT image of rectangular DNA origami designed to display a 20-nm-grid pattern of docking strands (inset displaying origami design). **c** Whole-sCMOS-chip field of view (FOV) of several thousand DNA origami. Images acquired with Gaussian and flat-top illumination are both segmented into concentric rings containing equal numbers of origami (~800 origami per segment) for downstream quantification. **d** Exemplary DNA origami and intensity traces from inner and outer segment (red and cyan, respectively) showing that binding events in the outer segment are missed by the spot detection algorithm for Gaussian illumination. **e** The effect illustrated in **d** leads to a decrease in the mean number of binding events per origami with radial distance for the Gaussian profile. Flat-top illumination allows robust spot detection over the whole FOV. **f** Inhomogeneous photobleaching of imager strands increases the mean bright time with radial distance for Gaussian illumination. **g** The effect observed in **f** leads to an overall broadening of the bright time distribution over the whole FOV. **h** Distinction of docking strands of different length via bright times. Position-dependent bright times for Gaussian illumination lead to non-separable populations. Scale bars, 20 nm in **b** and 40 nm in **d**. Error bars in **e** correspond to SEM

intensity traces from 20-nm-grids in segments 1 and 5, highlighting that for Gaussian illumination blinking events in the outer segments were not detected anymore, resulting in poor sampling of the DNA origami image. This is due to the fact that the inhomogeneous profile of Gaussian illumination leads to a systematic decrease of the net gradient in DNA-PAINT raw images with increasing radial distance from the center (Supplementary Figure 2). The same effect was visible when comparing the average number of apparent binding events per 20-nm-grid between the segments (Fig. 2e). However, images acquired with flat-top illumination showed a constant net gradient resulting in a homogeneous spot detection efficiency (Fig. 2d and

Supplementary Figure 2) and ultimately in a constant number of binding events (Fig. 2e).

Next, we investigated the illumination effects on the bright times of imager binding events using our 20-nm-grids. As the localization precision in SMLM increases with the number of detected photons per acquisition frame[25,26], it is generally advisable to adapt camera integration times, dye switching duty cycles, and photon emission rates to obtain optimal localization precision. While the finite photon budget of fixed dyes in approaches like STORM or PALM sets a practical limit to the number of photons per switching cycle[27], PAINT-based approaches have the advantage that every blinking event originates from a "fresh" dye, thus the full photon budget of this dye can be harvested for superior localization precision. However, this comes at the cost of potentially bleaching a certain fraction of imager strands before they have dissociated from their targets. In order to enable precise adjustment of binding and bleaching times for e.g., qPAINT quantification, this bleaching probability should be constant over the FOV. For a Gaussian illumination profile, we observed that imager strands (9 nucleotides in length) binding to the center of the field of view photobleach faster than in the outer segments, as one would expect (Fig. 2f). In contrast, images acquired with flat-top illumination exhibited homogeneous bright times for the same imager species throughout the FOV. The radial bright time dependence for Gaussian illumination resulted in a broadening of the total bright time distribution over the FOV by a factor of $\sigma_G/\sigma_{FT} = 1.6$ compared to flat-top illumination (Fig. 2g). Inhomogeneous bleaching conditions have direct implications for quantitative statements based on the blinking kinetics from DNA-PAINT images. Figure 2h shows that for DNA-PAINT images of 20-nm-grids with either shorter-binding 8 nucleotide-long (nt) or longer-binding 9-nt-long docking strands acquired with the same imager under identical conditions, it was not possible to distinguish between the two bright time populations comparing segments 1 and 5 for Gaussian illumination (but it still allows for differentiation within each segment, see Supplementary Figure 3a). However, flat-top illumination allowed us to clearly separate bright time distributions over the full FOV. Analogously to Fig. 2g the total bright time distributions for both 8-nt and 9-nt 20-nm-grids are narrower for flat-top illumination (Supplementary Figure 3b). Enhanced control over the bleaching behavior allowed us to both resolve single 20-nm-grid structures (see Supplementary Figure 4) and simultaneously distinguish between short and long binding duration with high fidelity.

Uniform localization precision and mislocalization filtering. In order to obtain a measure of how precise a single DNA-PAINT docking strand could be localized, we used a previously developed "averaging" tool in Picasso that allowed us to pick all 20-nm-grids in an image and to align them onto a model grid[28]. Figure 3a displays the averaged images of more than 700 structures each from segments 1 (red) and 5 (cyan) for the same sample imaged with Gaussian and flat-top illumination (a 20 × 20 subset of individual 20-nm-grid images can be found in Supplementary Figure 5). The histograms represent the spatial distribution of localizations along the dashed lines. A double Gaussian fit recovered the designed docking strand spacing of ~20 nm. The evident loss of resolution in the Gaussian average from segment 5 compared to segment 1 is confirmed by the broadened peaks in the histograms which increased by almost a factor of two (localization precision from ~2.0 to ~3.5 nm). On the contrary, in the flat-top image only a minor decrease in localization precision was observed (~10%). As previously mentioned, the localization uncertainty in SMLM is inversely proportional to the square-root of the number of detected photons. We identified a three-fold decrease in the average number of detected photons per localization event from ~15,000 to ~5,000 comparing segments 1 and 5 for Gaussian illumination and attributed this as the main cause for the decrease in localization precision (Fig. 3b). Segment-wise calculation of the localization precision based on Nearest Neighbor Analysis[5,29] (NeNA) confirmed this relation (Fig. 3c). Nevertheless, we also observed a radial decrease in photon number and localization precision for the image acquired with flat-top illumination. Since this effect is decoupled from the excitation profile, we attribute this to finite aperture effects that become increasingly apparent in the periphery when increasing the FOV. However, this only leads to minor radial performance and image resolution loss (~10 %) compared to the performance decrease due to inhomogeneous excitation in the case of Gaussian illumination.

In order to benchmark the overall localization precision for flat-top illumination, we designed and imaged DNA origami structures with a 10-nm-grid pattern of docking strands. We could resolve the individual docking strands even in segment 5, demonstrating better than 10 nm spatial resolution over the entire FOV, ~130 µm in diameter (Fig. 3d).

Straightforward filtering capabilities during image post-processing are an additional advantage of using flat-top illumination. Figure 3e depicts the photon count distribution for a 20-nm-grid sample imaged with Gaussian (top) and flat-top illumination (bottom). In contrast to Gaussian illumination, we were able to identify two distinct peaks in the distribution from the image acquired with the flat-top profile. The first peak at 25,800 photons is attributed to localizations originating from single imager binding events. The second peak is located at roughly twice the number of photons (53,200) and represents localizations originating from two imager strands bound simultaneously to the same structure. The top panel in Fig. 3f illustrates that these multi-emitter events result in mislocalizations, thus degrading the overall image quality. In contrast to the Gaussian profile (only in segment 1 the photon count distribution indicates two peaks, see Supplementary Figure 6), flat-top illumination allowed us to robustly use an upper threshold limit over the whole FOV at the $1/e^2$ value of the first peak for filtering out these mislocalizations during post-processing and thereby considerably improving the quality of the super-resolved image (Fig. 3f, bottom).

Improved large field-of-view cellular imaging with DNA-PAINT. After identifying and quantifying the effects caused by inhomogeneous illumination on DNA origami structures, we applied flat-top illumination for imaging cellular structures with DNA-PAINT to highlight the differences in obtainable overall image quality researchers should expect on common samples. Figure 4a shows SR images of the microtubule network in fixed COS-7 cells labeled using primary and DNA-conjugated secondary antibodies[5,30] and subsequent DNA-PAINT imaging for Gaussian (left) and flat-top illumination (right) acquired with the full camera sensor resulting in a field-of-view of 130 × 130 µm^2. The magnified regions in the center and the border of the image (segment 1 and 5 as defined in Fig. 2c) recorded using Gaussian illumination show an increasing loss of localizations towards the periphery due to the limited spot-detection efficiency (see Fig. 4b, bottom left). In contrast, we obtain a uniform localization density using flat-top illumination, confirming the earlier observations for DNA origami experiments (Fig. 4b, right. Find a detailed two-level zoomed cell image in Supplementary Figure 7). The white arrows point to regions of accumulated multi-emitter mislocalizations in between the densely-labeled microtubules (for

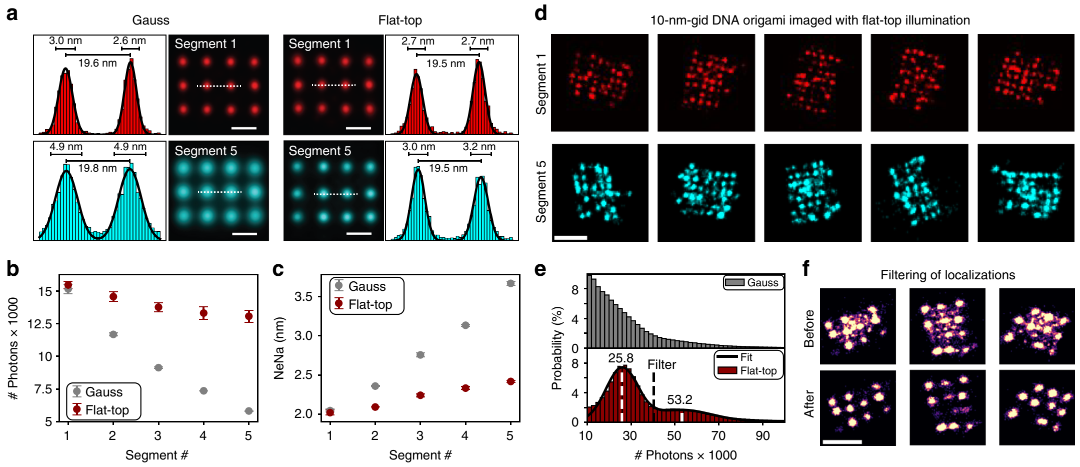

Fig. 3 Localization precision of 2 nm over 130 × 130 μm^2 FOV with flat-top illumination. **a** Averaged images of 20-nm-grid structures (~800 per segment, see Fig. 2c for definition of segments) show radial decrease in resolution using Gaussian illumination, while flat-top illumination maintains high spatial resolution. Fit results for peak-to-peak distance and standard deviation displayed above. **b** Mean number of detected photons per localization per frame. **c** Localization precision calculated by nearest neighbor analysis (NeNA) **d** 10-nm-grid DNA origami design for whole-chip resolution benchmarking under flat-top illumination. **e** Photon count histogram for flat-top illumination indicating two peaks for the case of single binding and simultaneous binding events of two imager strands to a 20-nm grid. **f** Filtering out simultaneous binding events above single binding threshold (filter in **e** set $1/e^2$ value of first distribution) allowing the removal of "cross talk" localizations in between two active docking strands. Scale bars, 20 nm in **a**, 50 nm in **d** and **f**. Error bars in **b** and **c** correspond to SEM

magnified illustration see Supplementary Figure 8). These could again be identified in all photon count histograms in Fig. 4c, except for segment 5 of the image acquired using Gaussian illumination. Figure 4d demonstrates the gain in image quality for both segments of the flat-top image after removal of all localizations above the $1/e^2$ value of the single emitter peak. The distributions of localizations in the boxed regions along the indicated directions in Fig. 4d show two distinct peaks originating from the 2D projection of a homogenously-labeled rod. Even in the periphery of the full camera sensor image we recovered a peak-to-peak distance of ~37 nm which is in good agreement with previously reported values from SR studies[5,19,30,31]. Despite the radial quality loss in the image acquired with Gaussian illumination, we could also identify and remove multi-emitter mislocalizations in the center of the image (Supplementary Figure 9).

Overall, high-throughput DNA-PAINT SMLM employing large FOVs can hence benefit from flat-top illumination without substantial trade-off in image quality.

Discussion

We here presented a quantitative super resolution study of flat-top TIRF illumination for DNA-PAINT. We demonstrated that flat-top illumination improves the quantification accuracy in DNA-PAINT data by enabling both homogeneous spatial resolution and precise kinetic blinking parameters over large FOVs. In addition, uniform illumination gives rise to new features in the experimental observables, that can be used during straightforward post-processing. This includes a more robust spot detection and enabled us to effectively remove multi-emitter artifacts without the use of computationally demanding multi-emitter localization algorithms[13–17]. We achieved the latter by simple photon number thresholding in the resulting localization datasets. We want to note, that using this threshold to omit multi-emitter mislocalizations does not necessarily lead to a reduced image quality due to missed localizations in DNA-PAINT, as we can collect a considerably larger amount of total localizations per docking strand due to the repetitive nature of image acquisition.

Furthermore, improved control over the photobleaching conditions allowed us to distinguish apparent identical structures of different docking strand length independent of their position within the FOV. This could be exploited for non-spectral multiplexing in DNA-PAINT super resolution microscopy in the future. We think that these numerous advantages will significantly enhance the statistical treatment of single-molecule microscopy data, since a flat-top illumination allows the use of the complete FOV for further analysis and can hence pave new routes for high-throughput experiments. Furthermore, a uniform TIR excitation will improve single-molecule fluorescence-based binding affinity studies on surfaces, e.g., by SI-FCS[32], since photophysical effects can be treated globally and can therefore be decoupled from local changes caused by other physical effects. In cases where phototoxicity has to be minimized[33], flat-top illumination can provide precise control over the whole FOV.

Regarding the comparison of Gaussian and flat-top illumination several of our findings can also directly improve image quality for quantitative DNA-PAINT with a Gaussian excitation profile, when segment-wise analysis of parameters is employed. With regard to biological samples, however, segmented analysis will presumably be most beneficial in the case of compact, separable protein structures such as nuclear pore complexes compared to continuous networks such as the cytoskeleton or large organelle structures. Using this segmentation approach, we showed that in the center segment it is also possible to remove multi-emitter localizations for more precise and quantitative data interpretation. Furthermore, the differentiation between structures with short and long binding docking strands is also possible within each segment, but obviously this comes at the cost that the overall statistics is divided by the number of introduced segments.

In conclusion however, we are convinced that the advantages arising from flat-top TIR illumination—especially with regards to

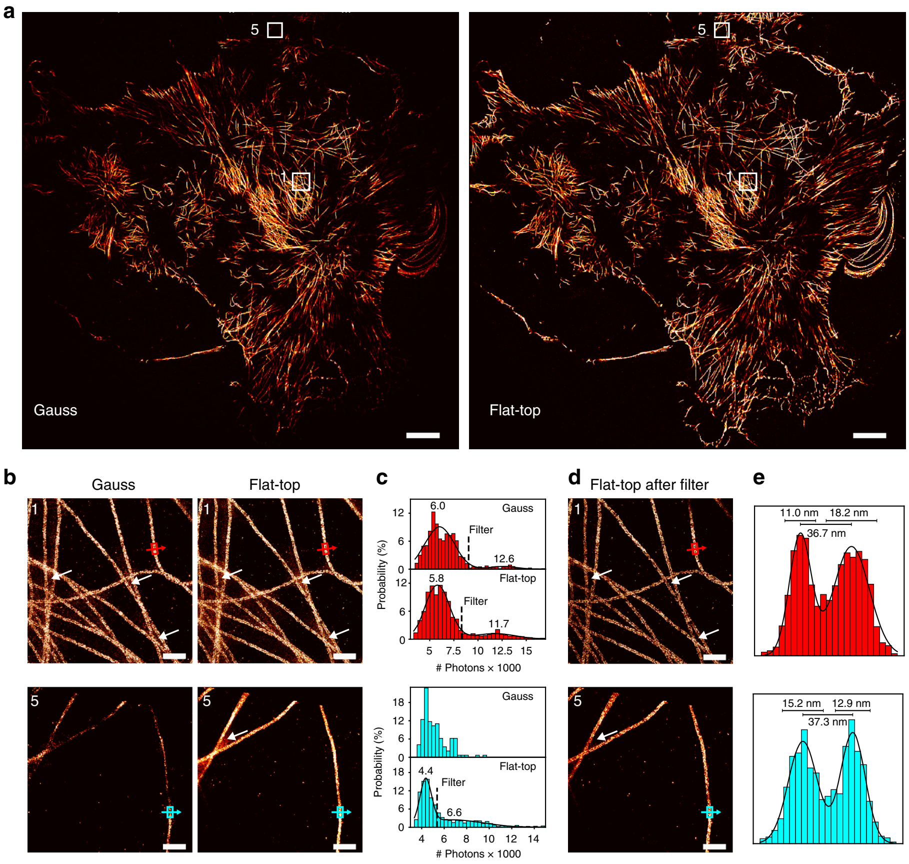

Fig. 4 Artifact removal for uniform and quantitative cellular DNA-PAINT imaging. **a** Full camera chip (130 × 130 μm^2) DNA-PAINT image of the microtubule network in fixed COS-7 cells acquired using Gauss illumination (left) and the same field of view for flat-top illumination (right). **b** Magnified sections from segment 1 and segment 5 (as defined in Fig. 2a) highlighting the image quality in the center and the border region of the camera chip. White arrows point to artifacts due to multi-emitter mislocalizations. **c** Photon count histograms for box regions in images from **b**. Double Gaussian fit allows identification and removal of multi-emitter mislocalizations (threshold at $1/e^2$ of first peak) except for segment 5 for Gaussian illumination. **d** Filtered flat-top images from **b** displaying enhanced image quality after removing mislocalization artifacts. **e** Intensity profiles across single microtubules indicated in **d**. Scale bars, 10 μm in **a**, 500 nm in **b**, **d**

the ease-of-use and availability of commercial beam shaping devices—are clearly superior and we believe they might become a standard feature for TIRF microscopy.

Methods

Materials. Unmodified, dye-labeled, and biotinylated DNA oligonucleotides were purchased from MWG Eurofins. DNA scaffold strands were purchased from Tilibit (p7249, identical to M13mp18). Streptavidin (cat: S-888) and glass slides (cat: 10756991) were ordered from Thermo Fisher. Coverslips were purchased from Marienfeld (cat: 0107052). PEG-8000 was purchased from Merck (cat: 6510-1KG). Tris 1M pH 8.0 (cat: AM9856), EDTA 0.5M pH 8.0 (cat: AM9261), Magnesium 1M (cat: AM9530G) and Sodium Chloride 5M (cat: AM9759) were ordered from Ambion. Ultrapure water was obtained from a Milli-Q filter machine. Tween-20 (cat: P9416-50ML), Glycerol (cat: G5516-500ML), Methanol (cat: 32213-2.5L), BSA-Biotin (cat: A8549), Protocatechuate 3,4-Dioxygenase Pseudomonas (PCD) (cat: P8279), 3,4-Dihydroxybenzoic acid (PCA) (cat: 37580-25G-F) and (+-)-6-Hydroxy-2,5,7,8-tetra-methylchromane-2-carboxylic acid (Trolox) (cat: 238813-5G) were ordered from Sigma-Aldrich. Twinsil two-component glue was purchased from Picodent (cat: 13001000). Monoclonal antibodies against alpha-tubulin (cat: MA1-80017) was purchased from Thermo Scientific. The secondary antibodies Anti-Rat (cat: 712-005-150) were purchased from Jackson ImmunoResearch.

Buffers. Five buffers were used for sample preparation and imaging: Buffer A (10 mM Tris-HCl pH 7.5, 100 mM NaCl, 0.05% Tween 20, pH 7.5); Buffer B (5 mM Tris-HCl pH0 8, 10 mM MgCl2, 1 mM EDTA, 0.05% Tween 20, pH 8); Buffer C (1× PBS pH 8, 500 mM NaCl, pH 8); 100× Trolox: 100 mg Trolox, 430 μl 100% methanol, 345 μl of 1M NaOH in 3.2 ml H2O. 40× PCA: 154 mg PCA, 10 ml water, and NaOH were mixed and adjusted to pH 9.0. 100× PCD: 9.3 mg PCD, 13.3 ml of buffer (100 mM Tris-HCl pH 8, 50 mM KCl, 1 mM EDTA, 50% glycerol).

DNA origami design, assembly, and purification. DNA origami structures were designed using the design module of Picasso[5] (see Supplementary Figure 10). Folding of structures was performed using the following components: single-stranded DNA scaffold (0.01 μM), core staples (0.5 μM), biotin staples (0.5 μM), modified staples (each 0.5 μM), 1× folding buffer in a total of 50 μl for each sample. Annealing was done by cooling the mixture from 80 to 25 °C in 3 h in a thermocycler. Structures were purified using PEG-precipitation[34].

DNA origami sample preparation. A glass slide was glued onto a coverslip with the help of double-sided tape (Scotch, cat. no. 665D) to form a flow chamber with inner volume of ~20 µl. First, 20 µl of biotin-labeled bovine albumin (1 mg/ml, dissolved in buffer A) was flushed into the chamber and incubated for 2 min. The chamber was then washed with 40 µl of buffer A. Twenty microliterof streptavidin (0.5 mg/ml, dissolved in buffer A) was then flushed through the chamber and incubated for 2 min. After washing with 40 µl of buffer A and subsequently with 40 µl of buffer B, 20 µl of biotin-labeled DNA structures (1:80 dilution in buffer B from purified DNA-origami stock) were flushed into the chamber and incubated for 10 min. The chamber was washed with 40 µl of buffer B. Finally, 40 µl of the imager solution was flushed into the chamber, which was subsequently sealed with two-component glue before imaging. A list of all staples can be found in Supplementary Tables 1 and 2.

Cell sample preparation. COS7 cells were cultured with Eagle's minimum essential medium fortified with 10% FBS with penicillin and streptomycin and were incubated at 37 °C with 5% CO_2. At ~30% confluence, cells were seeded into Eppendorf 8-well chambered cover glass ~24 h before fixation and were grown to ~70% confluence. For fixation, the samples were pre-fixed and pre-permeabilized with 0.4% glutaraldehyde and 0.25% Triton X-100 for 90 s. Next, the cells were quickly rinsed with 1× PBS once followed by fixation with 3% glutaraldehyde for 15 min. Afterwards, samples were rinsed twice (5 min) with 1× PBS and then quenched with 0.1% $NaBH_4$ for 7 min. After rinsing four times with 1× PBS for 30 s, 60 s, and twice for 5 min, samples were blocked and permeabilized with 3% BSA and 0.25% Triton X-100 for 2 h. Then, samples were incubated with 10 µg/ml of primary antibodies (1:100 dilution) in a solution with 3% BSA and 0.1% Triton X-100 at 4 °C overnight. Cells were rinsed three times (5 min each) with 1× PBS. Next, they were incubated with 10 µg/ml of labeled secondary antibodies (1:100 dilution) in a solution with 3% BSA and 0.1% Triton X-100 at room temperature for 1 h. For fiducial based drift correction, the samples were incubated with gold nanoparticles with a 1:1 dilution in 1× PBS for 5 min. Finally, samples were rinsed three times with 1× PBS before adding imager solution.

Super-resolution microscopy setup. Fluorescence imaging was carried out on an inverted custom-built microscope (see setup sketch in Supplementary Figure 1) in an objective-type TIRF configuration with an oil-immersion objective (Olympus UAPON, 100×, NA 1.49). One laser was used for excitation: 561 nm (1 W, DPSS-system, MPB). Laser power was adjusted by polarization rotation with a half-wave plate (Thorlabs, WPH05M-561) before passing a polarizing beam-splitter cube (Thorlabs, PBS101). To spatially clean the beam-profile the laser light was coupled into a single-mode polarization-maintaining fiber (Thorlabs, P3-488PM-FC-2) using an aspheric lens (Thorlabs, C610TME-A). The coupling polarization into the fiber was adjusted using a zero-order half wave plate (Thorlabs, WPH05M-561). The laser light was re-collimated after the fiber using an achromatic doublet lens (Thorlabs, AC254-050-A-ML) resulting in a collimated FWHM beam diameter of ~6 mm. The laser light was split into two paths of approximately equal length using a combination of two flip mirrors (Thorlabs, FM90/M). In one path the laser light was unaltered resulting in a Gaussian beam profile for excitation. In the other path a diffractive beam shaper device (AdlOptica, piShaper 6_6_VIS) transformed the Gaussian beam profile in a collimated flat-top profile. Both paths were realigned to each other and passed the same downstream optics. Switching between the two illumination schemes can therefore be achieved by flipping two mirrors simultaneously. The laser beam diameter was magnified by a factor of 2.5 using a custom-built Telescope (Thorlabs, AC254-030-A-ML and Thorlabs, AC508-075-A-ML). The laser light was coupled into the microscope objective using an achromatic doublet lens (Thorlabs, AC508-180-A-ML) and a dichroic beam splitter (AHF, F68-785). Fluorescence light was spectrally filtered with an emission filter (AHF Analysentechnik, 605/64) and imaged on a sCMOS camera (Andor, Zyla 4.2) without further magnification (Thorlabs, TTL180-A) resulting in an effective pixel size of 130 nm (after 2 × 2 binning). Microscopy samples were mounted on a x-y-z stage (ASI, S31121010FT and ASI, FTP2050) that was used for focusing with the microscope objective being at fixed position. Our custom TIRF setup was used for all Figures.

Imaging conditions. All fluorescence microscopy data was recorded on the full sensor (2048 × 2048 pixels, pixel size: 6.5 µm) of our SCMOS camera operated with the open source acquisition software µManager[35] at a read out rate of 200 MHz and a dynamic range of 16 bit. Detailed imaging conditions for all main and supplementary figures can be found in Supplementary Table 3. The laser power refers to the power measured after the fiber (see Supplementary Figure 1). As can be seen in Fig. 1b, the mean intensity of the flat-top profile is at around 60 % of the Gaussian peak intensity, when operated at the same power. Supplementary Figure 11 illustrates that by an respective power increase we can adjust the flat-top profile to the Gaussian peak intensity. Sequence design of imager and docking strands can be found in Supplementary Table 4.

Super-resolution reconstruction. Raw fluorescence data was subjected to spot-finding and subsequent super-resolution reconstruction using the localize module of the Picasso software package[5]. Localizations were then loaded into Picasso's render module and drift-corrected. DNA origamis were automatically selected using the "Pick similar" function with the following settings: pick radius: 143 nm; standard deviation: 1.5, 1.7, 1.9 (subsequently). After automated selection, picked areas were saved as "Picked localizations" for further processing.

Kinetic analysis. Picasso's render module[5] allows automatic recognition of ROIs within the rendered super-resolution image by searching for similarity in the localization distribution to pre-selected user defined regions of specific size. The resulting ROIs of the complete set of localizations are referred to as "picks" (Supplementary Figure 12a). We calculated characteristic quantities associated with the temporal distribution of localization events within each of these picks with a custom written python script (see Supplementary Figure 12). Since the automated selection of ROIs cannot distinguish between repetitive (specific) and non-repetitive (unspecific) blinking behavior we implemented a filtering procedure based on the temporal distribution of localization events.

Filtering. By looking at the temporal distribution of the localization events (trace) associated to a single pick we can define its mean and standard deviation. We refer to these parameters as the mean (localization) frame and its standard deviation (std) in the units of frames. Repetitive transient binding to DNA origami throughout the measurement leads hence to a mean (localization) frame of roughly half the number of total frames in the acquisition window with a large standard deviation (Supplementary Figure 12b, left panel). In contrast non-repetitive binding will result in a mean (localization) frame located within the frames of their unique occurrence randomly distributed throughout the acquisition window and a small standard deviation (Supplementary Figure 12b, right panel). Plotting the distribution of the mean (localization) frame and its standard deviation over all automatically selected ROIs thus allows clear identification of a major population of picked areas showing repetitive blinking while outliers indicating non-repetitive blinking behavior can be disregarded for further analysis (Supplementary Figure 12c and d).

Averaging. Picked origami structures were averaged to a designed model structure using the average3 module of Picasso with a pixel oversampling of 40 and setting a custom symmetry of 180 degree[28].

Reporting summary. Further information on experimental design is available in the Nature Research Reporting Summary linked to this article.

Code availability. All code supporting the findings of this study is available from the corresponding author upon request.

Data availability

The data that support the findings of this study are available from the corresponding authors upon reasonable request.

Received: 29 October 2018 Accepted: 19 February 2019
Published online: 20 March 2019

References

1. Betzig, E. et al. Imaging intracellular fluorescent proteins at nanometer resolution. *Science* **313**, 1642 LP–1641645 (2006).
2. Rust, M. J., Bates, M. & Zhuang, X. Sub-diffraction-limit imaging by stochastic optical reconstruction microscopy (STORM). *Nat. Methods* **3**, 793 (2006).
3. Sharonov, A. & Hochstrasser, R. M. Wide-field subdiffraction imaging by accumulated binding of diffusing probes. *Proc. Natl Acad. Sci.* **103**, 18911–18916 (2006).
4. Sauer, M. & Heilemann, M. Single-molecule localization microscopy in eukaryotes. *Chem. Rev.* **117**, 7478–7509 (2017).
5. Schnitzbauer, J., Strauss, M. T., Schlichthaerle, T., Schueder, F. & Jungmann, R. Super-resolution microscopy with DNA-PAINT. *Nat. Protoc.* **12**, 1198 (2017).
6. Axelrod, D. Cell-substrate contacts illuminated by total internal reflection fluorescence. *J. Cell. Biol.* **89**, 141 LP–141145 (1981).
7. Tokunaga, M., Imamoto, N. & Sakata-Sogawa, K. Highly inclined thin illumination enables clear single-molecule imaging in cells. *Nat. Methods* **5**, 159 (2008).
8. Schueder, F. et al. Multiplexed 3D super-resolution imaging of whole cells using spinning disk confocal microscopy and DNA-PAINT. *Nat. Commun.* **8**, 2090 (2017).
9. Jungmann, R. et al. Multiplexed 3D cellular super-resolution imaging with DNA-PAINT and exchange-PAINT. *Nat. Methods* **11**, 313 (2014).

10. Jungmann, R. et al. Quantitative super-resolution imaging with qPAINT. *Nat. Methods* **13**, 439 (2016).
11. Axelrod, D. B. T.-M. in C. B. in *Biophysical Tools for Biologists: In Vivo Techniques*, (eds.) John J. Correia and H. William Detrich, Vol. 2 169–221 (Academic Press, San Diego, 2008). https://doi.org/10.1016/S0091-679X(08)00607-9
12. Yang, Q., Karpikov, A., Toomre, D. & Duncan, J. S. 3-D reconstruction of microtubules from multi-angle total internal reflection fluorescence microscopy using Bayesian framework. *IEEE Trans. Image Process.* **20**, 2248–2259 (2011).
13. Huang, F., Schwartz, S. L., Byars, J. M. & Lidke, K. A. Simultaneous multiple-emitter fitting for single molecule super-resolution imaging. *Biomed. Opt. Express* **2**, 1377–1393 (2011).
14. Holden, S. J., Uphoff, S. & Kapanidis, A. N. DAOSTORM: an algorithm for high- density super-resolution microscopy. *Nat. Methods* **8**, 279 (2011).
15. Zhu, L., Zhang, W., Elnatan, D. & Huang, B. Faster STORM using compressed sensing. *Nat. Methods* **9**, 721 (2012).
16. Burnette, D. T., Sengupta, P., Dai, Y., Lippincott-Schwartz, J. & Kachar, B. Bleaching/blinking assisted localization microscopy for superresolution imaging using standard fluorescent molecules. *Proc. Natl Acad. Sci.* **108**, 21081–21086 (2011).
17. Marsh, R. J. et al. Artifact-free high-density localization microscopy analysis. *Nat. Methods* **15**, 689–692 (2018).
18. Deschamps, J., Rowald, A. & Ries, J. Efficient homogeneous illumination and optical sectioning for quantitative single-molecule localization microscopy. *Opt. Express* **24**, 28080–28090 (2016).
19. Douglass, K. M., Sieben, C., Archetti, A., Lambert, A. & Manley, S. Super-resolution imaging of multiple cells by optimized flat-field epi-illumination. *Nat. Photonics* **10**, 705 (2016).
20. Rowlands, C. J., Ströhl, F., Ramirez, P. P. V., Scherer, K. M. & Kaminski, C. F. Flat-field super-resolution localization microscopy with a low-cost refractive beam-shaping element. *Sci. Rep.* **8**, 5630 (2018).
21. Frieden, B. R. Lossless conversion of a plane laser wave to a plane wave of uniform irradiance. *Appl. Opt.* **4**, 1400–1403 (1965).
22. Hoffnagle, J. A. & Jefferson, C. M. Design and performance of a refractive optical system that converts a Gaussian to a flattop beam. *Appl. Opt.* **39**, 5488–5499 (2000).
23. Khaw, I. et al. Flat-field illumination for quantitative fluorescence imaging. *Opt. Express* **26**, 15276–15288 (2018).
24. Pyle, J. R. & Chen, J. Photobleaching of YOYO-1 in super-resolution single DNA fluorescence imaging. *Beilstein J. Nanotechnol.* **8**, 2296–2306 (2017).
25. Thompson, R. E., Larson, D. R. & Webb, W. W. Precise nanometer localization analysis for individual fluorescent probes. *Biophys. J.* **82**, 2775–2783 (2002).
26. Deschout, H. et al. Precisely and accurately localizing single emitters in fluorescence microscopy. *Nat. Methods* **11**, 253 (2014).
27. Baddeley, D. & Bewersdorf, J. Biological insight from super-resolution microscopy: what we can learn from localization-based images. *Annu. Rev. Biochem.* **87**, 1–25 (2018).
28. Strauss, M. T., Schueder, F., Haas, D., Nickels, P. C. & Jungmann, R. Quantifying absolute addressability in DNA origami with molecular resolution. *Nat. Commun.* **9**, 1600 (2018).
29. Endesfelder, U., Malkusch, S., Fricke, F. & Heilemann, M. A simple method to estimate the average localization precision of a single-molecule localization microscopy experiment. *Histochem. Cell Biol.* **141**, 629–638 (2014).
30. Agasti, S. S. et al. DNA-barcoded labeling probes for highly multiplexed exchange-PAINT imaging. *Chem. Sci.* **8**, 3080–3091 (2017).
31. Dempsey, G. T., Vaughan, J. C., Chen, K. H., Bates, M. & Zhuang, X. Evaluation of fluorophores for optimal performance in localization-based super-resolution imaging. *Nat. Methods* **8**, 1027 (2011).
32. Mücksch, J. et al. Quantifying reversible surface binding via surface-integrated fluorescence correlation spectroscopy. *Nano Lett.* **18**, 3185–3192 (2018).
33. Blumhardt, P. et al. Photo-induced depletion of binding sites in DNA-PAINT microscopy. *Molecules* **23**, 3165 (2018). https://doi.org/10.3390/molecules23123165
34. Stahl, E., Martin, T. G., Praetorius, F. & Dietz, H. Facile and scalable preparation of pure and dense DNA origami solutions. *Angew. Chem. Int. Ed.* **53**, 12735–12740 (2014).
35. Edelstein, A. D. et al. Advanced methods of microscope control using μManager software. *J. Biol. Methods* **1**, e10 (2014). https://doi.org/10.14440/jbm.2014.36

Acknowledgements

We thank Julian Bauer, Patrick Schueler, Bianca Sperl and Sigrid Bauer for experimental support. F.St., and J.S. acknowledge support by the QBM graduate school and the Center for Nanoscience Munich. This work has been supported in part by the German Research Foundation through the Emmy Noether Program (DFG JU 2957/1-1 to R.J.), the SFB1032 (projects A11 and A09 to R.J. and P.S.), the European Research Council through an ERC Starting Grant (MolMap; grant agreement number 680241 to R.J.) and the Max Planck Society (P.S. and R.J.).

Author contributions

F.St. and J.S. built the microscope, designed and performed experiments, analyzed data, and wrote the manuscript. F.Sc. designed DNA origami structures, performed cell experiments and wrote the manuscript. F.St., J.S., F.Sc., and R.J. conceived of the study. R. J. supervised the study, interpreted data, and wrote the manuscript. P.S. supervised the study and wrote the manuscript. All authors reviewed and approved the manuscript.

Additional information

Supplementary Information accompanies this paper at https://doi.org/10.1038/s41467-019-09064-6.

Competing interests: The authors declare no competing interests.

Reprints and permission information is available online at http://npg.nature.com/reprintsandpermissions/

Journal peer review information: *Nature Communications* thanks the anonymous reviewers for their contribution to the peer review of this work. Peer reviewer reports are available.

Publisher's note: Springer Nature remains neutral with regard to jurisdictional claims in published maps and institutional affiliations.

Open Access This article is licensed under a Creative Commons Attribution 4.0 International License, which permits use, sharing, adaptation, distribution and reproduction in any medium or format, as long as you give appropriate credit to the original author(s) and the source, provide a link to the Creative Commons license, and indicate if changes were made. The images or other third party material in this article are included in the article's Creative Commons license, unless indicated otherwise in a credit line to the material. If material is not included in the article's Creative Commons license and your intended use is not permitted by statutory regulation or exceeds the permitted use, you will need to obtain permission directly from the copyright holder. To view a copy of this license, visit http://creativecommons.org/licenses/by/4.0/.

© The Author(s) 2019

Supplementary Information

Flat-top TIRF illumination boosts DNA-PAINT imaging and quantification

Stehr, Stein et al.

Supplementary Figure 1	Schematic of custom-built super-resolution microscopy setup
Supplementary Figure 2	Spot detection and net gradient
Supplementary Figure 3	Bright time distributions for 8-nt vs. 9-nt docking site length
Supplementary Figure 4	Averaged 20-nm-grid image for 8-nt vs. 9-nt docking sites length for flat-top excitation
Supplementary Figure 5	Individual origami images for averaging
Supplementary Figure 6	Segment-wise photon count distribution Gauss vs. Flat-top
Supplementary Figure 7	Uniform spot-detection efficiency for cellular DNA-PAINT imaging
Supplementary Figure 8	Mislocalization removal by multi-emitter filtering
Supplementary Figure 9	Mislocalization removal by multi-emitter filtering for Gaussian illumination
Supplementary Figure 10	DNA origami grid designs
Supplementary Figure 11	Laser power comparison Gauss vs. Flat-Top
Supplementary Figure 12	Filtering by temporal distribution of localizations
Supplementary Table 1	List of core staples
Supplementary Table 2	List of biotinylated staples
Supplementary Table 3	Imaging parameters
Supplementary Table 4	DNA-PAINT imager sequences

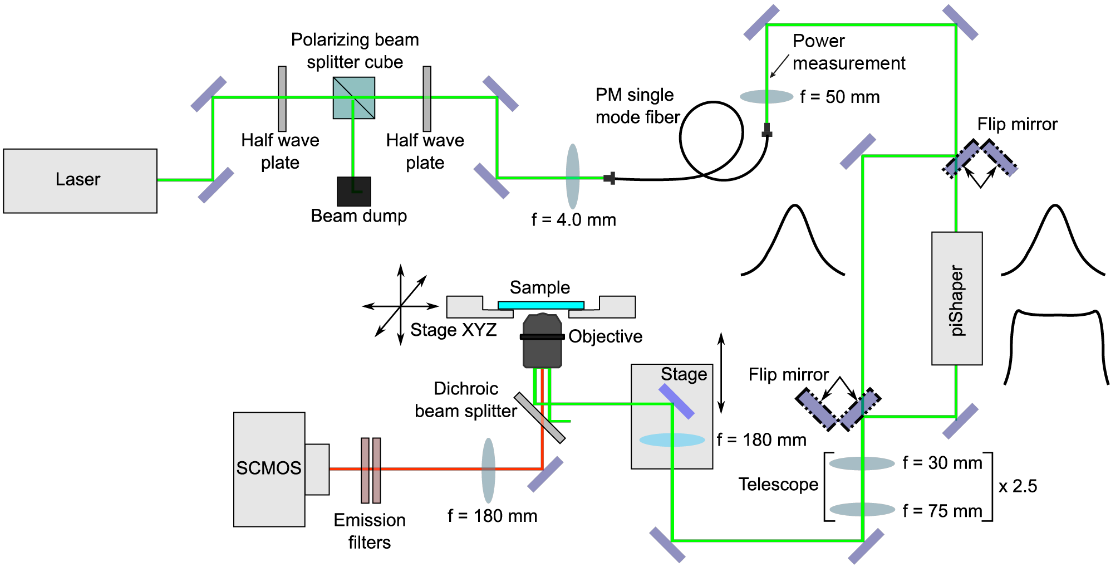
Laser
Polarizing beam splitter cube
Half wave plate
Half wave plate
Beam dump
f = 4.0 mm
PM single mode fiber
Power measurement
f = 50 mm
Flip mirror
piShaper
Sample
Stage XYZ
Objective
Dichroic beam splitter
Stage
f = 180 mm
Flip mirror
Telescope
f = 30 mm
f = 75 mm
x 2.5
SCMOS
Emission filters
f = 180 mm

Supplementary Figure 1 | Schematic of custom-built super-resolution microscopy setup. Blue rectangles indicate dielectric mirrors, ellipses indicate lenses.

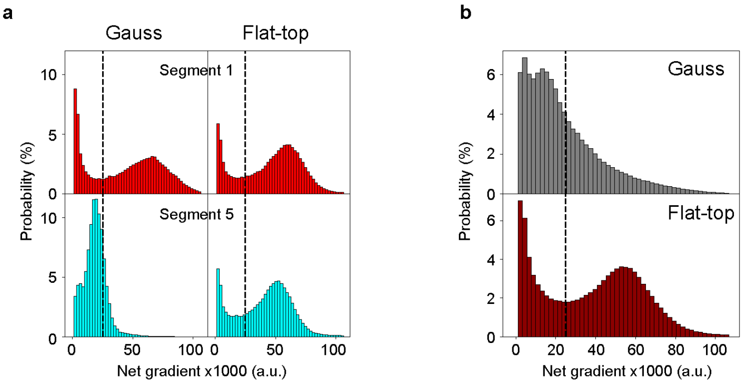

Supplementary Figure 2 | Spot detection and net gradient. a Net gradient histograms comparing segments 1 and 5 of 20-nm-grid images acquired with Gaussian and flat-top illumination. For DNA-PAINT (but also for SMLM in general) a localization algorithm implemented in Picasso[1] distinguishes between bright blinking events and background noise by computing the net gradient between adjacent pixels in the raw images. A threshold value (dashed line) is chosen manually such that in the center (segment 1) only blinking events and no background is recognized. Due to the inhomogeneous illumination of a Gaussian profile the net gradient in segment 5 does not reach this threshold anymore and blinking events are not recognized. DNA-PAINT data acquired under flat-top illumination show a homogeneous net gradient comparing segments 1 and 5. **b** Net gradient sum histograms for the two images from **a**

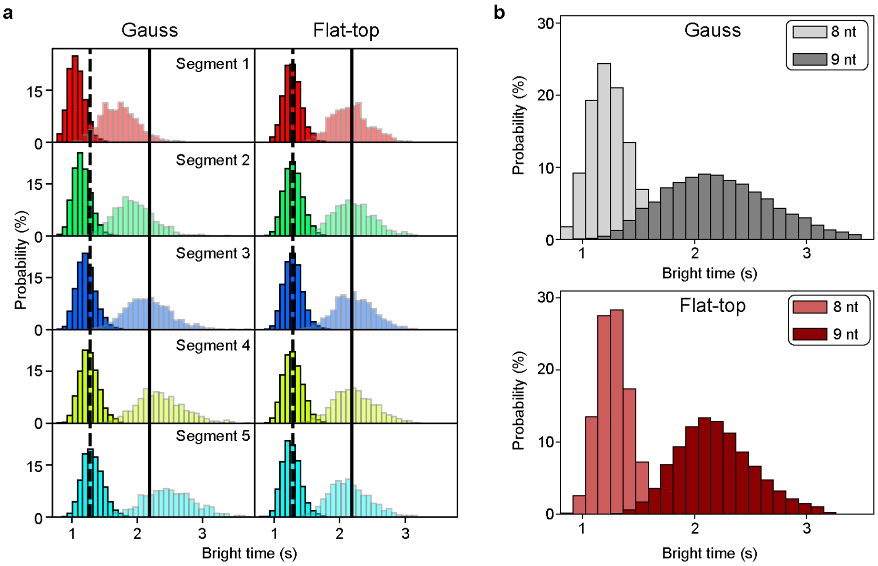

Supplementary Figure 3 | Bright time distributions for 8-nt vs. 9-nt docking site length. a Segmented bright time histograms for 20-nm-grids with 8-nt docking sites (opaque) and 9-nt docking site length (transparent) for Gauss and flat-top illumination. Mean bright times (over all segments) for flat-top illumination are indicated by dashed lines for 8-nt and solid lines for 9-nt. **b** Total bright time distributions for 8-nt vs 9-nt

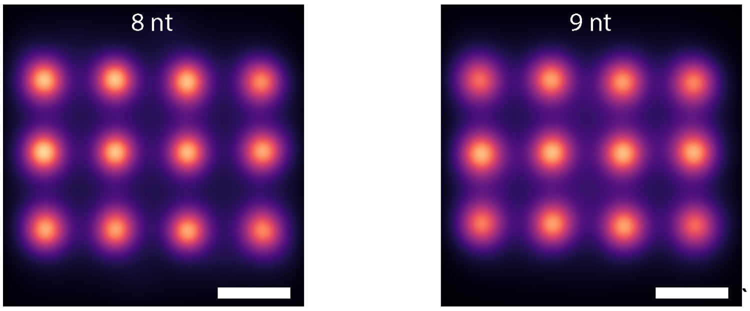

Supplementary Figure 4 | Averaged 20-nm-grid image for 8-nt vs. 9-nt docking sites for flat-top excitation. Over 8.000 DNA origami over the whole FOV for the flat-top data sets (8nt and 9nt docking strands) in Figure 2h and Supplementary Figure 5 were averaged and confirms that 20-nm resolution is conserved while origamis can be identified according to their bright times. Scale bars: 20 nm.

3

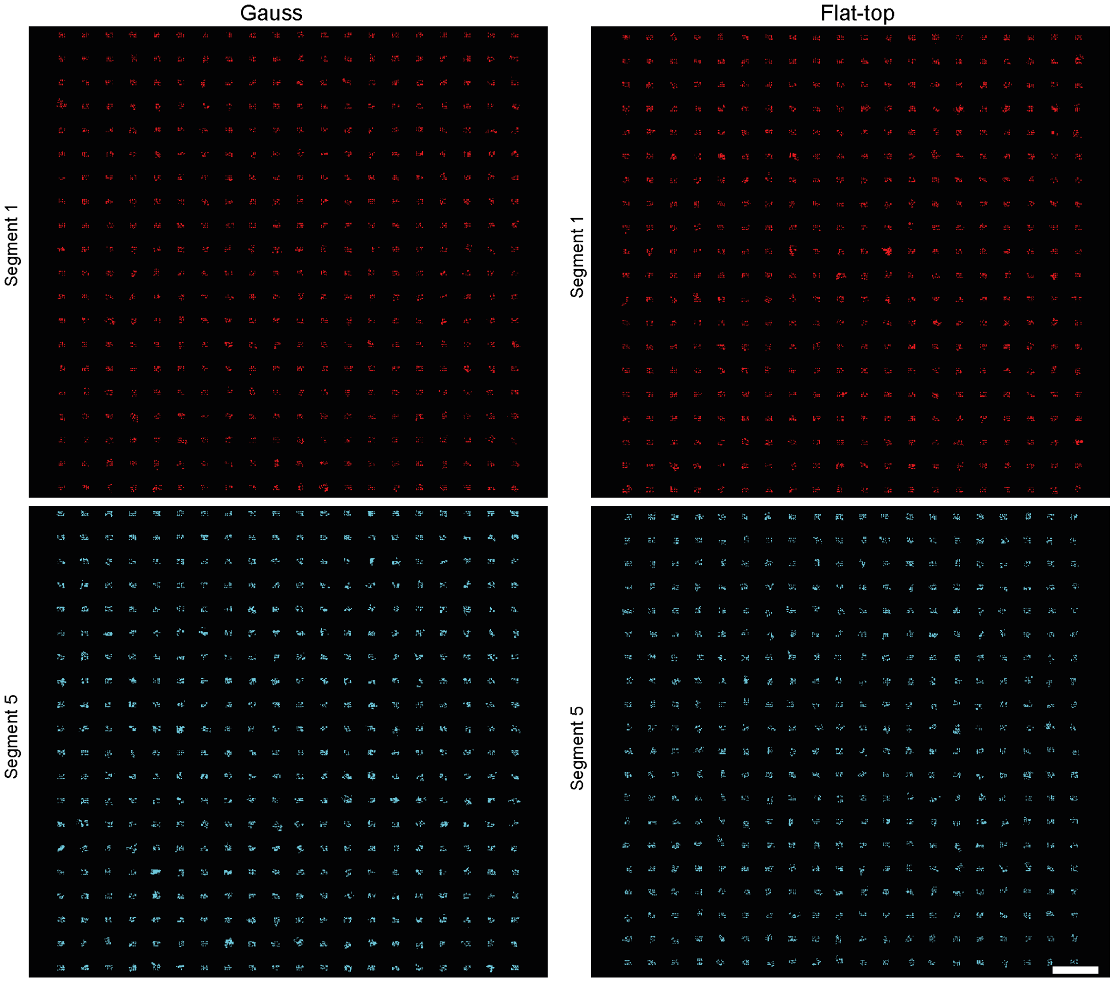
Gauss
Flat-top
Segment 1
Segment 1
Segment 5
Segment 5

Supplementary Figure 5 | Individual origami images for averaging. Image showing 400 DNA origami structures extracted from segment 1 (red) and segment 5 (cyan) for DNA-PAINT images acquired with Gaussian (left) and flat-top illumination (right). In total more than 700 structures were used for averaging in Figure 3a. Scale bar: 500 nm.

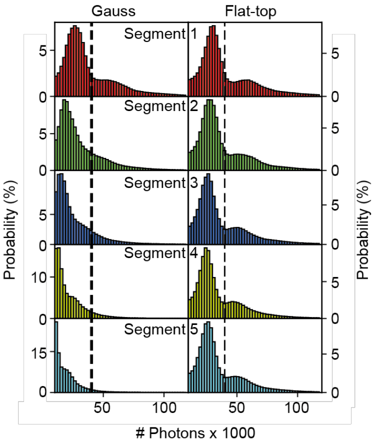

Supplementary Figure 6 | Segment-wise photon count distribution Gauss vs Flat-top.

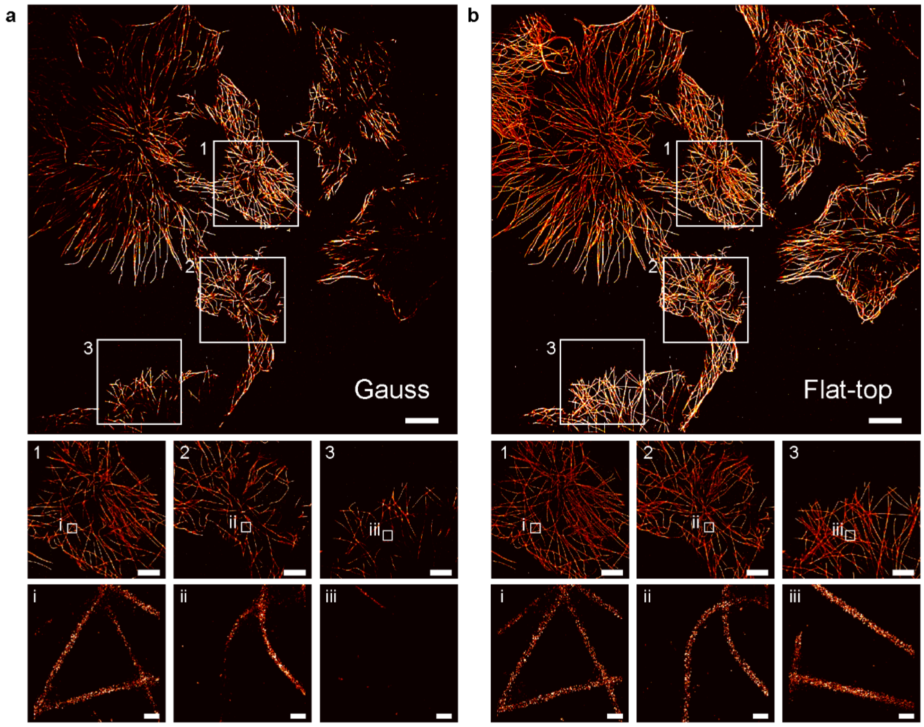

Supplementary Figure 7 | Uniform spot-detection efficiency for cellular DNA-PAINT imaging. a (top) Full camera chip (130×130 µm^2) DNA-PAINT image of the microtubule network in fixed COS-7 cells acquired using Gaussian illumination. (middle row) Three boxes highlighting the image quality in the center, intermediate and border region of the camera chip. (bottom row) Second-level zooms i)-iii) highlighting the inhomogeneous localization density over the whole image **b** Image of the same field of view as in **a** acquired with flat-top illumination profile for uniform localization density and image quality. Scale bars, 10 µm top images, 4 µm in middle row and 200 nm in bottom row.

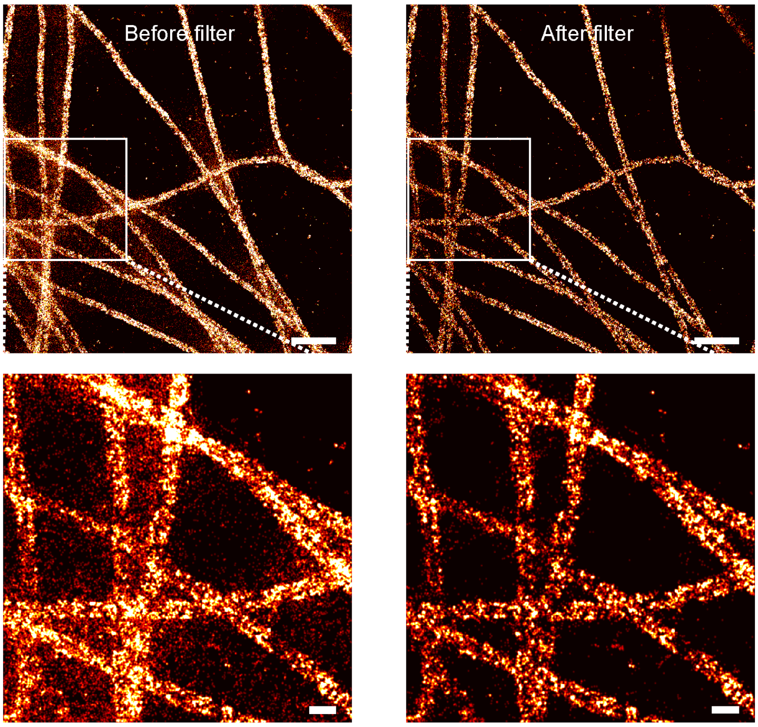

Supplementary Figure 8 | Mislocalization removal by multi-emitter filtering. Magnified region of cell image acquired under flat-top illumination (as in Figure 4b). Scale bars, top 500 nm, bottom 100 nm.

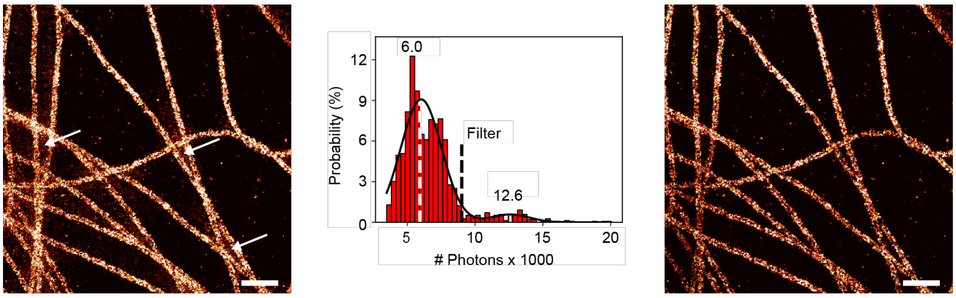

Supplementary Figure 9 | Mislocalization removal by multi-emitter filtering for Gaussian illumination. Magnified region of cell image acquired under Gaussian illumination (as in Figure 4b). Scale bars 500 nm.

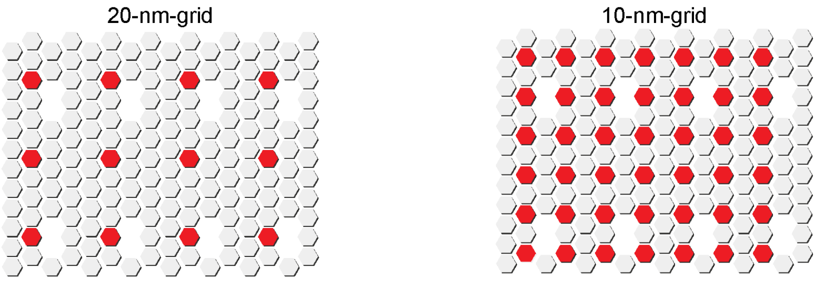

Supplementary Figure 10 | DNA origami grid designs. Picasso Design[1] schematic for 20- and 10-nm-grids. Red hexagons indicate extended staple strands for DNA-PAINT imaging. Missing hexagons indicate the position of extended staple strands on the opposite side, which are functionalized with biotin for surface immobilization.

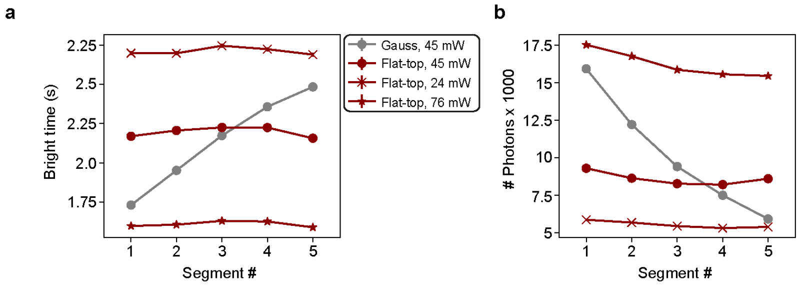

Supplementary Figure 11 | Laser power comparison Gauss vs. Flat-Top. a Mean bright time per segment for 9-nt 20-nm-grids **b** Mean number of detected photons per localization with respect to each segment for same data sets as in **a**.

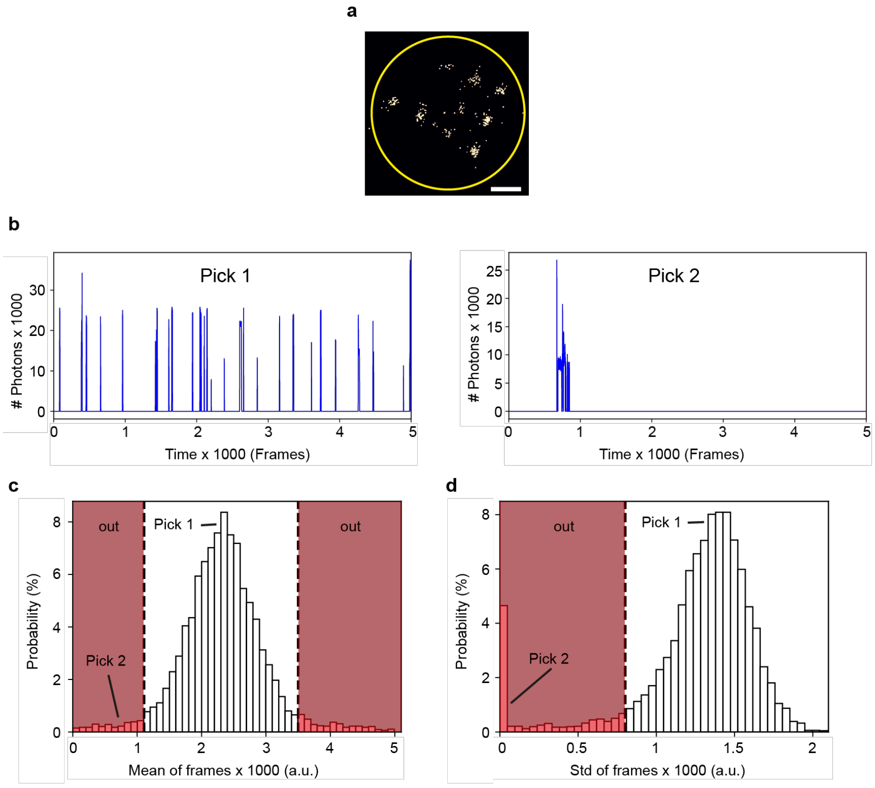

Supplementary Figure 12 | Filtering by temporal distribution of localizations. a Exemplary auto-selected ROI (yellow circle) of a 20-nm grid in the rendered super-resolution image **b** Typical intensity traces from picks showing repetitive (left) and non-repetitive blinking behavior (right) **c** Exemplary distribution of the mean (localization) frame of all auto-selected picks and **d** the respective distribution for the standard deviation. Values corresponding to picks shown in **b** are indicated. Red areas in both **c** and **d** are discarded before further analysis.

Supplementary Table 1 | List of core staples

Position	Name	Sequence
A1	21[32]23[31]BLK	TTTTCACTCAAAGGGCGAAAAACCATCACC
B1	23[32]22[48]BLK	CAAATCAAGTTTTTTGGGGTCGAAACGTGGA
C1	21[56]23[63]BLK	AGCTGATTGCCCTTCAGAGTCCACTATTAAAGGGTGCCGT
D1	23[64]22[80]BLK	AAAGCACTAAATCGGAACCCTAATCCAGTT
E1	21[96]23[95]BLK	AGCAAGCGTAGGGTTGAGTGTTGTAGGGAGCC
F1	23[96]22[112]BLK	CCCGATTTAGAGCTTGACGGGGAAAAAGAATA
G1	21[120]23[127]BLK	CCCAGCAGGCGAAAAATCCCTTATAAATCAAGCCGGCG
H1	21[160]22[144]BLK	TCAATATCGAACCTCAAATATCAATTCCGAAA
I1	23[128]23[159]BLK	AACGTGGCGAGAAAGGAAGGGAAACCAGTAA
J1	23[160]22[176]BLK	TAAAAGGGACATTCTGGCCAACAAAGCATC
K1	21[184]23[191]BLK	TCAACAGTTGAAAGGAGCAAATGAAAAATCTAGAGATAGA
L1	23[192]22[208]BLK	ACCCTTCTGACCTGAAAGCGTAAGACGCTGAG
M1	21[224]23[223]BLK	CTTTAGGGCCTGCAACAGTGCCAATACGTG
N1	23[224]22[240]BLK	GCACAGACAATATTTTTGAATGGGGTCAGTA
O1	21[248]23[255]BLK	AGATTAGAGCCGTCAAAAAACAGAGGTGAGGCCTATTAGT
P1	23[256]22[272]BLK	CTTTAATGCGCGAACTGATAGCCCCACCAG
A2	19[32]21[31]BLK	GTCGACTTCGGCCAACGCGCGGGGTTTTTC
B2	22[47]20[48]BLK	CTCCAACGCAGTGAGACGGGCAACCAGCTGCA
D2	22[79]20[80]BLK	TGGAACAACCGCCTGGCCCTGAGGCCCGCT
E2	19[96]21[95]BLK	CTGTGTGATTGCGTTGCGCTCACTAGAGTTGC
F2	22[111]20[112]BLK	GCCCGAGAGTCCACGCTGGTTTGCAGCTAACT
H2	19[160]20[144]BLK	GCAATTCACATATTCCTGATTATCAAAGTGTA
I2	22[143]21[159]BLK	TCGGCAAATCCTGTTTGATGGTGGACCCTCAA
J2	22[175]20[176]BLK	ACCTTGCTTGGTCAGTTGGCAAAGAGCGGA
L2	22[207]20[208]BLK	AGCCAGCAATTGAGGAAGGTTATCATCATTTT
M2	19[224]21[223]BLK	CTACCATAGTTTGAGTAACATTTAAAATAT
N2	22[239]20[240]BLK	TTAACACCAGCACTAACAACTAATCGTTATTA
P2	22[271]20[272]BLK	CAGAAGATTAGATAATACATTTGTCGACAA
A3	17[32]19[31]BLK	TGCATCTTTCCCAGTCACGACGGCCTGCAG
B3	20[47]18[48]BLK	TTAATGAACTAGAGGATCCCCGGGGGGTAACG
D3	20[79]18[80]BLK	TTCCAGTCGTAATCATGGTCATAAAAGGGG
E3	17[96]19[95]BLK	GCTTTCCGATTACGCCAGCTGGCGGCTGTTTC
F3	20[111]18[112]BLK	CACATTAAAATTGTTATCCGCTCATGCGGGCC
H3	17[160]18[144]BLK	AGAAAACAAAGAAGATGATGAAACAGGCTGCG
I3	20[143]19[159]BLK	AAGCCTGGTACGAGCCGGAAGCATAGATGATG
J3	20[175]18[176]BLK	ATTATCATTCAATATAATCCTGACAATTAC

L3	20[207]18[208]BLK	GCGGAACATCTGAATAATGGAAGGTACAAAAT
M3	17[224]19[223]BLK	CATAAATCTTTGAATACCAAGTGTTAGAAC
N3	20[239]18[240]BLK	ATTTTAAAATCAAAATTATTTGCACGGATTCG
P3	20[271]18[272]BLK	CTCGTATTAGAAATTGCGTAGATACAGTAC
A4	15[32]17[31]BLK	TAATCAGCGGATTGACCGTAATCGTAACCG
B4	18[47]16[48]BLK	CCAGGGTTGCCAGTTTGAGGGGACCCGTGGGA
C4	15[64]18[64]BLK	GTATAAGCCAACCCGTCGGATTCTGACGACAGTATCGGCCGCAAGGCG
D4	18[79]16[80]BLK	GATGTGCTTCAGGAAGATCGCACAATGTGA
E4	15[96]17[95]BLK	ATATTTTGGCTTTCATCAACATTATCCAGCCA
F4	18[111]16[112]BLK	TCTTCGCTGCACCGCTTCTGGTGCGGCCTTCC
G4	15[128]18[128]BLK	TAAATCAAAATAATTCGCGTCTCGGAAACCAGGCAAAGGGAAGG
H4	15[160]16[144]BLK	ATCGCAAGTATGTAAATGCTGATGATAGGAAC
I4	18[143]17[159]BLK	CAACTGTTGCGCCATTCGCCATTCAAACATCA
J4	18[175]16[176]BLK	CTGAGCAAAAATTAATTACATTTTGGGTTA
K4	15[192]18[192]BLK	TCAAATATAACCTCCGGCTTAGGTAACAATTTCATTTGAAGGCGAATT
L4	18[207]16[208]BLK	CGCGCAGATTACCTTTTTTAATGGGAGAGACT
M4	15[224]17[223]BLK	CCTAAATCAAAATCATAGGTCTAAACAGTA
N4	18[239]16[240]BLK	CCTGATTGCAATATATGTGAGTGATCAATAGT
O4	15[256]18[256]BLK	GTGATAAAAAGACGCTGAGAAGAGATAACCTTGCTTCTGTTCGGGAGA
P4	18[271]16[272]BLK	CTTTTACAAAATCGTCGCTATTAGCGATAG
A5	13[32]15[31]BLK	AACGCAAAATCGATGAACGGTACCGGTTGA
B5	16[47]14[48]BLK	ACAAACGGAAAAGCCCCAAAAACACTGGAGCA
C5	13[64]15[63]BLK	TATATTTTGTCATTGCCTGAGAGTGGAAGATT
D5	16[79]14[80]BLK	GCGAGTAAAAATATTTAAATTGTTACAAAG
E5	13[96]15[95]BLK	TAGGTAAACTATTTTTGAGAGATCAAACGTTA
F5	16[111]14[112]BLK	TGTAGCCATTAAAATTCGCATTAAATGCCGGA
G5	13[128]15[127]BLK	GAGACAGCTAGCTGATAAATTAATTTTTGT
H5	13[160]14[144]BLK	GTAATAAGTTAGGCAGAGGCATTTATGATATT
I5	16[143]15[159]BLK	GCCATCAAGCTCATTTTTTAACCACAAATCCA
J5	16[175]14[176]BLK	TATAACTAACAAAGAACGCGAGAACGCCAA
K5	13[192]15[191]BLK	GTAAAGTAATCGCCATATTTAACAAAACTTTT
L5	16[207]14[208]BLK	ACCTTTTTATTTTAGTTAATTTCATAGGGCTT
M5	13[224]15[223]BLK	ACAACATGCCAACGCTCAACAGTCTTCTGA
N5	16[239]14[240]BLK	GAATTTATTTAATGGTTTGAAATATTCTTACC
O5	13[256]15[255]BLK	GTTTATCAATATGCGTTATACAAACCGACCGT
P5	16[271]14[272]BLK	CTTAGATTTAAGGCGTTAAATAAAGCCTGT
A6	11[32]13[31]BLK	AACAGTTTTGTACCAAAAACATTTTATTTC
B6	14[47]12[48]BLK	AACAAGAGGGATAAAAATTTTTAGCATAAAGC

C6	11[64]13[63]BLK	GATTTAGTCAATAAAGCCTCAGAGAACCCTCA
D6	14[79]12[80]BLK	GCTATCAGAAATGCAATGCCTGAATTAGCA
E6	11[96]13[95]BLK	AATGGTCAACAGGCAAGGCAAAGAGTAATGTG
F6	14[111]12[112]BLK	GAGGGTAGGATTCAAAAGGGTGAGACATCCAA
G6	11[128]13[127]BLK	TTTGGGGATAGTAGTAGCATTAAAAGGCCG
H6	11[160]12[144]BLK	CCAATAGCTCATCGTAGGAATCATGGCATCAA
I6	14[143]13[159]BLK	CAACCGTTTCAAATCACCATCAATTCGAGCCA
J6	14[175]12[176]BLK	CATGTAATAGAATATAAAGTACCAAGCCGT
K6	11[192]13[191]BLK	TATCCGGTCTCATCGAGAACAAGCGACAAAAG
L6	14[207]12[208]BLK	AATTGAGAATTCTGTCCAGACGACTAAACCAA
M6	11[224]13[223]BLK	GCGAACCTCCAAGAACGGGTATGACAATAA
N6	14[239]12[240]BLK	AGTATAAAGTTCAGCTAATGCAGATGTCTTTC
O6	11[256]13[255]BLK	GCCTTAAACCAATCAATAATCGGCACGCGCCT
P6	14[271]12[272]BLK	TTAGTATCACAATAGATAAGTCCACGAGCA
A7	9[32]11[31]BLK	TTTACCCCAACATGTTTTAAATTTCCATAT
B7	12[47]10[48]BLK	TAAATCGGGATTCCCAATTCTGCGATATAATG
C7	9[64]11[63]BLK	CGGATTGCAGAGCTTAATTGCTGAAACGAGTA
D7	12[79]10[80]BLK	AAATTAAGTTGACCATTAGATACTTTTGCG
E7	9[96]11[95]BLK	CGAAAGACTTTGATAAGAGGTCATATTTCGCA
F7	12[111]10[112]BLK	TAAATCATATAACCTGTTTAGCTAACCTTTAA
G7	9[128]11[127]BLK	GCTTCAATCAGGATTAGAGAGTTATTTTCA
H7	9[160]10[144]BLK	AGAGAGAAAAAAATGAAAATAGCAAGCAAACT
I7	12[143]11[159]BLK	TTCTACTACGCGAGCTGAAAAGGTTACCGCGC
J7	12[175]10[176]BLK	TTTTATTTAAGCAAATCAGATATTTTTTGT
K7	9[192]11[191]BLK	TTAGACGGCCAAATAAGAAACGATAGAAGGCT
L7	12[207]10[208]BLK	GTACCGCAATTCTAAGAACGCGAGTATTATTT
M7	9[224]11[223]BLK	AAAGTCACAAAATAAACAGCCAGCGTTTTA
N7	12[239]10[240]BLK	CTTATCATTCCCGACTTGCGGGAGCCTAATTT
O7	9[256]11[255]BLK	GAGAGATAGAGCGTCTTTCCAGAGGTTTTGAA
P7	12[271]10[272]BLK	TGTAGAAATCAAGATTAGTTGCTCTTACCA
A8	7[32]9[31]BLK	TTTAGGACAAATGCTTTAAACAATCAGGTC
B8	10[47]8[48]BLK	CTGTAGCTTGACTATTATAGTCAGTTCATTGA
C8	7[56]9[63]BLK	ATGCAGATACATAACGGGAATCGTCATAAATAAAGCAAAG
D8	10[79]8[80]BLK	GATGGCTTATCAAAAAGATTAAGAGCGTCC
E8	7[96]9[95]BLK	TAAGAGCAAATGTTTAGACTGGATAGGAAGCC
F8	10[111]8[112]BLK	TTGCTCCTTTCAAATATCGCGTTTGAGGGGGT
G8	7[120]9[127]BLK	CGTTTACCAGACGACAAAGAAGTTTTGCCATAATTCGA
H8	7[160]8[144]BLK	TTATTACGAAGAACTGGCATGATTGCGAGAGG

I8	10[143]9[159]BLK	CCAACAGGAGCGAACCAGACCGGAGCCTTTAC
J8	10[175]8[176]BLK	TTAACGTCTAACATAAAAACAGGTAACGGA
K8	7[184]9[191]BLK	CGTAGAAAATACATACCGAGGAAACGCAATAAGAAGCGCA
L8	10[207]8[208]BLK	ATCCCAATGAGAATTAACTGAACAGTTACCAG
M8	7[224]9[223]BLK	AACGCAAAGATAGCCGAACAAACCCTGAAC
N8	10[239]8[240]BLK	GCCAGTTAGAGGGTAATTGAGCGCTTTAAGAA
O8	7[248]9[255]BLK	GTTTATTTTGTCACAATCTTACCGAAGCCCTTTAATATCA
P8	10[271]8[272]BLK	ACGCTAACACCCACAAGAATTGAAAATAGC
A9	5[32]7[31]BLK	CATCAAGTAAAACGAACTAACGAGTTGAGA
B9	8[47]6[48]BLK	ATCCCCCTATACCACATTCAACTAGAAAAATC
D9	8[79]6[80]BLK	AATACTGCCCAAAAGGAATTACGTGGCTCA
E9	5[96]7[95]BLK	TCATTCAGATGCGATTTTAAGAACAGGCATAG
F9	8[111]6[112]BLK	AATAGTAAACACTATCATAACCCTCATTGTGA
H9	5[160]6[144]BLK	GCAAGGCCTCACCAGTAGCACCATGGGCTTGA
I9	8[143]7[159]BLK	CTTTTGCAGATAAAAACCAAAATAAAGACTCC
J9	8[175]6[176]BLK	ATACCCAACAGTATGTTAGCAAATTAGAGC
L9	8[207]6[208]BLK	AAGGAAACATAAAGGTGGCAACATTATCACCG
M9	5[224]7[223]BLK	TCAAGTTTCATTAAAGGTGAATATAAAAGA
N9	8[239]6[240]BLK	AAGTAAGCAGACACCACGGAATAATATTGACG
P9	8[271]6[272]BLK	AATAGCTATCAATAGAAAATTCAACATTCA
A10	3[32]5[31]BLK	AATACGTTTGAAAGAGGACAGACTGACCTT
B10	6[47]4[48]BLK	TACGTTAAAGTAATCTTGACAAGAACCGAACT
D10	6[79]4[80]BLK	TTATACCACCAAATCAACGTAACGAACGAG
E10	3[96]5[95]BLK	ACACTCATCCATGTTACTTAGCCGAAAGCTGC
F10	6[111]4[112]BLK	ATTACCTTTGAATAAGGCTTGCCCAAATCCGC
H10	3[160]4[144]BLK	TTGACAGGCCACCACCAGAGCCGCGATTTGTA
I10	6[143]5[159]BLK	GATGGTTTGAACGAGTAGTAAATTTACCATTA
J10	6[175]4[176]BLK	CAGCAAAAGGAAACGTCACCAATGAGCCGC
L10	6[207]4[208]BLK	TCACCGACGCACCGTAATCAGTAGCAGAACCG
M10	3[224]5[223]BLK	TTAAAGCCAGAGCCGCCACCCTCGACAGAA
N10	6[239]4[240]BLK	GAAATTATTGCCTTTAGCGTCAGACCGGAACC
P10	6[271]4[272]BLK	ACCGATTGTCGGCATTTTCGGTCATAATCA
A11	1[32]3[31]BLK	AGGCTCCAGAGGCTTTGAGGACACGGGTAA
B11	4[47]2[48]BLK	GACCAACTAATGCCACTACGAAGGGGGTAGCA
C11	1[64]4[64]BLK	TTTATCAGGACAGCATCGGAACGACACCAACCTAAAACGAGGTCAATC
D11	4[79]2[80]BLK	GCGCAGACAAGAGGCAAAAGAATCCCTCAG
E11	1[96]3[95]BLK	AAACAGCTTTTTGCGGGATCGTCAACACTAAA
F11	4[111]2[112]BLK	GACCTGCTCTTTGACCCCCAGCGAGGGAGTTA

G11	1[128]4[128]BLK	TGACAACTCGCTGAGGCTTGCATTATACCAAGCGCGATGATAAA
H11	1[160]2[144]BLK	TTAGGATTGGCTGAGACTCCTCAATAACCGAT
I11	4[143]3[159]BLK	TCATCGCCAACAAAGTACAACGGACGCCAGCA
J11	4[175]2[176]BLK	CACCAGAAAGGTTGAGGCAGGTCATGAAAG
K11	1[192]4[192]BLK	GCGGATAACCTATTATTCTGAAACAGACGATTGGCCTTGAAGAGCCAC
L11	4[207]2[208]BLK	CCACCCTCTATTCACAAACAAATACCTGCCTA
M11	1[224]3[223]BLK	GTATAGCAAACAGTTAATGCCCAATCCTCA
N11	4[239]2[240]BLK	GCCTCCCTCAGAATGGAAAGCGCAGTAACAGT
O11	1[256]4[256]BLK	CAGGAGGTGGGGTCAGTGCCTTGAGTCTCTGAATTTACCGGGAACCAG
P11	4[271]2[272]BLK	AAATCACCTTCCAGTAAGCGTCAGTAATAA
A12	0[47]1[31]BLK	AGAAAGGAACAACTAAAGGAATTCAAAAAAA
B12	2[47]0[48]BLK	ACGGCTACAAAAGGAGCCTTTAATGTGAGAAT
C12	0[79]1[63]BLK	ACAACTTTCAACAGTTTCAGCGGATGTATCGG
D12	2[79]0[80]BLK	CAGCGAAACTTGCTTTCGAGGTGTTGCTAA
E12	0[111]1[95]BLK	TAAATGAATTTTCTGTATGGGATTAATTTCTT
F12	2[111]0[112]BLK	AAGGCCGCTGATACCGATAGTTGCGACGTTAG
G12	0[143]1[127]BLK	TCTAAAGTTTTGTCGTCTTTCCAGCCGACAA
H12	0[175]0[144]BLK	TCCACAGACAGCCCTCATAGTTAGCGTAACGA
I12	2[143]1[159]BLK	ATATTCGGAACCATCGCCCACGCAGAGAAGGA
J12	2[175]0[176]BLK	TATTAAGAAGCGGGGTTTTGCTCGTAGCAT
K12	0[207]1[191]BLK	TCACCAGTACAAACTACAACGCCTAGTACCAG
L12	2[207]0[208]BLK	TTTCGGAAGTGCCGTCGAGAGGGTGAGTTTCG
M12	0[239]1[223]BLK	AGGAACCCATGTACCGTAACACTTGATATAA
N12	2[239]0[240]BLK	GCCCGTATCCGGAATAGGTGTATCAGCCCAAT
O12	0[271]1[255]BLK	CCACCCTCATTTTCAGGGATAGCAACCGTACT
P12	2[271]0[272]BLK	GTTTTAACTTAGTACCGCCACCCAGAGCCA

Supplementary Table 2 | List of biotinylated staples

No	Pos	Name	Sequence	Mod
1	C02	18[63]20[56]BIOTIN	ATTAAGTTTACCGAGCTCGAATTCGGGAAACCTGTCGTGC	5'-BT
2	C09	4[63]6[56]BIOTIN	ATAAGGGAACCGGATATTCATTACGTCAGGACGTTGGGAA	5'-BT
3	G02	18[127]20[120]BIOTIN	GCGATCGGCAATTCCACACAACAGGTGCCTAATGAGTG	5'-BT
4	G09	4[127]6[120]BIOTIN	TTGTGTCGTGACGAGAAACACCAAATTTCAACTTTAAT	5'-BT
5	K02	18[191]20[184]BIOTIN	ATTCATTTTTGTTTGGATTATACTAAGAAACCACCAGAAG	5'-BT
6	K09	4[191]6[184]BIOTIN	CACCCTCAGAAACCATCGATAGCATTGAGCCATTTGGGAA	5'-BT

7	O02	18[255]20[248]BIOTIN	AACAATAACGTAAAACAGAAATAAAAATCCTTTGCCCGAA	5'-BT
8	O09	4[255]6[248]BIOTIN	AGCCACCACTGTAGCGCGTTTTCAAGGGAGGGAAGGTAAA	5'-BT

Supplementary Table 3 | Imaging parameters

Figure	Sample	Origami dilution (after PEG purification)	Docking site sequence	Imager concentration (nM)	Imaging Buffer	Laser power before objective (mW)	Exposure time (ms)	Frames	Binning
1	20-nm-grid	1:1	P1 (9 nt)	4	B	Gauss: 1.5 Flat-top: 2.4	200	200	16x16
2c,d,e SI_Fig. 2	20-nm-grid	1:80	P1 (9 nt)	4	B	Gauss: 45 Flat-top: 77	200	5,000	2x2
2f,g 2h (9 nt) SI_Fig. 3,4 (9 nt)	20-nm grid	1:80	P1 (9 nt)	4	B	Gauss: 45 Flat-top: 45	200	13,000	2x2
2h (8 nt) SI_Fig. 3,4 (8 nt)	20-nm-grid	1:80	P1 (8 nt)	4	B	Gauss: 45 Flat-top: 45	200	13,000	2x2
3a,b,c SI_Fig. 5	20-nm-grid	1:80	P1 (9 nt)	4	B	Gauss: 45 Flat-top: 77	200	5,000	2x2
3d	10-nm-grid	1:100	P1 (9 nt)	0.5	1× B 1× Trolox 1× PCA 1× PCD	Flat-top: 77	200	25,000	2x2
3e,f SI_Fig. 6	20-nm-grid	1:80	P1 (9 nt)	20	B	Gauss: 78 Flat-top: 132	200	10,000	2x2
4 SI_Fig. 8,9	COS-7	-	P1 (8 nt)	0.15	1× C 1× Trolox 1× PCA 1× PCD	Gauss: 42 Flat-top: 25	150	60,000	2x2
SI_Fig. 7	COS-7	-	P1 (9 nt)	0.2	1× C 1× Trolox 1× PCA 1× PCD	Gauss: 90 Flat-top: 153	150	13,000	2x2
SI_Fig. 11	20-nm-grid	1:80	P1 (9 nt)	4	B	Gauss: 45 Flat-top: 24, 45, 76	200	5,000	2x2

Supplementary Table 4 | Used DNA-PAINT sequences

Shortname (docking site length)	**Docking sequence**	**Imager sequence**	**Experiment**
P1 (9 nt)	TT ATACATCTA	CTAGATGTAT-Cy3b	All except the ones stated below
P1 (8 nt)	TT ATACATCT	CTAGATGTAT-Cy3b	Fig. 2h SI_Fig. 6
P1 (10 nt)	TT ATACATCTAG	AGATGTAT-Cy3b	Fig. 4 SI_Fig. 8

Supplementary references

1. Schnitzbauer, J., Strauss, M. T., Schlichthaerle, T., Schueder, F. & Jungmann, R. Super-resolution microscopy with DNA-PAINT. *Nat. Protoc.* **12**, 1198 (2017).

5

Accelerating DNA-PAINT Imaging

5.1 Motivation and Summary

Compared to other popular SMLM approaches such as STORM or PALM, DNA-PAINT was so far hindered by its rather slow image acquisition, typically requiring several hours for obtaining highest spatial resolution [37]. Within the work presented in this chapter, we accelerated DNA-PAINT image acquisition by an order of magnitude without sacrificing image quality or resolution. In order to achieve this, the imager association rate k_{on} was enhanced by a combination of optimized sequence design [99] and buffer ion composition. In combination with the flat-top TIRF microscope [93] (see Chapter 4), cellular DNA-PAINT imaging of large FOVs is performed within 200 seconds. While this acceleration paves way for high-throughput cellular imaging, the enhancement in k_{on} is furthermore particularly useful for quantitative approaches such as lbFCS [97] and qPAINT [39], as it leads to improved binding statistics per time unit for more precise molecular counting.

5.2 Publication P3: An order of magnitude faster DNA-PAINT imaging by optimized sequence design and buffer conditions

An order of magnitude faster DNA-PAINT imaging by optimized sequence design and buffer conditions

Florian Schueder, Johannes Stein, Florian Stehr, Alexander Auer,
Bianca Sperl, Maximilian T. Strauss, Petra Schwille and Ralf Jungmann

Author contributions:

F.Schueder conceived and performed experiments, analyzed data and contributed to the writing of the manuscript. **J.S.** and F.Stehr developed instrumentation. A.A. developed instrumentation and analyzed data. B.S. developed labeling reagents. M.T.S. developed software. P.S. supervised part of the study. R.J. conceived and supervised the study, interpreted data and wrote the manuscript. **All authors** reviewed and approved the manuscript.

published in

Nature Methods (2019), 16, 11, 1101-1104

Reprinted from [100] with permission from Springer Nature, copyright (2019).

nature methods

BRIEF COMMUNICATION
https://doi.org/10.1038/s41592-019-0584-7

An order of magnitude faster DNA-PAINT imaging by optimized sequence design and buffer conditions

Florian Schueder[1,2], Johannes Stein[2], Florian Stehr[2], Alexander Auer[1,2], Bianca Sperl[2], Maximilian T. Strauss[1,2], Petra Schwille[2] and Ralf Jungmann[1,2*]

DNA points accumulation in nanoscale topography (DNA-PAINT) is a relatively easy-to-implement super-resolution technique. However, image acquisition is slow compared to most other approaches. Here, we overcome this limitation by designing optimized DNA sequences and buffer conditions. We demonstrate our approach in vitro with DNA origami and in situ using cell samples, and achieve an order of magnitude faster imaging speeds without compromising image quality or spatial resolution. This improvement now makes DNA-PAINT applicable to high-throughput studies.

Advances in optical super-resolution techniques have enabled the visualization of biological processes below the classical diffraction limit of light[1]. DNA-PAINT[2] is a simple implementation of single-molecule localization microscopy (SMLM) with a spatial resolution better than 5 nm, as recently demonstrated on artificial DNA nanostructures[2,3]. While novel labeling approaches[4] are poised to bring this resolution to cellular targets, one chief limitation of DNA-PAINT has thus far been the comparably slow image acquisition speed, lasting up to several hours for the highest spatial resolution examples[2,3].

To understand this limitation, it is important to briefly review the image formation process in DNA-PAINT. The apparent 'blinking' of target molecules necessary for downstream SMLM is achieved by the transient binding interaction of a short, dye-labeled DNA oligonucleotide (imager) to its target-bound complementary (docking) strand. While the dwell-time of the bound state (also denoted bright time, τ_b) can be adjusted almost arbitrarily by, for example, the length or GC-content—among other factors—of the formed DNA duplex (for example, from sub-ms to minutes), tuning the dwell-time of the unbound state (also termed dark time, τ_d) can be achieved by either adjusting the concentration of imager strands in solution or by modulating the hybridization kinetics (for example, the association rate k_{on}). However, increasing the imager concentration for faster acquisition comes with several disadvantages. Due to the nonfluorogenic nature of the imager strands (that is, they also fluoresce in the unbound state), increasing their concentration directly results in an increase in background fluorescence. This sets an upper limit for their concentration to maintain the required signal-to-background ratio essential for high-resolution reconstruction. This issue has been recently addressed using FRET-based imager probes to suppress fluorescent background[5,6]. However, FRET-based approaches come at the disadvantage of reduced spatial resolution due to the following facts: (1) energy transfer between donor and acceptor is not 100% efficient; (2) donor dyes in the blue spectrum (for example, ATTO 488) have limited molecular brightness and (3) after energy transfer to far-red dyes (for example, ATTO 647N), camera sensitivity is not optimal (compared to, for example, dyes emitting at around 600 nm).

To overcome these limitations and enhance the speed of DNA-PAINT without sacrificing signal-to-background or spatial resolution, here we turn our attention to the optimization of DNA hybridization conditions to minimize the dark time τ_d. We quantitatively investigate the influence of DNA sequence and buffer salinity on hybridization kinetics using rationally designed DNA origami structures. We show, that by optimizing both sequence and buffer composition, a 10× speed-up in DNA-PAINT image acquisition can be readily achieved, while maintaining its sub-5-nm resolution capabilities. We also demonstrate that this increased imaging speed leads to more precise counting capabilities in qPAINT[7,8] experiments, now allowing the distinction between monomer and dimer populations in a few hundred seconds rather than hours. The speed-up furthermore allows us to obtain cellular super-resolution images at classical DNA-PAINT acquisition speed with substantially reduced fluorescence background and thus increased spatial resolution. Finally, by combining our speed-optimized sequence and conditions with recently improved flat-top total internal reflection fluorescence (TIRF) instrumentation[9], we are now able to perform one square millimeter cellular DNA-PAINT image acquisition at high spatial resolution, paving the route for high-throughput studies.

To enable speed-optimized DNA-PAINT, we first turned our attention to the sequence-dependency of DNA hybridization rates, which can vary over a large range in both theoretical and experimental studies, as well as buffer-composition-dependent effects (Fig. 1a; see also Supplementary Figs. 1 and 2)[10–14]. We chose one of our standard DNA-PAINT sequences (termed 'P1') and compared its dark times, τ_d, under identical experimental conditions to the best-performing (shortest resulting τ_d) sequences of a recent study from the Dietz laboratory[13]. From here, we rationally designed suitable sequences for DNA-PAINT using two rules: (1) using only a combination of A and G or T and C bases to avoid potential self-interactions (see Supplementary Fig. 3) leading to transient hairpin formation[15] and (2) tune the free energy of the DNA duplex so that the resulting bright times become suitable for DNA-PAINT imaging. Out of a pool of eight tested sequence variants (see Supplementary Figs. 4–6 and Supplementary Tables 1 and 2), we chose the best-performing candidate based on the following selection criteria: (1) shortest dark time (see also Supplementary Table 1) and (2) tightest possible distribution for dark and bright time (see Supplementary Figs. 4–6). The

---

[1]Faculty of Physics and Center for Nanoscience, Ludwig Maximilian University, Munich, Germany. [2]Max Planck Institute of Biochemistry, Martinsried, Germany. *e-mail: jungmann@biochem.mpg.de

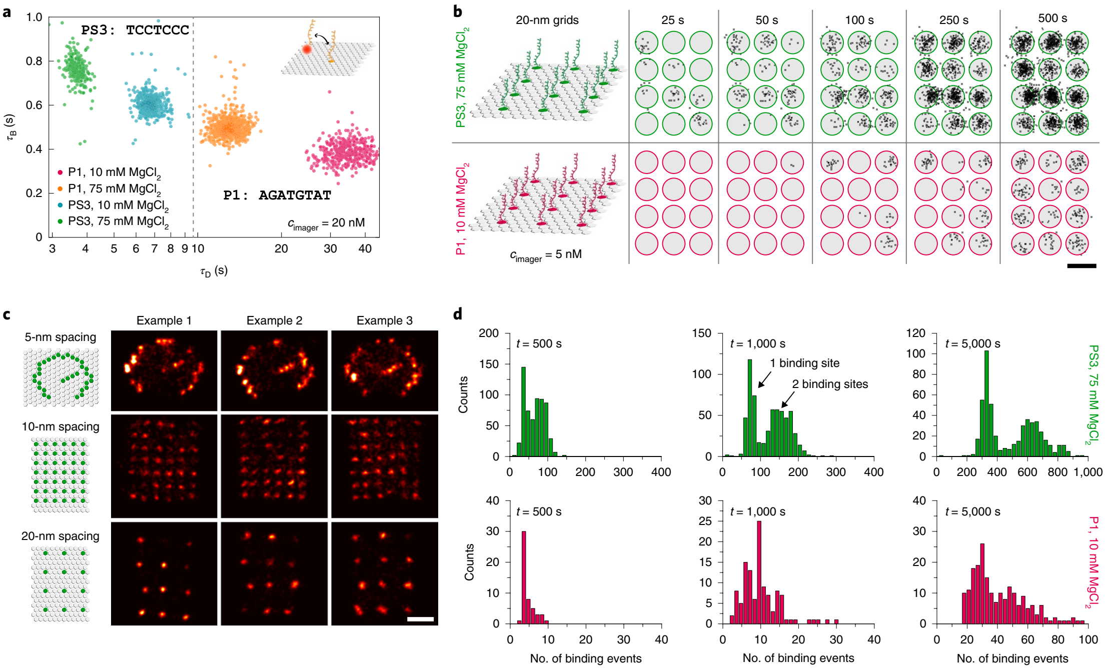

Fig. 1 | Kinetic analysis of speed-optimized DNA-PAINT. a, Scatterplot showing bright versus dark times measured with a one-binding-site DNA origami structure (see top right inset) in 1× TE buffer for P1 (classical DNA-PAINT sequence) supplemented with 10 mM $MgCl_2$ (magenta) ($N = 437$), 75 mM $MgCl_2$ (orange) ($N = 685$), PS3 (speed-optimized DNA-PAINT sequence) with 10 mM $MgCl_2$ (cyan) ($N = 473$) and 75 mM $MgCl_2$ (green) ($N = 224$) at an imager concentration (c_{imager}) of 20 nM. **b**, Time evolution of a single 20-nm grid structure for PS3 in 1× TE buffer with 75 mM $MgCl_2$ (top row) and for P1 in 1× TE buffer with 10 mM $MgCl_2$ (bottom row). **c**, 'Speedometer' logo (5 nm), 10- and 20-nm grid DNA origami structures visualized after 25 min of imaging with speed-optimized DNA-PAINT (three examples are shown for each structure, each experiment was repeated three times independently). **d**, Speed-optimized qPAINT on DNA origami structures (see Supplementary Fig. 9 for details of the structure) for counting of single versus double binding sites (mimicking monomer versus dimer distinction of, for example, cell surface receptor proteins). In the speed-optimized case (top row), the two populations (representing one and two binding sites) can already be distinguished after ~500 s ($N = 615$), while for the classical DNA-PAINT case (bottom row), this only starts to become possible after ~5,000 s ($N = 206$). Scale bars, 20 nm (**b**,**c**).

best-performing sequence (termed 'PS3') led to an approximately 5× shorter dark time, τ_d (Fig. 1a, comparing cyan and magenta). We then investigated the effect of buffer salinity on hybridization kinetics in DNA-PAINT. We screened $MgCl_2$ concentrations starting from our standard concentration of 10 mM up to 75 mM and achieved another two-fold speed increase for 75 mM $MgCl_2$ (see Supplementary Figs. 7 and 8 and Supplementary Table 1). Combining both sequence and buffer optimization, we achieved a ten-fold image acquisition speed-up (Fig. 1a, comparing magenta and green).

Using the optimized association rates, we first assayed the increase in sampling speed by imaging so-called 20-nm grid DNA origami structures (Supplementary Fig. 9). Comparing the speed-optimized (Fig. 1b, top row) to classical conditions (Fig. 1b, bottom) at the same imager concentration of 5 nM clearly shows the difference in temporal sampling: while the individual grid points of the DNA origami structure for the optimized case are clearly visible after ~50 s (Fig. 1b, top row), it takes more than 500 s for the classical case (Fig. 1b, bottom row). We were able to reproduce the speed increase in further experiments using a different dye (Atto643, see Supplementary Fig. 10).

Next, to demonstrate that the enhanced sampling speed does not come at the cost of reduced spatial resolution, we used speed-optimized DNA-PAINT to image a variety of 20-, 10- and 5-nm patterns on DNA origami structures (Supplementary Fig. 9). While in earlier attempts[2,3] imaging of 5-nm patterns took more than 7 h, this could now be achieved in 25 min (Fig. 1c).

Speed-optimized DNA-PAINT also improves molecular counting with qPAINT[7]. qPAINT uses the fact that for a given imager concentration, a specific, predictable binding frequency to a target strand on a molecule of interest is achieved. For N targets of interest, this binding frequency is thus N times higher. However, the precision of this approach is highly dependent on the number of events collected per target region. This is considerably improved in speed-optimized DNA-PAINT by gathering more binding events and thus increasing statistics in a shorter amount of time. We tested the improved counting capability in a rather challenging setting by trying to distinguish one from two docking sites on DNA origami (mimicking, for example, the case of distinguishing monomeric receptors from dimerized receptors on the plasma membrane of cells) in the shortest amount of time (Fig. 1d). For speed-optimized qPAINT, we could distinguish monomer from dimer populations in as little as 500 s, while for classical qPAINT (employing P1 as imager sequence) the two populations only became distinguishable after ~5,000 s.

Next we turned our attention to optimized cellular in situ imaging, where instead of focusing on increased speed we demonstrate

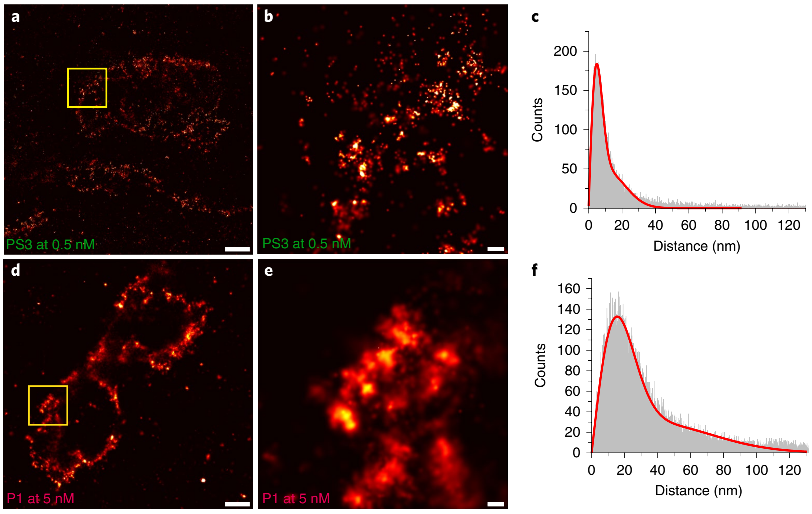

Fig. 2 | Improved resolution through speed-optimized cellular DNA-PAINT. **a**, Super-resolution image of Golgi apparatus (GOLGA5) using sequence PS3 at 0.5 nM ~2.5 μm inside the cell. **b**, Zoom-in of the highlighted area in **a**. **c**, Localization precision is 4.6 nm. **d**, Super-resolution of the same target using P1 at 5 nM. **e**, Zoom-in of the highlighted area **d**. **f**, Localization precision is 14.6 nm. Each experiment was repeated three times independently. Scale bars, 500 nm (**a**,**d**); 50 nm (**b**,**e**).

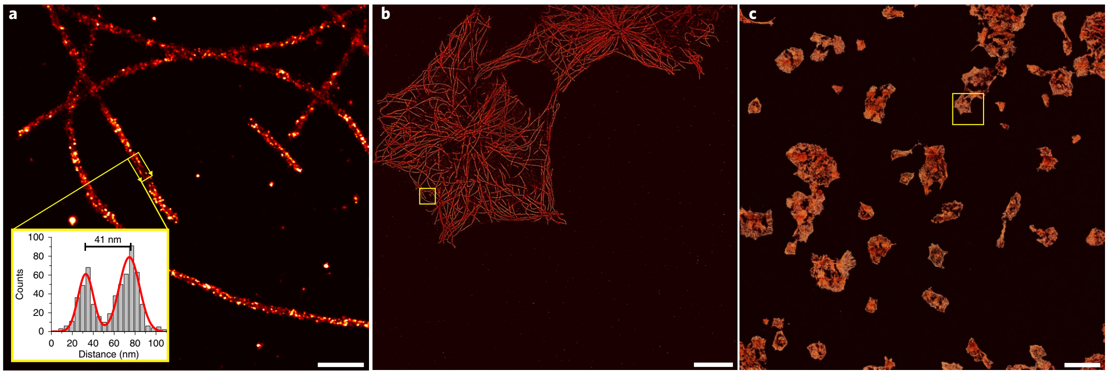

Fig. 3 | Large field of view imaging of microtubule-stained COS-7 cells with speed-optimized DNA-PAINT. **a**, 4 × 4 μm^2 speed-optimized microtubule imaging in COS-7 cells. Inset: A cross-sectional histogram analysis of the highlighted area shows the resolvable 'hollowness' of microtubules. **b**, 100 × 100 μm^2 zoom-out containing the area from **a** (highlighted). **c**, 1,000 × 1,000 μm^2 zoom-out containing the area from **b** (highlighted). The whole 1 mm^2 image was acquired in 8 h and consists of 144 single DNA-PAINT tiles (acquisition time per single tile, 200 s). This experiment was repeated three times independently. Scale bars, 100 μm (**a**); 10 μm (**b**); 500 nm (**c**).

improved volumetric imaging. Here, the improved imaging conditions allowed us to obtain cellular DNA-PAINT data in the same acquisition time as in the classical case, however, with a drastically reduced fluorescence background and thus increased localization precision and resolution (Fig. 2). The reduced background fluorescence improves imaging of targets in cells that are located further away from the coverslip interface (for example, Golgi apparatus). To demonstrate this advantage, we compared DNA-PAINT imaging of the Golgi complex ~2.5 μm away from the coverslip (using HILO imaging[16]) using the optimized sampling conditions at a concentration of 500 pM and the classical case at a concentration of 5 nM (see also Supplementary Figs. 11 and 12). Due to the lower background for the optimized conditions (Fig. 2a,b), we were able to achieve a localization precision of 4.6 nm based on nearest neighbor analysis[17] (Fig. 2c). For the standard DNA-PAINT case (Fig. 2d,e) the achievable localization precision was considerably worse at 14.6 nm (Fig. 2f).

Finally, with speed-optimized DNA-PAINT, high-throughput experiments are within reach. To illustrate this, we performed DNA-PAINT super-resolution imaging over a large field of view for potential cellular high-throughput studies. We imaged COS-7 cells stained for microtubules in an automated fashion[18] over an area larger than 1 mm^2 (consisting of 144 single DNA-PAINT images) in as little as 8 h, while reaching a localization precision of ~8 nm

(Fig. 3). We note that for this specific experiment, we opted for a 6 nucleotide long imager sequence to achieve more rapid strand dissociation. This is advisable to obtain 'true' single-molecule blinking events (and preventing multiple simultaneous binding events per diffraction-limited area) in more densely labeled microtubule samples. A zoom-in into a 4 × 4 μm^2 area illustrates the high spatial resolution that is still achievable, clearly resolving the hollowness of immunostained microtubule structures[19]. Consecutive zoom-outs (Fig. 3b,c) allow us to put this into spatial context of a larger than 1 mm^2 area (Supplementary Video 1) (an interactive image can be found at http://speedpaint.jungmannlab.org).

In conclusion, we here present a straightforward way to speed up DNA-PAINT image acquisition by an order of magnitude without sacrificing the advantages of classical DNA-PAINT (for example, high-resolution and precise molecular counting) compared to, for example, FRET-PAINT approaches[5,6,20] (see also Supplementary Fig. 13). This development opens the door to high-throughput cellular studies and more precise counting due to significant increase in sampling.

The speed increase becomes especially important when extending single- to multi-plane image acquisition throughout whole cells, where the acquisition time is additionally prolonged due to the fact that multiple planes have to be acquired[21,22]. We envision that in combination with automation for high content screening[23], our speed-optimized DNA-PAINT will allow researchers to tackle questions in biological heterogeneity (for example, chromatin structure imaging in hundreds of cells) in a more accessible high-throughput manner. Finally, faster dynamics will make DNA-PAINT more compatible with live-cell applications such as particle tracking[4] and potential downstream live-cell super-resolution imaging.

Online content

Any methods, additional references, Nature Research reporting summaries, source data, statements of code and data availability and associated accession codes are available at https://doi.org/10.1038/s41592-019-0584-7.

Received: 22 May 2019; Accepted: 26 August 2019;
Published online: 07 October 2019

References

1. Sahl, S. J., Hell, S. W. & Jakobs, S. *Nat. Rev. Mol. Cell Biol.* **18**, 685–701 (2017).
2. Schnitzbauer, J., Strauss, M. T., Schlichthaerle, T., Schueder, F. & Jungmann, R. *Nat. Protoc.* **12**, 1198–1228 (2017).
3. Dai, M., Jungmann, R. & Yin, P. *Nat. Nanotechnol.* **11**, 798–807 (2016).
4. Strauss, S. et al. *Nat. Methods* **15**, 685–688 (2018).
5. Auer, A., Strauss, M. T., Schlichthaerle, T. & Jungmann, R. *Nano Lett.* **17**, 6428–6434 (2017).
6. Lee, J., Park, S. & Hohng, S. *Mol. Brain* **11**, 70 (2018).
7. Jungmann, R. et al. *Nat. Methods* **13**, 439–442 (2016).
8. Jayasinghe, I. et al. *Cell Rep.* **22**, 557–567 (2018).
9. Stehr, F., Stein, J., Schueder, F., Schwille, P. & Jungmann, R. *Nat. Commun.* **10**, 1268 (2019).
10. Ouldridge, T. E., Sulc, P., Romano, F., Doye, J. P. & Louis, A. A. *Nucleic Acids Res* **41**, 8886–8895 (2013).
11. Cisse, I. I., Kim, H. & Ha, T. *Nat. Struct. Mol. Biol.* **19**, 623–627 (2012).
12. He, G., Li, J., Ci, H., Qi, C. & Guo, X. *Angew. Chem. Int Ed. Engl.* **55**, 9036–9040 (2016).
13. Schickinger, M., Zacharias, M. & Dietz, H. *Proc. Natl. Acad. Sci. USA* **115**, E7512–E7521 (2018).
14. Zhang, J. X. et al. *Nat. Chem.* **10**, 91–98 (2018).
15. Zadeh, J. N. et al. *J. Comput Chem.* **32**, 170–173 (2011).
16. Tokunaga, M., Imamoto, N. & Sakata-Sogawa, K. *Nat. Methods* **5**, 159–161 (2008).
17. Endesfelder, U., Malkusch, S., Fricke, F. & Heilemann, M. *Histochem Cell Biol.* **141**, 629–638 (2014).
18. Edelstein, A. D. et al. *J. Biol. Methods* **1**, pii: e10. (2014).
19. Vaughan, J. C., Jia, S. & Zhuang, X. *Nat. Methods* **9**, 1181–1184 (2012).
20. Lee, J., Park, S., Kang, W. & Hohng, S. *Mol. Brain* **10**, 63 (2017).
21. Schueder, F. et al. *Nat. Commun.* **8**, 2090 (2017).
22. Legant, W. R. et al. *Nat. Methods* **13**, 359–365 (2016).
23. Beghin, A. et al. *Nat. Methods* **14**, 1184–1190 (2017).

Acknowledgements

We thank J. Bauer and P. Schueler for initial experiments. We thank J. Lara-Gutiérrez and G. Cardone for fruitful discussions. This work has been supported in part by the German Research Foundation through the Emmy Noether Program (no. DFG JU 2957/1-1), the SFB1032 (project no. A11), the European Research Council through an ERC Starting Grant (MolMap; grant agreement no. 680241), the Allen Distinguished Investigator Program through the Paul G. Allen Frontiers Group, the Max Planck Foundation and the Max Planck Society. J.S., F.Stehr and A.A. acknowledge support by the QBM graduate school. M.T.S. acknowledges support from the International Max Planck Research School for Molecular and Cellular Life Sciences.

Author contributions

F.Schueder conceived and performed experiments, analyzed data and contributed to the writing of the manuscript. J.S. and F.Stehr developed instrumentation. A.A. developed instrumentation and analyzed data. B.S. developed labeling reagents. M.T.S. developed software. P.S. supervised part of the study. R.J. conceived and supervised the study, interpreted data and wrote the manuscript. All authors reviewed and approved the manuscript.

Competing interests

The authors declare no competing interests.

Additional information

Supplementary information is available for this paper at https://doi.org/10.1038/s41592-019-0584-7.

Correspondence and requests for materials should be addressed to R.J.

Peer review information Rita Strack was the primary editor on this article and managed its editorial process and peer review in collaboration with the rest of the editorial team.

Reprints and permissions information is available at www.nature.com/reprints.

Publisher's note Springer Nature remains neutral with regard to jurisdictional claims in published maps and institutional affiliations.

© The Author(s), under exclusive licence to Springer Nature America, Inc. 2019

Methods

Materials. Unmodified DNA oligonucleotides, Atto643-modified DNA oligonucleotides and biotinylated DNA oligonucleotides were purchased from MWG Eurofins. Cy3B-modified DNA oligonucleotides were custom ordered from Metabion. M13mp18 scaffold was obtained from Tilibit. Tris 1 M pH 8.0 (catalog no. AM9856), EDTA 0.5 M pH 8.0 (catalog no. AM9261), magnesium 1 M (catalog no. AM9530G) and sodium chloride 5 M (catalog no. AM9759) were obtained from Ambion. Ultrapure water (catalog no. 10977-035) was purchased from Gibco. Polyethylene glycol (PEG)-8000 (catalog no. 6510-1KG) was purchased from Merck. Streptavidin (catalog no. S-888) was purchased from Thermo Fisher. BSA-Biotin (catalog no. A8549) was obtained from Sigma-Aldrich. Coverslips (catalog no. 0107032) and glass slides (catalog no. 10756991) were purchased from Marienfeld and Thermo Fisher. Double-sided tape (catalog no. 665D) was ordered from Scotch. Two component silica twinsil speed 22 (catalog nos. 1300 1002) was ordered from picodent. Tween 20 (catalog no. P9416-50ML), glycerol (catalog no. 65516-500ml), methanol (catalog no. 32213-2.5L), protocatechuate 3,4-dioxygenase pseudomonas (PCD) (catalog no. P8279), 3,4-dihydroxybenzoic acid (PCA) (catalog no. 37580-25G-F) and (+−)-6-hydroxy-2,5,7,8-tetra-methylchromane-2-carboxylic acid (Trolox) (catalog no. 238813-5G) were ordered from Sigma. Potassium chloride (catalog no. 6781.1) was ordered from Carl Roth. Sodium hydroxide (catalog no. 31627.290) was purchased from VWR. Dulbecco's modified Eagle medium (DMEM) (catalog no. 10566016) was ordered from Thermo Fisher Scientific. Fetal bovine serum (FBS) (catalog no. 10500-064), 1× phosphate buffered saline (PBS) pH 7.2 (catalog no. 20012-019), 0.05% Trypsin–EDTA (catalog no. 25300-054) and were purchased from Thermo Fisher Scientific. HeLa cells were purchased from the Leibniz Institute DSMZ (catalog no. ACC-57). COS-7 cells were a gift from A. Ulrich's laboratory. Glass-bottomed eight-well µ-slides (catalog no. 80827) were ordered from ibidi. Falcon tissue culture flasks (catalog no. 734-0965) were ordered from VWR. Paraformaldehyde (catalog no. 15710) and glutaraldehyde (catalog no. 16220) were obtained from Electron Microscopy Sciences. Bovine serum albumin (catalog no. A4503-10G) was ordered from Sigma-Aldrich. Triton X-100 (catalog no. 6683.1), sodium borohydride >97% (catalog no. 4051.1) and ammonium chloride (catalog no. K298.1) were purchased from Roth. Monoclonal antibodies against alpha-tubulin (used, 1:200) (catalog no. MA1-80017) were purchased from Thermo Scientific. Polyclonal antibodies against GolgA5 (catalog no. HPA000992) were obtained from Atlas Antibodies (dilution 1:200). Secondary antibodies anti-Rat (catalog no. 712-005-150) (used in a 1:100 dilution) and anti-Rabbit (catalog no. 711-005-152) (used in a 1:100 dilution) were purchased from Jackson ImmunoResearch. 90 nm diameter gold nanoparticles (catalog no. G-90-100) were ordered from cytodiagnostics.

Buffers. Five buffers were used for sample preparation and imaging: buffer A (10 mM Tris-HCl pH 7.5, 100 mM NaCl, 0.05% Tween 20, pH 7.5); buffer B (10 mM $MgCl_2$, 5 mM Tris-HCl pH 8, 1 mM EDTA, 0.05% Tween 20, pH 8), buffer B 25 mM $MgCl_2$, buffer B 50 mM $MgCl_2$ and buffer B 75 mM $MgCl_2$. For the experiments in Figs. 1b,c, 2 and 3 and Supplementary Figs. 1, 2, 4–8, 10c,d and 13 the corresponding imaging buffer was supplemented with: 1× Trolox, 1× PCA and 1× PCD (see paragraph below for details). This photostabilization system allowed us to maximize the number of photons per event and thus achieve optimal spatial resolution[2,24].

Trolox, PCA and PCD. Here, 100× Trolox:100 mg Trolox, 430 µl 100% methanol, 345 µl 1 M NaOH in 3.2 ml H_2O. 40× PCA: 154 mg PCA, 10 ml water and NaOH were mixed and the pH was adjusted to 9.0. Then, 100× PCD:9.3 mg PCD, 13.3 ml of buffer was used (100 mM Tris-HCl pH 8, 50 mM KCl, 1 mM EDTA, 50% glycerol).

DNA origami self-assembly. All DNA origami structures were designed with the Picasso design tool (see Supplementary Fig. 9)[2]. Self-assembly of DNA origami was accomplished in a one-pot reaction mix with 50 µl total volume, consisting of 10 nM scaffold strand (for the sequence, see Supplementary Data 1), 100 nM folding staples (Supplementary Data 2–5), 10 nM (or 1 µM (Fig. 1b,c)) biotinylated staples (Supplementary Table 3) and 1 µM of docking site strands (for a list of DNA-PAINT handles see Supplementary Table 4) (5′ staple-docking-site-3′) in folding buffer (1× TE buffer with 12.5 mM $MgCl_2$). The reaction mix was then subjected to a thermal annealing ramp using a thermocycler. The reaction mix was first incubated at 80 °C for 5 min and then immediately cooled down to 60 °C. Subsequently, the sample was cooled from 60 to 4 °C in steps of 1 °C per 3.21 min and then held at 4 °C.

DNA origami PEG purification. Here, 5-nm logo, 10- and 20-nm grid DNA origami structures (Fig. 1b,c) were purified via three rounds of PEG precipitation by adding the same volume of PEG-buffer, centrifuging at 14,000*g* at 4 °C for 30 min, removing the supernatant and resuspending in folding buffer.

DNA origami sample preparation. For sample preparation, a piece of coverslip and a glass slide were sandwiched together by two strips of double-sided tape to form a flow chamber with inner volume of ~20 µl. First, 20 µl of biotin labeled bovine albumin (1 mg ml⁻¹, dissolved in buffer A) was flushed into the chamber and incubated for 2 min. The chamber was then washed with 40 µl of buffer A. A volume of 20 µl of streptavidin (0.5 mg ml⁻¹, dissolved in buffer A) was then flushed through the chamber and allowed to bind for 2 min. After washing with 20 µl of buffer A and subsequently with 20 µl of buffer B, 20 µl of biotin labeled DNA structures (~200 pM) in buffer B were flushed into the chamber and incubated for 2 min. The chamber was washed with 40 µl of buffer B. Finally, 20 µl of the imager solution in the corresponding imaging buffer (see Supplementary Table 5) was flushed into the chamber, which was subsequently sealed with two-component silica before imaging.

Antibody conjugation. Antibodies were conjugated to DNA-PAINT docking sites via maleimide-PEG2-succinimidyl ester chemistry as previously reported[2,25].

Cell culture. HeLa cells and COS-7 cells were passaged every other day and used between passage number 5 and 20. The cells were maintained in DMEM supplemented with 1% sodium-pyruvate and 10% FBS. Passaging was performed using 1× PBS and Trypsin–EDTA 0.05%. Then, 24 h before immunostaining, cells were seeded on ibidi eight-well glass coverslips at 30,000 cells per well.

Cell fixation (microtubules). For fixation, the samples were pre-fixed and pre-permeabilized with 0.4% glutaraldehyde and 0.25% Triton X-100 for 90 s. Next, the cells were quickly rinsed with 1× PBS once followed by fixation with 3% glutaraldehyde for 15 min. Afterward, samples were rinsed twice (5 min) with 1× PBS and then quenched with 0.1% NaBH4 for 7 min. After rinsing four times with 1× PBS for 30 s, 60 s and twice for 5 min, samples were blocked and permeabilized with 3% BSA and 0.25% Triton X-100 for 2 h. Then, samples were incubated with 10 µg ml⁻¹ of primary antibodies (1:200 dilution) in a solution with 3% BSA and 0.1% Triton X-100 at 4 °C overnight. Cells were rinsed three times (5 min each) with 1× PBS. Next, they were incubated with 10 µg ml⁻¹ of labeled secondary antibodies (1:100 dilution) in a solution with 3% BSA and 0.1% Triton X-100 at room temperature for 2 h. For fiducial based drift correction, the samples were incubated with gold nanoparticles with a 1:1 dilution in 1× PBS for 5 min. Finally, samples were rinsed three times with 1× PBS before adding imager solution.

Cell fixation (Golgi). Cells were fixed with 4% PFA for 10 min. Afterward, samples were rinsed twice (5 min) with 1× PBS and then quenched with 0.1% $NaBH_4$ for 7 min. After four washes (30 s, 60 s, 2 × 5 min) cells were blocked permeabilized with 3% BSA and 0.25% Triton X-100 at room temperature for 2 h. Next, cells were incubated with the polyclonal GolgA5 antibody (dilution 1:200) in 3% BSA and 0.1% Trion X-100 at 4 °C overnight. Cells were rinsed three times (5 min each) with 1× PBS. Next, they were incubated with 10 µg ml⁻¹ of DNA labeled anti-rabbit secondary antibodies (1:100 dilution) in a solution with 3% BSA and 0.1% Triton X-100 at room temperature for 1 h. For fiducial based drift correction, the samples were incubated with gold nanoparticles with a 1:1 dilution in 1× PBS for 5 min. Finally, samples were rinsed three times with 1× PBS before adding imager solution.

Super-resolution microscope setup 1. Imaging was partly carried out (see Imaging conditions) on an inverted custom-built microscope in an objective-type TIRF configuration with an oil-immersion objective (Olympus UAPON, 100×, numerical aperture 1.49)[9]. Two lasers were used for excitation: 561 nm (MPB Communications Inc., 1W, DPSS-system) and 640 nm (MPB Communications Inc., 1W, DPSS-system). Laser power was adjusted by polarization rotation with a half-wave plate before passing a polarizing beam-splitter cube. To spatially clean the beam profile the laser light was coupled into a single-mode polarization-maintaining fiber. The coupling polarization into the fiber was adjusted using a zero-order half-wave plate. The laser light was re-collimated after the fiber resulting in a collimated full-width half-maximum beam diameter of ~6 mm. The beam was then coupled into a diffractive beam shaper device (AdlOptica, piShaper 6_6_VIS) transformed the Gaussian beam profile in a collimated flat-top profile. The laser beam diameter was magnified by a factor of ×2.5 using a custom-built telescope. The laser light was coupled into the microscope objective and a dichroic beam splitter (AHF Analysentechnik, F68-785). Fluorescence light was spectrally filtered with an emission filter (AHF Analysentechnik, 605/64 and 705/100) and imaged on a sCMOS camera (Andor, Zyla 4.2 Plus) without further magnification resulting in an effective pixel size of 130 nm (after 2 × 2 binning). A focus stabilization system (ASI, CRISP at 850 nm) in the excitation path of the microscope in a feedback loop with the piezo actuated sample holder (PIEZOCONCEPT, LT-Z-100) maintained the focus during acquisition. The samples were placed in a stage top temperature chamber (Okolab, H101-Mini) connected to a water-based thermostat. The same thermostat was used to actively stabilize the objective temperature to 23 °C (±0.1).

Super-resolution microscope setup 2. Fluorescence imaging was partly carried out (see Imaging conditions) on an inverted microscope (Nikon Instruments, Eclipse Ti2) with the Perfect Focus System, applying an objective-type TIRF configuration with an oil-immersion objective (Nikon Instruments, Apo SR TIRF ×100, numerical aperture 1.49, Oil). A 561 nm (MPB Communications Inc., 2W, DPSS-system) laser was used for excitation. The laser beam was passed through cleanup filters (Chroma Technology, ZET561/10) and coupled into the microscope objective using a beam splitter (Chroma Technology, ZT561rdc). Fluorescence light was spectrally filtered with an emission filter (Chroma Technology, ET600/50 m and ET575lp) and imaged on a sCMOS camera (Andor, Zyla 4.2 Plus) without further magnification, resulting in an effective pixel size of 130 nm (after 2 × 2 binning).

Imaging conditions. In Fig. 1a, imaging was done with the super-resolution microscope setup 1. Imaging was carried out using an imager strand concentration of 20 nM in imaging buffer (see Supplementary Table 5). Here, 30,000 frames were acquired at 100 ms exposure time. The readout bandwidth was set to 200 MHz. Laser power (at 561 nm) was set to 2 mW (measured before the back focal plane (BFP) of the objective), corresponding to 11 W cm^{-2} at the sample plane.

In Fig. 1b, imaging was done with super-resolution microscope setup 1. Images were acquired with an imager strand concentration of 5 nM (PS3-Cy3B and P1-Cy3B) in imaging buffer. Here, 10,000 frames were acquired at 20 ms exposure time. The readout bandwidth was set to 200 MHz. Laser power (at 561 nm) was set to 130 mW (measured at the BFP of the objective). corresponding to 950 W cm^{-2} at the sample plane.

In Fig. 1c, imaging was carried out with super-resolution microscope setup 1. Images were acquired with an imager strand concentration of 5 nM of PS3-Cy3B in imaging buffer. Here, 5,000 frames were acquired at 300 ms exposure time and a readout bandwidth of 200 MHz. Laser power (at 560 nm) was set to 130 mW (measured before the BFP of the objective), corresponding to 950 W cm^{-2} at the sample plane.

In Fig. 1d, imaging was done with super-resolution microscope setup 1. Images were acquired with an imager strand concentration of 5 nM of (PS3-Cy3B and P1-Cy3B) in imaging buffer. Here, 50,000 frames were acquired at 100 ms exposure time and a readout bandwidth of 200 MHz. Laser power (at 560 nm) was set to 2 mW (measured before the BFP of the objective), corresponding to 11 W cm^{-2} at the sample plane.

In Fig. 2, imaging was done with super-resolution microscope setup 2. Imaging was carried out using an imager strand concentration of 500 pM (PS3-Cy3B) and 5 nM (P1-Cy3B) in imaging buffer. Here, 20,000 frames were acquired at 100 ms exposure time. The readout bandwidth was set to 200 MHz. Laser power (at 561 nm) was set to 20 mW (measured before the BFP of the objective), corresponding to 400 W cm^{-2} at the sample plane.

In Fig. 3, imaging was done with super-resolution microscope setup 1. Images were acquired with an imager strand concentration of 1 nM (PS3-Cy3B (6 nt) imager) in cell imaging buffer. Here, 10,000 frames were acquired at 20 ms exposure time for every tile. The readout bandwidth was set to 200 MHz. Laser power (at 561 nm) was set to 120 mW (measured at the BFP of the objective), corresponding to 900 W cm^{-2} at the sample plane. One field of view was set to 720 × 720 pixel at a pixel size of 130 nm. The image acquisition was carried out in a 12 × 12 grid scan with an overlap of 8 μm.

All the imaging conditions are also listed in Supplementary Table 5. For all imager strand sequences see Supplementary Table 2.

Image analysis. Raw fluorescence data was subjected to spot-finding and subsequent super-resolution reconstruction using the 'Picasso' software package[2]. The drift correction was performed with a redundant cross-correlation and gold particles as fiducials.

Reporting summary. Further information on research design is available in the Nature Research Reporting Summary linked to this article.

Data availability

All raw data is available upon reasonable request from the authors.

References

24. Aitken, C. E., Marshall, R. A. & Puglisi, J. D. *Biophysical J.* **94**, 1826–1835 (2008).
25. Agasti, S. S. et al. *Chem. Sci.* **8**, 3080–3091 (2017).

nature methods
SUPPLEMENTARY INFORMATION
https://doi.org/10.1038/s41592-019-0584-7

In the format provided by the authors and unedited.

An order of magnitude faster DNA-PAINT imaging by optimized sequence design and buffer conditions

Florian Schueder[1,2], Johannes Stein[2], Florian Stehr[2], Alexander Auer[1,2], Bianca Sperl[2], Maximilian T. Strauss[1,2], Petra Schwille[2] and Ralf Jungmann[1,2]*

[1]Faculty of Physics and Center for Nanoscience, Ludwig Maximilian University, Munich, Germany. [2]Max Planck Institute of Biochemistry, Martinsried, Germany. *e-mail: jungmann@biochem.mpg.de

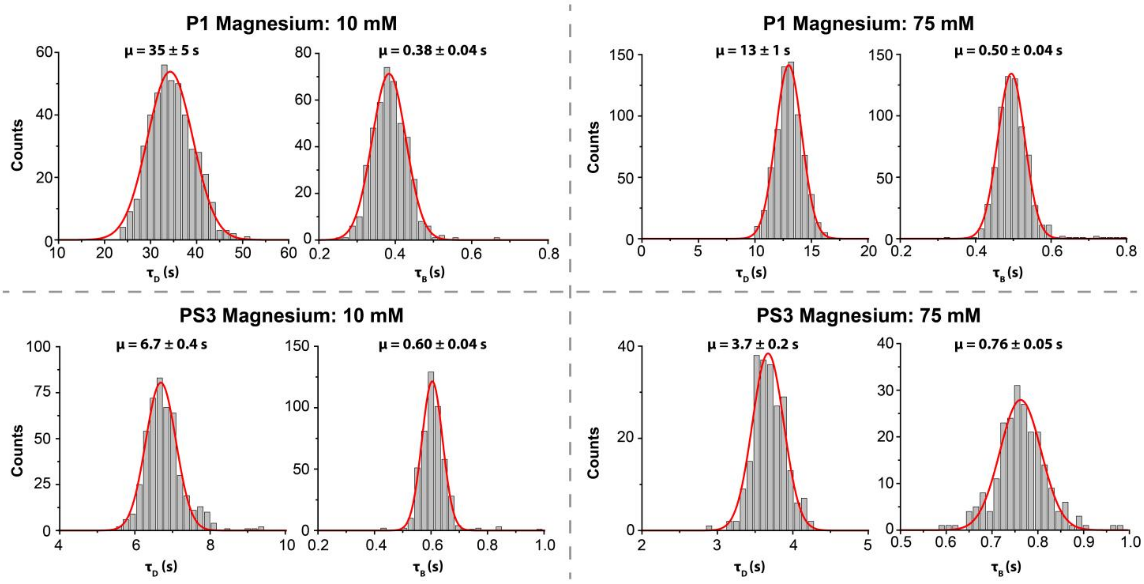

Supplementary Figure 1

Dark and bright time distributions (values indicate mean and standard deviation) for PS3 and P1 at 10 and 75 mM $MgCl_2$ (P1 10 mM $MgCl_2$ N = 437, P1 75 mM $MgCl_2$ N = 685, PS3 10 mM $MgCl_2$ N = 473, PS3 75 mM $MgCl_2$ N = 224). Each experiment was repeated three times independently.

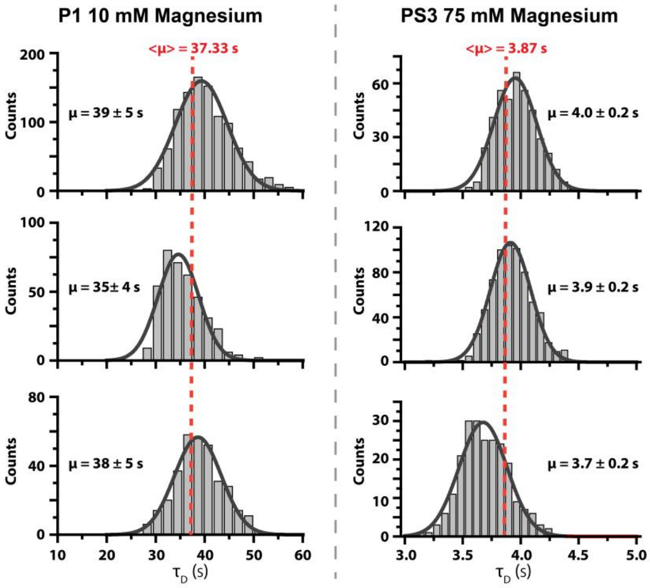

Supplementary Figure 2

Repeats for P1 and PS3

Comparison of dark times (values indicating mean and standard deviation) for P1 at 10 mM $MgCl_2$ concentration and PS3 at 75 mM Magnesium concentration for three independent repeated experiments. Average dark time for P1 at 10 mM is τ_D=37.68 s and for PS3 at 75 mM τ_D=3.84 s (P1 10 mM $MgCl_2$ N = 3010, N = 2123, N = 1585 (top to bottom) PS3 75 mM $MgCl_2$ N = 506, N = 693, N = 293 (top to bottom)).

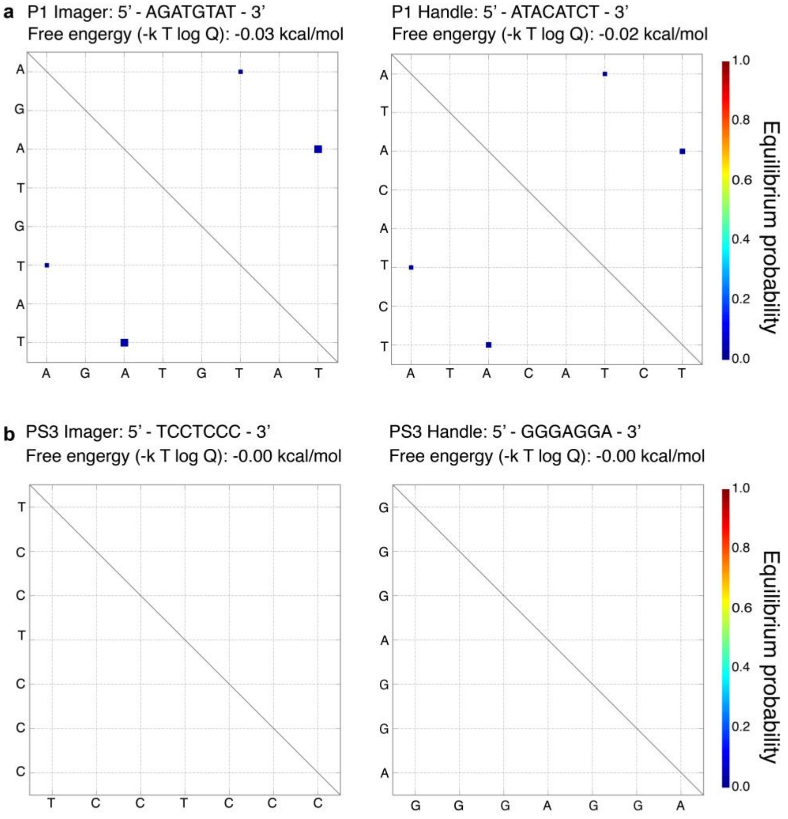

Supplementary Figure 3

Sequence analysis for P1 and PS3

While the classical P1 DNA-PAINT sequence has potential self-interactions, the PS3 sequence as exemplary speed-optimized DNA-PAINT sequence shows no self-interactions for handle and imager sequence in Nupack (Zadeh, J.N. et al. NUPACK: Analysis and design of nucleic acid systems. *J Comput Chem* **32**, 170-173 (2011).) pair probability diagrams (position, color, and size of squares represent pair probabilities where color and size scale with the interaction probability). (**a**) Calculations for P1 imager and docking sequence performed with 50 mM NaCl and 10 mM $MgCl_2$ at 23 ºC. (**b**) Calculations for PS3 imager and docking sequence performed with 50 mM NaCl and 75 mM $MgCl_2$ at 23 ºC.

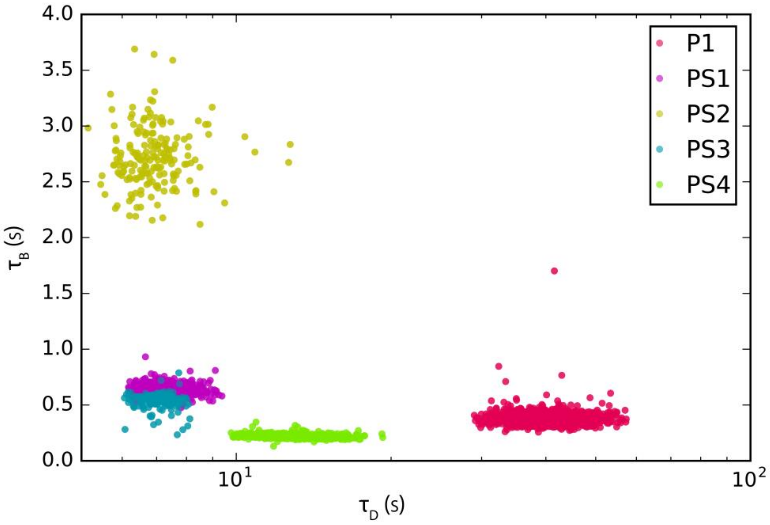

Supplementary Figure 4

Kinetic comparison of PS1 to PS4 with P1

All PS sequences show a significantly shorter τ_D compared to the classical P1 DNA-PAINT sequence (P1: N = 1032, PS1: N = 613, PS2: N = 187, PS3: N = 357, PS4: N = 689). Mean values for τ_D and τ_B for all distributions can be found in **Supplementary Table 1**.

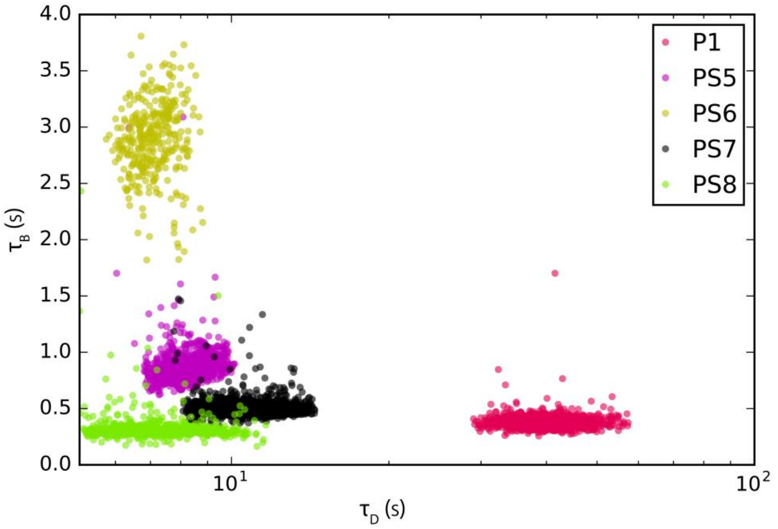

Supplementary Figure 5

Kinetic comparison of PS5 to PS8 with P1

All PS sequences show a scientifically shorter τ_D compared to the classical P1 DNA-PAINT sequence (P1: N = 1032, PS5: N = 841, PS6: N = 347, PS7: N = 1511, PS8: N =960). Mean values for τ_D and τ_B for all distributions can be found in **Supplementary Table 1**.

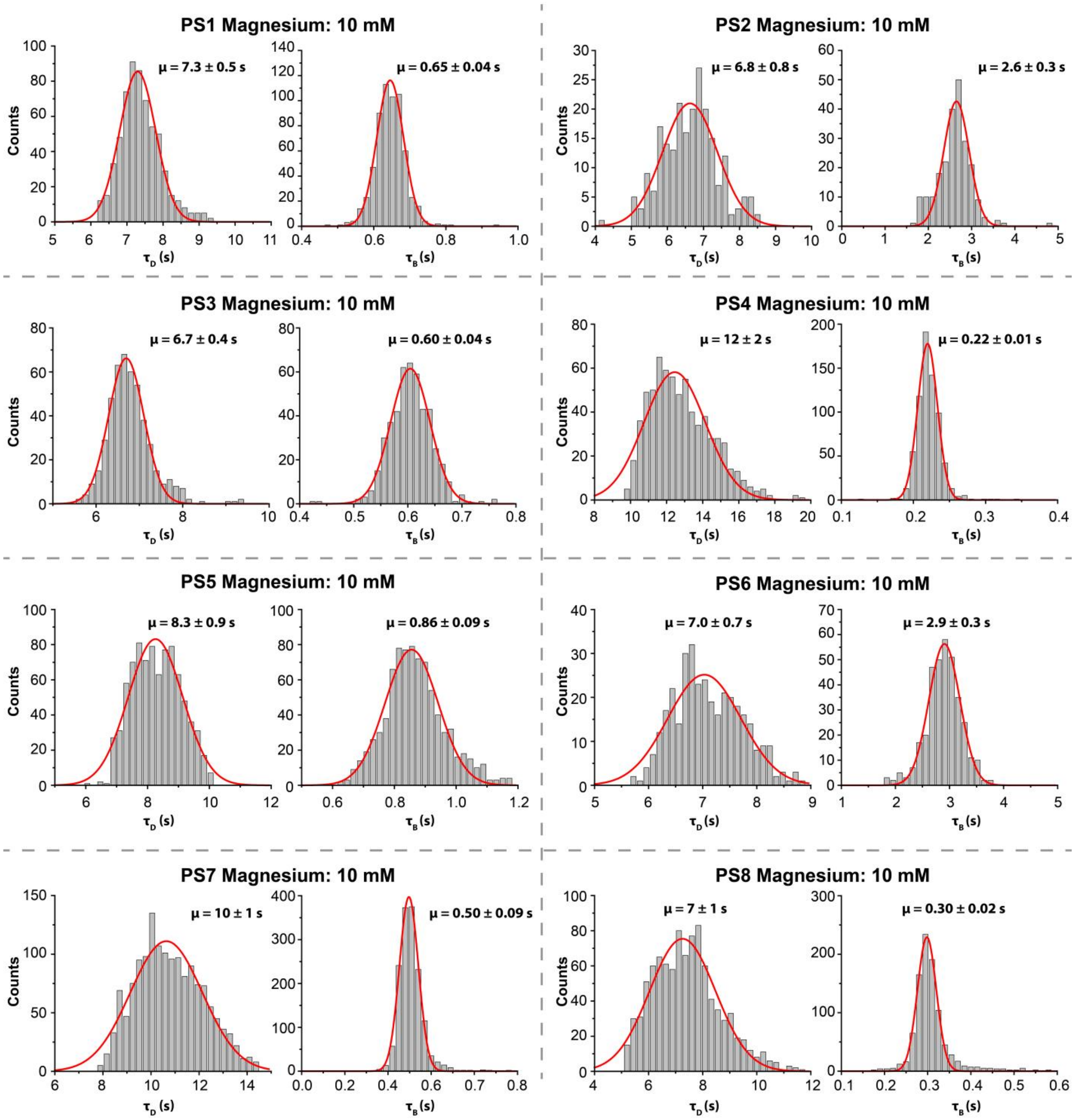

Supplementary Figure 6

Dark and bright time distributions (values indicate mean and standard deviation) for PS1 – PS8 at 10 mM Magnesium concentration (PS1: N = 613, PS2: N = 187, PS3: N = 357, PS4: N = 689, PS5: N = 841, PS6: N = 347, PS7: N = 1511, PS8: N =960). Each experiment was repeated three times independently.

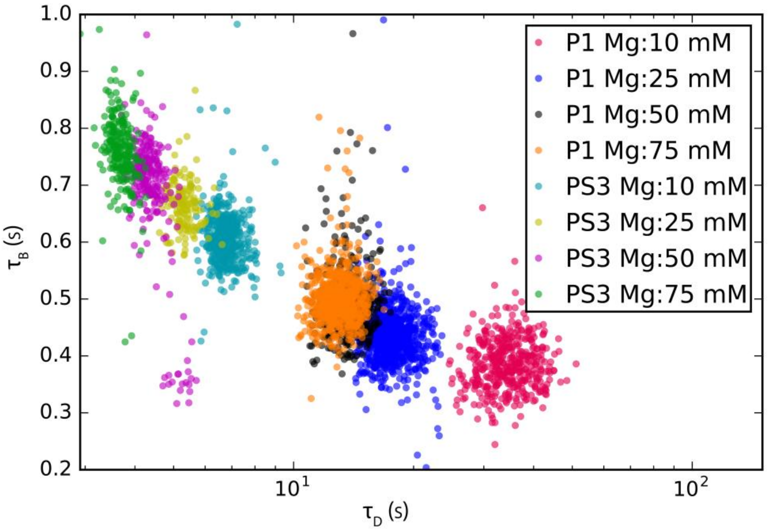

Supplementary Figure 7

Magnesium concentration series for P1 and PS3

By increasing the buffer salinity, τ_B increases and τ_D decreases. This trend is clearly visible for both (P1 and PS3) magnesium concentration series (P1 10 mM $MgCl_2$: N = 437, P1 25 mM $MgCl_2$: N = 772, P1 50 mM $MgCl_2$: N = 490, P1 75 mM $MgCl_2$: N = 685, PS3 10 mM $MgCl_2$: N = 473, PS3 25 mM $MgCl_2$: N = 146, PS3 50 mM $MgCl_2$: N = 260, PS3 75 mM $MgCl_2$: N = 224). Mean values for τ_D and τ_B for all distributions can be found in **Supplementary Table 1**.

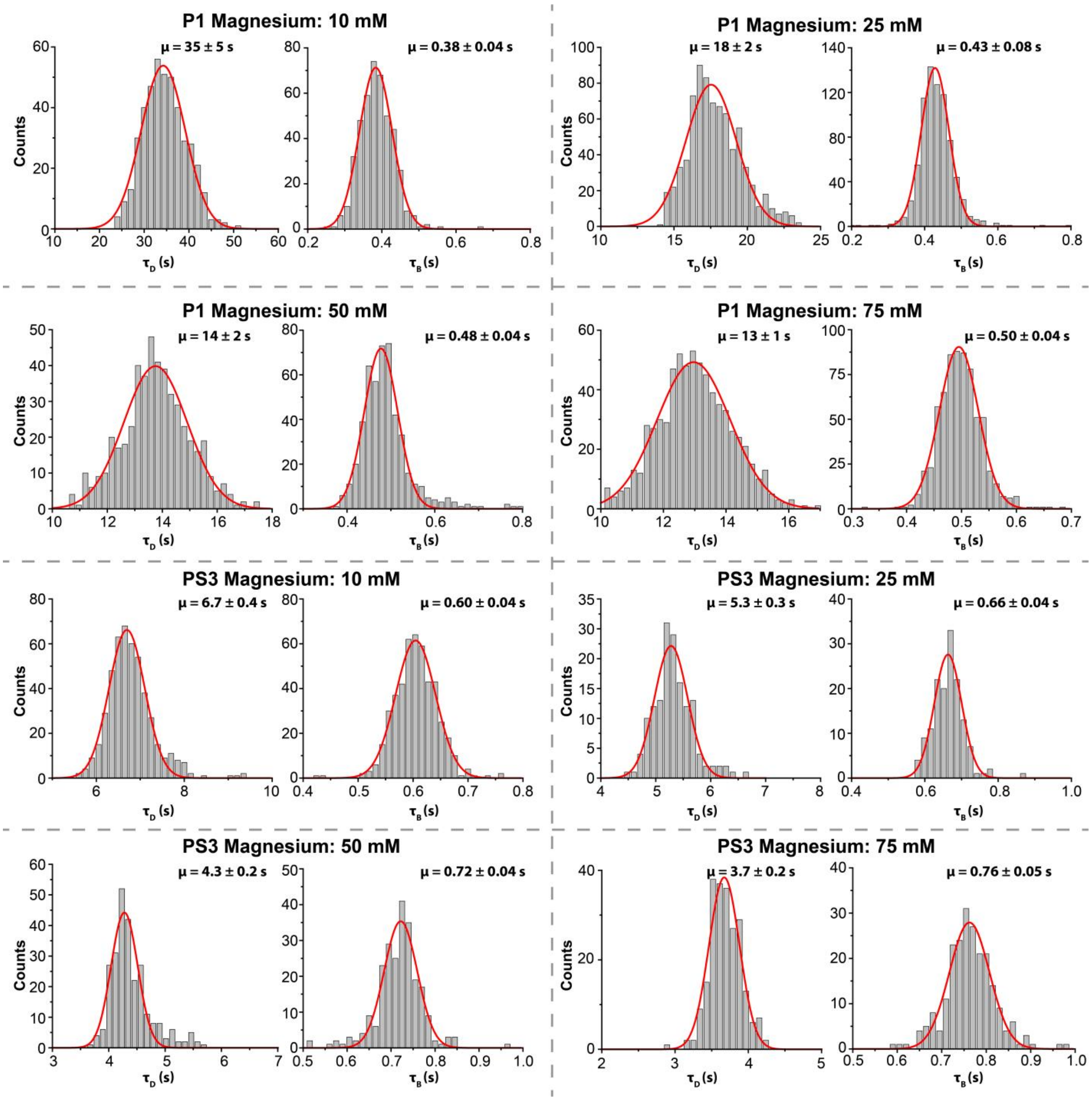

Supplementary Figure 8

Dark and bright time distributions (values indicate mean and standard deviation) for P1 and PS3 at 10, 25, 50, and 75 mM $MgCl_2$ (P1 10 mM $MgCl_2$: N = 437, P1 25 mM $MgCl_2$: N = 772, P1 50 mM $MgCl_2$: N = 490, P1 75 mM $MgCl_2$: N = 685, PS3 10 mM $MgCl_2$: N = 473, PS3 25 mM $MgCl_2$: N = 146, PS3 50 mM $MgCl_2$: N = 260, PS3 75 mM $MgCl_2$: N = 224). Each experiment was repeated three times independently.

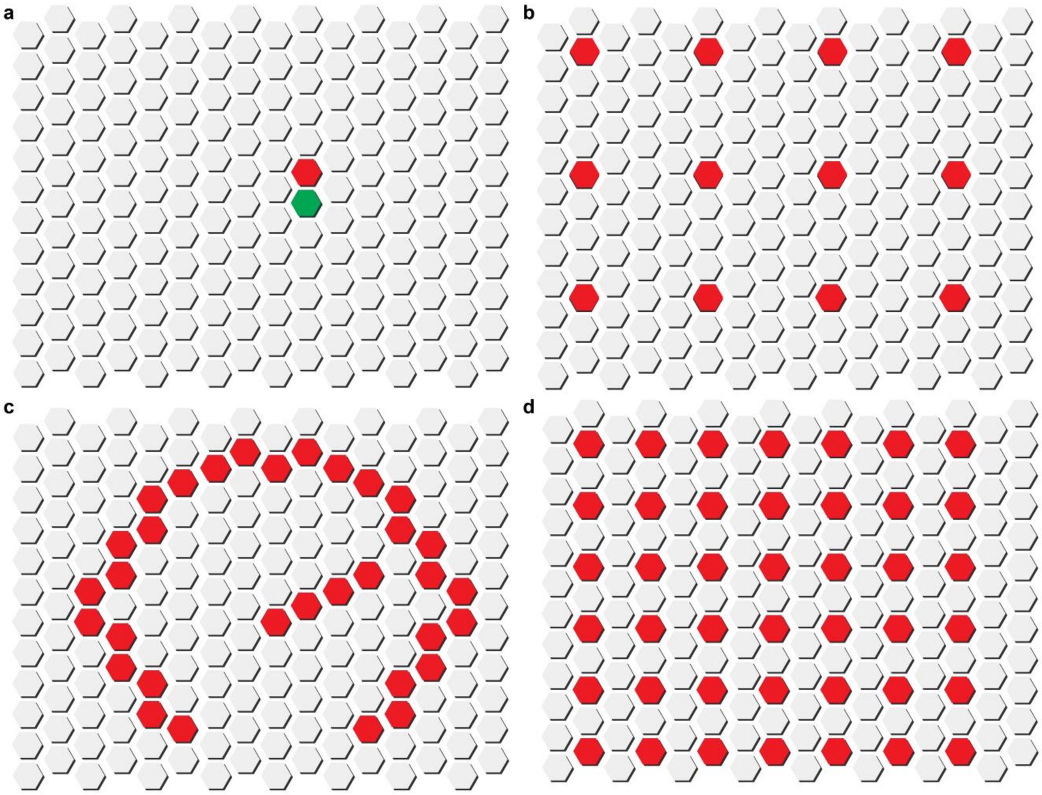

Supplementary Figure 9

DNA origami designs for *in vitro* experiments

(**a**) 1× docking site and 2× docking site DNA origami (used for Data in **Fig. 1a, 1d, Supplementary Fig. 1, 2, 4-8 and 10**). For the 1× docking site only the red position was extended for the 2× docking site structure the red and the green position were extended. A detailed DNA staple list can be found in **Supplementary Data 2**. (**b**) 20-nm-grid DNA origami structure design. A detailed DNA staple list can be found in **Supplementary Data 3, 6**. (**c**) Speed logo (5 nm) DNA origami structure design. A detailed DNA staple list can be found in **Supplementary Data 4**. (**d**) 10-nm-grid DNA origami structure design. A detailed DNA staple list can be found in **Supplementary Data 5**.

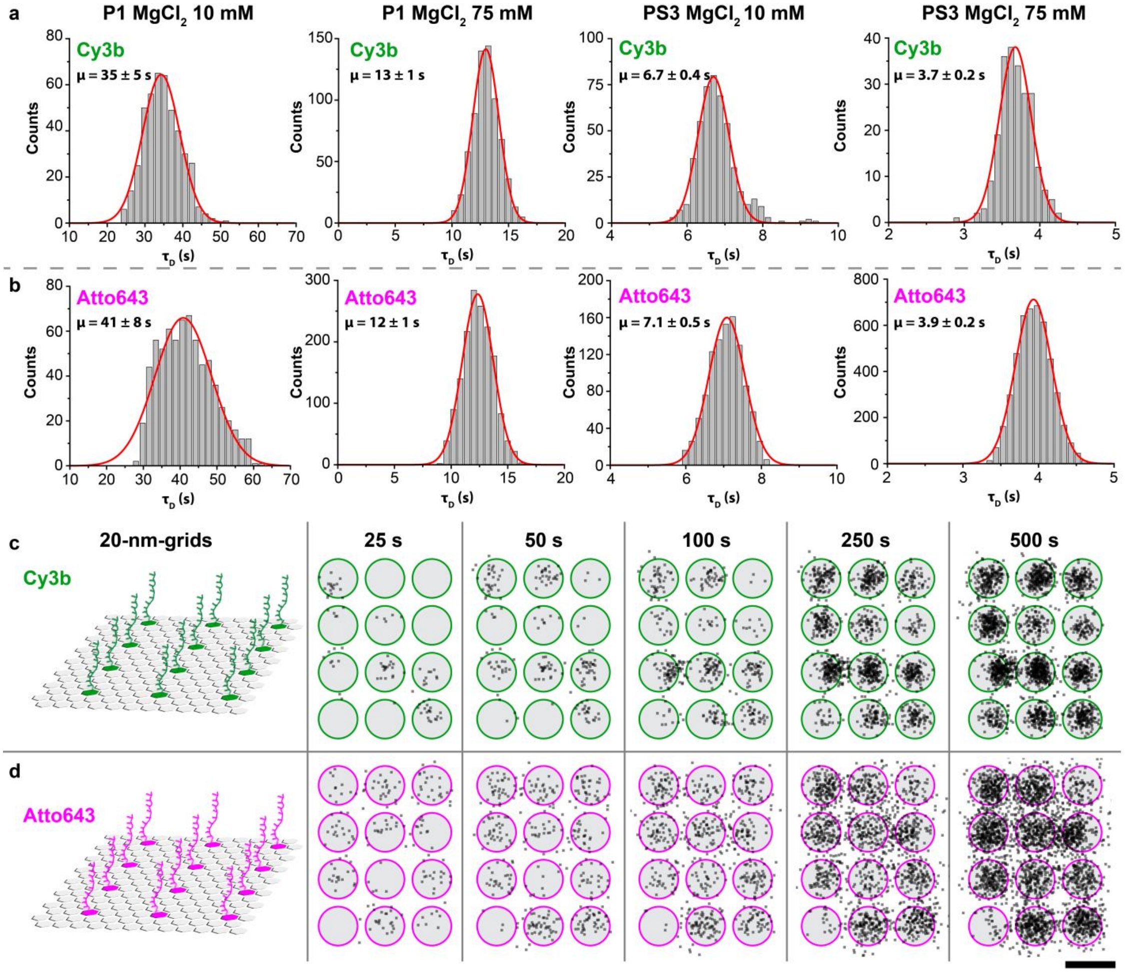

Supplementary Figure 10

Comparison of Cy3b- and Atto643-labeled oligos

(**a**) Dark time distributions alongside mean and standard deviation for Cy3b-labeled imager strands for P1 and PS3 at 10 and 75 mM MgCl$_2$, respectively. (P1 10mM N = 437, P1 75 mM N = 685, PS3 10mM N = 473, PS3 75 mM N = 224) (**b**) Dark time distributions alongside mean and standard deviation for Atto643-labeled imager strands for P1 and PS3 at 10 and 75 mM MgCl$_2$, respectively. (P1 10mM N = 694, P1 75 mM N = 1578, PS3 10mM N = 1048, PS3 75 mM N = 4709) (**c**) Time evolution of a single 20-nm-grid structure for Cy3b-labeled PS3 in 1xTE Buffer with 75 mM MgCl$_2$. (**d**) Time evolution of a single 20-nm-grid structure for Atto643-labeled PS3 in 1xTE Buffer with 75 mM MgCl$_2$. Scale bar: 20 nm.

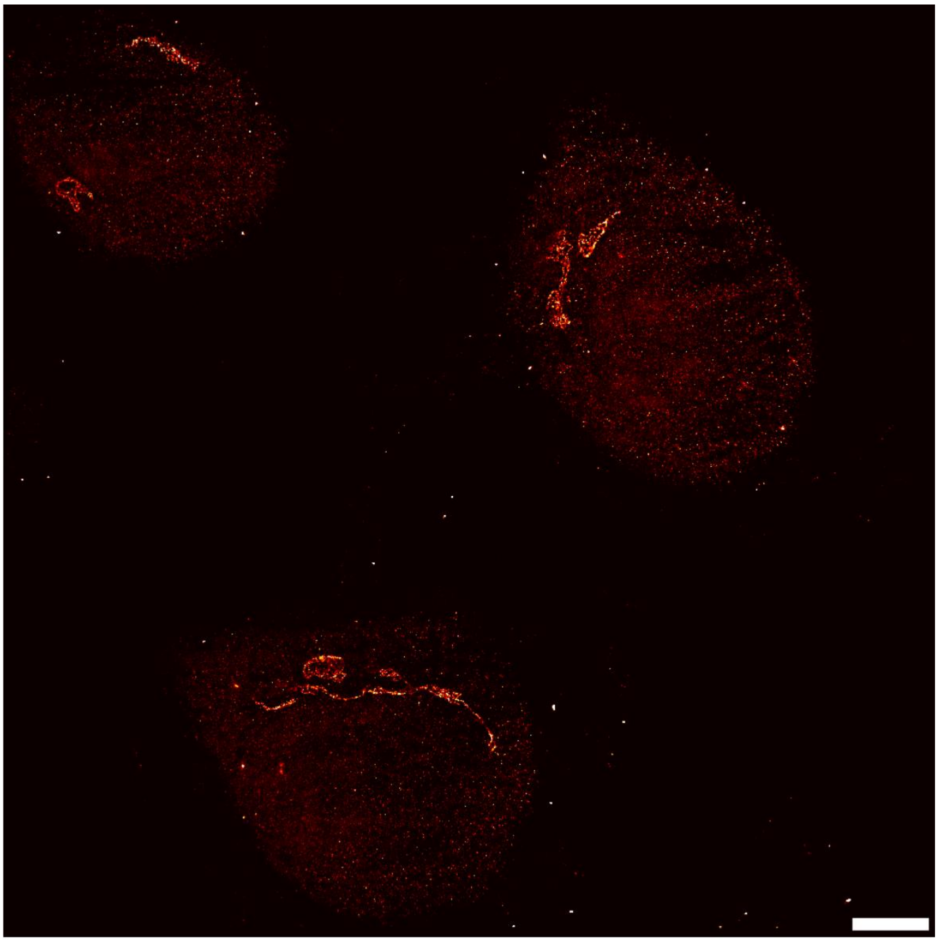

Supplementary Figure 11

Whole field of view of Golgi experiment with PS3 @ 75 mM $MgCl_2$. This experiment was repeated three times independently.

Imager concentration 0.5 nM. Scale bar: 5 µm.

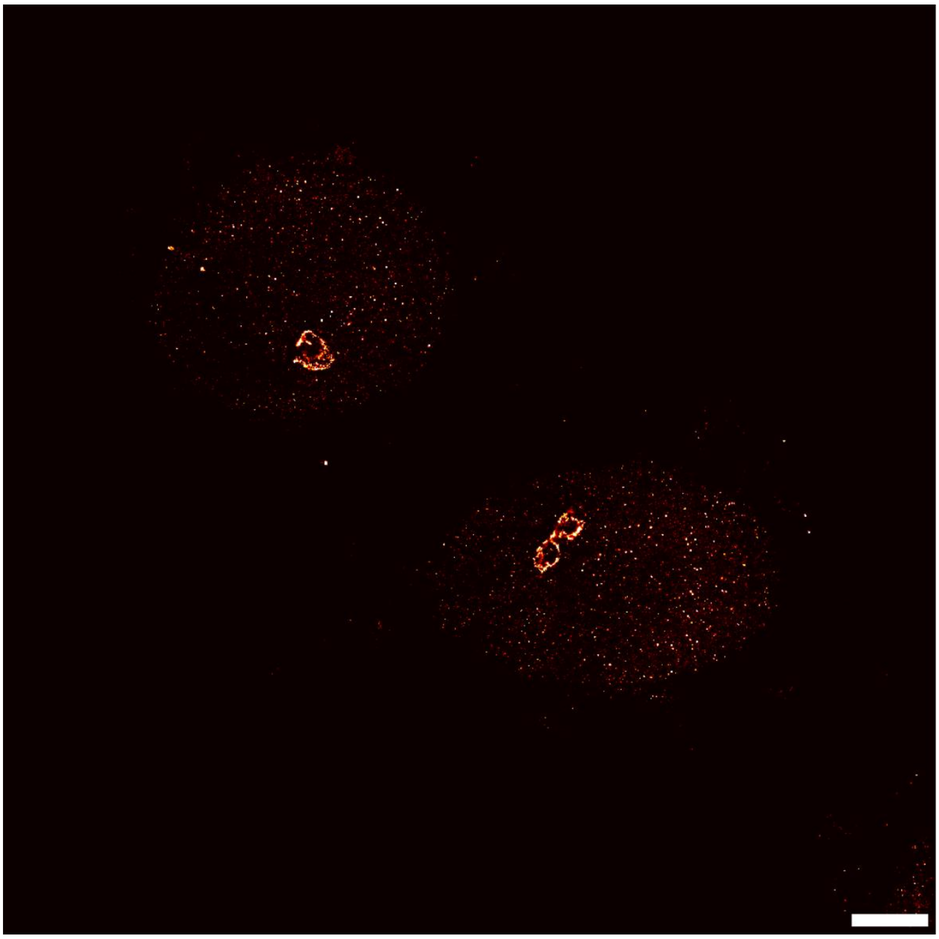

Supplementary Figure 12

Whole field of view of Golgi experiment with P1 @ 10 mM $MgCl_2$. This experiment was repeated three times independently.

Imager concentration: 5 nM. Scale bar: 5 µm.

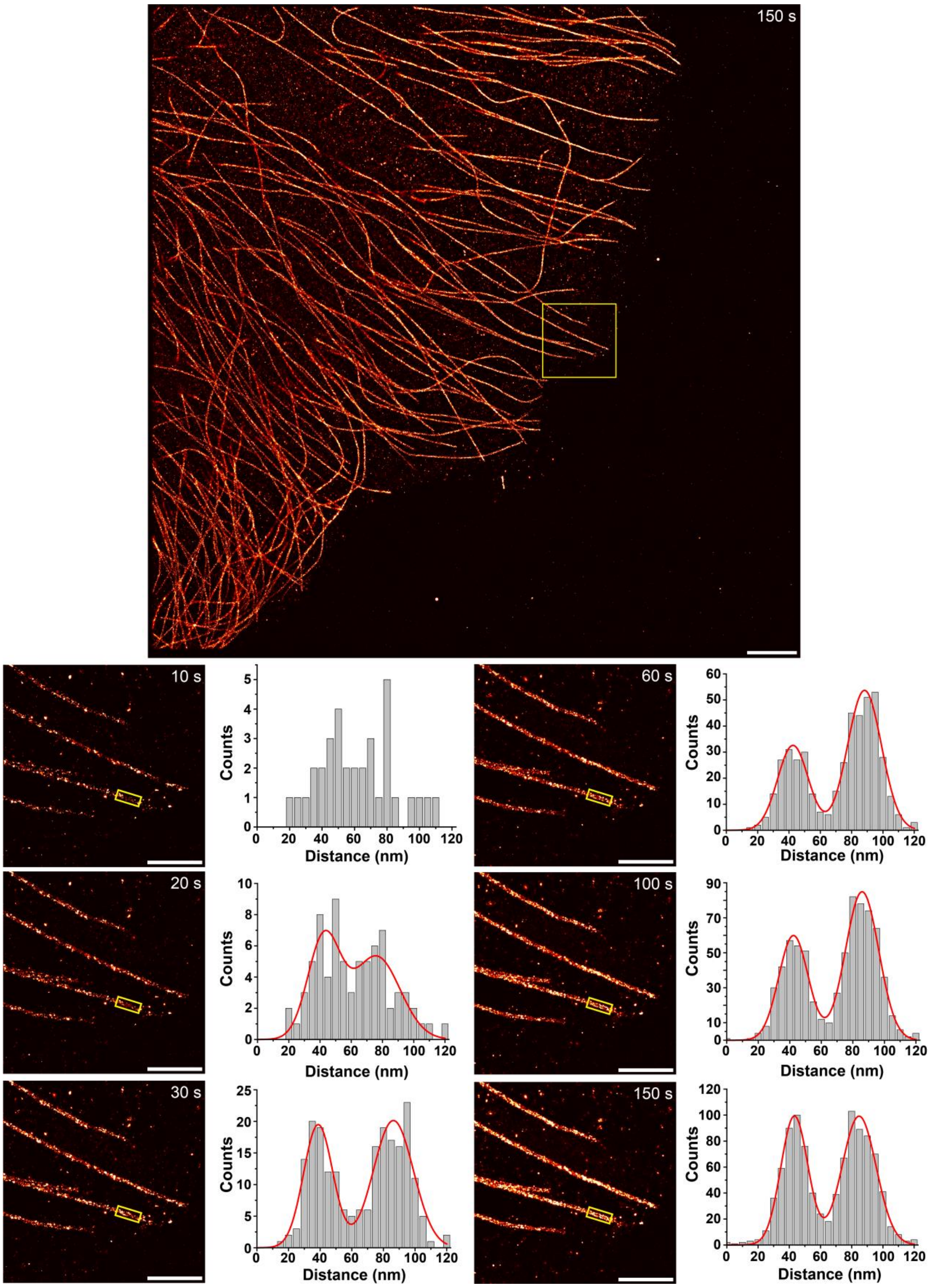
150 s
10 s
20 s
30 s
60 s
100 s
150 s
Counts
Distance (nm)
0
20
40
60
80
100
120

Supplementary Figure 13

Time evolution of speed-optimized microtubule imaging

Top panel shows an overview image of a microtubule network in fixed cells after 150 s. Bottom panels depict a zoom-in (highlighted in the overview image) after 10, 20, 30, 60, 100 and 150 s imaging time, respectively. The histograms present a cross-sectional histogram analysis of the highlighted area in the zoom-ins. After ~30 s of imaging with speed-optimized DNA-PAINT the 'hollowness' of the microtubules can be visualized. Localization precision (Endesfelder, U., Malkusch, S., Fricke, F. & Heilemann, M. A simple method to estimate the average localization precision of a single-molecule localization microscopy experiment. *Histochem Cell Biol* **141**, 629-638 (2014).): ~8 nm. Achievable spatial resolution: ~19 nm. We note that this high spatiotemporal resolution is currently not achievable with approaches such as FRET-PAINT. This experiment was repeated three times independently. Scale bars: 5 µm (overview), 2 µm (zoom-ins).

Supplementary Table 1 | Sequence kinetics (mean values)

Imager Name	**Imager Concentration**	**Magnesium Concentration**	**τ_B (mean±std)**	**τ_D (mean±std)**	**k_{on}**	**k_{off}**
P1*	20 nM	10 mM	0.38±0.04 s	35±5 s	$1.25 * 10^6$ (1/Mol*s)	2.63 1/s
PS1*	20 nM	10 mM	0.65±0.04 s	7.3±0.5 s	$6.8 * 10^6$ (1/Mol*s)	1.54 1/s
PS2*	20 nM	10 mM	2.6±0.3 s	6.8±0.8 s	$5.5 * 10^6$ (1/Mol*s)	0.53 1/s
PS3*	20 nM	10 mM	0.60±0.04 s	6.7±0.4 s	$7.1 * 10^6$ (1/Mol*s)	1.85 1/s
PS4*	20 nM	10 mM	0.22±0.01 s	12±2 s	$3.9 * 10^6$ (1/Mol*s)	4.55 1/s
PS5*	20 nM	10 mM	0.86±0.09 s	8.3±0.9 s	$6.0 * 10^6$ (1/Mol*s)	1.10 1/s
PS6*	20 nM	10 mM	2.9±0.3 s	7.0±0.7 s	$7.0 * 10^6$ (1/Mol*s)	0.34 1/s
PS7*	20 nM	10 mM	0.50±0.09 s	10±1 s	$4.6 * 10^6$ (1/Mol*s)	1.96 1/s
PS8*	20 nM	10 mM	0.30±0.02 s	7±1 s	$6.7 * 10^6$ (1/Mol*s)	3.13 1/s
P1*	20 nM	25 mM	0.43±0.08 s	18±2 s	$2.8 * 10^6$ (1/Mol*s)	2.33 1/s
P1*	20 nM	50 mM	0.48±0.04 s	14±2 s	$3.6 * 10^6$ (1/Mol*s)	2.00 1/s
P1*	20 nM	75 mM	0.50±0.04 s	13±1 s	$3.8 * 10^6$ (1/Mol*s)	2.00 1/s
PS3*	20 nM	25 mM	0.66±0.04 s	5.3±0.3 s	$9.4 * 10^6$ (1/Mol*s)	1.52 1/s
PS3*	20 nM	50 mM	0.72±0.04 s	4.3±0.2 s	$11.4 * 10^6$ (1/Mol*s)	1.45 1/s
PS3*	20 nM	75 mM	0.76±0.05 s	3.7±0.2 s	$13.6 * 10^6$ (1/Mol*s)	1.32 1/s

Supplementary Table 2 | Imager sequences

Imager name	**Sequence**	**5'-mod**	**3'-mod**	**Vendor**
P1*	AGATGTAT	None	Cy3B	MetaBion
P1*	AGATGTAT	None	ATTO 643	Eurofins Genomics
PS1*	CCTCCTC	None	Cy3B	MetaBion
PS2*	TCCTCCTC	None	Cy3B	MetaBion
PS3*	TCCTCCC	None	Cy3B	MetaBion
PS3*	TCCTCCC	None	ATTO 643	Eurofins Genomics
PS3* – (6 nt)	TCCTCC	None	Cy3B	MetaBion
PS4*	TCCTCCT	None	Cy3B	MetaBion
PS5*	GAGGAGG	None	Cy3B	MetaBion
PS6*	GAGGAGGA	None	Cy3B	MetaBion
PS7*	GGGAGGA	None	Cy3B	MetaBion
PS8*	AGGAGGA	None	Cy3B	MetaBion

Supplementary Table 3 | List of biotinylated DNA staple strands

No	Position	Name	Sequence	Mod
1	C02	18[63]20[56]BIOTIN	ATTAAGTTTACCGAGCTCGAATTCGGGAAACCTGTCGTGC	5'-BT
2	C09	4[63]6[56]BIOTIN	ATAAGGGAACCGGATATTCATTACGTCAGGACGTTGGGAA	5'-BT
3	G02	18[127]20[120]BIOTIN	GCGATCGGCAATTCCACACAACAGGTGCCTAATGAGTG	5'-BT
4	G09	4[127]6[120]BIOTIN	TTGTGTCGTGACGAGAAACACCAAATTTCAACTTTAAT	5'-BT
5	K02	18[191]20[184]BIOTIN	ATTCATTTTTGTTTGGATTATACTAAGAAACCACCAGAAG	5'-BT
6	K09	4[191]6[184]BIOTIN	CACCCTCAGAAACCATCGATAGCATTGAGCCATTTGGGAA	5'-BT
7	O02	18[255]20[248]BIOTIN	AACAATAACGTAAAACAGAAATAAAAATCCTTTGCCCGAA	5'-BT
8	O09	4[255]6[248]BIOTIN	AGCCACCACTGTAGCGCGTTTTCAAGGGAGGGAAGGTAAA	5'-BT

Supplementary Table 4 | Handle sequences

Handle Name	Sequence	5'-mod	3'-mod	Vendor
P1	ATACATCT	Staple DNA origami	None	IDT
P1	ATACATCT	Thiol (AB conjugation)	None	Eurofins Genomics
PS1	GAGGAGG	Staple DNA origami	None	IDT
PS2	GAGGAGGA	Staple DNA origami	None	IDT
PS3	GGGAGGA	Staple DNA origami	None	IDT
PS3	GGGAGGA	Thiol (AB conjugation)	None	Eurofins Genomics
PS4	AGGAGGA	Staple DNA origami	None	IDT
PS5	CCTCCTC	Staple DNA origami	None	IDT
PS6	TCCTCCTC	Staple DNA origami	None	IDT
PS7	TCCTCCC	Staple DNA origami	None	IDT
PS8	TCCTCCT	Staple DNA origami	None	IDT

Supplementary Table 5 | Imaging parameters

Dataset	Parameters	Buffer	Power	Setup
Figure 1a & Supplementary Figure 1,2, 4-8	100 ms, 30k Frames, 20 nM	B, B-25mM-Mg, B-50mM-Mg, B-75mM-Mg	11 W/cm^2	1
Figure 1b	50 ms, 10k Frames, 5 nM, P1 & PS3	B, B-75mM-Mg	950 W/cm^2	1
Figure 1c	300 ms, 5k Frames, 5 nM, PS3	B-75mM-Mg	950 W/cm^2	1
Figure 1d	100 ms, 50k Frames, 5 nM, P1 & PS3	B, B-75mM-Mg	11 W/cm^2	1
Figure 2a,b & Supplementary Figure 11	100 ms, 20k Frames, 0.5 nM, PS3	B-75mM-Mg	400 W/cm^2	2
Figure 2d,e & Supplementary Figure 12	100 ms, 20k Frames, 5 nM, P1	B	400 W/cm^2	2
Figure 3	20 ms, 10k Frames (per tile), 1 nM, PS3 (6 nt)	B-75mM-Mg	900 W/cm^2	1
Supplementary Figure 10	50 ms, 10k Frames, 5 nM, P1 & PS3	B-75mM-Mg	950 W/cm^2	1
Supplementary Figure 13	10 ms, 15k Frames, 5 nM, PS3 (6 nt)	B-75mM-Mg	900 W/cm^2	2

6

Localization-Based Fluorescence Correlation Spectroscopy

6.1 Motivation and Summary

Within this chapter, the first experimental application of lbFCS is presented aiming at the prevailing problem of molecular counting in SMLM [43, 105]. Extensive efforts have been made particularly for STORM/PALM in order to infer copy numbers of target molecules from localization clusters within SMLM data [106–119]. However, these approaches require either a priori knowledge of the blinking dynamics, the expected number of localizations per fluorophore or a subset of localization clusters of assumed single targets serving as a calibration reference. Despite successful applications to biological targets, it is hard, if not impossible, to proof the validity of external calibrations and a priori assumptions within a complex sample, leaving room for potentially biased counting results. A calibration-dependent molecular counting approach has previously been developed also for DNA-PAINT, termed qPAINT [39]. Here, we introduce lbFCS as the first self-calibrating molecular counting approach in combination with DNA-PAINT, without the requirements of a priori assumptions on a subset of localization clusters or blinking kinetics. We first validate our theoretical framework derived in Section 2.3.2 for measuring ligand binding kinetics to individual surface-immobilized receptors mimicked by imager binding to DNA origami carrying a single docking strand. Subsequently, we increase the number of docking strands per DNA origami and demonstrate that lbFCS allows absolute molecular counting independent of the localization cluster density.

6.2 PUBLICATION P4: Toward Absolute Molecular Numbers in DNA-PAINT

Toward Absolute Molecular Numbers in DNA-PAINT

Johannes Stein, Florian Stehr, Patrick Schueler, Philipp Blumhardt,
Florian Schueder, Jonas Mücksch, Ralf Jungmann and Petra Schwille

Author contributions:

J.S. and F.Stehr contributed equally. **J.S.**, F.Stehr, R.J., and P.Schwille conceived the study. **J.S.** designed and performed the experiments, analyzed and interpreted the data, and wrote the manuscript. F.Stehr designed and performed the experiments, analyzed and interpreted data, and wrote the manuscript. F.Stehr wrote the code and **J.S.** edited code. P.Schueler folded DNA origami structures, performed experiments, and analyzed data. P.B., F.Schueder and J.M. performed initial experiments and interpreted the data. R.J. and P.Schwille supervised the study. **All authors** revised the manuscript and have given approval to the final version of the manuscript.

published in

Nano Letters (2019), 19, 11, 8182-8190

Reprinted from [97] under the CC BY-NC 4.0 license.

Downloaded via 193.175.2.17 on December 30, 2019 at 11:32:30 (UTC).
See https://pubs.acs.org/sharingguidelines for options on how to legitimately share published articles.

This is an open access article published under a Creative Commons Attribution (CC-BY) License, which permits unrestricted use, distribution and reproduction in any medium, provided the author and source are cited.

ACS Editors' Choice
Letter
NANO LETTERS
Cite This: *Nano Lett.* 2019, 19, 8182−8190
pubs.acs.org/NanoLett

Toward Absolute Molecular Numbers in DNA-PAINT

Johannes Stein,[†,§] Florian Stehr,[†,§] Patrick Schueler,[†] Philipp Blumhardt,[†] Florian Schueder,[†,‡] Jonas Mücksch,[†] Ralf Jungmann,[†,‡] and Petra Schwille*,[†]

[†]Max Planck Institute of Biochemistry, 82152 Martinsried, Germany
[‡]Faculty of Physics, Ludwig Maximilian University, 80539 Munich, Germany

S *Supporting Information*

ABSTRACT: Single-molecule localization microscopy (SMLM) has revolutionized optical microscopy, extending resolution down to the level of individual molecules. However, the actual counting of molecules relies on preliminary knowledge of the blinking behavior of individual targets or on a calibration to a reference. In particular for biological applications, great care has to be taken because a plethora of factors influence the quality and applicability of calibration-dependent approaches to count targets in localization clusters particularly in SMLM data obtained from heterogeneous samples. Here, we present localization-based fluorescence correlation spectroscopy (lbFCS) as the first absolute molecular counting approach for DNA-points accumulation for imaging in nanoscale topography (PAINT) microscopy and, to our knowledge, for SMLM in general. We demonstrate that lbFCS overcomes the limitation of previous DNA-PAINT counting and allows the quantification of target molecules independent of the localization cluster density. In accordance with the promising results of our systematic proof-of-principle study on DNA origami structures as idealized targets, lbFCS could potentially also provide quantitative access to more challenging biological targets featuring heterogeneous cluster sizes in the future.

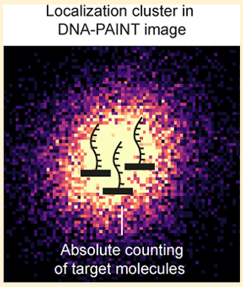
Localization cluster in DNA-PAINT image
Absolute counting of target molecules

KEYWORDS: *DNA-PAINT, super-resolution microscopy, single-molecule localization microscopy (SMLM), molecular counting, fluorescence correlation spectroscopy (FCS)*

The advent of super-resolution (SR) microscopy has revolutionized life science research by providing visual access to specific biological structures at the nanoscale.[1−4] The SR methods summarized as single-molecule localization microscopy (SMLM), such as stochastic optical reconstruction microscopy[3] (STORM), photoactivated localization microscopy[4] (PALM), and (DNA)-points accumulation for imaging in nanoscale topography[5,6] (PAINT) circumvent the diffraction limit by acquiring image sequences of a "blinking" target structure by stochastically activating only a small subset of all fluorescent labels at a time. Thus, these methods enable localization of individual dye molecules in each camera frame and downstream rendering of SR images from the localizations obtained over all frames. Based on the fact that each targeted molecule contributes a certain number of localizations to the SR image, SMLM has been employed as a quantitative tool to count molecules for nearly a decade.[7,8] Extensive efforts have been made in this direction particularly for the methods STORM/PALM[7−22] mostly based on either (i) a priori knowledge of the blinking dynamics or the number of localizations per fluorescence marker (e.g., via supplementary experiments or theoretical modeling) or (ii) on an initial calibration directly within the sample by using isolated localization clusters originating from an assumed number of fluorescent molecules as a reference. Because a multitude of factors can influence the blinking dynamics locally in the sample,[7,8] a calibration directly within the sample as in (ii) is presumably the preferred option. Either way, however, when applying one of these counting approaches to localization clusters of unknown size, only relative counting results are obtained, determined by the a priori assumptions or by the assumed number of molecules within reference localization clusters.

In the special case of DNA-PAINT, an approach for molecular counting has been proposed, termed quantitative PAINT (qPAINT),[23] which exploits the programmable hybridization of single-stranded and fluorescently labeled DNA probes ("imagers") to their complementary "docking strands" (DSs) fixed as labels to the target molecules. DNA-PAINT hence decouples the necessary "blinking" in SMLM from the photophysical properties of the fluorescent markers.[7,24] However, when extracting DNA hybridization dynamics from DNA-PAINT data for molecular counting, one still has to consider several pitfalls both at the stage of data acquisition and post processing. On the acquisition side, this includes the choice of optimized illumination schemes for uniform spot detection efficiency[25] as well as minimizing photoinduced damage.[26] As typically high laser intensities are used in order to gain spatial resolution,[27] fluorescence bursts recorded during DNA-PAINT acquisition are usually limited

Received: August 28, 2019
Revised: September 16, 2019
Published: September 19, 2019

© 2019 American Chemical Society

DOI: 10.1021/acs.nanolett.9b03546
Nano Lett. 2019, 19, 8182−8190

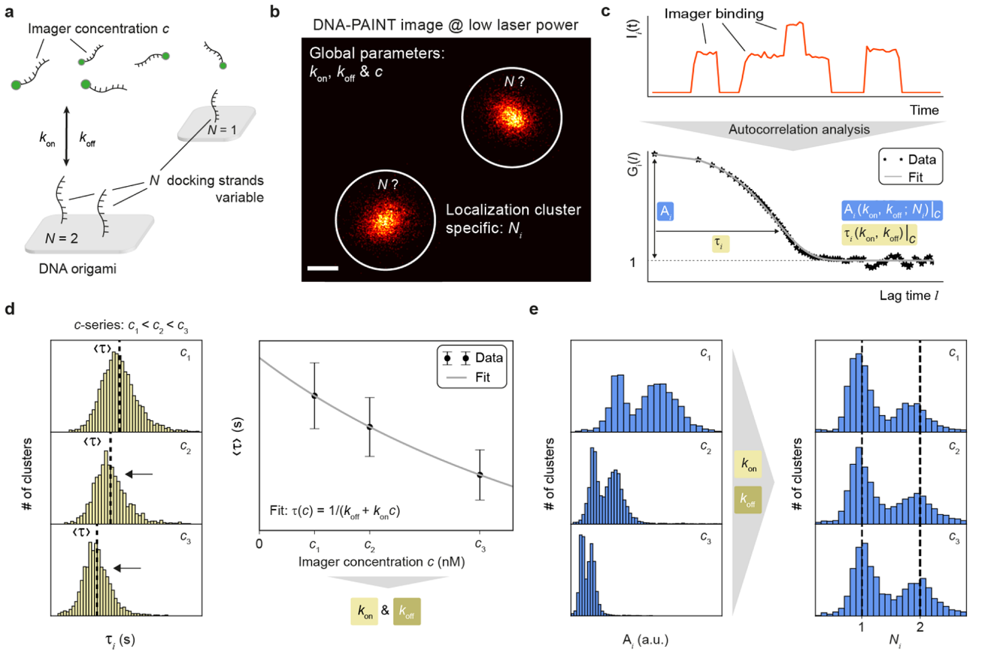

Figure 1. Principle of absolute molecular counting with lbFCS. (a) DNA-PAINT schematic for imaging DNA origami nanostructures exhibiting a variable number of docking strands (DSs) N (either $N = 1$ or $N = 2$). (b) DNA-PAINT image acquired at low laser power showing the two DNA origami from (a). The spatial resolution does not suffice to robustly distinguish the number of DSs N_i in the DNA-PAINT image. All localization clusters in an image are automatically detected as circular "picks" (white circles) for downstream DS counting analysis. (c) Top: for each pick, the intensity versus time trace containing the temporal information on imager binding and unbinding is analyzed by computing the autocorrelation function. Bottom: the computed autocorrelation curve of the intensity trace shows a characteristic monoexponential decay and is well described by the fit model with the two parameters amplitude A_i and characteristic decay time τ_i (eqs 1 and 2). (d) Extraction of DNA hybridization rates via imager concentration series. Left: histograms of τ_i distributions from all identified localization clusters (passing the filtering procedure as in Supplementary Figure 3) in the DNA-PAINT images of the same target, measured at three different imager concentrations c. The mean ⟨τ⟩ (black dashed lines) decreases with c, as expected from eq 2. Right: Fitting eq 2 to ⟨τ⟩ versus c yields k_{on} and k_{off}. (e) Left: distribution of A_i obtained from the same clusters as in the histograms in (d). Right: reformulating eq 1 and inserting (k_{on}, k_{off}, c) allows to convert each A_i to the number of DSs N_i in each cluster over all samples with peaks at $N = 1$ and $N = 2$ (black dashed lines). Scale bars: 50 nm in (b). Error bars correspond to standard deviation.

by photobleaching of the dye rather than the actual dissociation of the imager strands—an effect that can be accompanied by the photoinduced depletion of DSs during the course of a measurement.[26] Furthermore, qPAINT requires adjustment of the imager concentration to the expected density of DSs, limiting the applicability to biological samples, which might exhibit a heterogeneous distribution of DS densities.[23] On the postprocessing side, counting with qPAINT is also relative as it relies on the calibration to the hybridization kinetics of single DSs.[23]

In this study, we introduce localization-based fluorescence correlation spectroscopy (lbFCS) as a quantitative tool for DNA-PAINT that, to our knowledge, for the first time allows absolute molecular ensemble counting in clusters of SMLM data. We first show that autocorrelation analysis of fluorescence fluctuations similar to classical FCS[28,29] can be applied to localization clusters in DNA-PAINT images (i.e., the rendered localizations) of DNA origami structures[30] allowing the extraction of imager binding kinetics. Following previous work,[31] our approach is based on imaging a sample at three different imager concentrations allowing extraction of the hybridization rates via lbFCS at a precision of better than 5% and, most importantly, independent of the number of DSs per localization cluster. The DNA hybridization rates obtained over all localization clusters serve as calibration for lbFCS to subsequently count the number of DSs per cluster in each of the three samples. In order to minimize photoinduced damage and to obtain the true imager binding kinetics, we reduce the laser intensity for lbFCS measurements to a minimum while still allowing for efficient spot detection but at the cost of spatial resolution. In a benchmark study of lbFCS on DNA origami structures with a predesigned number of DSs, we additionally image each field of view (FOV) first at a low and then at a high laser power. This allows us to spatially resolve individual DSs as a visual ground truth for the lbFCS counting results over all localization clusters. Finally, we show that via lbFCS we can extend the restriction of qPAINT where the cluster densities (number of DSs) determine the applicable imager concentration. Over a wide range of cluster densities, we show that lbFCS counting results are in good agreement with the visual ground truth.

DOI: 10.1021/acs.nanolett.9b03546
Nano Lett. 2019, 19, 8182−8190

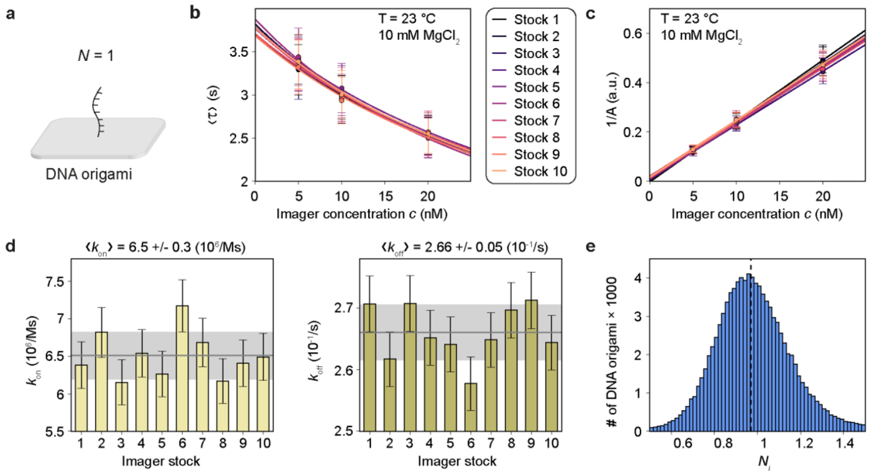

Figure 2. Experimental validation of lbFCS. (a) The 1DS structures with $N = 1$ for testing the lbFCS approach. (b) Repetition of 10 concentration series each with freshly prepared imager stocks (10 × 3 samples). $\langle\tau\rangle$ versus c fit for each concentration series demonstrating high reproducibility. (c) $1/A$ versus c fits show similar reproducibility. The fits passing through the origin yield that the concentration ratios were adjusted correctly. (d) Sets of k_{on} (left, light green) and k_{off} (right, dark green) extracted from the fits in (b) for each imager stock. Mean and standard deviation are given as gray line and light gray area, respectively. (e) Histogram of lbFCS counting results N over all 30 samples from the concentration series on 1DS structures. The black dashed line indicates the median at $N = 0.97 \pm 0.11$. Error bars correspond to standard deviation in the case of $\langle\tau\rangle$, k_{on}, and k_{off} and interquartile range in the case of $1/A$.

Results and Discussion. *The Principle of lbFCS.* As model targets for molecular counting with DNA-PAINT in this study we employed DNA origami,[30] a method allowing the precise and large scale production of artificial nanostructures from DNA as building material. In the context of DNA-PAINT, DNA origami have been extensively used for creating nanometer patterns of DSs as ideal benchmarking systems for the obtainable spatial resolution of the used microscope.[6,32,33] In the following, we outline how to count the number of DSs on DNA origami structures in DNA-PAINT images with lbFCS (a detailed step-by-step description of all analysis steps can be found in Supplementary Figure 1). Figure 1a shows a DNA-PAINT schematic of two surface-immobilized DNA origami, one with two DSs ($N = 2$) and the other with a single DS ($N = 1$). Freely diffusing imagers bind to the DSs at association rate k_{on} and unbind at dissociation rate k_{off}, thereby generating the characteristic blinking required for downstream SMLM reconstruction. The concentration of imager strands is denoted as c. DNA-PAINT imaging was performed on a custom-built total internal reflection fluorescence (TIRF) microscope with a homogeneous ("flat-top") intensity profile for optimized acquisition conditions[25] and temperature control (see Supplementary Figure 2a for a detailed setup sketch). A low laser power was selected to obtain imager dissociation rates unbiased by photobleaching (Supplementary Figure 2b) while still preserving the ability of robust spot detection. Albeit the reduction in laser power minimizes photoinduced damage during acquisition, it comes at the cost of reduced spatial resolution leaving clusters of localizations that do not allow counting of the number of DSs by eye (Figure 1b). However, lbFCS allows to count the number of DSs per structure solely based on the assumptions that (1) every target structure in the sample is subject to the same imager concentration c and (2) all individual DSs of the target structures bind imager strands with equal hybridization rates given by k_{on} and k_{off}. This implies that the values k_{on} and k_{off} are determined for all structures in one sample (i.e., globally) by the designed sequence of the DS and the imager strand for a fixed set of environmental conditions (temperature, buffer, and so forth). Around each automatically detected cluster i in an image we define a circular region referred to as "pick" (white circles in Figure 1b) for which we plot the respective intensity versus time trace $I_i(t)$ containing the temporal information on imager binding and unbinding to the specific target structure (Figure 1c, top). From these, we subsequently compute the autocorrelation curves $G_i(l)$ (Figure 1c, bottom) which are well described by the monoexponential fit model previously derived for surface-integrated (SI)-FCS:[31,34,35] $G_i(l) = A_i e^{l/\tau_i} + 1$. Here, l is defined as the autocorrelation lag time, A_i as the amplitude of the autocorrelation function at zero lag time $G_i(l = 0)$ and τ_i as the characteristic exponential decay constant. Following previous derivations,[31,34,35] the model parameters are defined as

$$A_i(k_{on}, k_{off}; N_i)|_c = \frac{1}{N_i}\frac{k_{off}}{k_{on}c} \tag{1}$$

and

$$\tau_i(k_{on}, k_{off})|_c = \frac{1}{k_{on}c + k_{off}} \tag{2}$$

Referring to the previous assumptions of global hybridization rates and imager concentration, one can readily see that τ_i is only a function of the global rate constants k_{on} and k_{off} meaning that all picks in one sample of imager concentration c should yield the same value of τ_i within the uncertainty of the measurement. As a consequence the mean value $\langle\tau\rangle$ over all

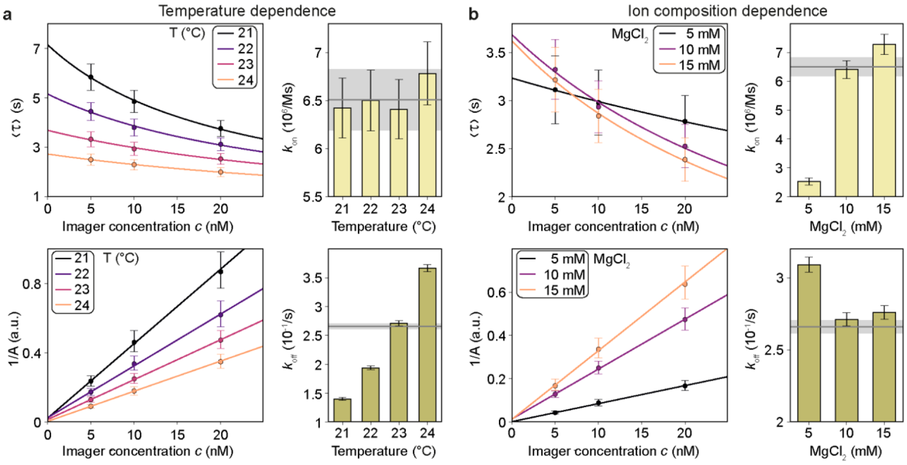

Figure 3. Temperature and ion composition affecting DNA hybridization rates. (a) lbFCS concentration series with 1DS samples at different temperatures, highlighting the temperature dependence of DNA hybridization rates (at fixed [MgCl$_2$] = 10 mM). (b) lbFCS concentration series with 1DS samples at different MgCl$_2$ concentrations affecting the DNA hybridization rates (at fixed T = 23 °C). Gray lines and light gray shaded areas correspond to the mean and the standard deviation, respectively, of the hybridization rates at standard conditions (T = 23 °C and [MgCl$_2$] = 10 mM, see Figure 2d). Error bars correspond to standard deviation in the case of $\langle\tau\rangle$, k_{on}, and k_{off} and interquartile range in the case of $1/A$.

picks suffices for the extraction of the rate constants. The amplitude A_i in contrast is subject to the same global parameters but additionally depends on the number of DSs N_i in each pick. lbFCS makes use of these dependencies in order to extract both the hybridization rate constants k_{on} and k_{off} and the number of DSs N_i in each pick by the following procedure. First, we prepare and image three DNA origami samples (here exemplarily containing both $N = 1$ and $N = 2$ DNA origami structures) at three different imager concentrations ($c_1 < c_2 < c_3$) and automatically detect all clusters in the three resulting SR images (see Supplementary Figure 1). Next, we autocorrelate all intensity traces and remove clusters exhibiting nonrepetitive binding and/or binding dynamics deviating from a clear monoexponential behavior in a filtering step before further analysis (see Supplementary Figure 3). The left panel in Figure 1d shows the resulting τ_i histograms for all remaining clusters in each of the three images. As expected from eq 2, we observe a shift of the distributions toward lower values with increasing c corresponding to a decrease of the mean value $\langle\tau\rangle$. Following the aforementioned reasoning, the mean value $\langle\tau\rangle$ for each imager concentration c (Figure 1d, right panel) yields the global rate constants k_{on} and k_{off} by fitting eq 2. An analogous approach has been previously demonstrated using SI-FCS for the same system (i.e., DNA-PAINT on surface immobilized DNA origami) using an ensemble autocorrelation analysis of the raw intensity fluctuations integrated over larger arrays of camera pixels (originating from thousands of DNA origami), which allowed for the extraction of imager hybridization rates via a concentration series.[31] Here, we show that this approach can be directly transferred to each localization cluster in a DNA-PAINT image of subdiffraction spatial resolution. This allows one to make further use of the amplitude A_i of each pick for molecular counting. According to eq 1, A_i depends on the number of DSs in each cluster resulting in a distribution exhibiting two peaks (for DNA origami either with $N = 1$ or $N = 2$) in addition to the also concentration-dependent shift, as can be seen in the left panel of Figure 1e. Each A_i value can be converted into N_i by reformulating eq 1 to $N_i = \frac{1}{A_i}\frac{k_{off}}{k_{on}c}$ (Figure 1e, right) and inserting the now available rate constants k_{on} and k_{off} together with the respective imager concentration c of each measurement. Figure 1e, right, shows the distribution of the number of DSs present in each localization cluster (i.e., either one or two DSs).

Validation of lbFCS. In order to demonstrate the ability of lbFCS to extract DNA hybridization rates and to count DSs in DNA-PAINT images acquired at low laser power, we first explored the case of a DNA origami design exhibiting just a single DS ($N = 1$, referred to as "1DS"), as depicted in Figure 2a, because it is the only case of an implicit counting ground truth. In 10 repetitions of the same experiment over the course of 2 months, we prepared fresh imager stocks at 5, 10, and 20 nM for subsequent low laser power imaging on 1DS samples (10 × 3 samples, standard conditions: imaging buffer containing 10 mM MgCl$_2$ and temperature controlled at 23 ± 0.1 °C). lbFCS analysis of the localization clusters showed a good reproducibility with respect to the output parameters τ_i and A_i (Figure 2b,c). The mean (error bar, standard deviation) denoted as $\langle\tau\rangle$ of the τ_i distribution and the median (error bar, interquartile range) denoted as A of the A_i distribution (N and N_i) are shown whenever a statistical quantity of an ensemble is presented. The representation of $1/A$ in Figure 2c is chosen to verify the linear dependency on c (see eq 1). In addition, the plot serves as a control for whether the imager concentrations have been adjusted in the correct ratios when the fit of eq 1 intersects the y-axis at the origin. Figure 2d shows the scatter in k_{on} and k_{off} resulting from the 10 fits in Figure 2b. Over all measurements, we obtained the mean hybridization rates of $\langle k_{on}\rangle = (6.5 \pm 0.3) \times 10^6\ \mathrm{M}^{-1}\ \mathrm{s}^{-1}$ and $\langle k_{off}\rangle = (2.66 \pm 0.05) \times 10^{-1}\ \mathrm{s}^{-1}$ with standard deviations below 5% and 2%, respectively, proving high reproducibility. We attribute this

DOI: 10.1021/acs.nanolett.9b03546
Nano Lett. 2019, 19, 8182−8190

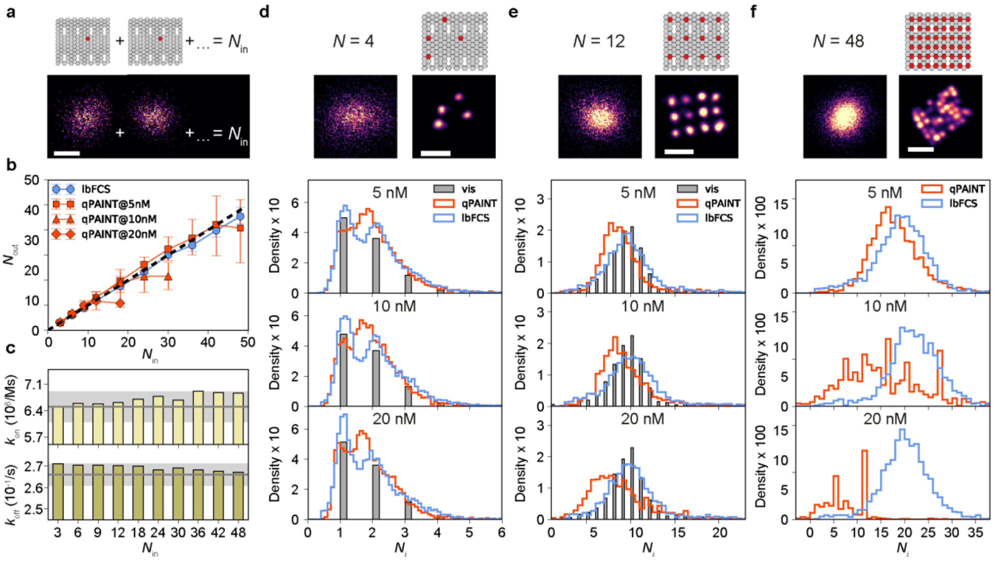

Figure 4. Counting of docking strands on DNA origami. (a) Binning of experimental 1DS localization clusters (taken from stock measurements 1–3, see Figure 2) for computationally increasing the number of DSs N_{in} as input for further testing of counting performance. (b) Median of the counting result N_{out} versus N_{in} comparing the counting results obtained via qPAINT at different imager concentrations (red) versus lbFCS (blue); sum over all imager concentrations displayed (see Supplementary Figure 9 for individual lbFCS and qPAINT results). The black dashed line displays a line through the origin of slope one as expected for ideal counting results (i.e., $N_{out} = N_{in}$). (c) lbFCS extracts correct hybridization rates within the measurement uncertainty independent of N_{in} (k_{on} and k_{off} means (gray lines) and STDs (light gray areas) from Figure 2d). (d) Top: DNA origami design with $N = 4$ DSs. Exemplary image of the same structure from the low laser power image (left) and the high laser power image for visual counting (right). Bottom: counting results for visual counting (gray), qPAINT (red) and lbFCS (blue). (e) Same as (d), but for $N = 12$ DSs DNA origami design. Intensity traces that do not exhibit dark times anymore (see Supplementary Figure 7) cannot be analyzed via qPAINT and are not shown in the histograms. Refer to Supplementary Table 1 for total numbers of analyzable clusters per histogram. (f) Same as (d,e) but for $N = 48$ DSs DNA origami design (no visual count histogram due to too tight DS spacing (10 nm) for robust spot detection). Scale bars: 40 nm in (a,d–f). Error bars in (b) correspond to interquartile range.

high precision to the fact that we are able to minimize the influence of unspecific binding to the surface (Supplementary Figure 4) by only analyzing detected clusters which, in addition, passed the filter criteria (see Supplementary Figure 3). Next, the values (k_{on}, k_{off}) for each stock were used to count the number of DSs in each of the three samples of the respective concentration series. Figure 2e shows the histogram of N_i over all 30 samples (>90% of all data points lie within the x-axis limits; >97 k localization clusters in total) with the median at $N = 0.97 \pm 0.11$, which is in good agreement with the initial design of the 1DS structures.

The counting ability of lbFCS is based on the assumption that k_{on} and k_{off} are global parameters which do not change during the course of the concentration series measurements. It is hence essential to precisely control the experimental conditions affecting DNA hybridization, such as temperature and buffer ion composition. In order to quantitatively assay these effects, we first repeated the concentration series on 1DS samples at 21–24 °C (1 °C increments, all at 10 mM $MgCl_2$), a temperature range which we observed due to the heating of the often enclosed sample space of commercial microscopes during imaging. As reported in many DNA hybridization studies before,[32,36−38] Figure 3a shows that the dissociation rates change considerably (up to ~2.5-fold) over this temperature range, whereas the association rates do not change within the measurement error and show no observable trend. We also varied the ion composition by changing the standard of 10 mM $MgCl_2$ by ±5 mM (at 23 °C) and again used lbFCS to monitor the effects on both rates, such as the 3-fold increase in k_{on} between 5 and 10 mM (Figure 3b). However, as long as the rates are kept constant for all three concentration measurements, lbFCS yields the correct counting result of $N_i = 1$, independent of the actual temperature or ion composition (Supplementary Figure 5). Finally, the question of how precisely the absolute imager concentrations must be controlled needs to be addressed. In Supplementary Figure 6, we reanalyzed one of the stock measurement series at standard conditions as presented in Figure 1b–e by intentionally assuming higher or lower absolute imager concentrations while keeping the correct concentration ratios. The results clearly show that wrong absolute imager concentrations neither affect the absolute counting ability of lbFCS nor the resulting dissociation rate k_{off} as long as the correct concentration ratios are preserved (for which the $1/A$ fit provides control when crossing the origin). However, due to the product $k_{on}c$ in eq 2, assumed imager concentrations deviating from the "true" value by a factor of x will result in an obtained association rate multiplied by the inverse factor x^{-1}. To avoid this ambiguity in order to (relatively) compare obtained association rates we performed a control concentration series on 1DS origamis using the same imager stock at standard conditions (see Figure 2b−e) for every measurement in this study.

Molecular Counting. As a next step, we tested the performance of lbFCS by arbitrarily grouping clusters of $N = 1$ obtained from earlier 1DS experiments (data taken from stock measurements 1−3; see Figure 2) into clusters of defined $N > 1$ ($\equiv N_{\mathrm{in}}$) which is equivalent to the simple computational addition of their respective intensity versus time traces (see Figure 4a). This way, we created localization clusters of up to $N_{\mathrm{in}} = 48$ for each imager concentration ($c = 5$, 10, and 20 nM) and analyzed them using lbFCS and qPAINT. It should be mentioned at this point that in contrast to lbFCS the counting of DSs with qPAINT needs a calibration[23] by the influx rate $k_{\mathrm{on}}^{\mathrm{qPAINT}}c$ obtained from clusters containing a single DS only (see Supplementary Figure 7 for the principle of the qPAINT approach). Supplementary Figure 8 displays the results as obtained by qPAINT analysis of the 1DS experiments of Figure 2b−e. The following results from molecular counting with qPAINT hence rely on a calibration association rate of $k_{\mathrm{on}}^{\mathrm{qPAINT}} = (7.7 \pm 0.2) \times 10^6\ \mathrm{M}^{-1}\ \mathrm{s}^{-1}$. With respect to the error we would like to note that also $k_{\mathrm{on}}^{\mathrm{qPAINT}}$ is profiting from the filtering procedure introduced in Supplementary Figure 3, which in turn is based on the unique property of the autocorrelation analysis of lbFCS to identify and exclude clusters exhibiting dynamics that deviate from a clear monoexponential behavior.

Figure 4b displays the analysis results N_{out} versus N_{in} for both analysis methods (for lbFCS the sum over all three imager concentrations is displayed. See Supplementary Figure 9a−c for individual results at $c = 5$, 10, and 20 nM, respectively). As expected, lbFCS does not show any concentration dependence and yields the correct counting results ($N_{\mathrm{out}} = N_{\mathrm{in}}$, indicated by black dashed line) over the whole range of N_{in}. In contrast, qPAINT starts underestimating the correct number of DSs at a certain cluster size, an effect depending on the imager concentration (whereas for $c = 5$ nM qPAINT starts deviating from the linear relation at $N_{\mathrm{in}} \sim 48$, for $c = 20$ nM the deviation already occurs at $N_{\mathrm{in}} \sim 12$). As explained in Supplementary Figure 10, this is due to the increasing occurrence of simultaneous imager binding to multiple DSs within the same cluster. Because the qPAINT algorithm is based on the extraction of dark times from the intensity versus time trace of a cluster, its intrinsic limit given a certain imager concentration is determined by the maximum number of DSs per cluster N at which the corresponding intensity trace exhibits only few and, ultimately, no dark times at all anymore (in other words, the cluster is continuously fluorescing during data acquisition due to constant imager turnover). In accordance with this consideration, Figure 4b shows that the higher the imager concentration, the faster this limit determined by N is reached (see Supplementary Figure 9 for a detailed analysis of the number of unique dark times extracted per cluster for the last qPAINT data points for $c = 5$, 10, and 20 nM at $N = 48$, 30, and 18, respectively). It should be discussed, however, that our DNA-PAINT data deviates from the type of data previously subjected to qPAINT analysis[23] in two aspects: (i) due to the low laser intensity, the bright times are an order of magnitude longer (i.e., not limited by fast photobleaching as in classical high-resolution DNA-PAINT) and (ii) the imager-DS sequence design employed in this study has a significantly higher $k_{\mathrm{on}}^{\mathrm{qPAINT}}$ (here $7.7 \times 10^6\ \mathrm{M}^{-1}\ \mathrm{s}^{-1}$ versus previously[23] $1 \times 10^6\ \mathrm{M}^{-1}\ \mathrm{s}^{-1}$). Hence, our probability of simultaneous binding events is largely increased for a given N and imager concentration c (i.e., the limit of qPAINT is reached already for much smaller N compared to the previous study[23]).

Having confirmed that lbFCS allows molecular counting over this wide range of DS densities independent of the imager concentration, we next validated the assumption that lbFCS can extract the correct DNA hybridization rates independent of N. Figure 4c displays that for all N_{in} we obtained the same hybridization rates within the measurement uncertainty verifying eq 2 and confirming that τ_i is indeed independent of the number of DSs per cluster.

In order to fully experimentally benchmark the counting performance of lbFCS, we designed DNA origami species with higher numbers of DSs ($N = 4$, 12, and 48). Like for the 1DS structures, we prepared three samples per DNA origami species at $c = 5$, 10, and 20 nM and measured each sample first at low laser power. Directly after each low power measurement, we imaged the same FOV at high laser power in order to obtain visual references at high resolution assignable to each of the localization clusters from the low power measurement. The top panel in Figure 4d depicts the $N = 4$ DNA origami design, an example DNA-PAINT image of a single structure acquired at low laser power (left) and the respective high power image exhibiting the four DSs in the designed pattern (right). We subsequently applied a spot detection algorithm to the high power image in order to automatically count the number of present DSs as a ground truth for the lbFCS and qPAINT results from the low laser power images. The efficiency by which individual staple strands are incorporated into each DNA origami during the folding process is limited and also position dependent,[39] that is, only very few structures feature all DSs from the initial design. The lower panel in Figure 4d shows the counting results of lbFCS (blue) and qPAINT (red) from the low power measurements as well as the visual counting results (gray) from the high power measurements for the three samples of $N = 4$ structures. Folding of this DNA origami design resulted in structures primarily exhibiting one or two DSs, which can be seen at the distinct peaks in all lbFCS distributions and which is furthermore in good agreement with the visual reference (refer to Supplementary Figure 11a for a comparison of the lbFCS/qPAINT performance with respect to individual integers from the visual inspection). Also qPAINT yields a distribution covering the lbFCS and visual results, even for the sample imaged at $c = 20$ nM (as expected from Figure 4b for the regime $N < 6$). In contrast, the qPAINT distribution does not feature clear and distinct peaks. Figure 4e illustrates the counting results for the measurement series on the $N = 12$ structures. Again lbFCS produces counting results which correlate well with the visual counting reference (see Supplementary Figure 11b for integer-wise comparison with visual inspection), both peaking at around $N \approx 10$ and both exhibiting the same distribution shape. However, for qPAINT we obtained a slightly left-shifted distribution even for the sample imaged at $c = 5$ nM, which further increased and broadened for the $c = 10$ and 20 nM samples. As expected from Figure 4b, intensity traces extracted from these samples started to lack enough unique dark times for qPAINT analysis (compare Supplementary Figures 7 and 9. The total number of analyzable clusters in each data set from Figure 4d−f are given in Supplementary Table 1). At last, we imaged the series of samples containing $N = 48$ structures (Figure 4f). As can be seen in the top panel, we were able to partially resolve the DSs tightly packed at a 10 nm spacing in the DNA-PAINT images. However, the spatial resolution did not suffice to robustly run the spot detection algorithm earlier employed for the $N = 4$ and $N = 12$ origami for an unbiased visual ground truth. The DS incorporation efficiency leads to a broader spread in the actual number of DSs over all DNA origami structures with increasing N, which is in agreement with a broadening in the distribution of counted DSs by lbFCS compared to the previous DNA origami designs with less DSs. However, for all three imager concentrations lbFCS yielded the same counting results with a median of around $N \approx 25$. Although for the $c = 5$ nM sample the qPAINT results are in relatively good agreement with lbFCS, the distribution for the 10 nM sample is broadened and again shifted to the left due to lacking unique dark times extractable from the respective intensity versus time traces. As expected from Figure 4b, for $c = 20$ nM the DS density of the DNA origami design is already beyond the applicable limit of qPAINT since almost 75% of all clusters did not exhibit a single dark time anymore (see Supplementary Table 1).

Finally, we investigated whether even during the low laser power measurements the effect of photoinduced DS depletion via reactive oxygen species (ROS) generated upon excitation of dye molecules can be observed, as previously described by Blumhardt et al.[26] For the $N = 12$ structure, we repeated the concentration series with fresh samples this time measuring four times longer than a usual low power measurement without the use of an oxygen scavenging and triplet state quenching system (4×30 min). We then temporally segmented the total data set into four subsets and analyzed each subset individually via lbFCS. Supplementary Figure 12a depicts the resulting $\langle\tau\rangle$ versus c dependencies for all segments. We observed no significant difference between the time segments indicating that hybridization rates were unaffected and giving direct evidence that there was no bleaching of the imager solution (i.e., decreasing c) during the course of the 2 h measurement. Bearing this in mind, the clear change in $1/A$ versus c as shown in Supplementary Figure 12b is a direct consequence of the depletion of DSs leading to a decrease in N (compare eq 1). Supplementary Figure 12c shows the counting results over all segments normalized to the value of the first segment for every concentration. For an imager concentration of 20 nM, more than 20% of the DSs were depleted after 2 h of measurement. Furthermore, we observed an increase of the depletion rate with increasing imager concentration which is in agreement with previous results showing that the probability of photo-induced damage scales with the DS occupancy.[26] With respect to the results in Supplementary Figure 12b, this additionally explains why an offset in $1/A$ is becoming apparent for the later segments, as the $1/A$ values of different concentrations already originate from origamis of different N due to different depletion rates.

One of the proposed strategies to circumvent DS depletion is the use of oxygen scavenging systems such as pyranose oxidase, catalase, and glucose (POC) to directly remove ROS from the solution upon generation.[26] We repeated the same extended low power measurement series with POC and Trolox (a commonly used triplet state quencher) added to the imaging buffer. Subsequent lbFCS analysis revealed neither changes in $\langle\tau\rangle$ nor in $1/A$ over the four time segments (Supplementary Figure 12d,e). Hence, usage of oxygen scavenging systems allows one to virtually eliminate DS depletion during the low laser power measurements for lbFCS (Supplementary Figure 12e,f).

In conclusion, we presented lbFCS as an absolute counting approach for DNA-PAINT microscopy in a proof-of-principle study targeting DNA origami structures as ideal samples. On the basis of imaging a target of interest at several imager concentrations, we showed that lbFCS allows the extraction of imager hybridization rates at high precision from target clusters independent of the number of DSs within a cluster, which subsequently serves as calibration for counting of DS numbers within all clusters. We first confirmed the measurement principle on DNA origami exhibiting only a single DS and assayed the measurement uncertainty and the influence of experimental conditions such as temperature and buffer ion concentration. Next, we examined the performance of lbFCS to count the increasing number of DSs per cluster and compared the obtained results to the state-of-the-art DNA-PAINT counting approach qPAINT. We first increased the cluster size in a controlled way by grouping experimentally obtained clusters containing only a single DS into clusters of defined N. The obtained results show that lbFCS yields the correct counts over a range of more than 40 DSs for various imager concentrations in contrast to qPAINT. In addition, the extracted hybridization rates were unaffected by the number of DSs per cluster within the measurement uncertainty. Subsequent experimental benchmarking of lbFCS on DNA origami structures exhibiting multiple DSs yielded counts in good agreement with the visual ground truth obtained from high-resolution images from the respective FOVs. Finally, we could confirm previous results regarding the depletion of DSs in DNA-PAINT.[26] lbFCS is sensitive enough to detect slight changes in N due to depleted DSs and gave direct evidence that neither the hybridization rates nor the "effective" imager concentrations were affected by the employed low laser intensities during image acquisition. The usage of oxygen scavenging systems helped to virtually eliminate the depletion of DSs, underlining the applicability of our approach.

The work presented in this study was based on surface-immobilized DNA origami structures as model targets for DNA-PAINT microscopy. It should be highlighted that in this case all presented counting results here could also be obtained correctly via qPAINT when the imager concentration is adjusted according to the DS density. qPAINT could in principle also deal with samples containing heterogeneous cluster densities by imaging the sample at different imager concentrations. We particularly see the strength of lbFCS in future applications to DNA-PAINT data of biological samples, where it might be hard to identify enough single DSs for a robust calibration of the qPAINT influx rate. Additionally, local factors such as charge differences or steric hindrance effects introduced, for example, by the labeling linker to the target molecule, might lead to changes in the imager association rate limiting the applicability of the calibration rate obtained from DSs on DNA origami. While lbFCS could potentially solve these problems, the way toward cellular samples bears several difficulties that still remain to be tested. These include, among others, the effects of elevated background fluorescence, robust cluster identification and demands on achievable spatial resolution. We further would like to point out that lbFCS in its current state relies on the identification of spatially well-separated clusters and is hence not applicable to continuous structures (e.g., filaments).

Despite the focus on molecular counting presented here, the scope of lbFCS essentially exceeds the study of specific DNA–DNA interactions as in DNA-PAINT. We see promising applications translating the high precision of lbFCS to study specific and reversible DNA–protein and protein–protein interactions with one of the species immobilized on a surface. In addition, lbFCS could also find application in structural in vitro studies to count subunits of immobilized multimeric complexes.

When targeting fixed cells, however, future work needs to address possible local changes in DNA hybridization rates, which might lead to large deviations between DSs and clusters. A next step in this direction will be combining lbFCS with Exchange-PAINT[40] in order to acquire the imager concentration series at the same FOV of a sample, potentially providing access to local changes in hybridization rates and allowing direct calibration with the cluster-specific rates for more robust counting. Finally, the same FOV would be imaged at high laser intensity for obtaining a DNA-PAINT image at highest spatial resolution. Complementing high-resolution DNA-PAINT images with an additional layer of robust quantitative information obtained via lbFCS has the potential to move the technology away from artificial or well-studied structures toward physiologically relevant targets and, ultimately, biological discovery.

■ ASSOCIATED CONTENT

Ⓢ Supporting Information

The Supporting Information is available free of charge on the ACS Publications website at DOI: 10.1021/acs.nanolett.9b03546.

Supplementary methods and figures (PDF)

■ AUTHOR INFORMATION

Corresponding Author

*E-mail: schwille@biochem.mpg.de.

ORCID

Johannes Stein: 0000-0002-1335-1120
Florian Schueder: 0000-0003-3412-5066
Jonas Mücksch: 0000-0002-1469-6956
Ralf Jungmann: 0000-0003-4607-3312
Petra Schwille: 0000-0002-6106-4847

Author Contributions

J.S., F.Stehr, R.J., and P.Schwille conceived the study. J.S. designed and performed the experiments, analyzed and interpreted the data, and wrote the manuscript. F.Stehr designed and performed the experiments, analyzed and interpreted data, and wrote the manuscript. F.Stehr wrote the code and J.S. edited code. P.Schueler folded DNA origami structures, performed experiments, and analyzed data. P.B., F.Schueder and J.M. performed initial experiments and interpreted the data. R.J. and P.Schwille supervised the study. All authors revised the manuscript and have given approval to the final version of the manuscript.

Author Contributions

§J.S. and F. Stehr contributed equally.

Funding

This work has been supported in part by the German Research Foundation through the Emmy Noether Program (DFG JU 2957/1-1 to R.J.), the SFB1032 (projects A11 and A09 to R.J. and P. Schwille), the European Research Council through an ERC Starting Grant (MolMap; Grant Agreement 680241 to R.J.) and the Max Planck Society (P.Schwille and R.J.).

Notes

The authors declare no competing financial interest.

■ ACKNOWLEDGMENTS

We thank Julian Bauer, Tamara Heermann, Henri Franquelim, Sigrid Bauer, and Katharina Nakel for experimental assistance and helpful discussions. J.S. and F. Stehr acknowledge support from Graduate School of Quantitative Bioscience Munich (QBM). P.B. and J.M. acknowledge support from the International Max Planck Research School for Molecular and Cellular Life Sciences (IMPRS-LS). All authors acknowledge support from the Center for Nano Science (CeNS).

■ ABBREVIATIONS

SMLM, single-molecule localization microscopy; (q)PAINT, (quantitative) points accumulation for imaging in nanoscale topography; DS, docking strand; FCS, fluorescence correlation spectroscopy; lbFCS, localization-based FCS; TIRF, total internal reflection fluorescence; SI-FCS, surface-integrated FCS; FOV, field of view; ROS, reactive oxygen species; POC, pyranose oxidase, catalase, and glucose

■ REFERENCES

(1) Hell, S. W.; Wichmann, J. Breaking the diffraction resolution limit by stimulated emission: stimulated-emission-depletion fluorescence microscopy. *Opt. Lett.* **1994**, *19*, 780–782.

(2) Hell, S. W.; et al. The 2015 super-resolution microscopy roadmap. *J. Phys. D: Appl. Phys.* **2015**, *48*, 443001.

(3) Rust, M. J.; Bates, M.; Zhuang, X. Sub-diffraction-limit imaging by stochastic optical reconstruction microscopy (STORM). *Nat. Methods* **2006**, *3*, 793.

(4) Betzig, E.; et al. Imaging Intracellular Fluorescent Proteins at Nanometer Resolution. *Science (Washington, DC, U. S.)* **2006**, *313*, 1642–1645.

(5) Sharonov, A.; Hochstrasser, R. M. Wide-field subdiffraction imaging by accumulated binding of diffusing probes. *Proc. Natl. Acad. Sci. U. S. A.* **2006**, *103*, 18911–18916.

(6) Schnitzbauer, J.; Strauss, M. T.; Schlichthaerle, T.; Schueder, F.; Jungmann, R. Super-resolution microscopy with DNA-PAINT. *Nat. Protoc.* **2017**, *12*, 1198.

(7) Baddeley, D.; Bewersdorf, J. Biological Insight from Super-Resolution Microscopy: What We Can Learn from Localization-Based Images. *Annu. Rev. Biochem.* **2018**, *87*, 965–989.

(8) Nicovich, P. R.; Owen, D. M.; Gaus, K. Turning single-molecule localization microscopy into a quantitative bioanalytical tool. *Nat. Protoc.* **2017**, *12*, 453.

(9) Annibale, P.; Vanni, S.; Scarselli, M.; Rothlisberger, U.; Radenovic, A. Quantitative Photo Activated Localization Microscopy: Unraveling the Effects of Photoblinking. *PLoS One* **2011**, *6*, No. e22678.

(10) Annibale, P.; Vanni, S.; Scarselli, M.; Rothlisberger, U.; Radenovic, A. Identification of clustering artifacts in photoactivated localization microscopy. *Nat. Methods* **2011**, *8*, 527.

(11) Hummer, G.; Fricke, F.; Heilemann, M. Model-independent counting of molecules in single-molecule localization microscopy. *Mol. Biol. Cell* **2016**, *27*, 3637–3644.

(12) Laplante, C.; Huang, F.; Tebbs, I. R.; Bewersdorf, J.; Pollard, T. D. Molecular organization of cytokinesis nodes and contractile rings by super-resolution fluorescence microscopy of live fission yeast. *Proc. Natl. Acad. Sci. U. S. A.* **2016**, *113*, E5876–LP-E5885.

(13) Nino, D.; Rafiei, N.; Wang, Y.; Zilman, A.; Milstein, J. N. Molecular Counting with Localization Microscopy: A Bayesian Estimate Based on Fluorophore Statistics. *Biophys. J.* **2017**, *112*, 1777–1785.

(14) Golfetto, O.; et al. A Platform To Enhance Quantitative Single Molecule Localization Microscopy. *J. Am. Chem. Soc.* **2018**, *140*, 12785−12797.

(15) Coltharp, C.; Kessler, R. P.; Xiao, J. Accurate Construction of Photoactivated Localization Microscopy (PALM) Images for Quantitative Measurements. *PLoS One* **2012**, *7*, No. e51725.

(16) Lee, S.-H.; Shin, J. Y.; Lee, A.; Bustamante, C. Counting single photoactivatable fluorescent molecules by photoactivated localization microscopy (PALM). *Proc. Natl. Acad. Sci. U. S. A.* **2012**, *109*, 17436−17441.

(17) Nan, X.; et al. Single-molecule superresolution imaging allows quantitative analysis of RAF multimer formation and signaling. *Proc. Natl. Acad. Sci. U. S. A.* **2013**, *110*, 18519−18524.

(18) Puchner, E. M.; Walter, J. M.; Kasper, R.; Huang, B.; Lim, W. A. Counting molecules in single organelles with superresolution microscopy allows tracking of the endosome maturation trajectory. *Proc. Natl. Acad. Sci. U. S. A.* **2013**, *110*, 16015−16020.

(19) Ehmann, N.; et al. Quantitative super-resolution imaging of Bruchpilot distinguishes active zone states. *Nat. Commun.* **2014**, *5*, 4650.

(20) Fricke, F.; Beaudouin, J.; Eils, R.; Heilemann, M. One, two or three? Probing the stoichiometry of membrane proteins by single-molecule localization microscopy. *Sci. Rep.* **2015**, *5*, 14072.

(21) Ricci, M. A.; Manzo, C.; García-Parajo, M. F.; Lakadamyali, M.; Cosma, M. P. Chromatin Fibers Are Formed by Heterogeneous Groups of Nucleosomes In Vivo. *Cell* **2015**, *160*, 1145−1158.

(22) Rollins, G. C.; Shin, J. Y.; Bustamante, C.; Pressé, S. Stochastic approach to the molecular counting problem in superresolution microscopy. *Proc. Natl. Acad. Sci. U. S. A.* **2015**, *112*, E110−LP-E118.

(23) Jungmann, R.; et al. Quantitative super-resolution imaging with qPAINT. *Nat. Methods* **2016**, *13*, 439.

(24) Nikić, I.; et al. Debugging Eukaryotic Genetic Code Expansion for Site-Specific Click-PAINT Super-Resolution Microscopy. *Angew. Chem., Int. Ed.* **2016**, *55*, 16172−16176.

(25) Stehr, F.; Stein, J.; Schueder, F.; Schwille, P.; Jungmann, R. Flat-top TIRF illumination boosts DNA-PAINT imaging and quantification. *Nat. Commun.* **2019**, *10*, 1268.

(26) Blumhardt, P. Photo-Induced Depletion of Binding Sites in DNA-PAINT Microscopy. *Molecules* **2018**, *23*, 3165.

(27) Deschout, H.; et al. Precisely and accurately localizing single emitters in fluorescence microscopy. *Nat. Methods* **2014**, *11*, 253.

(28) Magde, D.; Elson, E.; Webb, W. W. Thermodynamic Fluctuations in a Reacting System—Measurement by Fluorescence Correlation Spectroscopy. *Phys. Rev. Lett.* **1972**, *29*, 705−708.

(29) Eigen, M.; Rigler, R. Sorting single molecules: application to diagnostics and evolutionary biotechnology. *Proc. Natl. Acad. Sci. U. S. A.* **1994**, *91*, 5740−5747.

(30) Rothemund, P. W.; Folding, K. DNA to create nanoscale shapes and patterns. *Nature* **2006**, *440*, 297.

(31) Mücksch, J.; et al. Quantifying Reversible Surface Binding via Surface-Integrated Fluorescence Correlation Spectroscopy. *Nano Lett.* **2018**, *18*, 3185−3192.

(32) Jungmann, R.; et al. Single-Molecule Kinetics and Super-Resolution Microscopy by Fluorescence Imaging of Transient Binding on DNA Origami. *Nano Lett.* **2010**, *10*, 4756−4761.

(33) Steinhauer, C.; Jungmann, R.; Sobey, T. L.; Simmel, F. C.; Tinnefeld, P. DNA Origami as a Nanoscopic Ruler for Super-Resolution Microscopy. *Angew. Chem., Int. Ed.* **2009**, *48*, 8870−8873.

(34) Thompson, N. L.; Burghardt, T. P.; Axelrod, D. Measuring surface dynamics of biomolecules by total internal reflection fluorescence with photobleaching recovery or correlation spectroscopy. *Biophys. J.* **1981**, *33*, 435−454.

(35) Starr, T. E.; Thompson, N. L. Total Internal Reflection with Fluorescence Correlation Spectroscopy: Combined Surface Reaction and Solution Diffusion. *Biophys. J.* **2001**, *80*, 1575−1584.

(36) Howorka, S.; Movileanu, L.; Braha, O.; Bayley, H. Kinetics of duplex formation for individual DNA strands within a single protein nanopore. *Proc. Natl. Acad. Sci. U. S. A.* **2001**, *98*, 12996−13001.

(37) Dupuis, N. F.; Holmstrom, E. D.; Nesbitt, D. J. Single-molecule kinetics reveal cation-promoted DNA duplex formation through ordering of single-stranded helices. *Biophys. J.* **2013**, *105*, 756−766.

(38) Ouldridge, T. E.; Šulc, P.; Romano, F.; Doye, J. P. K.; Louis, A. A. DNA hybridization kinetics: Zippering, internal displacement and sequence dependence. *Nucleic Acids Res.* **2013**, *41*, 8886−8895.

(39) Strauss, M. T.; Schueder, F.; Haas, D.; Nickels, P. C.; Jungmann, R. Quantifying absolute addressability in DNA origami with molecular resolution. *Nat. Commun.* **2018**, *9*, 1600.

(40) Jungmann, R.; et al. Multiplexed 3D cellular super-resolution imaging with DNA-PAINT and Exchange-PAINT. *Nat. Methods* **2014**, *11*, 313.

Supporting Information

Towards absolute molecular numbers in DNA-PAINT

Johannes Stein[†,‡], Florian Stehr[†,‡], Patrick Schueler[†], Philipp Blumhardt[†], Florian Schueder[†,§], Jonas Mücksch[†], Ralf Jungmann[†,§] and Petra Schwille[†,*]

[†]Max Planck Institute of Biochemistry, 82152 Martinsried near Munich, Germany.
[§]Faculty of Physics, Ludwig Maximilian University, 80539 Munich, Germany.

Supplementary Methods	
Supplementary Figure 1	**Step-by-step guide through lbFCS analysis**
Supplementary Figure 2	**Custom-built TIRF microscope and laser power series**
Supplementary Figure 3	**Filtering out clusters whose intensity vs. time traces exhibit flawed dynamics**
Supplementary Figure 4	**Unspecific surface binding interactions**
Supplementary Figure 5	**1DS counting results for lbFCS at varying temperature and MgC_2 concentration**
Supplementary Figure 6	**Self-calibrating counting independent of absolute imager concentration**
Supplementary Figure 7	**The qPAINT approach**
Supplementary Figure 8	**qPAINT calibration from single docking strands**
Supplementary Figure 9	**N_{out} vs. N_{in} at varying imager concentrations**
Supplementary Figure 10	**Simultaneous binding in dense clusters limits qPAINT**
Supplementary Figure 11	**N_{out} vs. N_{vis} comparison per integer from visual counting results**
Supplementary Figure 12	**Depletion of docking strands for DNA-PAINT imaging at low laser power**
Supplementary Table 1	**Total number of analyzed clusters for lbFCS/qPAINT counting**
Supplementary Table 2	**Used DNA-PAINT sequences**
Supplementary Table 3	**Parameters for analysis steps**

Supplementary methods

Materials

Unmodified, dye-labeled, and biotinylated DNA oligonucleotides were purchased from MWG Eurofins. DNA scaffold strands were purchased from Tilibit (p7249, identical to M13mp18). Streptavidin was purchased from Thermo Fisher (cat: S-888). BSA-Biotin was obtained from Sigma-Aldrich (cat: A8549). Glass slides were ordered from Thermo Fisher (cat: 10756991) and coverslips were purchased from Marienfeld (cat: 0107032). Freeze 'N Squeeze columns were ordered from Bio-Rad (cat: 732-6165). Tris 1M pH 8.0 (cat: AM9856), EDTA 0.5M pH 8.0 (cat: AM9261), Magnesium 1M (cat: AM9530G) and Sodium Chloride 5M (cat: AM9759) were ordered from Ambion. Ultrapure water (cat: 10977-035) was purchased from Thermo Fisher Scientific. Tween-20 (cat: P9416-50ML), Glycerol (cat. 65516-500ml) and (+-)-6-Hydroxy-2,5,7,8-tetra-methylchromane-2-carboxylic acid (Trolox) (cat: 238813-5G) were purchased from Sigma-Aldrich. Two-component epoxy glue (cat: 886519 - 62) was purchased from Conrad Electronic SE.

Buffers

Four buffers were used for sample preparation and imaging: Buffer A+ (10 mM Tris-HCl pH 7.5, 100 mM NaCl, 0.05% Tween 20, pH 7.5); Buffer B+ (5 mM Tris-HCl pH 8.0, 10 mM MgCl2, 1 mM EDTA, 0.05% Tween 20, pH 8); Enzyme buffer for POC oxygen scavenging system (10 mM Tris pH 7.5, 50 mM KCl, 20% glycerol); 10x folding buffer (100 mM Tris,10 mM EDTA pH 8.0, 125 mM MgCl2).

DNA origami design, assembly and purification

DNA origami structures were designed using the design module of Picasso[1] (see **Figure 4**, top for docking strand positions). Folding of structures was performed using the following components: single-stranded DNA scaffold (0.01 µM), core staples (0.5 µM), biotin staples (0.5 µM), modified staples (each 0.5 µM), 1× folding buffer in a total of 50 µl for each sample. Annealing was done by cooling the mixture from 80 to 25 °C in 3 h in a thermocycler. Structures were purified using gel electrophoresis (3 h at 60 V). For detailed instructions see[1,2].

DNA origami sample preparation

DNA origami samples were prepared as described before[1]. A glass slide was glued onto a coverslip with the help of double-sided tape (Scotch, cat. no. 665D) to form a flow chamber with inner volume of ~20 µl. First, 20 µl of biotin-labeled bovine albumin (1 mg/ml, dissolved in buffer A+) was flushed into the chamber and incubated for 3 min. The chamber was then washed with 40 µl of buffer A+. 20 µl of streptavidin (0.5 mg/ml, dissolved in buffer A+) was then flushed through the chamber and incubated for 3 min. After washing with 40 µl of buffer A+ and subsequently with 40 µl of buffer B+, 20 µl of biotin-labeled DNA structures (dilution from DNA origami stock dependent on origami yield after gel purification. Adjusted for each origami species individually to obtain sparse DNA origami surface density. Starting dilution ~1:4) were flushed into the chamber and incubated for 10 min. The chamber was washed with 40 µl of buffer B+. Finally, 40 µl of the imager solution was flushed into the chamber, which was subsequently sealed with two-component epoxy glue before imaging. Adjustment of imager concentrations: The imager concentrations used for all experiments were c = 5, 10 and 20 nM. As described in **Supplementary Figure 6**, we first prepared a larger volume of 20 nM imager solution, from which in two subsequent 1:1 dilution steps the 10 nM and 5 nM solutions were prepared. Sequence design of imager and docking strands can be found in **Supplementary Table 2**.

Super-resolution microscopy setup

Fluorescence imaging was carried out on an inverted custom-built microscope[3] (see setup sketch in **Supplementary Figure 2**a) in an objective-type TIRF configuration with an oil-immersion objective (Olympus UAPON, 100×, NA 1.49). One laser was used for excitation: 561 nm (1 W, DPSS-system, MPB). Laser power was adjusted by polarization rotation with a half-wave plate (Thorlabs, WPH05M-561) before passing a polarizing beam-splitter cube (Thorlabs, PBS101). To spatially clean the beam-profile the laser light was coupled into a single-mode polarization-maintaining fiber (Thorlabs, P3-488PM-FC-2) using an aspheric lens (Thorlabs, C610TME-A). The coupling polarization into the fiber was adjusted using a zero-order half wave plate (Thorlabs, WPH05M-561). The laser light was re-collimated after the fiber using an achromatic doublet lens (Thorlabs, AC254-050-A-ML) resulting in a collimated FWHM beam diameter of ~6 mm. The Gaussian laser beam profile was transformed into a collimated flat-top profile using a refractive beam shaping device (AdlOptica, piShaper 6_6_VIS). The laser beam diameter was magnified by a factor of 2.5 using a custom-built telescope (Thorlabs, AC254-030-A-ML and Thorlabs, AC508-075-A-ML). The laser light was coupled into the microscope objective using an achromatic doublet lens (Thorlabs, AC508-180-A-ML) and a dichroic beam splitter (AHF, F68-785). Fluorescence light was spectrally filtered with a laser notch filter (AHF, F40-072) and a bandpass filter (AHF Analysentechnik, 605/64) and imaged on a sCMOS camera (Andor, Zyla 4.2) without further magnification (Thorlabs, TTL180-A) resulting in an effective pixel size of 130 nm (after 2 × 2 binning). Microscopy samples were mounted into a closed water-based temperature chamber (Okolab, H101-CRYO-BL) on a x-y-z stage (ASI, S31121010FT and ASI, FTP2050) that was used for focusing with the microscope objective being at fixed position. The temperature of the objective was actively controlled using the same water cycle as the temperature chamber. Focus stabilization was achieved via the CRISP autofocus system (ASI @ 850 nm) in a feedback loop with a piezo actuator (Piezoconcept, Z-INSERT100) moving the sample. The CRISP was coupled into the excitation path of the microscope using a long pass dichroic mirror (Thorlabs, DMLP650L). Our custom TIRF setup was used for all Figures.

Imaging conditions

All fluorescence microscopy data was recorded with our sCMOS camera (2048 × 2048 pixels, pixel size: 6.5 µm). The camera was operated with the open source acquisition software µManager[4] at 2x2 binning and cropped to the center 700 × 700 pixel FOV. The exposure time was set to 200 ms, the read out rate to 200 MHz and the dynamic range to 16 bit. For lbFCS measurements the laser power was set to 1.4 mW (see **Supplementary Figure 2**), corresponding to an average intensity of ~10 W/cm^2 over the circular illuminated area of 130 μm in diameter. The acquisition lengths for lbFCS measurements were set to: 9,000 frames (c = 20 & 10 nM) and 18,000 frames (c = 5 nM). Longer acquisition lengths at lower imager concentrations ensure that sufficient imager binding events are registered from each DS cluster as a prerequisite for robust autocorrelation analysis[5]. For high resolution imaging the laser power was set to 70 mW (intensity of ~500 W/cm^2) and the acquisition length to 5,000 frames.

Super-resolution reconstruction & data analysis

Refer to **Supplementary Figure 1** for a detailed step-by-step guide through all processing steps after data acquisition. The lbFCS software package and installation instructions are available at https://github.com/schwille-paint/lbFCS. A full integration in the Picasso[1] software package is currently under construction.

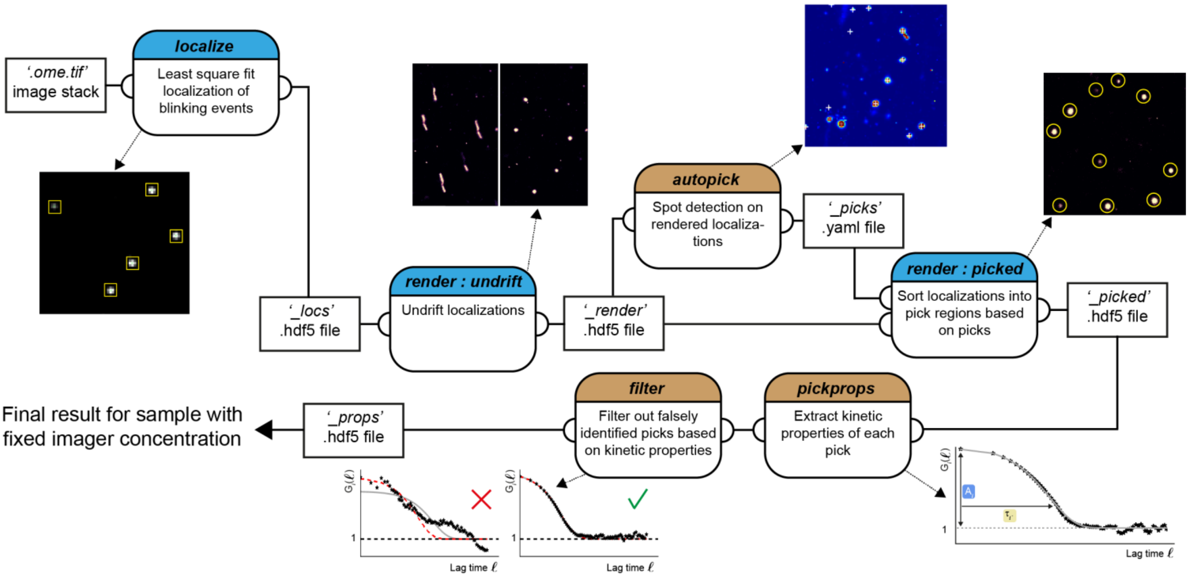
‘.ome.tif’ image stack
localize
Least square fit localization of blinking events
‘_locs’ .hdf5 file
render : undrift
Undrift localizations
‘_render’ .hdf5 file
autopick
Spot detection on rendered localizations
‘_picks’ .yaml file
render : picked
Sort localizations into pick regions based on picks
‘_picked’ .hdf5 file
Final result for sample with fixed imager concentration
‘_props’ .hdf5 file
filter
Filter out falsely identified picks based on kinetic properties
pickprops
Extract kinetic properties of each pick
G(ℓ)
1
Lag time ℓ
A
τ_l

Supplementary Figure 1. Step-by-step guide through lbFCS analysis. (a) Software flow diagram depicting how final autocorrelation analysis result is obtained from DNA-PAINT raw-data. Rectangles represent saved data containing custom file extension and data format. Rounded boxes represent modules from ‘picasso’ python package[1] (blue) (https://github.com/jungmannlab/picasso) or custom python modules (ocher) (see **Supplementary Materials**) with half open circles indicating either input or output files according to flow direction. All additional input parameters of the modules used are listed in **Supplementary Table 3**. For a detailed description on the ‘filter’ module see **Supplementary Figure 3**.

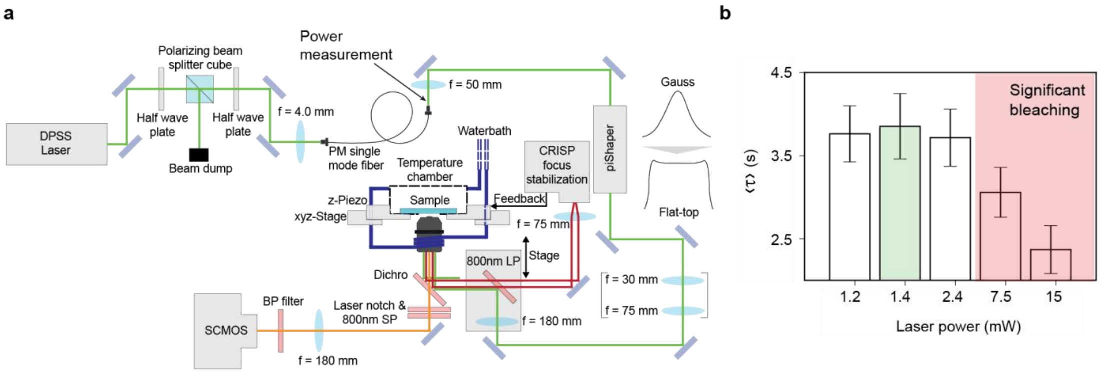
a
b
Power measurement
Polarizing beam splitter cube
DPSS Laser
Half wave plate
Half wave plate
Beam dump
f = 4.0 mm
f = 50 mm
PM single mode fiber
Waterbath
Temperature chamber
CRISP focus stabilization
piShaper
Gauss
Flat-top
z-Piezo
Sample
xyz-Stage
Feedback
f = 75 mm
800nm LP
Stage
Dichro
f = 30 mm
f = 75 mm
SCMOS
BP filter
Laser notch & 800nm SP
f = 180 mm
f = 180 mm
4.5
3.5
2.5
⟨τ⟩ (s)
Significant bleaching
1.2
1.4
2.4
7.5
15
Laser power (mW)

Supplementary Figure 2. Custom-built TIRF microscope and laser power series. (a) Sketch of custom-built TIRF microscope. See Supplementary Methods for details on components. (b). Power series on sample containing single docking strand DNA origami at 21°C (the temperature condition yielding the longest imager residence times, i.e. lowest k_{off}). The laser power was measured after the fiber exit (see (a)). The red area highlights the regime where the laser power is high enough to photobleach the dye molecules of bound imager strands before dissociation which therefore significantly affects the extracted values of $\langle\tau\rangle$. We chose a laser power at ~1.4 mW (green), where we did not affect the extracted rates but were still able to robustly detect fluorescence bursts for super-resolution reconstruction.

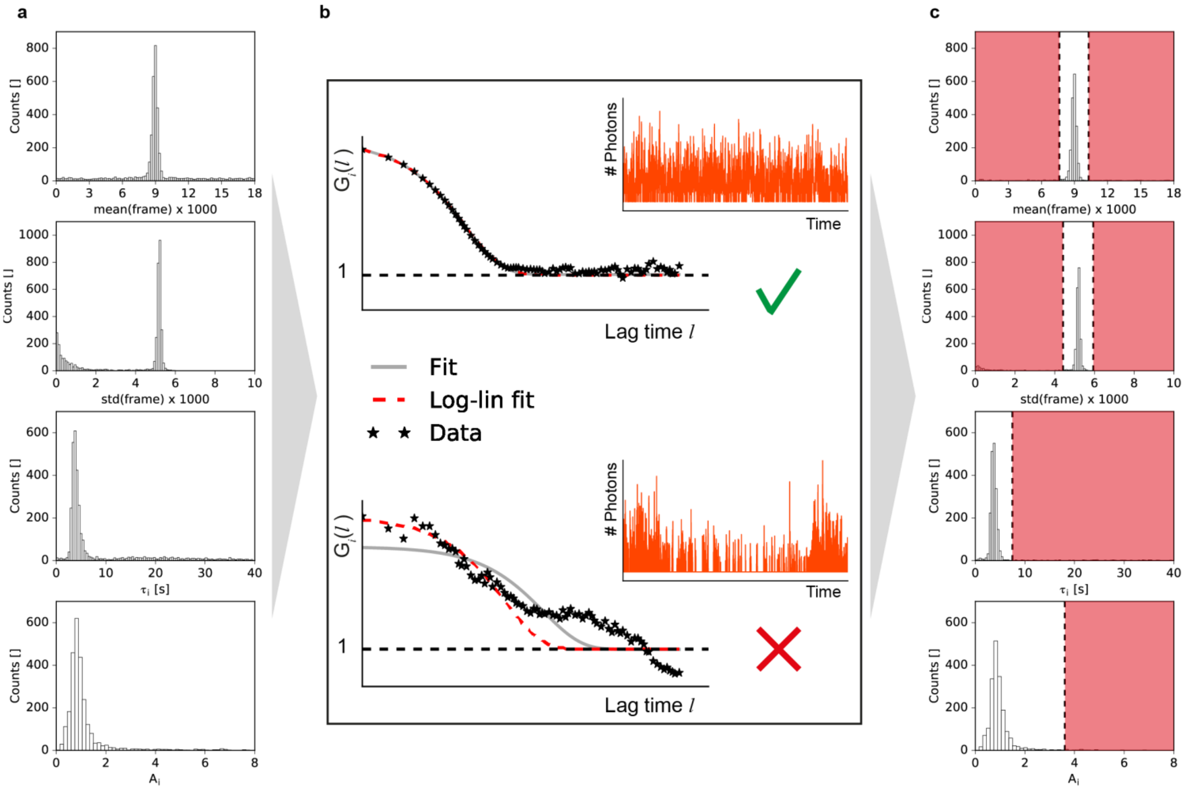

Supplementary Figure 3. Filtering out clusters whose intensity vs. time traces exhibit flawed dynamics. (a) Final distributions of kinetic variables as obtained before 'filter' module (see **Supplementary Figure 1**) over all picks of a sample containing DNA origami with 12 DSs at *c* = 5 nM. The variable mean(frame) and std(frame) refer to the mean (standard deviation) of the timestamp (frame) of all localizations in a pick. (b) The 'pickprops' module (see **Supplementary Figure 1**) applies two fitting procedures to the autocorrelated intensity vs. time trace (black stars): (1) a non-linear least square fit according to the equation $\mathrm{G}_i(l) = \mathrm{A}_i e^{l/\tau_i} + 1$ (gray) and, (2) a linear fit to the logarithmized autocorrelation function using the logarithmic form of the same equation $\log(\mathrm{G}_i(l) - 1) = \mathrm{A}_i + l/\tau_i$ (red dashed). The linearized logarithmic fit does only take into account the first 10 data points of the autocorrelation. In the first filtering step the two different τ_i for each pick obtained by the two fitting approaches are compared. If the value τ_i as resulting by (2) deviates more than 20 % of the value τ_i as resulting by (1) the pick is disregarded for further analysis. The resulting distributions over all picks after this filtering step are shown in (c). In the second filtering step the median over all picks for each of the variables mean(frame), std(frame), τ_i and A_i is calculated. Picks with the following attributes are disregarded for further analysis (indicated by the red area): mean(frame) < 0.85 x median or > 1.15 x median, std(frame) < 0.85 median, τ_i > 2 x median, A_i > 4 x median.

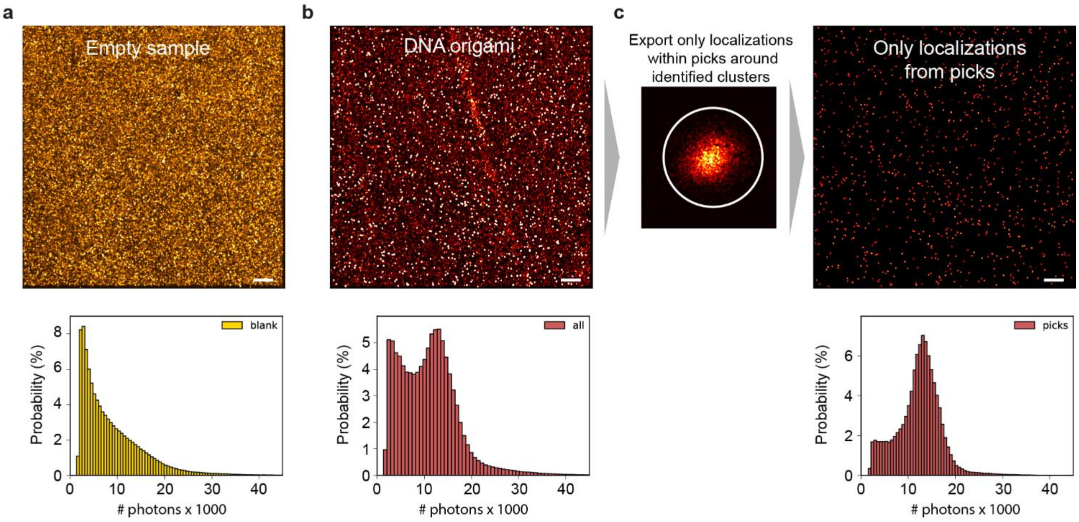

Supplementary Figure 4. Unspecific surface binding interactions. (a) DNA-PAINT image of a surface-passivated sample (BSA-Biotin-Streptavidin, see sample preparation in **Supplementary Methods**) containing no DNA origami but only 10 nM imager in the solution. Unspecific binding of imager to the surface is registered as blinking events leading to a homogeneous distribution of localizations over the surface. The histogram below shows the number of photons counted in each localization event. (b) DNA-PAINT image of sample containing DNA origami acquired under the same conditions as (a). DNA origami appear as bright spots whereas unspecific binding still leads to a homogeneous surface coverage of localizations. The photon count histogram now displays a distinct peak around 13,000 originating from specific binding interactions to DNA origami in addition to the same unspecific distribution as in (a). (c) For further lbFCS analysis we only process localizations within identified localization clusters (picks, white circle, see also **Figure 1**b). The photon count histogram of the localizations from all picks exhibits the same peak as in (b) from specific binding interactions but localizations originating from unspecific binding are minimized. Scale bars, 5 μm.

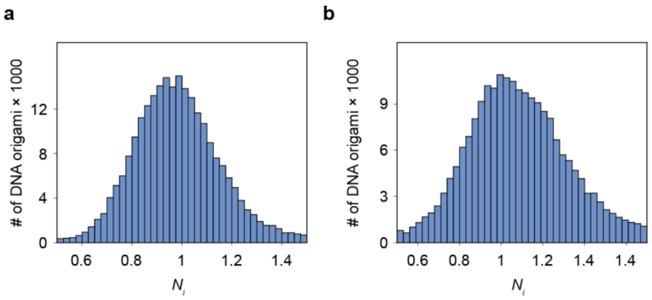

Supplementary Figure 5. 1DS counting results for lbFCS at varying temperature and MgC_2 concentration. (a) Sum of the counting results for lbFCS measurements at 21 - 24 °C (see **Figure 3**a). (b) Sum of the counting results for lbFCS measurements at 5-15 mM $MgCl_2$ (see **Figure 3**b).

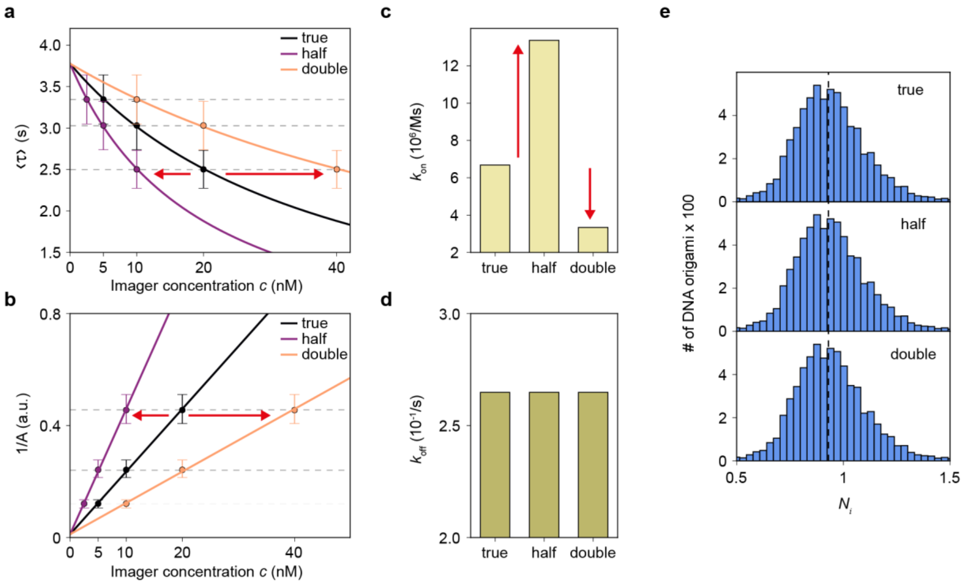

Supplementary Figure 6. Self-calibrating counting independent of absolute imager concentration. (a) As described in the **Supplementary Methods** (sample preparation) we adjusted the imager concentrations to *c* = 5, 10 and 20 nM starting with the highest concentration *c* = 20 nM which we subsequently diluted twice at a ratio 1:1. Here, we illustrate that the counting ability of lbFCS does in fact not depend on the absolute imager concentration. The black ⟨τ⟩ vs. *c* fit shows the results of the lbFCS measurement series on samples containing 1DS origami structures (referred to as "true" due to *c* = 5, 10 and 20 nM). Next, we assume that we actually failed to adjust the first dilution by a factor of 2 to 40 nM instead of 20 nM resulting in a horizontal shift of the three measurement points to the right (red arrow). The orange ⟨τ⟩ vs. *c* curve hence fits the data points at *c* = 10, 20 and 40 nM ("double"). Similarly, we go through the "half" scenario where we started with 10 nM and ended up with 5 and 2.5 nM shifting the data points horizontally to the left (red arrow, purple fit). (b) Same as (a) but for 1/A obtained from the three data sets. As described in the main text, all three fits cross pass through the origin since the concentration ratios are still conserved. (c) k_{on} obtained from the three ⟨τ⟩ vs. *c* fits in (a). The relative offset in the imager concentration *c* inversely translates into an offset in k_{on} (i.e. k_{on} doubles for "half" and halves for "double". See **eq. 2**) (d) k_{off} obtained from the three ⟨τ⟩ vs. *c* fits in (a). k_{off} is unaffected by the introduced offset in *c* (also visible at the identical y-axis intersections in (a). Compare **eq. 2** for *c*→0). (e) lbFCS yields identical counting results (sum N_i over the three measurements displayed) independent of the introduced offset in *c* as it cancels out when multiplied by k_{on}: $N_i = \frac{1}{A_i}\frac{k_{off}}{k_{on}c}$.

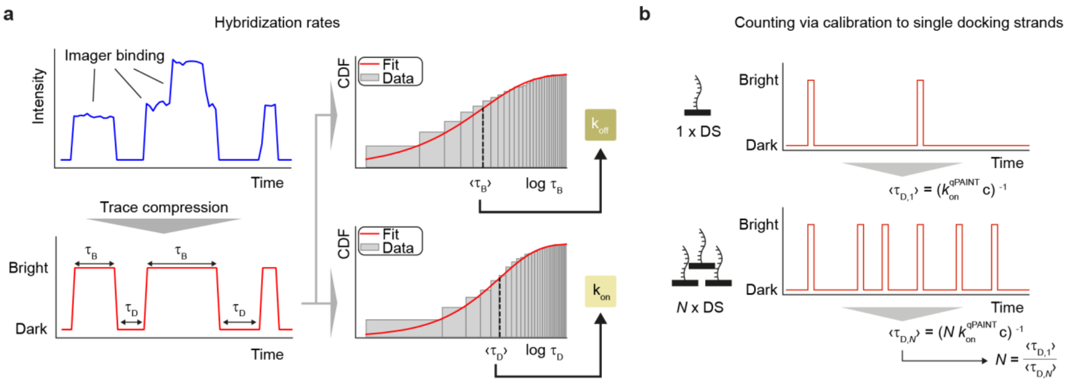
a
Hybridization rates
Imager binding
Intensity
Time
Trace compression
Bright
Dark
τB
τD
Time
CDF
Fit
Data
⟨τB⟩
log τB
koff
CDF
Fit
Data
⟨τD⟩
log τD
kon
b
Counting via calibration to single docking strands
1 x DS
Bright
Dark
Time
⟨τD,1⟩ = (kon^qPAINT c)^-1
N x DS
Bright
Dark
Time
⟨τD,N⟩ = (N kon^qPAINT c)^-1
N = ⟨τD,1⟩ / ⟨τD,N⟩

Supplementary Figure 7. The qPAINT approach. (a) Current standard for extracting imager hybridization kinetics from DNA-PAINT data. The intensity vs. time trace (blue) is compressed into a system of two states (red): i) Bright (bound imager) and ii) Dark (no imager). Here, information regarding simultaneous binding of multiple imagers resulting in higher intensity values is lost. All dwell times in both states, referred to as bright times τ_B and dark times τ_D, are extracted from the compressed trace and processed into cumulative histograms. Short disruptions of fluorescence bursts in the intensity trace (i.e. between two bright times) less than a predefined ‘ignore’ parameter are discarded (i.e. the two bright times a treated as one bright time with the combined duration. Standard: ignore = 1 frame). The histograms are fitted with the fit model[1] $F(\tau_m) = \left(1 - \exp\left(\frac{\tau_m}{\langle\tau_m\rangle}\right)\right) a + b$, where $m = \mathrm{B}, \mathrm{D}$ and the angle brackets denote the mean of the respective distribution. a and b are empirical fit parameters introduced for improved qPAINT counting performance (see implementation at https://github.com/jungmannlab/picasso[1]). In order to apply this fit model with three parameters to an intensity vs. time trace from a localization cluster, the trace needs to exhibit at least three unique dark times (e.g. two dark times of lengths = 2 frames, three dark time of lengths = 5 frames and one dark time of length 11 frames. See **Supplementary Figure 9**). The imager hybridization rates can be obtained via the following relations[1,6,7]: $k_{off} = \langle\tau_\mathrm{B}\rangle^{-1}$ and $k_{on}c = \langle\tau_\mathrm{D}\rangle^{-1}$. (b) Counting with qPAINT relies on calibration to the imager influx rate during a DNA-PAINT measurement obtained from single docking strands (1DS). The influx rate is defined as the inverse mean dark time obtained from a 1DS fluorescence vs. intensity trace $\langle\tau_{\mathrm{D},1}\rangle^{-1} = k_{on}^{qPAINT}c$. qPAINT is based on the assumption that a cluster of *N* DS will produce an intensity vs. time trace with a mean dark time $\langle\tau_{\mathrm{D},N}\rangle$ shortened by a factor of *N* compared to a 1DS. Hence, qPAINT counting results for each localization cluster *i* are obtained via the relation: $N_i = (k_{on}^{qPAINT} c \times \langle\tau_{\mathrm{D},i}\rangle)^{-1} = \langle\tau_{\mathrm{D},1}\rangle / \langle\tau_{\mathrm{D},i}\rangle$.

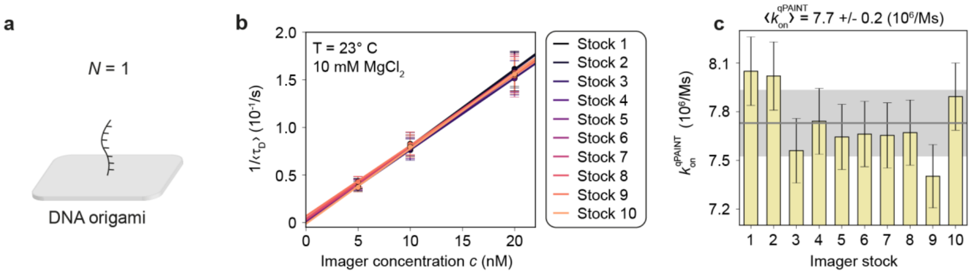

Supplementary Figure 8. qPAINT calibration from single docking strands. (a) For qPAINT calibration we used the measurements obtained on 1DS structures as in **Figure 2**a-e. (b) $1/\langle\tau_\mathrm{D}\rangle$ vs. *c* fit for the 10 concentration series. As defined in **Supplementary Figure 7**, $1/\langle\tau_\mathrm{D}\rangle = k_{on}^{qPAINT}c$ which means that k_{on}^{qPAINT} required for qPAINT calibration can directly be read off the slope of the fit. (c) Scatter in k_{on}^{qPAINT} obtained from fits in (b). Mean and standard deviation are indicated as grey line and light grey area, respectively. The mean of $\langle k_{on}^{qPAINT}\rangle$ = (7.7 ± 0.2 × 10^6) M^{-1}s^{-1} was used as calibration for all qPAINT counting results. We would like to note that the high precision in k_{on}^{qPAINT} is due to profiting from the filtering procedure introduced in **Supplementary Figure 3**, which in turn is based on the unique property of the autocorrelation analysis of lbFCS to identify and exclude docking strands exhibiting flawed dynamics.

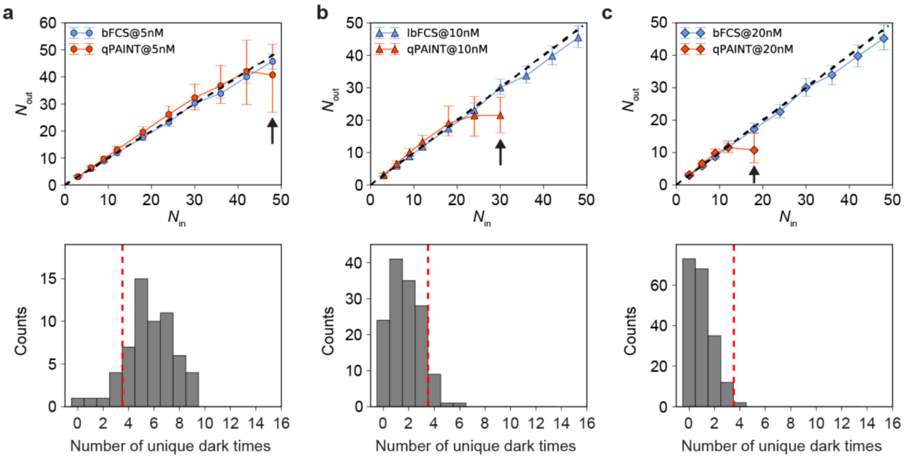

Supplementary Figure 9. N_out vs. N_in at varying imager concentrations. (a) Top: median of the counting results N_out vs. N_in plot comparing the results obtained via qPAINT (red) vs. lbFCS (blue) at *c* = *5* nM as in **Figure 4**b. The black dashed line displays a line through the origin of slope one as expected for ideal counting results (i.e. $N_\mathrm{out} = N_\mathrm{in}$). The first qPAINT data point at *N* = 48 deviating from the ideal behavior is indicated by a black arrow. Bottom: histogram showing the number of unique dark times per intensity vs. time trace for the *N* = 48 qPAINT data point. The dashed red line indicates the minimum of three unique dark times per intensity trace required for the fit described in **Supplementary Figure 7**. In case a trace exhibited less than three unique dark times, we assigned the mean dark time obtained over all fits to the cluster. Clusters, i.e. traces featuring no dark time at all were discarded from further analysis. (b) Top: same as in (a), but for *c* = 10 nM. Bottom: the majority of clusters in the data set indicated by the black arrow at *N* = 30 exhibit less than the required three unique dark times. (c) Same as in (a-b), but for *c* = 20 nM. Histogram of unique dark times displayed for the data point at *N* = 18.

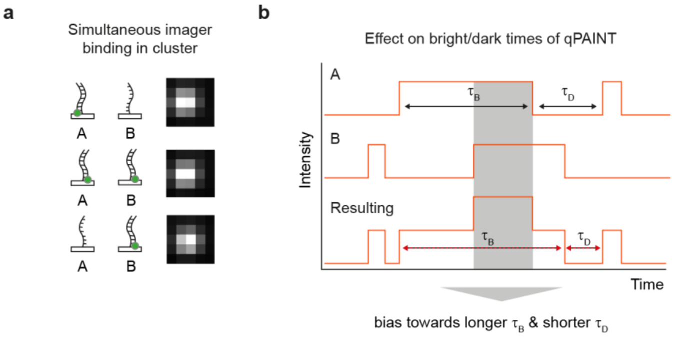
a
Simultaneous imager binding in cluster
A
B
b
Effect on bright/dark times of qPAINT
Intensity
A
B
Resulting
τ_B
τ_D
Time
bias towards longer τ_B & shorter τ_D

Supplementary Figure 10. Simultaneous binding in dense clusters limits qPAINT. (a) Schematic of the case of simultaneous binding of imagers to two docking strands A and B in close proximity. The diffraction limited images indicate an increase in fluorescence intensity when an imager is bound to both docking strands compared to when only a single imager is bound. (b) Individual intensity vs. time traces for DS A and B. The duration of simultaneous binding is shaded in grey. The resulting intensity vs. time trace (bottom) extracted from the localization cluster of the two DSs exhibits an extended bright event and shortened dark event (black-red dashed double arrows) when analyzed according to qPAINT (see **Supplementary Figure 7**). To avoid simultaneous binding events limiting this approach the imager concentration has to be adjusted accordingly to the expected target density.

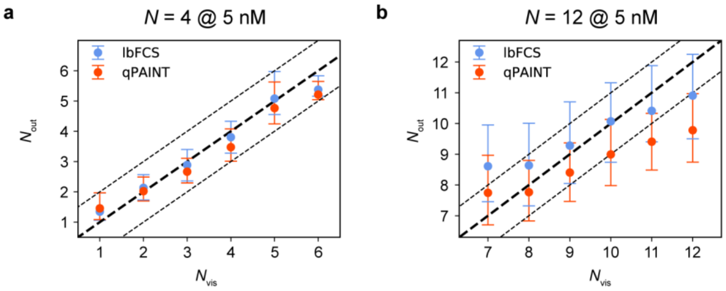

Supplementary Figure 11. N_{out} vs. N_{vis} comparison per integer from visual counting results. (a) lbFCS/qPAINT counting results for the $N = 4$ data set at $c = 5$ nM compared to visual counting results. The bold black line indicates the line through the origin of slope one as expected for ideal counting (i.e. $N_{out} = N_{vis}$). The light black dashed lines indicate a counting error of ± 1. This implies that for each N_{vis} more than 50 % of all clusters fulfill the criterion abs($N_{out} - N_{vis}$) < 1. (b) Same as in (a) but for the $N = 12$ data set at $c = 5$ nM. Error bars correspond to interquartile range.

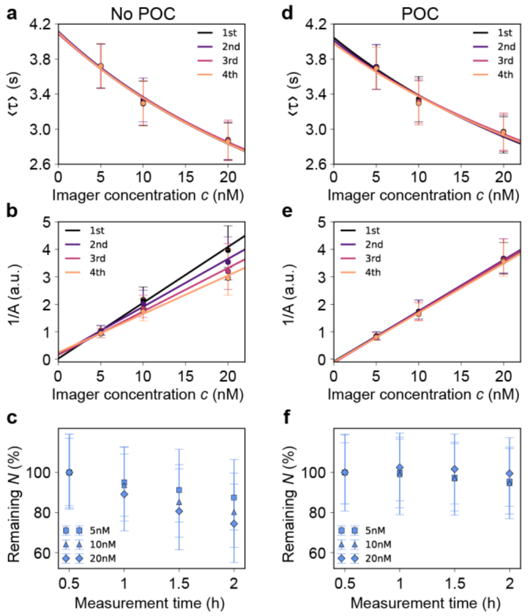

Supplementary Figure 12. Depletion of docking strands for DNA-PAINT imaging at low laser power. (a) Three-point concentration series for DNA origami samples (N = 12) each measured for 2 h (4 × longer than standard lbFCS measurement time). The data sets were temporally divided into 4 segments and each analyzed via lbFCS. The four respective overlapping ⟨τ⟩ vs. c fits yield that neither of the global parameters k_{on}, k_{off} and c changed over the acquisition time. (b) In contrast, the four 1/A vs. c fits clearly change over time as a result of DS depletion occurring even at low laser power. (c) DS depletion rate normalized to the lbFCS counting results from the first segment. (d) Repeat of the same concentration series as in (a) with POC + Trolox added to the imaging solution also indicating constant global parameters over time. (e) In contrast to (b) with POC + Trolox 1/A does also not change over time. (f) Negligible depletion rate of DS for POC + Trolox. Error bars in (c) and (f) correspond to interquartile range.

Supplementary Table 1 | Total number of analyzed clusters for lbFCS/qPAINT counting

N	*c* (nM)	No. of automatically detected clusters	No. of clusters after filtering	No. of clusters after removal of $N_{vis} = 0$	No. of clusters for lbFCS analysis	No. of clusters for qPAINT analysis	Reference
4	5	28,166	12,815	10,963	10,963	10,963	**Figure 4d** (top)
4	10	18,824	6,343	5,245	5,245	5,245	**Figure 4d** (middle)
4	20	24,775	7,399	6,090	6,090	6,090	**Figure 4d** (bottom)
12	5	3,825	1,782	1,781	1,781	1,781	**Figure 4e** (top)
12	10	4,288	1,779	1,778	1,778	1,777	**Figure 4e** (middle)
12	20	3,662	1,200	1,200	1,200	1,171	**Figure 4e** (bottom)
48	5	9,743	3,829	n.a.	3,829	3,822	**Figure 4f** (top)
48	10	3,899	1,653	n.a.	1,653	1,496	**Figure 4f** (middle)
48	20	9,949	1,584	n.a.	1,584	419	**Figure 4f** (bottom)

Supplementary Table 2 | Used DNA-PAINT sequences

Shortname (docking strand length)	Docking strand sequence	Imager sequence	Experiment
PS6 (8 nt)	TT TCCTCCTC	GAGGAGGA-Cy3b	All experiments

Supplementary Table 3 | Parameters for analysis steps

Module	Parameters
localize	Net gradient = 400 Quantum efficiency = 0.82 (from Camera Specs) Sensitivity = 0.53 (from Camera Specs) Box size = 5 pixel Background = 70
render : undrift	No of segments for RCC drift correction: 500
autopick	Oversampling = 5 Net gradient = 300
render : picked	Pick diameter = 2 pixel
pickprops	Ignore = 1 (for qPAINT analysis, see **Supplementary Figure 7**)
filter	n.a.

Supplementary references

1. Schnitzbauer, J., Strauss, M. T., Schlichthaerle, T., Schueder, F. & Jungmann, R. Super-resolution microscopy with DNA-PAINT. *Nat. Protoc.* **12**, 1198 (2017).
2. Strauss, M. T., Schueder, F., Haas, D., Nickels, P. C. & Jungmann, R. Quantifying absolute addressability in DNA origami with molecular resolution. *Nat. Commun.* **9**, 1600 (2018).
3. Stehr, F., Stein, J., Schueder, F., Schwille, P. & Jungmann, R. Flat-top TIRF illumination boosts DNA-PAINT imaging and quantification. *Nat. Commun.* **10**, 1268 (2019).
4. Edelstein, A. D. *et al.* Advanced methods of microscope control using μManager software. *J. Biol. Methods; Vol 1, No 2* (2014).
5. Mücksch, J. *et al.* Quantifying Reversible Surface Binding via Surface-Integrated Fluorescence Correlation Spectroscopy. *Nano Lett.* **18**, 3185–3192 (2018).
6. Jungmann, R. *et al.* Single-Molecule Kinetics and Super-Resolution Microscopy by Fluorescence Imaging of Transient Binding on DNA Origami. *Nano Lett.* **10**, 4756–4761 (2010).
7. Jungmann, R. *et al.* Quantitative super-resolution imaging with qPAINT. *Nat. Methods* **13**, 439 (2016).

Part III

Additional Results and Discussion

7

Advancing Localization-Based Fluorescence Correlation Spectroscopy

7.1 Introduction

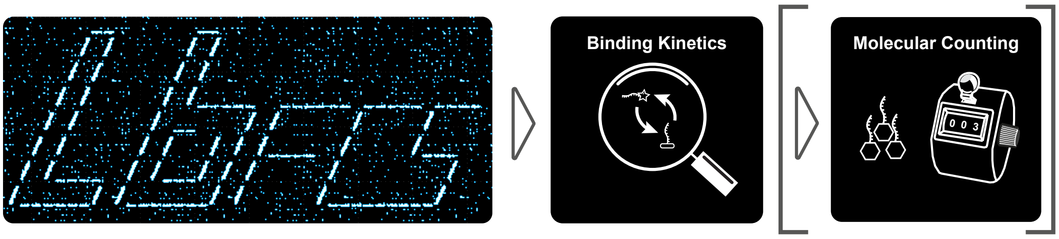

Figure 7.1. Generalization of the Concept of lbFCS. Primarily, lbFCS is a method to precisely measure the binding kinetics of ligand-receptor interactions. Optionally, the measured binding rates can be used downstream for molecular counting of receptor copy numbers.

In Chapter 6, we demonstrated the first experimental application of lbFCS in combination with DNA-PAINT. Our main focus in this first study was targeted at a fundamental problem in the field of quantiative SMLM: translating the number of localizations in a super-resolved SMLM image into actual copy numbers of target molecules [43, 105]. While addressing the SMLM counting problem was in fact our main motivation when developing the method in the first place, it is important to abstract lbFCS from this specialized context in hindsight. The two-step workflow of lbFCS can be generalized as i) measuring the binding kinetics of ligand-receptor interactions (mimicked by DNA hybridization in [97]) and ii) using the obtained rates for absolute counting of receptor numbers (mimicked by docking strands in [97]). In this generalized wording, it becomes immediately clear that the second step is fully optional in case one solely intends to determine the binding kinetics of a system of interest (see schematic in Fig. 7.1). In fact, characterization of ligand-receptor interactions plays a pivotal role in the life sciences, not only in fundamental biological research, but also in drug development [120–123].

The purpose of this chapter is, therefore, to equally stress the applicability of lbFCS as a tool for affinity studies with a potentially larger interest group besides its specialized application for molecular counting. In the first section, we revisit the current workflow of measuring binding kinetics with lbFCS and optimize it with respect to the number of used samples and measurement time (on the model system of DNA hybridization), achieving a 4× improvement from over currently 3 h to only 50 min without a loss in measurement precision. In the second section, we focus on developments of lbFCS with respect to molecular counting in combination with DNA-PAINT. We present an improved direct counting framework without relying on the absolute imager concentrations and validate the approach *in silico* and *in vitro* using DNA origami. Furthermore, we demonstrate that lbFCS allows molecular counting even in a single sample by repeatedly exchanging the imaging buffer. The second section ends with the first cellular counting application of lbFCS, targeting nucleoporins in the nuclear pore complex of fixed human U2OS cells. The chapter closes with an overview of both the overall potential and the possible pitfalls of both applications of lbFCS with respect to rate determination and molecular counting.

7.2 Measuring Bimolecular Binding Rates at the Single Molecule Level

The rates at which biological interactions and dynamics occur are crucial parameters for understanding the fundamental processes of living systems and for devising strategies in targeting a multitude of diseases. Prominent examples are the turnover rate of an enzyme onto its substrate, the affinity at which an antibody binds its antigen or receptor-ligand interactions. Overall, they comprise all combinations of interactions between the constituting molecular families of living systems (i.e., proteins, nucleic acids, sugars and lipids), but also the effects of exogenous substances such as drugs and toxins on any of these biomolecules. Both the plethora and the complexity of these interactions have led to the development of a multitude of experimental approaches and techniques, allowing to characterize the type of interaction, overall affinities and, partially, also the underlying individual reaction rates. Approaches include biochemical affinity-based separation methods such as electrophoretic mobility shift assays [124], enzyme-linked immunosorbent assays [125] or affinity chromatography [126, 127]. Technically more elaborate biophysical approaches comprise FCS [15, 69, 70] and TIR-FCS [40, 74, 78, 128, 129], isothermal titration calorimetry[130–132], capillary electrophoresis [133–135], quartz crystal microbalance [136, 137], microscale thermophoresis [138–140], stopped-flow analysis [141–143] or surface plasmon resonance [144–146].

Considering that this long list is not even exhaustive, a detailed discussion of individual advantages or disadvantages of one method over the other is beyond the scope of this thesis. Generally, these methods can find complimentary applications in studying biomolecular interactions, and commonly the choice is determined by practical factors such as required sample volume, label-free detection ability, speed and precision of the measurement, the interaction type and whether it is sufficient to measure the dissociation constant K_D or also the underlying reaction rates. Even more pragmatically, the method of choice is determined by infrastructure accessibility and essentially the degree of available and/or required training.

While all of these methods have been succesfully applied in countless studies and have become standard tools in life science research, they all have one common peculiarity: they rely on ensemble measurements with the implication that potential heterogenities in and the stochastic nature of the interaction of interest are concealed in the averaged readout. Furthermore, the readout of an averaged interaction analysis bears potential risks of additional unwanted components biasing the targeted interaction without notice. Parallelized single molecule detection schemes, in contrast, allow to directly observe thousands of interacting molecules in parallel, not only providing sufficient statistics for precise ensemble descriptions, but even access down to single stochastic events [121, 122, 147]. Furthermore, nonspecific adsorption, particularly occuring for surface-based methods, can be efficiently excluded from analysis [97, 148]. Prominent approaches allowing a parallelized single molecule readout include zero-mode waveguides [149–151], nanopores [95, 152], FRET sensors [147, 153], magnetic tweezers [154–156], high-speed atomic force spectroscopy [157–159] and SMLM [36, 160–162].

SMLM-based approaches typically assay bimolecular interactions via immobilization of one binding partner on the surface of a glass slide to which its fluorescently-labeled and freely-diffusing partner molecule can bind [36, 160, 163]. While SMLM generally poses the requirement of a fluorescent label, possibly altering the interaction between the two molecules of interest, also label-free detection schemes have been proposed exploiting the competitive interaction between the fluorescently-labeled molecule and its unlabeled counterpart [164]. Monitoring thousands of molecules in parallel (typically via TIRF microscopy) allows to cumulate the dwell time distributions of both the bound state and the unbound state. As described in Chapter 2, from these one can directly calculate k_{on} and k_{off}.

With lbFCS we have introduced an alternative analysis approach for reading out the hybridization rates from SMLM-based surface-binding data. The main advantage of lbFCS is that it allows to obtain k_{on} and k_{off} independent of the number of immobilized target molecules within a localization cluster [97]. However, even for well-seperated individual target molecules lbFCS can be advantageous over a dwell-time-based analysis. First, dwell-time analysis typically relies on discarding short interruptions in the fluorescence traces by a so-called 'ignore' parameter [36], shifting the measured k_{off} to lower values. Furthermore, missing short binding events below the detection threshold/sampling rate can result in longer dark times in between events decreasing the measured k_{on} [165]. In contrast, lbFCS constitutes an unambiguous analysis framework without requiring to manually choose analysis parameters (such as the ignore parameter) in order to obtain both k_{on} and k_{off} [97]. Furthermore, lbFCS offers additional filtering capabilities to identify and exclude target molecules which exhibit improper binding interactions [97]. In the following section, we review the current workflow of lbFCS for quantifying bimolecular interactions, explore the optimization potential with respect to sample preparation and data acquisition and summarize our findings in the context of possible next steps.

7.2.1 The Current lbFCS Workflow

In Fig. 7.2 the current workflow of how to measure binding kinetics with lbFCS is depicted. As in Chapter 6, we follow the example of DNA origami labeled with a single docking strand ('1DS'). In order to determine k_{on} and k_{off} of fluorescently labeled imagers to 1DS origami, three sealed samples need to be prepared at imager concentrations (c) 5 nM, 10 nM and 20 nM (summing up to a total preparation time of ~60 min). Subsequently, all three samples are imaged for a total measurement time of 120 min. The automated analysis pipeline finally performs localization of emitters, rendering of the super-resolved images, automated localization cluster detection, autocorrelation analysis, filtering of each of the three data sets and, finally, fitting Eq. 2.38 (page 23) to the plot of $\langle\tau\rangle$ vs. c to directly obtain k_{on} and k_{off}. These post-processing steps take about ~10 min in total. We have shown in Chapter 6 that this workflow allowed us to repeatedly measure the kinetic rates at a experimental error of smaller than >5 %, despite sample-to-sample variations and freshly prepared imager stocks. However, this remarkable precision and repeatability is attained at the cost of over three hours of sample preparation, data acquisition and post-processing. While this might seem a reasonable time for certain individual experiments, it renders larger parameter scans such as the influence of buffer conditions on DNA hybridization impractical. The purpose of this first Section is to elucidate to which extent it is possible to reduce the experimental effort and time consumption while still maintaining an acceptable experimental precision.

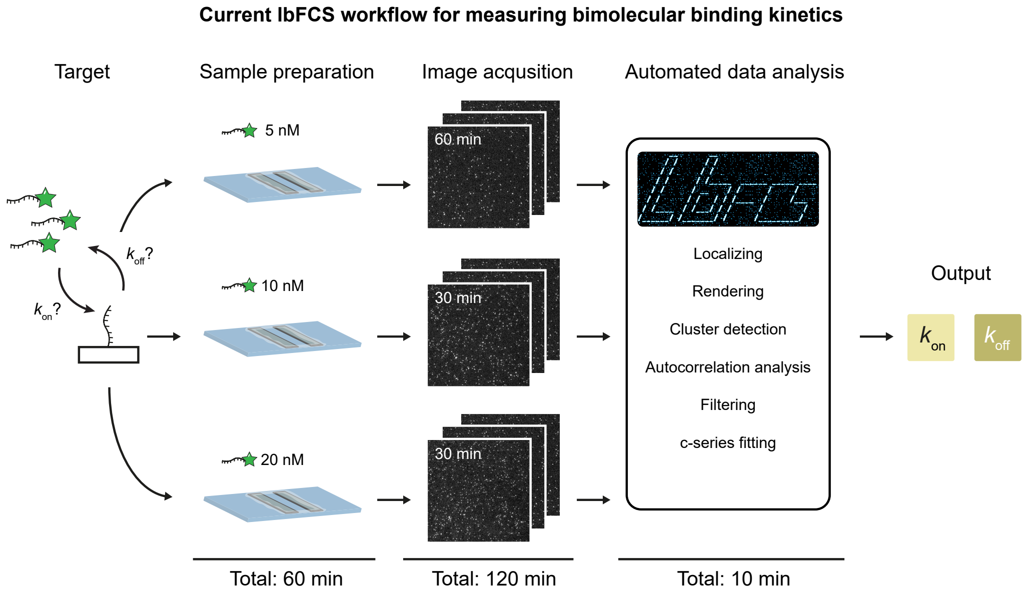
Current lbFCS workflow for measuring bimolecular binding kinetics
Target
Sample preparation
Image acqusition
Automated data analysis
5 nM
10 nM
20 nM
k_{off}?
k_{on}?
60 min
30 min
30 min
Localizing
Rendering
Cluster detection
Autocorrelation analysis
Filtering
c-series fitting
Output
k_{on}
k_{off}
Total: 60 min
Total: 120 min
Total: 10 min

Figure 7.2. Current lbFCS Workflow for Measuring Binding Kinetics. Exemplary description of the workflow determining the binding kinetics (k_{on} and k_{off}) of DNA hybridization using lbFCS.

7.2.2 Two-Point Concentration Series

First, we looked at the number of samples used for an lbFCS imager concentration series. As described in Chapter 6, rate determination follows fitting Eq. 2.38 to the plot of $\langle\tau\rangle$ vs. imager concentration. For this procedure at least two concentration points are required. Imaging a third imager concentration point was initially performed as a measure to increase the robustness of lbFCS. Using the data previously presented in Chapter 6, we employed varying combinations of pairs of imager concentrations (c_1, c_2) for the lbFCS pipeline and compared the outcome with the standard procedure of three concentration points (c_1, c_2, c_3). Prior to presenting new lbFCS results we want to state that for all presented data in this Chapter we followed the exact analysis pipeline as published in Chapter 6, with the exception of using A and τ obtained from the linearized exponential fit instead of the exponential fit (see Supplementary Fig. 3 in Chapter 6) due to a better convergence behavior.

RESULTS AND DISCUSSION

We used all possible combinations of three imager concentrations for stock 1-5 from Fig. 2 in Chapter 6): (5 nM, 10 nM), (10 nM, 20 nM) and (5 nM, 20 nM) in order to compare the experimental variations in resulting k_{on} and k_{off} with respect to the standard reference (5 nM, 10 nM, 20 nM) (see Fig. 7.3 a,b,c and d, respectively). The first row in Fig. 7.3 depicts the $\langle\tau\rangle$-vs.-c fits for the four combinations. While for (5 nM, 10 nM) we observed strong variations, this was more moderate for the combination of (10 nM, 20 nM). The combination of (5 nM, 20 nM), however, resulted in almost identical curves compared to the standard reference.

The $1/A$-vs.-c fits depicted in the second row of Fig. 7.3 overall seemed to be less affected by the choice of imager concentration points, but again (5 nM, 20 nM) produced curves similar to the reference.

The two bottom rows of Fig. 7.3 illustrate the resulting k_{on} and k_{off} obtained from each of the $\langle\tau\rangle$-vs.-c fits in the first row. The grey dashed line indicates the mean over all imager stocks and the grey shaded area the corresponding standard deviation. While the first two combinations (5 nM, 10 nM) and (10 nM, 20 nM) were prone to larger fluctuations in either k_{on} or k_{off}, the results for (5 nM, 20 nM) confirmed the visual impression from the fits and produced close to identical hybridization rates with respect to the three-point concentration series. The analysis results are summarized in Table 7.1 for a more quantitative overview. Overall, two imager concentration measurements seem to be sufficient for lbFCS analysis, however, combinations of close concentration points (i.e., (5 nM, 10 nM) and (10 nM, 20 nM)) turned out to be unfavorable due to larger experimental errors (e.g., up to 16.1 % in k_{on} and

Table 7.1. lbFCS Results for Hybridization Rates for 2-Point Concentration Series

Combination imager conc. (nM)	k_{on} **($10^6/Ms$)**	Δk_{on} **(%)**	k_{off} **($10^{-1}/s$)**	Δk_{off} **(%)**
(5, 10)	7.10 ± 1.14	16.1	2.72 ± 0.08	2.9
(10, 20)	6.64 ± 0.49	7.4	2.76 ± 0.10	3.6
(5, 20)	6.79 ± 0.17	2.5	2.73 ± 0.04	1.5
(5, 10, 20), reference	6.81 ± 0.20	2.9	2.73 ± 0.03	1.1

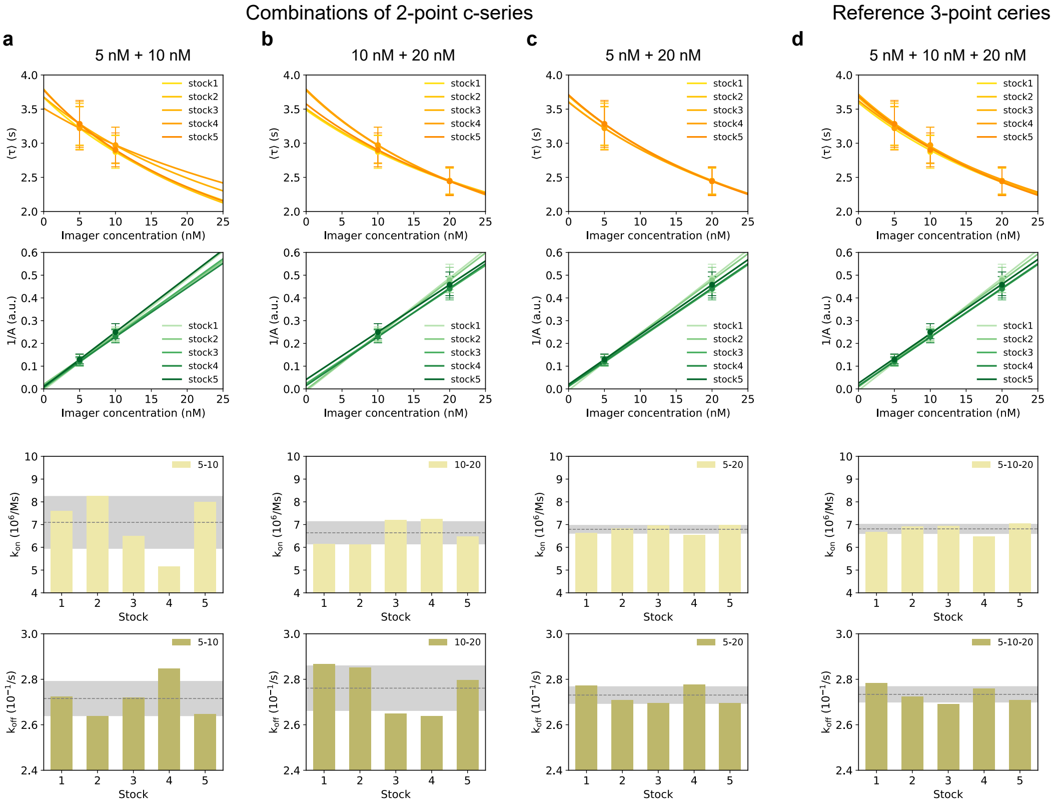

Figure 7.3. Two-Point lbFCS Concentration Series on 1DS Origami. a Using the data from [97] (imager stock 1-5; see Fig. 2 in Chapter 6) only the 5 nM and 10 nM data sets were used for lbFCS analysis. **b** Same as (a), but for 10 nM and 20 nM data sets. **c** Same as (a,b), but for 5 nM and 20 nM data sets. **d** Same as (a,b,c), but use of 5 nM, 10 nM and 20 nM data sets as a reference standard. First row: $\langle\tau\rangle$-vs.-c fits, second row: $1/A$-vs.-c fits, third row: k_{on} results and fourth row: k_{off} results. Error bars correspond to standard deviation in case of $\langle\tau\rangle$ and interquartile range in case of A.

3.6 % in k_{off}). The combination of (5 nM, 20 nM) turned out to be the optimal choice, reproducing the absolute values of k_{on} and k_{off} compared to the reference both at an experimental error <2.5 %.

7.2.3 Faster Image Acquisition

Next, we turned our attention towards shorter, i.e., faster image acqusition. Initially, we adjusted our total data acquisition times according to the ideal measurement times reported for SI-FCS [40] ($\sim 300\times$ longer than the expected decay constant τ). However, the signal of single localized intensity vs. time traces significantly differs from the surface-integrated signal of SI-FCS, due to additional contributions of 3D imager diffusion and unspecific surface interactions [40, 97]. Thus, we simulated synthetic intensity vs. time traces, mimicking a wide range of lbFCS measurement durations to assay the influence of measurement time on the obtained results. Subsequently, we experimentally confirmed the simulation results by temporally segmenting experimental data sets into shorter measurement times prior to lbFCS analysis.

RESULTS AND DISCUSSION

The simulation module for synthetic intensity vs. time traces which was used in this section was written by Florian Stehr and is published in the lbFCS repository (`https://github.com/schwille-paint/lbFCS`). After defining the initial parameters (i.e., number of docking strands N, k_{on}, k_{off}, the camera frame exposure time and imager concentration c) the module allows simulation of an arbitrary number of traces of desired duration (based on drawing exponentially distributed bright and dark times) directly into the output format "_picked.hdf5" for downstream lbFCS analysis (compare Suplementary Fig. 1 in Chapter 6). Note that the simulation in its current form does not include photon noise. Hence, it solely accounts for statistical uncertainty attributed to the finite number of independent fluctuations within the simulated measurement time.

Using our experimental conditions from [97] (N=1, $k_{\text{on}} = 6.5\times10^6$/Ms, $k_{\text{off}} = 0.28$/s, exposure time 200 ms and c = [5 nM, 20 nM]), 4,000 synthetic 1DS traces were simulated for the following measurement durations (in frames): 1,000, 2,000, 4,500, 9,000 and 18,000. Note that 9,000 frames (i.e., 30 min at exposure time 200 ms) is the current standard for 10 nM and 20 nM samples and 18,000 frames (i.e., 60 min) for 5 nM samples. The left panel in Fig. 7.4a displays the obtained $\langle\tau\rangle$ results obtained from lbFCS analysis of the simulated data which were overall in excellent agreement with the expected outcome (ground truth calculated by Eq. 2.38 on page 23 and indicated by the dashed lines). Inspection of the relative deviation of $\langle\tau\rangle$ with respect to the ground truth (see Fig. 7.4a, right panel) revealed that even at a simulated measurement time as short as 4,500 frames for both imager concentrations the deviation fell below 2 %. Furthermore, hardly any change was observed comparing 4,500 frames and 9,000 frames simulation time. Similarly, Fig. 7.4b shows the corresponding lbFCS results of A and the relative deviation to the ground truth (calculated by Eq. 2.39, page 23), respectively, confirming that also A as the second lbFCS fit parameter was determined at reasonable precision (<2 %) for simulation times as short as 4,500 frames and negligible gain was observed compared to measuring for 9,000 frames.

Overall, the simulation results suggest that for all three imager concentrations $\langle\tau\rangle$ and A can be reasonably well extracted from intensity vs. time traces as short as 15 min (4,500 frames). It should be highlighted, however, that the precision at which both observables can be measured increases with simulated measurement time, as indicated by the shrinking error bars. Hence, measurement time can become more important in lbFCS applications when it comes to resolving differences in closely lying populations of either variable.

As a next step, we investigated to which extent the simulation results translate to experimental data by performing temporal segmentation of experimental intensity vs. time traces prior to lbFCS analysis. Fig. 7.4c displays an exemplary trace from a data set acquired at 5 nM imager concentration. The black dashed lines indicate the cut off values to artificially shorten the data set into the previously simulated measurement times. Fig. 7.4d shows the resulting averaged autcorrelation curves (black circles) obtained for each measurement time and the grey shaded area indicates the standard deviation at each lag time. Both the linearized and the exponential fit are indicated by cyan and magenta dashed curves, respectively. The number of remaining intensity traces after filtering is given in the figure legend. Notably, this number increased significantly until 9,000 frames measurement time, in contrast to

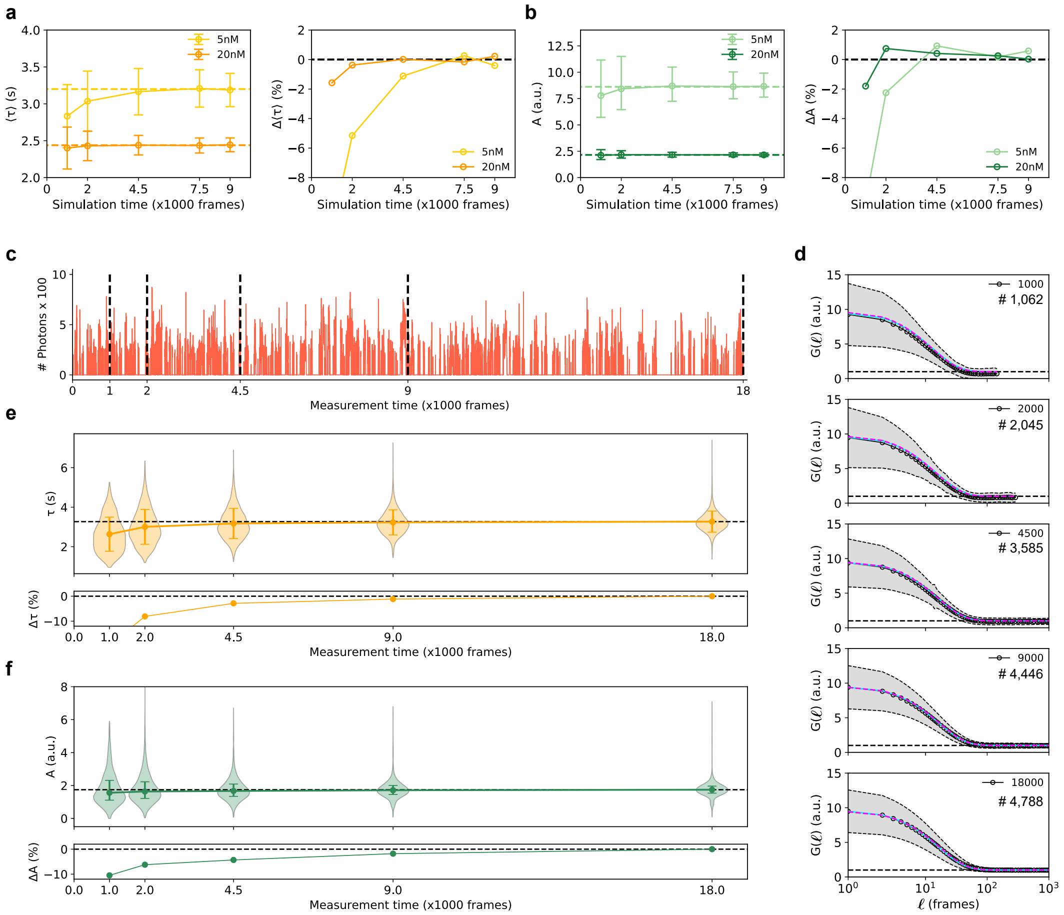

Figure 7.4. Temporal Segmentation - Towards Faster Data Acquisition. **a** Left: $\langle\tau\rangle$ results obtained from simulated intensity traces of varying duration at 5 nM and 20 nM imager concentration. Ground truth indicated by dashed lines. Right: Relative deviation from ground truth. **b** Left: A results obtained from simulated intensity traces of varying duration at 5 nM and 20 nM imager concentration. Ground truth indicated by dashed lines. Right: Relative deviation from ground truth. **c** Intensity vs. time trace from an experimental data set acquired at 5 nM imager concentration. Black dashed lines indicate cut off values for temporal segmentation prior to lbFCS analysis. **d** Averaged experimental autocorrelation curves $G(\tau)$ (black) obtained from lbFCS analysis of the entire temporally segmented data set. Grey shaded area depicts standard deviation at each lag time. Exponential and linear fit (see Chapter 6) indicated by magenta and cyan curves, respectively. **e** Resulting τ distributions obtained from lbFCS analysis in d. Relative deviation of the mean $\langle\tau\rangle$ given below with respect to the full measurement time (18,000 frames). **f** Resulting A distributions obtained from lbFCS analysis in d. Relative deviation of A (median) given below with respect to the full measurement time (18,000 frames). Error bars correspond to standard deviation in the case of τ and interquartile range in the case of A.

an only minor increase from 9,000 to 18,000 frames. This is explained by the fact that due to the shorter the observation time window becomes, the less likely it is that an intensity trace fullfils all filter criteria (compare Supplementary Fig. 3 in Chapter 6). We also observed that the standard deviation of $G(\ell)$ decreases with measurement time. Fig. 7.4e displays the resulting distributions of τ obtained from all linear fits

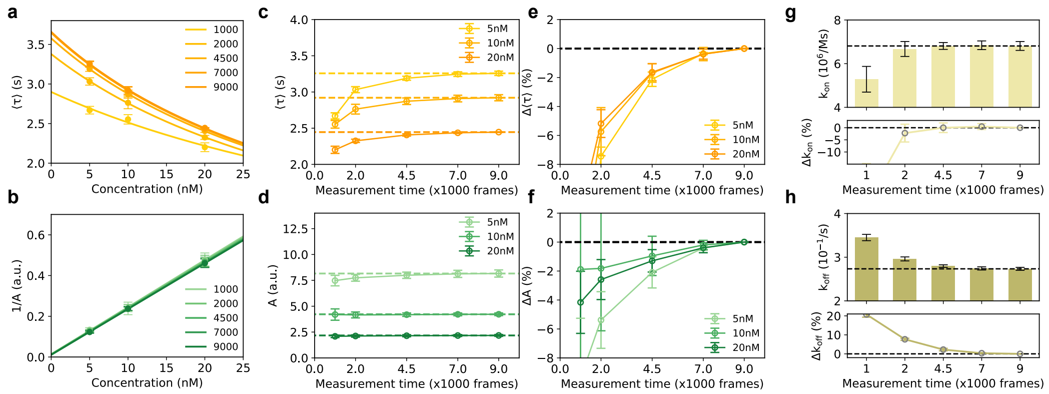

Figure 7.5. Temporal Segmentation Results of lbFCS Concentration Series. **a** Averaged $\langle\tau\rangle$-vs.-c fits for varying measurement durations averaged over lbFCS analysis results obtained from stocks 1-5 from [97] (see Fig. 2 in Chapter 6). **b** Averaged $1/A$-vs.-c fits obtained from the same data sets as in (a). **c** Plots of $\langle\tau\rangle$ vs. measurement time for varying imager concentrations. Dashed lines indicate the data point at 9,000 frames measurement time. **d** Plots of A vs. measurement time for varying imager concentrations. Dashed lines indicate the data point at 9,000 frames measurement time. **e** Plot of relative deviation of $\langle\tau\rangle$ with respect to 9,000 frames measurement time. **f** Plot of relative deviation of A with respect to 9,000 frames measurement time. **g** Plot of k_{on} vs. measurement time obtained from fits in (a). **h** Plot of k_{off} vs. measurement time obtained from fits in (a). All data points and error bars display mean and standard deviation, respectively, obtained from lbFCS analysis of the five c-series.

of each temporal segmentation of the data set. Analogous to the simulated data we observed an increase in τ with measurement time until it converges. Similarly, all resulting A-distributions are depicted in Fig. 7.4f, again in good agreement with the simulation results. Due to the neglegible difference in lbFCS observables between 9,000 and 18,000 frames measurement time we concluded that even at an imager concentration of 5nM a measurement time of 9,000 frames (30 min) is sufficient.

Next, all previous 1DS data sets from stock 1-5 were temporally segmented into all of the following meausrement durations: 1,000, 2,000, 4,500, 7,000 and 9,000 frames and reanalyzed by the lbFCS pipeline. Fig. 7.5a shows the resulting $\langle\tau\rangle$-vs.-c fits for each cut-off value averaged over all 5 imager stocks. We again observed the same behavior as for 5 nM also for the 10 nM and 20 nM data sets, showing first an increase and later close to convergence to the data point at the longest measurement time 9,000 frames. The $1/A$-vs.-c fits showed hardly any effect with respect to measurement time (see Fig. 7.5b).

Fig. 7.5c and d display plots of both $\langle\tau\rangle$ and A vs. measurement time, respectively. The dashed lines each represent the data point of the longest measurement time, which can be considered to be the most precise (since experimentally it is not possible to define a ground truth in constrast to previous simulations). The respective relative deviations normalized to the last data point are depicted in Fig. 7.5e and f. Remarkably, in line with the simulation results (compare Fig. 7.4a,b), also for the experimental data the relative deviation was <2 % for all three imager concentrations at a total measurement time of 15 min (4,500 frames) in both lbFCS observables. Finally, Fig. 7.5g and h depict the k_{on} and k_{off} results obtained from the $\langle\tau\rangle$-vs.-c fits in Fig. 7.5a. Again, the dashed lines represent the result at 9,000 frames measurement time, to which the relative deviation shown below the two plots was normalized. While k_{on} appeared to be understimated at short measurement times, k_{off} turns out to be overestimated. However, in accordance with the behavior of both lbFCS observables, a measurement time of only 4,500 frames retrieves binding rates nearly identical to those for 9,000 frames, which is also supported by the more quantitative overview of the results of the temporal segmentation provided in Table 7.2.

Table 7.2. lbFCS Results for Hybridization Rates for Shorter Measurement Times

Measurement Time (p. sample)	k_{on} **($10^6/Ms$)**	Δk_{on} **(%)**	k_{off} **($10^{-1}/s$)**	Δk_{off} **(%)**
1000 fr / 3.3 min	5.29 ± 0.59	11.2	3.45 ± 0.07	2.0
2000 fr / 6.7 min	6.67 ± 0.34	5.1	2.96 ± 0.05	1.7
4500 fr / 15 min	6.81 ± 0.16	2.4	2.80 ± 0.03	1.1
7000 fr / 23.3 min	6.84 ± 0.20	2.9	2.74 ± 0.04	1.5
9000 fr / 30 min	6.81 ± 0.20	2.9	2.73 ± 0.03	1.1

7.2.4 Fast Acquisition of Two-Point Concentration Series

In a last step, we combined the two previous findings and assayed the influence of temporal segmentation on the outcome of using the best performing two-point concentration series, i.e., the combination of 5 nM and 20 nM imager concentration.

RESULTS AND DISCUSSION

Fig. 7.6a depicts the corresponding $\langle\tau\rangle$-vs.-c fits for measurement times 2,000 frames, 4,500 frames and 9,000 frames (7 min, 15 min and 30 min, respectively), again showing converging behavior towards longer measurement times. Also the $1/A$-vs.-c fits depicted in Fig. 7.6b did not indicate any visually observable influence with respect to measurement time. Comparing the resulting k_{on} and k_{off} (Fig. 7.6c and d, respectively) we again observed only a minor effect between 4,500 frames and 9,000 frames measurement time. The summarized values in Table 7.3 indicate that using two samples with imager concentrations of 5 nM and 20 nM and a total measurement time of 4,500 frames per sample performs nearly identical as the initially-suggested three-point concentration series (compare Table 7.1). Remarkably, the results produced by a measurement time of 2,000 frames (~7 min) only deviate by ~2 % in k_{on} and by 6 % in k_{off} compared to 9,000 frames.

While we have previously shown that k_{off} is independent of the absolute imager concentrations [97] (only depending on the ratio of imager concentrations used in the samples), the obtained value of k_{on} depends on the absolute imager concentration (see Eq. 2.38). Here, an additional and inevitable error source is introduced by the experimentalist when adjusting the actual imager concentration in the sample. Overall, it is important to know how the uncertainties in the measured reaction rates translate into the uncertainty of K_{D}. In this perspective, it will be interesting to assay a well-known bimolecular reaction using lbFCS and compare the results obtained by a complementary method.

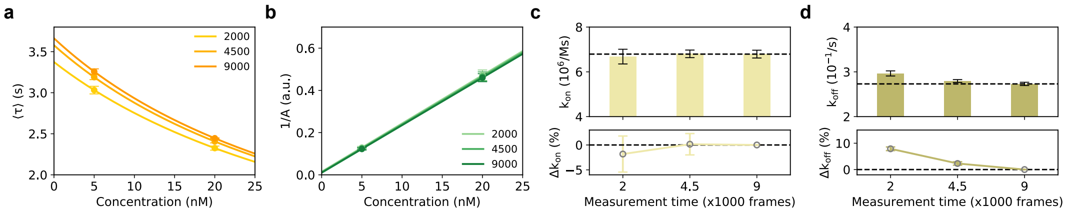

Figure 7.6. Faster Acquisition of Two-Point lbFCS Concentration Series. **a** Averaged $\langle\tau\rangle$-vs.-c fits for varying measurement durations averaged over lbFCS analysis results obtained from (5 nM, 20 nM) data sets from stocks 1-5 from [97] (see Fig. 2 in Chapter 6). **b** Averaged $1/A$-vs.-c fits obtained from the same data sets as in (a). **c** Plot of k_{on} vs. measurement time obtained from fits in (a). Plot of relative deviation of k_{on} with respect to 9,000 frames data point given below. **d** Plot of k_{off} vs. measurement time obtained from fits in (a). Plot of relative deviation of k_{off} with respect to 9,000 frames data point given below. All data points and error bars display mean and standard deviation, respectively, obtained from lbFCS analysis of the five two-point c-series.

Table 7.3. lbFCS Results for Two-Point Concentration Series at Shorter Measurement Times

Measurement Time (p. sample)	$\boldsymbol{k_{on}}$ **($10^6/Ms$)**	$\boldsymbol{\Delta k_{on}}$ **(%)**	$\boldsymbol{k_{off}}$ **($10^{-1}/s$)**	$\boldsymbol{\Delta k_{off}}$ **(%)**
2000 fr / 6.7 min	6.68 ± 0.33	4.9	2.96 ± 0.06	2.0
4500 fr / 15 min	6.80 ± 0.17	2.5	2.79 ± 0.03	1.1
9000 fr / 30 min	6.79 ± 0.17	2.5	2.73 ± 0.04	1.5

7.2.5 Conclusion

In the initially-proposed scheme of performing a concentration series in lbFCS, determination of k_{on} and k_{off} required a total of three hours, including both sample preparation and data acquisition. However, following the results presented in this section, we can obtain nearly identical results with only two concentration points at a total measurement time reduced by a factor of 4× down to 30 min. In certain applications, rate determination within an uncertainty of ~10 % might be sufficient, allowing to further reduce acquisition times, making lbFCS an attractive tool for fast kinetic assays over a wider range of parameters. However, the optimization presented within this chapter was tied to a specific imager-docking strand pair, at a given temperature and buffer composition. Varying any of these factors might induce significant changes to the uncertainties in determining both k_{on} and k_{off}. It is hence essential to explore a wider parameter space to obtain a more general formulation of the interdepencies between the experimental parameters, such as the ligand concentration or the measurement time and the expected reaction rates, which could be easily achieved via extended simulations. The applicability of lbFCS to slower, i.e., more stable interactions is in its current form limited by the photostability of the fluorescent label on the order of tens of seconds. However, photobleaching could be potentially circumvented by an intermittent illumination scheme for long time observation of surface-bound ligands. The applicability of lbFCS to faster interactions is ultimately limited by the camera acquisition speed and the brightness of the fluorophore, which determines the signal-to-noise ratio with respect to shot noise and read-out noise. This might become an increasingly severe factor at short camera exposure times.

7.3 Counting Single Molecules

Molecular counting with lbFCS relies on the precise determination of the binding rates and we can hence directly translate the findings of the previous section. In Chapter 6, we have demonstrated that lbFCS allows molecular counting in combination with DNA-PAINT on synthetic DNA origami structures. In the discussion of Chapter 6, we stated that - before being able to use lbFCS as a quantitative tool of discovery in fixed cells - further investigations are necessary on how some critical aspects of the measurement procedure can influence the experimental outcome. This included the implementation of an imager concentration series directly within the same sample (since with cellular targets the standard procedure of preparing individual samples per imager concentration leaves plenty of room for errors). Furthermore, when moving towards fixed cells, it has to be tested how well one can adjust the imager concentrations, since lbFCS in its current form relies on assuming the correct concentration ratios (compare Fig. 2c in Chapter 6). Additionally, it is not given that all docking strands within the complex three-dimensional environment of a fixed cell experience a global k_{on} and k_{off} and whether the reaction reaches equilibrium over reasonable time scales. Further complexity is added by imaging away from the surface using Highly Inclined and Laminated Optical Sheet (HILO) illumination [57], unspecific binding to cellular components and a potentially higher fluorescence background.

Following these considerations, within this chapter we demonstrate the possibility of performing an lbFCS concentration series within a single DNA origami sample by repeatedly washing and adding new imaging solutions. Furthermore, we devise an alternative counting approach based on the lbFCS observables, which circumvents the necessity of making assumptions on the absolute imager concentrations and, therefore, the correct concentration ratios. Finally, we apply lbFCS to cellular targets for the first time, identifiying clear limits of its current implementation while obtaining overall promising results.

7.3.1 From Two Concentration Measurements to a Revised Counting Approach

As a first step, we translated our previous insights that for our system (i.e., imager-docking strand design, temperature, buffer conditions), two concentration points are sufficient to precisely determine the hybridization rates, to the molecular counting problem. In view of applying lbFCS to fixed cellular targets, where the precise adjustment of imager concentrations might become difficult, we here devise an alternative counting approach that circumvents the assignment of a distinct (but assumed) imager concentration to each of the two data sets. Treating c as an additional experimental unknown, every lbFCS measurement has the unknowns (N, k_{on}, k_{off}, c_i). By introducing the effective association rate $\hat{k}_{on,i} = k_{\text{on}} c_i$, the experimental unknowns of two lbFCS measurements at different imager concentrations $c_{i=1,2}$ are (N, k_{off}, $\hat{k}_{on,1}$, $\hat{k}_{on,2}$). lbFCS analysis of the two measurements yields four observables (τ_1, A_1, τ_2, A_2), which exclusively depend on the four experimental unknowns. Accordingly, we can solve the set of equations and directly calculate (N, k_{off}, $\hat{k}_{on,1}$, $\hat{k}_{on,2}$) from the lbFCS observables. The equations are derived in the following section.

DERIVATION OF TWO-POINT CALCULUS

We start from Eq. 2.38 and Eq. 2.39 (both on page 23) for each concentration c_i, $i = (1,2)$:

$$\tau_i = \frac{1}{k_{\text{off}} + k_{\text{on}} c_i} = \frac{1}{k_{\text{off}} + \hat{k}_{on,i}} \tag{7.1}$$

$$A_i = \frac{1}{N} \frac{k_{\text{off}}}{k_{\text{on}} c_i} = \frac{1}{N} \frac{k_{\text{off}}}{\hat{k}_{on,i}} \tag{7.2}$$

where we have introduced the effective association rate $\hat{k}_{on,i} = k_{\text{on}} c_i$.
Rewriting Eq. 7.2 to N for $i = (1,2)$ allows to obtain the expression:

$$A_1 \hat{k}_{on,1} = A_2 \hat{k}_{on,2} \tag{7.3}$$

Performing $1/\tau_1 - 1/\tau_2$ with the help of Eq. 7.1 leads to:

$$\frac{1}{\tau_1} - \frac{1}{\tau_2} = \hat{k}_{on,1} + k_{\text{off}} - \hat{k}_{on,2} - k_{\text{off}} = \hat{k}_{on,1} - \hat{k}_{on,2} \tag{7.4}$$

Solving Eq. 7.4 for $\hat{k}_{on,1}$ leads to:

$$\hat{k}_{on,1} = \frac{1}{\tau_1} - \frac{1}{\tau_2} + \hat{k}_{on,2} \tag{7.5}$$

Inserting Eq. 7.3 solved for $\hat{k}_{on,2}$ into Eq. 7.5 yields:

$$\hat{k}_{on,1} = \frac{\frac{1}{\tau_1} - \frac{1}{\tau_2}}{1 - \frac{A_1}{A_2}} \tag{7.6}$$

Following the same considerations, we can derive the expression for $\hat{k}_{on,2}$:

$$\hat{k}_{on,2} = \frac{\frac{1}{\tau_2} - \frac{1}{\tau_1}}{1 - \frac{A_2}{A_1}} \tag{7.7}$$

Inserting either Eq. 7.6 or Eq. 7.7 into Eq. 7.1 yields k_{off}:

$$k_{\text{off}} = \frac{1}{\tau_1} - \frac{\frac{1}{\tau_1} - \frac{1}{\tau_2}}{1 - \frac{A_2}{A_1}} = \frac{1}{\tau_2} - \frac{\frac{1}{\tau_2} - \frac{1}{\tau_1}}{1 - \frac{A_2}{A_1}} \tag{7.8}$$

Knowing $\hat{k}_{on,1}$, $\hat{k}_{on,2}$ and k_{off}, Eq. 7.2 can be solved for N in order to obtain the counting results:

$$N = \frac{k_{\text{off}}}{A_1 \hat{k}_{on,1}} = \frac{k_{\text{off}}}{A_2 \hat{k}_{on,2}} \tag{7.9}$$

Note that we deliberately chose the notation of the effective association rates $\hat{k}_{on,i}$. It becomes evident that in order to count the number of docking strands N using this direct calculation approach, we do not need to assume values for the absolute imager concentrations c, in contrast to the fitting approach described in Chapter 6, where each set of lbFCS observables (A_i, τ_i) was assigned to a fixed value of c_i and subsequenly fitted by Eq. 2.38 (page 23). While for molecular counting it is sufficient to calculate with $\hat{k}_{on,i}$, it is of course possible to derive the global k_{on} simply by inserting the absolute concentration value $k_{\text{on}} = \hat{k}_{on,i}/c_i$.

We have previously shown for DNA origami experiments that we can adjust the imager concentrations reasonably well in individual samples (see Chapter 6). However, the direct calculation approach might become a significant advantage for cases of biological targets in which precise concentration adjustment might become difficult or potentially not possible anymore.

In the following, we assay the new direct counting approach *in silico* and *in vitro*, first using the previously introduced simulation module and subsequently on DNA origami targets. Furthermore, we additionally apply the temporal segmentation analysis as in the previous section in order to evaluate the influence of measurement time also on counting results.

RESULTS AND DISCUSSION

We assayed the influence of measurement time on all lbFCS parameters for the case of N=1 and N=12 for both simulated and experimental DNA origami data (see Fig. 7.7a-d, respectively) and compared the counting results obtained by the standard approach (referred to as ’fit’) or by direct calculation of N via the previously derived approach (referred to as ’direct’). All experimental data sets are from Chapter 6 (for N=1, the data sets from stock 1-5 were analyzed). Note that N=12 denotes number of docking strands on the origami design. The actual number of docking strands per DNA origami is in fact lower due to a limited docking strand incorporation efficiency during the origami folding process [166]. Here, we experimentally counted on average ~10 docking strands which is why a simulation input of N=10 was used.

The first row in Fig. 7.7 displays $\langle\tau\rangle$ vs. total measurement time (simulation time in case of simulated data) in all four cases. For both N=1 and N=10, simulated and experimental results are in relatively good agreement. However, looking at the relative deviation shown below each plot, for simulated data $\langle\tau\rangle$ converges faster to the true value (i.e., at 4,500 frames for N=1 and even at 2,000 frames for N=10), whereas experimentally $\langle\tau\rangle$ still increases by ~2 % between 4,500 and 9,000.

A similar behavior is observed when looking at A for all four cases, as depicted in the second row of Fig. 7.7. For N=10, simulation and experiment yield nearly identical results.

The third row in Fig. 7.7 shows the $\langle\tau\rangle$-vs.-c fits. Here, for both experimental data sets (N=1 and N=12) the curves differ from the respective simulated case by exhibiting an increase in $\langle\tau\rangle$ over measurement time, observable for both 5 nM and, significantly more, for 20 nM. A possible reason could be sample ageing effects, potentially resulting from a slight decrease of imager concentration over time. However, this effect would not result in a reduced k_{on} due to the simultaneous increase in τ for both imager concentrations at 5 nM and 20 nM, but is instead affecting only k_{off}, as observed in Fig. 7.6. The $1/A$-vs.-c fits displayed in the fourth row of Fig. 7.7 show good agreement between simulation and experiment.

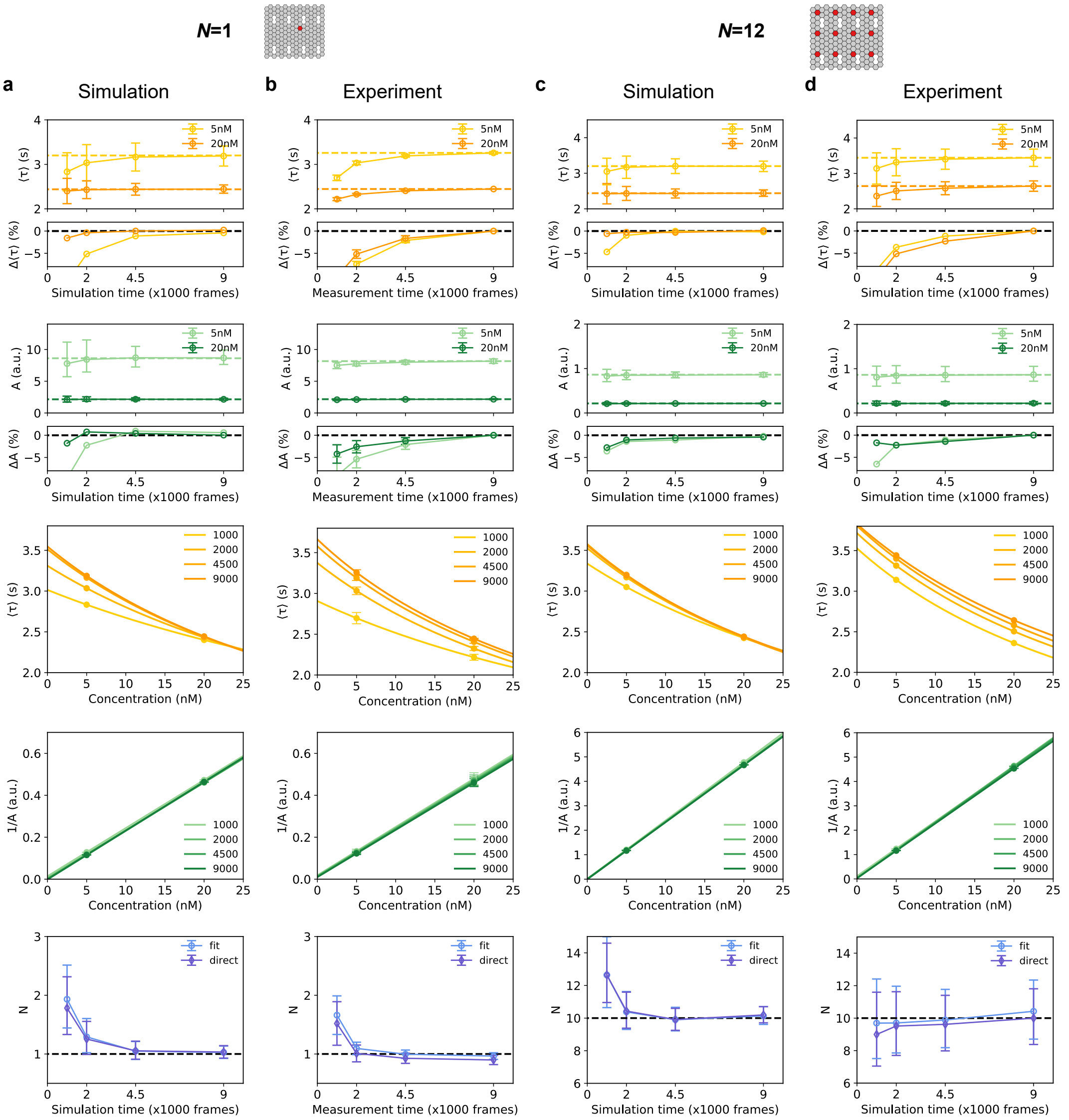

Figure 7.7. Temporal Segmentation and a New Counting Approach for lbFCS. a Results from lbFCS analysis of simulated data sets with N=1. **b** Results from lbFCS analysis of experimental data sets with N=1. Averaged results for stock 1-5 from [97] (see Chapter 6). **c** Results from lbFCS analysis of simulated data sets with N=10. **d** Results from lbFCS analysis of experimental data sets with $N = 12$. First row: $\langle\tau\rangle$ vs. measurement (simulation) time plots. Second row: A vs. measurement (simulation) time plots. Third row: $\langle\tau\rangle$ vs. imager concentration fits. Fourth row: $1/A$ vs. imager concentration fits. Fifth Row: Counting results obtained for standard 'fit' approach (blue) and new 'direct' approach (purple). Error bars in (a,c,d) correspond to standard deviation in case of $\langle\tau\rangle$ and interquartile range in case of A and N. Error bars in (b) correspond to standard deviation over data sets from stock 1-5.

Finally, the last row in Fig. 7.7 shows the counting results obtained by both methods, i.e., 'fit' (blue) and 'direct' (purple). Looking at the simulated data sets first (a and c), both counting approaches yield the correct counting results, verifying our derivations of the 'direct' approach. Also the counting results obtained from the experimental data sets (b and d) are in good agreement with the expected outcome and again, both counting methods produce very similar N values. Remarkably, the counting results also demonstrate that for molecular counting with our imager-docking strand system indeed 4,500 frames measurement time are sufficient to correctly count N=1. For N=12, convergence is observed even earlier (at 2,000 frames measurement time).

7.3.2 Concentration Series by Imager Exchange

Following up on the outlook provided in the original lbFCS publication [97] (see Chapter 6), an additional development was to perform the lbFCS concentration series directly within one sample by repeatedly exchanging the imaging buffer [38]. Since particularly for adressing cellular targets the assumption of a global N, on which lbFCS is based, is not necessarily given, this marks an essential milestone for the applicability of lbFCS beyond simplistic DNA origami targets. Here, we demonstrate that an lbFCS concentration series can be succesfully performed in just a single open chamber by repetitive buffer exchange.

Results and Discussion

In order to test lbFCS using imager exchange, we mixed DNA origami with a N=1 and N=12 docking strand design at a 1:1 ratio and prepared an open chamber of an Ibidi μ-Slide with a surface-immobilized mixture of both DNA origami species, as described in [97] (see Appendix A.1 for a detailed sample preparation protocol). Next, we placed the sample on the microscope and performed two repetitions of imager exchange series at concentrations 5 nM, 10 nM and 20 nM (in this order; see Fig. 7.8a schematic of exchange procedure). After each round of imaging, as much imaging buffer as possible was removed using a pipette, and the chamber was washed 3× with a total volume of 600 μl before the imaging buffer was added. Following our previous findings we imaged each round for 4,500 frames (15 min; see Appendix A.1 for detailed imaging protocol and parameters). Thereby, we ended up with a total of 6 data sets, two for each imager concentration. All data sets were analyzed using the automatized lbFCS pipeline except for the filtering step, since the standard filtering procedure assumes a unimodal distribution in A, which is not given in this case (remember $A \propto 1/N$; see Eq. 2.38 on page 23). Therefore, preliminary filtering was performed manually in order to separate the two origami species (see Appendix A.1 for detailed filtering parameters). Fig. 7.8b displays the distribution of localizations per detected localization cluster in each data set (5 nM data sets in light grey, 10 nM data sets in dark grey and 20 nM data sets in black). Remarkably, for each imager concentration both data sets perfectly align with each other, despite the full cycle of washing and imaging steps of the other concentrations laying in between. Additionally, for each imager concentration we observed two peaks - one originating from N=1 origami (left peak) and one from N=12 origami (right peak). Judging by eye, the relative positions of the peaks follow the expected shift according to the relative increase in imager concentration. The observed saturation behavior of the right, N=12 peak in the 20 nM data sets indicates that these origami were localized in almost all of the 4,500 frames.

Complementary insights are gained from looking at the photon count histograms (see Fig. 7.8c). Again, for each imager concentration both measurements yielded overlaying distributions, also indicating that exchange cycles of imager solutions

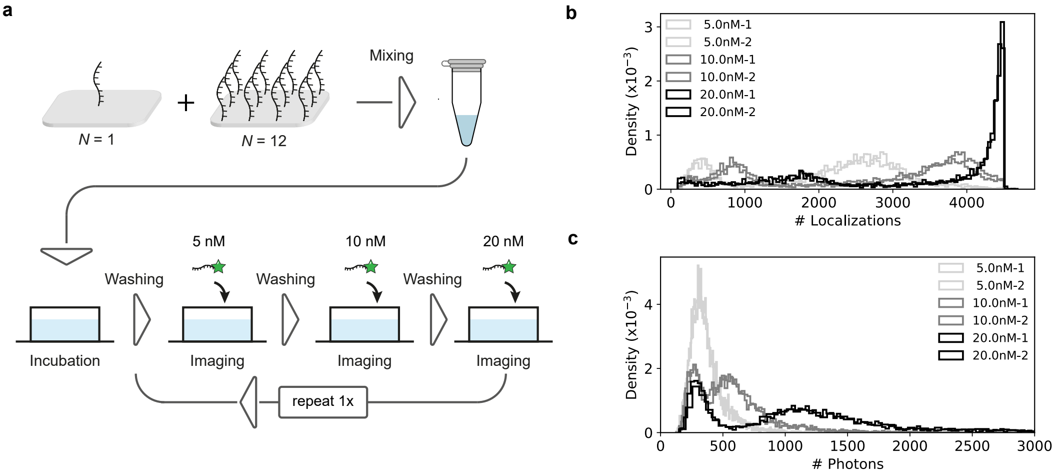

Figure 7.8. lbFCS Concentration Series via Imager Exchange. **a** Schematic of lbFCS molecular counting in combination with imager exchange. A mixture of N=1 and N=12 docking strand DNA origami were mixed at a 1:1 ratio and incubated in an open sample design. Imaging solution was repeatedly added and washed, as indicated in the cycle. **b** Histograms of number of localizations per localization cluster from the six data sets obtained in (a). **c** Histograms of average number of photons per localization from six data sets obtained in (a).

can be reproduced consistently. While for 5 nM only one large peak close to 400 photons is observed, at 10 nM a bimodal distribution is detected with two peaks, one at 300 photons and the second at 600 photons. At 20 nM imager concentration the right peak shifts to 1,200 photons while the first peak remains at 300 photons. These observations indicate that at 5 nM imager concentration both origami species cannot be differentiated according to their photon counts due to the predominant occurance of single binding events on N=12 origami (for N=1 origami, intrinsically only single binding events can occur). Therefore, the photon distributions of both origami species overlap in a single large peak centered around ~300 photons. The formation of the second peak for higher concentrations is due to multiple simultaneous binding events on N=12 origami (on average 2 simultenously bound imagers at 10 nM, i.e., the second peak at 2×300=600, and 4 simultaneously bound imagers at 20 nM, i.e., the second peak at 4×300=1,200).

After this first positive evaluation, we next isolated the N=1 and N=12 localization clusters in each of the 6 data sets for subsequent lbFCS analysis (based on the number of localizations per cluster. See Appendix A.1 for separation parameters). Fig. 7.9a shows the $\langle\tau\rangle$ vs. imager concentration fits for the N=1 species for both full concentration series (yellow and orange curve for first and second cycle, respectively). A reference concentration series obtained via the classic "three-sample" approach (compare Fig. 7.2) is displayed by the grey dashed curve. The high reproducability earlier observed in number of localizations and photon counts also manifests itself in the lbFCS observables, since both fits perfectly overlap. However, the fits describe the data points uncommonly poor, particularly compared to the reference. While the data points at 5 nM and 10 nM imager concentrations are in relatively good agreement with the reference, the 20 nM data point lies significantly below the expected outcome, causing the increased slope of the fits. The same behavior is observed for N=12

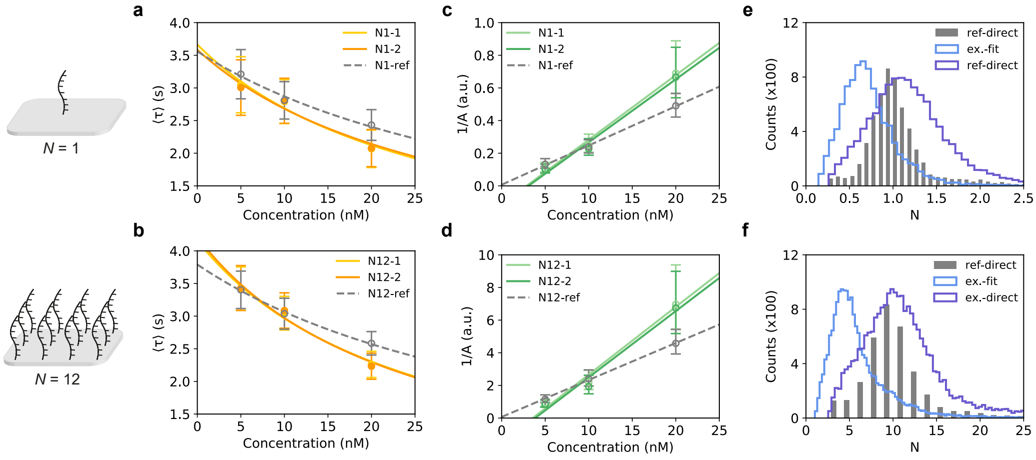

Figure 7.9. Counting Results of lbFCS via Imager Exchange. **a** $\langle\tau\rangle$ vs. imager concentration fits for N=1 DNA origami from exchange experiments (orange) and a classic three-sample concentration series (grey dashed). **b** $\langle\tau\rangle$ vs. imager concentration fits for N=12 DNA origami from exchange experiments (orange) and a classic three-sample concentration series (grey dashed). **c** $1/A$ vs. imager concentration fits for N=1 DNA origami from exchange experiments (green) and a classic three-sample concentration series (grey dashed). **d** $1/A$ vs. imager concentration fits for N=1 DNA origami from exchange experiments (green) and a classic three-sample concentration series (grey dashed). **e** Counting results for N=1 DNA origami from exchange experiments either from fit results in (a) (blue) or direct calculation using the 5 nM and 20 nM data sets (purple). The counting results from the reference lbFCS ceries in (a) are displayed in grey. **f** Counting results for N=12 DNA origami from exchange experiments either from fit results in (b) (blue) or direct calculation using the 5 nM and 20 nM data sets (purple). The counting results from the reference lbFCS ceries in (b) are displayed in grey. Error bars correspond to standard deviaiton in (a,b) and to interquartile range in (c,d).

species, again particularly the 20 nM data point lies below the reference concentration series (see Fig. 7.9b).

The $1/A$ vs. imager concentration fits for both DNA origami species are depicted in Fig. 7.9c and d (N=1 and N=12, respectively). Remember that the $1/A$ representation is chosen deliberately due to its linear dependency on c (see Eq. 2.39 on page 23) as a check that the imager concentrations were adjusted at the correct ratios (see also Fig. 2c in Chapter 6). This is indicated by $1/A$ passing through the origin as is the case for the two reference concentration series (grey dashed lines in Fig. 7.9c and d). Experimentally, however, we can observe for both origami species the same, strong deviation from the origin, mainly caused by outlying 20 nM data points. The fact that this deviation is global for both species is an indication for wrongly adjusted imager concentrations. Imagining a horizontal shift of all 20 nM points in Figs. 7.9a-d to the right to a concentration between 25-30 nM would more or less align reference and experimental fits. Remarkably, the offset of the 20 nM data points is well reproduced in the second exchange cycle, making an exchange pipetting error unlikely. Furthermore, following the standard procedure [97], the imaging solutions were prepared starting with the 20 nM concentration and were diluted twice at a ratio 1:1 to obtain 10 nM and 5 nM concentrations and the latter data points are close to the expected values compared to the reference. The deviation in the exchange concentration series could potentially arise from effects induced by the new and open sample design with a 10× larger sample volume or from pipetting error.

The implications of this finding for our actual motivation, however, namely the counting of the number of docking strands on each DNA origami species, become evident when looking at the counting results obtained for both the N=1 and the N=12 species (see Fig. 7.9e and f, respectively. See Appendix A.1 for details on calculation of N). The counting results of the reference concentration series (grey) yield distributions centered around 1 and 10 (as previously seen in Chapter 6). However, the counting results produced by the fitting approach (blue) clearly underestimates the number of docking strands in the case of both origami species. This is an artifact from fixing the concentrations at the assumed values of 5 nM, 10 nM and 20 nM during fitting, a well-proven procedure when dealing with individual samples [97], but clearly not when adjusting the concentrations at the correct ratios becomes difficult (see Fig. 7.9a-d).

Our new direct counting approach, in contrast, produces counting results (purple), which are in good agreement with the respective reference results (taking the alleged '5 nM' and '20 nM' data sets for direct calculation of N). This demonstrates the advantage of the new over the previous approach, circumventing potential error sources in adjusting the imager concentrations by only relying on the effective association rates $\hat{k}_{on,i}$, which can be directly computed from the lbFCS observables of both employed data sets.

7.3.3 First Application to Cellular Targets

The possibility to perform an lbFCS concentration series for molecular counting within a single sample with the help of imager exchange finally made cellular targets accessible. Before we move on we would like to briefly review the increase in complexity that lies within the step from counting docking strands on DNA origami to counting docking-strand-labeled molecules in fixed cells. On DNA origami we were able to precisely control the number of docking strands per origami species and, thus, expected unimodal distributions of counting results (scattering around the mean number of incorporated docking strands convoluted with the counting error of lbFCS). Furthermore, surface-immobilized DNA origami posed a 'two-dimensional' counting problem with all docking strands within one plane freely facing upwards to the solution, making our assumptions that all docking strands in a sample experience the same global imager concentration, k_{on} and k_{off} very likely. Molecular targets in fixed cells, in contrast, constitute a three-dimensional problem, to which the selective illumination benefits of TIRF microscopy close to the glass surface cannot necessarily be transferred, potentially limiting signal-to-noise and the accessible imager concentration regime. The main criterion for cellular targets to be accessible for lbFCS is discrete spatial organisation, i.e., in well-separated localization clusters (in contrast to large and continuous structures such as filament networks). Furthermore, docking strands have to be specifically attached to the target molecules of interest via a suitable labeling strategy. Residues of unspecific labels as well as nonspecific binding of imagers to other cellular components can cause false signals [167]. But most importantly, the dense matrix of fixed cellular components held together by crosslinking agents constitutes an entirely different environment through which imagers have to diffuse until they find their partnered docking strands. Keeping this in mind, our assumption that all docking strands inside a fixed cell experience the same global imager concentration and hybridization rates is, at least, questionable. Steric hinderance by the fixative or the labeling strategy as well as the degree of permeabilization, allowing an equilibrated imager diffusion within the cell and imager exchange with the outer volume can all become crucial factors determining the success of lbFCS as a quantitative tool for cellular targets.

It requires advanced biochemical know-how and additional control experiments to specifically attach DNA-PAINT docking strands to cellular targets and to devise a fixation and permeabilization protocol with the aim to meet all above-stated prerequisites. For us, the most reasonable step for finally moving from DNA origami to fixed cells was to find a target which was i) known to be sparsely distributed within the cell ensuring separated localization clusters, ii) of well-known stoichiometry for an estimation on the expected counting results and iii) for which the biochemical protocols of docking-strand labeling, cell fixation and premeabilization had already been sucessfully optimized for DNA-PAINT imaging. Fortunately, these requirements were all met by the Nuclear Pore Complexs (NPCs) of a U2OS cell line provided by the group of Ralf Jungmann as first cellular targets. Due to the importance for cytosolic transport from the nucleus to the cytosol, NPCs have been extensively studied in the past, which has led to significant advances with respect to their structural understanding [168–173]. Furthermore, a recent quantitative study by the lab of Jonas Ries demonstrated their potential as intracellular reference targets for quantitative super-resolution imaging [174]. In line with the optimized sample preparation and docking strand labeling protocol for DNA-PAINT imaging [175], NPCs constituted ideal first cellular targets for lbFCS. Precisely, we aimed at counting the copy numbers of nucleoporin NUP96 in the NPC, which presumably consist of two rings of 16 copies of NUP96 each (see Fig. 7.10a) [175].

Results and Discussion

Before presenting and discussing results, Kimberly Cramer, Sebastian Strauss and Bianca Sperl from the group of Ralf Jungmann are acknowledged for preparing and providing U2OS cell samples for DNA-PAINT imaging.

As described in [167, 175], U2OS cells with genetically-modified NUP96-EGFP were fixed and labeled with GFP nanobodies, which were previously conjugated with a single docking strand (see Fig. 7.10b). Here, we used the same imager and docking strand sequences as for previous DNA origami experiments within this Chapter. A control DNA-PAINT imaging experiment confirmed correct labeling of NPC (see Fig. 7.10c; detailed imaging parameters can be found in Appendix A.1). Note that in order to efficiently excite and localize bound imagers to NPCs further away from the surface of the glass slide, we reduced the incident angle of the laser beam leaving the regime of total internal reflection and using HILO illumination [57].

Starting our first lbFCS test using the 5 nM imager concentration in a new sample revealed that, even for our usually lowest imager concentration, we were hardly able to detect single binding events due to the extremely high background fluorescence in HILO (see 7.10d). Therefore, we performed an lbFCS concentration series at much lower imager concentrations of 50 pM, 100 pM and 200 pM. All data sets were acquired

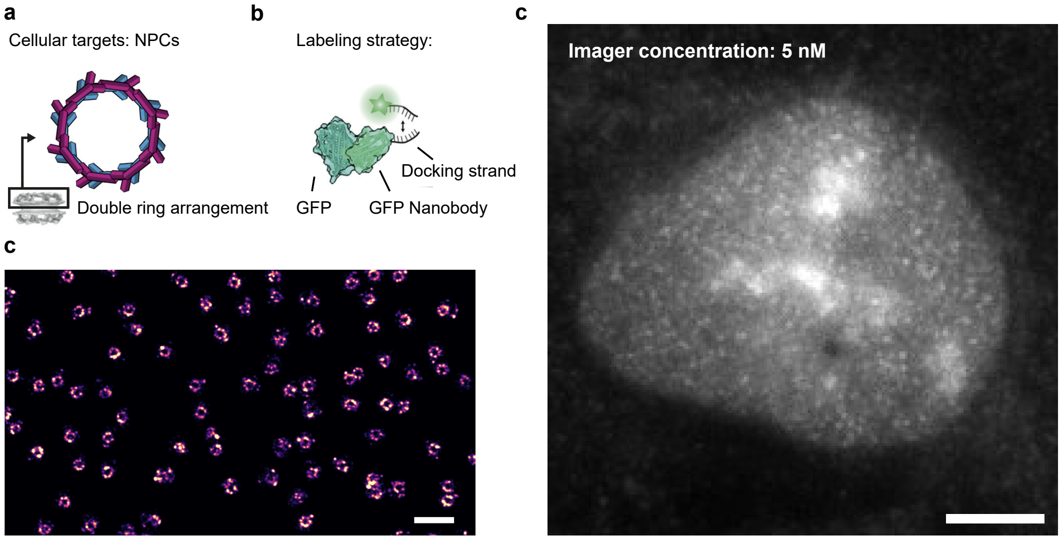

Figure 7.10. Nuclear Pore Complexes as First Cellular lbFCS Targets. **a** Cartoon of the nuclear pore Y complex from human U2OS cells. Both the nuclear ring (purple) and the cytoplasmic ring (blue) each consist of 16 copies of NUP96. **b** Cartoon illustration of a GFP nanobody modified with a docking strand for DNA-PAINT imaging. **c** Super-resolved DNA-PAINT image of NPCs. **d** Example image from first lbFCS attempt at 5 nM imager concentration. The high background fluorescence impedes localization of individual imager binding events. Scalebar: 500 nm in c, 5 μm in d. a and b reprinted and rearranged from [175]. (CC BY-NC 4.0).

on the same FOV and the imaging buffer was carefully exchanged in between the imaging rounds, as shown in Fig. 7.11a (the actual order was 100 pM, 200 pM and, lastly, 50 pM, but from the origami experiments shown in Fig. 7.8 we reasoned that the order of concentration steps can be arbitrarily chosen). A reference image of the FOV in the GFP channel is depicted in Fig. 7.11b. Due to the lower imager concentrations by two orders of magnitudes, we acquired each concentration data set at an extended imaging time of 18,000 frames (i.e., 1 hour; see Appendix A.1 for detailed imaging conditions and exchange protocols).

The example images from the raw data image sequences in Fig. 7.11c indicate increasing number of binding events for higher imager concentration. This visual impression is confirmed looking at the rendered DNA-PAINT images below, displaying an increase in brightness in line with the increase of imager concentration (see Fig. 7.11d). Despite repeated exchange of the imaging buffer the positions of the cells in the FOV were not perceptibly affected by the washing steps. When we aligned all three DNA-PAINT images from Fig. 7.11d, we were able to globally overlay the the three exchange rounds for every NPC even for diffent cells (see Fig. 7.11e). Displayed are picked localization clusters containing localizations in all three DNA-PAINT images. We used our automated cluster detection algorithm and discarded clusters that did not contain localizations in all three data sets. This finding is an important prerequisite for the applicability of lbFCS, i.e., that we can perform a concentration series without perturbing the spatial arrangements of the targets that we would like to count.

We processed all localization clusters of a total of 5 cells (white boxes in Fig. 7.12a), of which four were fully and one largely captured within the FOV. Prior to lbFCS analysis we investigated the number of localizations per localization cluster, similar to the previous DNA origami exchange experiments. Fig. 7.12b displays the distribution of localization counts per cluster for the three data sets (50 pM in light grey, 100 pM in grey and 200 pM in black). The observation of a rightward shift with increasing imager concentration quantitatively confirmed the visual impression during data acquisition and the brightness in the DNA-PAINT images (compare 7.8c and d). Next, we questioned whether binding within the fixed cells was of repetitive nature by analyzing the mean frame value for each localization cluster. Since we imaged each data set for total measurement time of 18,000 frames, we expected a mean frame value at around half the measurement time (9,000 frames) for docking strands that were continously visited by imagers throughout the whole measurement. The histograms in Fig. 7.12c show that this was indeed the case for all three data sets.

Finally, we analyzed the outcome of the lbFCS observables by first looking at the $\langle\tau\rangle$ vs. imager concentration plot (see Fig. 7.12d). In contrast to the usually observed behavior of decreasing $\langle\tau\rangle$ with concentration, we could not identify significant

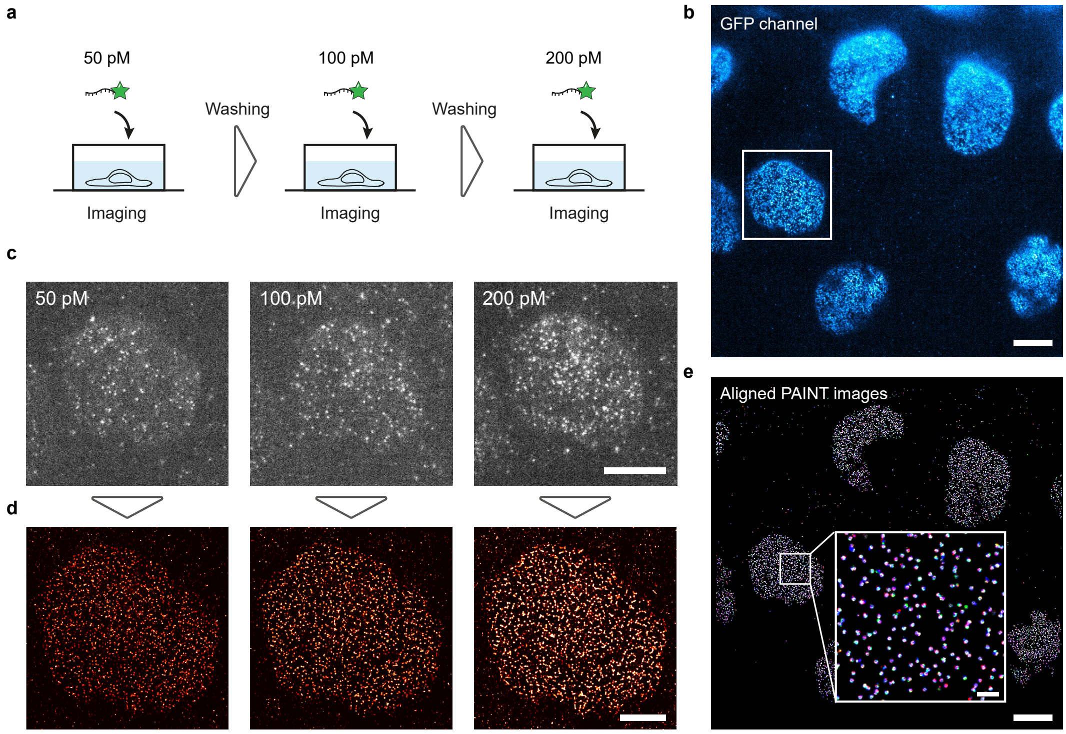

Figure 7.11. Exchange lbFCS Concentration Series on NPCs in Fixed U2OS Cells. **a** Exchange schematic of repeatedly imaging the same FOV of cells at 50 pM, 100 pM and 200 pM using imager exchange. **b** Reference image of the FOV before the lbFCS concentration series in the blue GFP channel. **c** Exemplary raw images from lbFCS data acquisition at 50 pM, 100 pM and 200 pM imager concentration of the cell indicated by the white square in b. **d** Super-resolved DNA-PAIT images rendered from the image stacks in c. All three images show the same cell as in c. **e** Global overlay of all three DNA-PAINT imaged aligned to each others. 50 pM data set in red, 100 pM data set in green and 200 pM data set in blue. Scalebars: 10 μm in b,e, 5 μm in c,d and 1 μm in inset in e.

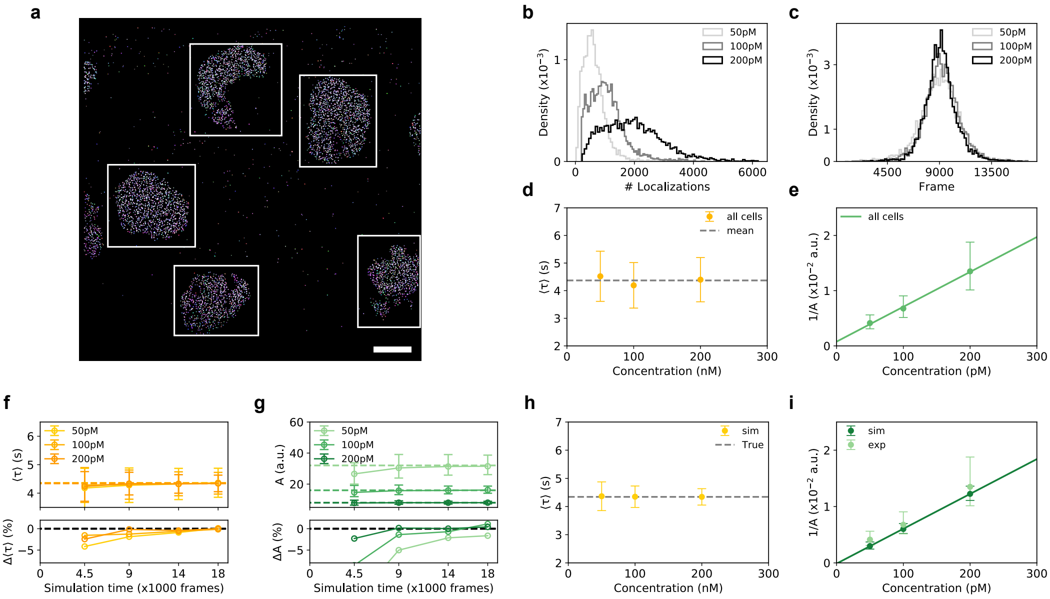

Figure 7.12. Results of Exchange lbFCS Concentration Series on Fixed U2OS Cells. **a** Aligned DNA-PAINT images indicating five cells (white boxes) which were subject to lbFCS analysis. **b** Distributions of number of localizations per detected localization clusters in cells from a. **c** Distributions of mean frame value per detected localization clusters in cells from a. **d** $\langle \tau \rangle$ vs. imager concentration plot from lbFCS analysis. Grey dashed line indicates the mean of the three data points. **e** $1/A$ vs. imager concentration plot and fit from lbFCS analysis. **f** Plot of $\langle \tau \rangle$ vs. simulated measurement time. Simulation parameters: $N = 22$; $k_{\text{on}} = 6.5 \times 10^6/\text{Ms}$; $k_{\text{off}} = 0.23/\text{s}$ (mean indicated in d), $c =$(50 pM, 100 pM and 200pM) and measurement times (4,500, 9,000, 14,000 and 18,000 frames at exposure time 0.2 s) **g** Plot of A vs. simulated measurement time. **h** Plot of $\langle \tau \rangle$ vs. imager concentration for simulated data. **i** Plot of $\langle \tau \rangle$ vs. imager concentration and fit for simulated data. The experimental results from e are plotted in light green. Scalebars: 10 μm in a.

changes between the different concentrations. The fit of Eq. 2.38 (page 23) did not succesfully converge, which is why only the mean of the three data points is plotted (grey dashed line). The $1/A$ vs. imager concentration fit, however, did follow the expected behavior, indicating that the correct imager concentration ratios were adjusted (again by intersection with the y-axis at the origin, see Fig. 7.12e). The reason for why we obtained the usual behavior in $1/A$, but not in τ, is explained in the following. According to Eq. 2.38 (page 23), τ depends on the inverse of the sum of $k_{\text{on}}c$ and k_{off}. Since k_{on} and k_{off} are global constants, it is the imager concentration c that determines whether the first summand or the second summand dominates. In accordance with previous considerations [40], very low imager concentrations $k_{\text{on}}c \to 0$ imply $\tau \approx 1/k_{\text{off}}$. The requirement of localizing single imager binding events, which forced us down to the picomolar range of imager concentration in the first place, resulted in the loss of our ability to use τ as a readout for determining both hybridization rates, but only k_{off} alone.

We tested this hypothesis in simulations using the experimentally measured $k_{\text{off}} = 0.23/\text{s}$ (taking the inverse of the mean in Fig. 7.12d), $k_{\text{on}} = 6.5 \times 10^6/\text{Ms}$ (the experimental value obtained in DNA origami experiments), $N = 22$ (assuming 32 NUP copies per localization cluster multiplied by the labeling efficiency of ~70 %, as recently reported for GFP-nanobody labeling [174]). Simulated measurement times were 4,500, 9,000, 14,000 and 18,000 frames and we used the experimental imager concentrations of 50 pM, 100 pM and 200 pM. Analyzing the simulated data sets via the lbFCS pipeline, we were able repoduce the expected outcome in τ and A, as indicated by the dashed lines as ground truth in Fig. 7.12f and g. However, the change in imager concentration in the picomolar range did expectedly not cause a measurable decrease in τ, but only affected A. While for A the relative deviation (shown below the two plots) shows a stronger dependence on the measurement time, overall the simulation results yield that for all three imager concentrations a measurement time of 18,000 frames should be sufficient to precisely determine both τ and A.

Lastly, we both plotted $\langle\tau\rangle$ and $1/A$ vs. imager concentration obtained from 18,000 frames simulations (Fig. 7.12h and i), again confirming our previous considerations that we can expect only observable changes in A, but not in τ for this low concentration range. However, both simulation and experiment show extremely good agreement in A (see Fig. 7.12i, dark green and light green, respectively), using an input of $k_{\text{on}} = 6.5 \times 10^6/\text{Ms}$ and N=22. This could be an indication for that i) the docking strands on the NPC-EGFP-nanobody inside the fixed U2OS cells experienced a similar association rate as in previous DNA origami experiments and ii) the labeling efficiency observed in our experiment agrees well with the reported 70 % [174]. Nonetheless, it should be stressed that due to their intertwined relationship $k_{\text{on}}N$ in A (see Eq. 2.39 on page 23), e.g., a k_{on} increased by factor of 2× in combination with only half of the number of docking strands $N/2$ would result in the same value for A. In order to truly use lbFCS as quantitative tool in cellular samples, it is, therefore, essential to further optimize the experimental conditions such that we can operate in an imager concentration regime that allows to induce an observable difference in τ, thereby providing access to both k_{on} and k_{off}, while still maintaining the high signal-to-noise ratio required for localizing single imager binding events.

7.3.4 Conclusion

To conclude, we were able to transfer both earlier findings obtained during the optimization process of rate determination, i.e., i) shorter measurement times and ii) using only two imager concentration points also to molecular counting with lbFCS. Based on this, we introduced a revised, direct counting framework that circumvents the need of assuming absolute imager concentration values during calculation of N. Next, we showed that lbFCS imager concentration series are possible within the same sample by repeated exchange of the imaging buffer and intermediate washing steps using a sample containing DNA origami with either a single or twelve docking strands. While these exchange series were extremely reproducible in both classical DNA-PAINT and lbFCS observables, we were not able to precisely adjust the imager concentration series, in contrast to the case of preparing three individual samples. However, here we could directly demonstrate the improvements of the direct lbFCS counting approach compared to the previously published framework. Finally, we demonstrated a first lbFCS concentration series on cellular structures targeting nucleoporin in the NPC of fixed U2OS cells. We found that the concentration range previously employed for DNA origami in the double digit nanomolar range is not usable in these cell experiments due to the high fluorescence background. Thus, we performed a first lbFCS concentration series on these targets in the picomolar range and observed numerous expedient results. Repeated imaging of the same FOV showed that, despite imager exchange and washing steps, the fixation protocol was robust enough, such that we were able to globally align the three obtained DNA-PAINT images down to the level of individual NPCs. Analysis of the detected localization clusters in five cells yielded repetitive imager binding in all three data sets and an increase of localizations proportional to the imager concentration.

The lbFCS analysis, however, revealed that imager concentrations in the picomolar range are too low to effect a measurable change in τ, losing the strength of lbFCS to obtain the hybridization rates as self calibration (but only k_{off}). However, A followed the expected behavior and indicated that we were able to adjust the imager concentrations at the desired ratios even inside the fixed cells. Assuming recent literature values for the labeling efficiency, k_{on} from DNA origami experiments and the experimentally observed k_{off}, we simulated synthetic data sets mimicking the experimental conditions. All simulation results were in good agreement with the experimental data, possibly indicating the rightfulness of our assumptions. However, there is an obvious need for further control experiments as well as for optimization of the experimental conditions, aiming at recuperating the self-calibrating nature of lbFCS.

8

In Vitro Reconstitution at Super-Resolution

8.1 Introduction

In the final chapter of this thesis, the results of a side project in collaboration with Beatrice Ramm are summarized. The project originated from the observation by Ramm *et al.* that the *E. coli* MinDE system can induce spatial sorting of membrane-bound molecules and cargo transport via surface traveling waves, when reconstituted *in vitro*. Here, we applied DNA-PAINT imaging with the aim to further elucidate this process on the scale of individual membrane-anchored DNA origami before and after initiation of MinDE surface wave formation. To our knowledge, this is the first structural super-resolution study in combination with a dynamic *in vitro* reconstituted protein system. Our results point towards promising applications of DNA-PAINT in the context of structural assemblies as formed by self-organizing proteins.

8.1.1 The MinCDE System

This short introduction to the MinCDE system is based on a recent and comprehensive review article by Ramm *et al.* [176], to which the interested reader is refered to for a more detailed summary.

The MinCDE system of *Escherichia coli* constitutes one of the best-studied reaction-diffusion systems in biology. As depicted in Fig. 8.1a, the proteins MinC (purple), MinD (green) and MinE (red) play a pivotal role in the complex mechanism of bacterial cell division. The proteins self-organize into periodic pole-to-pole oscillations on the inner plasma membrane of the rod-shaped bacteria and thereby define the site of division at midcell. The underlying mechanism is based on these oscillations giving rise to a time-averaged concentration minimum of MinC at midcell. As an inhibtor to the assembly of FtsZ - the main divisome protein - MinC thereby defines the site of the formation of the contractile FtsZ ring at the cell center [177–180].

Historically, mutations to the genetic locus *minB*, which encodes the three proteins, caused the formation of miniature cells and, thus, led to the first discovery [181, 182]. Together, MinC and MinD carry out the function of an inhibitor to cell division, whereas MinE acts as a topological specificity factor blocking septation at the cellular poles [183]. The first *in vivo* visualization of the characteristic oscillations by means of fluorescence microscopy in 1999 drew the attention of a larger audience of researcher to the MinCDE system [177, 184]. Almost a decade later, the first successful *in vitro* reconstitution of MinDE dynamics on supported lipid bilayers

(SLBs) as planar traveling surface waves was demonstrated [185] (see Fig. 8.1b). The ability to study the phenomenon under well-defined conditions and decoupled from the complexity of living cells has allowed researchers to accumulate an extensive theoretical understanding of the underlying mechanisms [186–188].

Fig. 8.1d illustrates the individual steps involved in spatio-temporal MinCDE pattern formation. Initally, freely-diffusing MinD dimerizes under ATP consumption allowing it to bind to the plasma membrane through its membrane targeting sequence (MTS) in a highly cooperative fashion [189]. Next, freely-diffusing dimeric MinC is recruited to the membrane via binding to membrane-associated MinD. The final phase of the oscillatory behavior is initiated when homodimerized MinE binds to MinD, causing the displacement of MinC back into the cell plasma. In a last step, MinE activates the ATPase activity of MinD leading to the monomerization of MinD and their subsequent detachement from the plasma membrane back to solution [190].

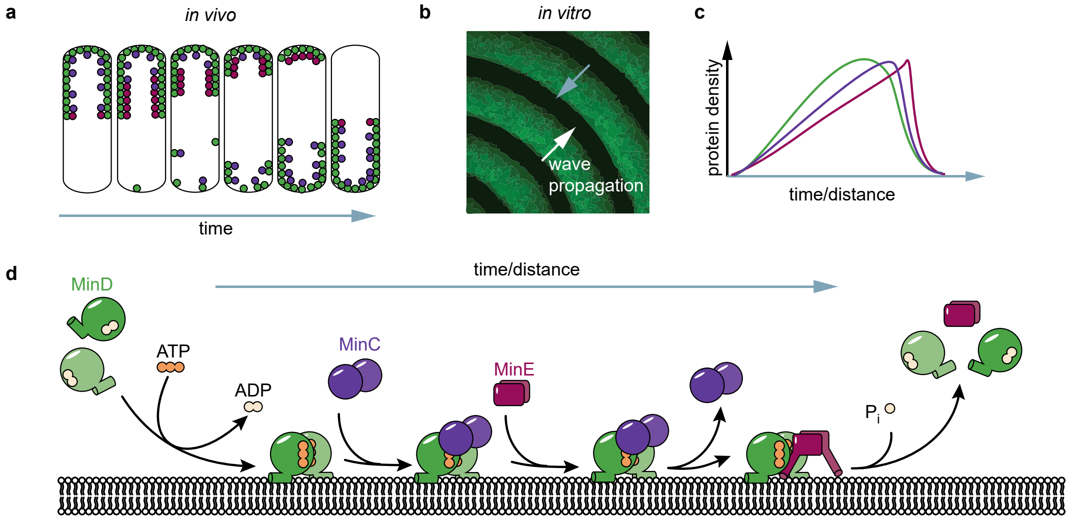

Figure 8.1. Principle of MinCDE Oscillations *in Vivo* and *in Vitro*. **a** Pole-to-pole oscillation schematic of MinCDE *in vivo*. **b** Planar traveling surface waves of MinCDE *in vitro*. **c** Schematic of spatial/temporal organisation of MinCDE in traveling waves. **d** Mechanistic schematic of MinCDE pattern formation. Reprinted from [176] (CC BY-NC 4.0).

8.1.2 Studying MinDE Pattern Formation *In Vitro* - Beyond FtsZ Positioning

Despite its crucial role *in vivo* of inhibiting FtsZ assembly, MinC is actually not required in the underlying process of pattern formation [185]: it has been demonstrated that surface traveling waves can be reconstituted on SLBs *in vitro* solely from MinD and MinE under the addition of ATP [185]. This fact gave rise to the question whether the laborious and ATP-expensive pole-to-pole oscillations of the Min system might have additional, so far uncharted functions beyond establishing the MinC concentration gradient. For instance, the ongoing debate regarding the mechanism of chromosome segregation in *E. coli* [191–193] lacking a ParABS system (driving active chromosome segregation in other prokaryotes) posed the question of an involvement of MinD as closest homolog to ParA [193]. As a second example for additional roles, a proteomics-based study showed that the Min system actively regulates the abundance of peripheral membrane proteins [194]. The latter is supported by recent *in vitro* studies demonstrating that MinDE surface-waves can displace and transport membrane-anchored molecules [195, 196]. Another recent finding by Glock *et al.* is the formation of stationary MinDE patterns, in which the individual proteins underlie the same dynamics as in waves, but the overall pattern remains static [197].

In the final paragraphs, the most recent findings by Ramm *et al.* [195] studying the regulation and transport of membrane-bound molecules on SLBs by MinDE traveling waves are outlined in brief, allowing a direct transition to the experimental results presented in this chapter. The schematic in Fig. 8.2a depicts the first model system mimicking a protein that binds reversibly to the membrane termed mCh-MTS, consisting of a C-terminal amphipathic helix (the MTS from MinD of *Bacillus subtilis*) fused to the fluorescent protein mCherry [195]. Whereas addition of solely mCh-MTS to SLBs resulted in a homogeneous membrane coverage, co-reconstitution with traveling MinDE waves (Fig. 8.2a, top image) led to anticorrelated pattern formation of mCh-MTS (Fig. 8.2a, bottom image) [195]. Subsequently, the experiment was repeated using fluorescently-labeled streptavidin which can freely diffuse on the SLB in 2D but is almost permanently bound to the membrane via biotinylated lipids (Fig. 8.2b) [195]. Again, co-reconstitution with surface-propagating MinDE waves induced an anticorrelated dynamic to the streptavidin molecules from an initially

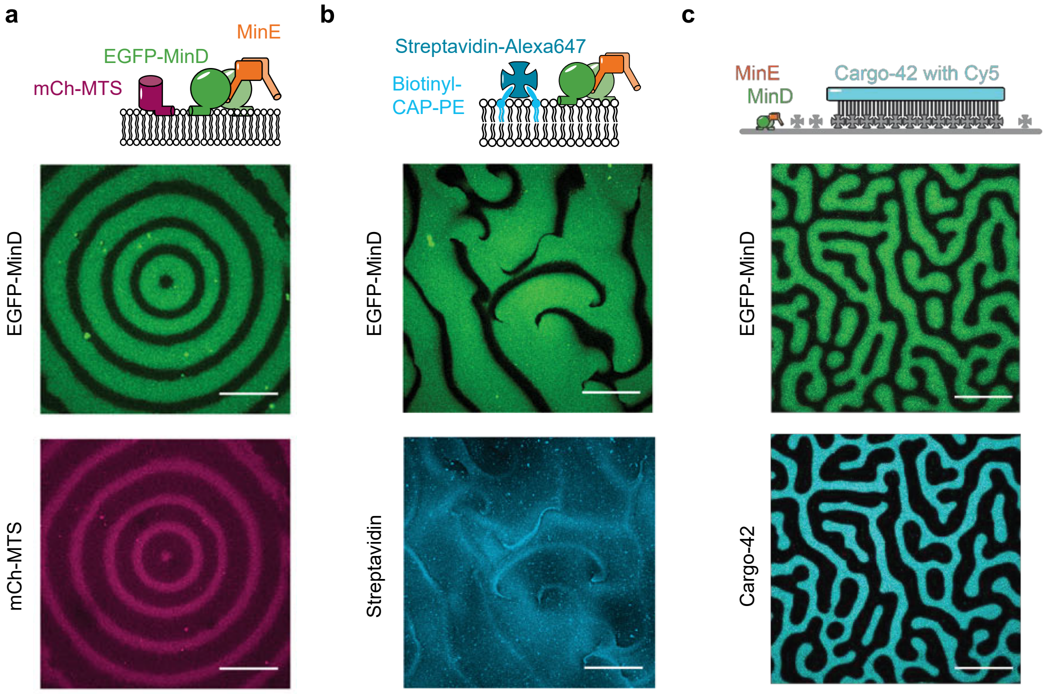

Figure 8.2. Nonspecific Cargo Positioning *in Vitro* by MinDE. **a** Co-reconstitution of mCherry-fused MTS (derived from *B. subtilis* MinD) and MinDE surface waves *in vitro* on SLB. **b** Co-reconstitution of membrane-anchored streptavidin (labeled with Alexa647) and MinDE surface waves *in vitro* on SLB. **c** Co-reconstitution of membrane-anchored DNA origami (tethered via biotinylated-lipid and streptavidin linker; labeled with Cy5) and static MinDE surface pattern on SLB. Scale bars, 50 μm. a,b reprinted, rearranged and relabeled from [195]. c reprinted, rearranged and relabeled from [198] (CC BY-NC 4.0).

homogeneous distribution (Fig. 8.2b, top image and bottom image, respectively) [195, 196]. Remarkably, due to its confinement to the membrane, streptavidin was depleted from certain membrane areas over time (in contrast to mCh-MTS being continuously replenished from solution) [195]. The proposed mechanism of these nonspecific interactions with membrane-bound molecules was MinDE acting as a moving diffusion barrier [195].

In their current preprint, Ramm *et al.* set out to further investigate the underlying mechanism of spatio-temporal transport of cargo by MinDE and present a theoretical framework based on diffusiophoresis [198]. The study is based on investigating MinDE-dependent transport of DNA origami, which serve as large cargo and are tethered to the membrane via multiple biotinylated single-stranded oligo extensions to membrane-bound streptavidin (see schematic in Fig. 8.2c) [198]. Upon co-reconstitution with stationary MinDE patterns, membrane-associated DNA origami were shown to be transported into the minima of the pattern during the pattern formation process (Fig. 8.2c, top and bottom, respectively) [198]. The deficient resolution of diffraction-limited fluorescence images did not allow to investigate the packing of DNA origami in these minima so far. For this reason we applied DNA-PAINT imaging to MinDE-positioned DNA origami with the aim to i) eventually resolve any structural information on DNA origami packing and to ii) probe the general applicability of DNA-based SMLM to a dynamic biological system reconstituted *in vitro*.

8.2 Results

Before presenting and discussing results, Beatrice Ramm is acknowledged for DNA origami folding and preparation of MinDE-SLB samples for joint DNA-PAINT experiments. Alena Khmelinskaia is acknowledged for the origami design.

8.2.1 DNA-PAINT Imaging of DNA Origami Positioned by MinDE

For DNA-PAINT imaging we employed the same DNA origami design as in [198], consisting of a rod-shaped 20-helix bundle (dimensions: 110x16x8 nm), but functionalized with 5 docking strands on the top (see Fig. 8.3a). The bottom side of the DNA origami offered max. 42 sites for modification with biotinylated strands for surface/membrane attachement (here only 2× biotin-extensions were used). Both 'head' and 'tail' of each DNA origami futhermore had 6 single-stranded extensions allowing to induce a cross-linking reaction via addition of a fully-complementary single strand at any point during an experiment and thereby immobilization of DNA origami ('head-to-tail polymerization'). All imaging experiments were performed on the custom-built TIRF microscope described in Chapter 4 (for detailed imaging parameters and sample preparation see Appendix A.2).

We first imaged the DNA origami surface-immobilized via BSA-biotin-streptavidin on a glass slide as a control for succesful folding. Exemplary origami images from the data set are depicted in Fig. 8.3b. After visually confirming the origami design of 5 docking strands at a ~20 nm spacing, we proceeded to co-reconstituion experiments on lipid bilayers. SLB samples with freely-diffusing and membrane-bound DNA origami (2×) were prepared in an open chamber allowing for fluid exchange. After

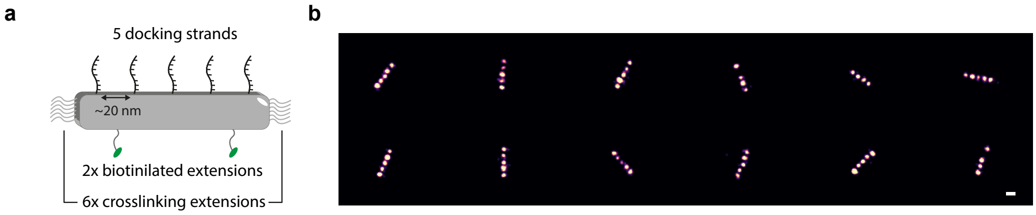

Figure 8.3. DNA Origami Design. **a** Schematic of DNA origami design with 5x docking strands for DNA-PAINT, 2× biotinylated extensions for surface/membrane attachement and 6× crosslinking extensions each on head and tail. **b** Exemplary DNA-PAINT images of surface-immobilized DNA origami visually confirming the designed docking strand pattern. Scale bars: 20 nm in b.

addition of imager strands to the sample for a final concentration of 10 nM, we added MinDE and ATP to initiate the process of pattern formation. After 30 minutes a static MinDE pattern had formed (Fig. 8.4a, EGFP-MinD channel) and immobilizing crosslinking strands were added to the flow-cell before starting DNA-PAINT image acquisition. Characteristic blinking due to imager binding predominantly in the regions of prior MinDE minima revealed repositioning of DNA origami already during acquisition of the image stack (see Fig. 8.4b). Localization and rendering of the super-resolved image confirmed this visual impression, clearly showing the anticorrelated spatial distribution of DNA origami with respect to the MinDE pattern, as depicted in Fig. 8.4c. Two zoom-ins (as indicated by the white boxes in 8.4a and c) show magnified regions of the MinDE pattern and the super-resolved image as well as a joint overlay in the center (see Fig. 8.4d). Inspection of the zoom-in in the DNA-PAINT image (Fig. 8.4d, right) revealed that the DNA origami appeared to be packed at a higher density within the central regions than towards the borders. Furthermore, we observed almost no unspecific localizations in those regions between the DNA origami, i.e., within the MinDE maxima. This is in contrast to the standard sample design of immobilized DNA origami directly on glass, where nonspecific adsorption of imagers is pervasive (compare Supplementary Fig. 4 in Chapter 6). Possible reasons for this could be surface passivation induced by the lipid membrane or by MinDE. Despite the crosslinking of DNA origami after successful formation of the MinDE pattern, the resolution of the the super-resolved image was not sufficient to globally identify any form of higher spatial arrangement of the repositioned DNA origami. Direct comparison of the two zoom-ins revealed (Fig. 8.4d, center) that the dense regions in the DNA-PAINT image perfectly co-localized with the minima in the MinDE pattern. However, the broader circumference of less packed DNA origami was clearly not observable in the EGFP-MinD image yielding a MinDE-coverage of these regions. After finishing the first imaging round in the evening, we found that repetitive imager binding was still active, when returning to the microscope the next morning. Hence, we started a second imaging round at a different FOV and rendered its super-resolved image (see Fig. 8.4e). Crosslinking of the DNA origami preserved the macroscopic spatial organisiation induced by the MinDE pattern, but we could no longer observe regions of high and low origami densities. Potentially, this was due to the inactivation of the MinDE dynamics as a result of sample aging and/or depletion of ATP. DNA origami covering significantly more area on the SLB compared to the Fig. 8.4c, in addition to the absence of a density gradient, could be an indication for relaxation of the origami confinement due to MinDE inactivity. A second observation was an increased localization precision in this second imaging round compared to the first image. As illustrated by the magnified regions in Fig. 8.4f, it was now possible to partially resolve individual docking strands on DNA origami and networks of crosslinked origami, particularly in the periphery. In the center areas, however, the linear pattern of only 5 docking strands per DNA origami did not allow to unambiguously identify neither individual orientations nor higher order origami packing.

8.2.2 Crosslinking DNA Origami Prior to MinDE Reconstitution

It was previously shown for polymerized FtsZ that the repositioning ability of MinDE was limited to freely-diffusing cargo on a SLB [176]. We were, therefore, interested in the influence of MinDE pattern formation on an already-crosslinked and rigid network of DNA origami on a SLB. For this purpose, we prepared a sample of diffusing DNA origami on a SLB as previously described, but this time adding the crosslinking DNA strands before addition of the MinDE system. This way, we aimed at polymerizing the DNA origami into a network, sufficiently immobile for DNA-PAINT imaging. Fig. 8.5a depicts the super-resolved image showing chains and networks of DNA origami allowing to clearly identify individual structures. After this first imaging round, we added MinDE and ATP to the same sample initiating the process of pattern formation. Waiting for 30 min, a stationary MinDE pattern had formed across the FOV, as depicted in Fig. 8.5d. We repeated a second round of DNA-PAINT imaging to investigate the effect of MinDE pattern formation onto the pre-formed DNA origami structure on the SLB. In line with the results obtained previously for FtsZ [195], the MinDE pattern did not seem to have a major influence onto the underlying structure, which was still fully covering the membrane (see Fig. 8.5b). We next aligned and overlayed both super-resolved images (pre- and post-MinDE pattern formation; red and green, respectively) finding a close-to-perfect colocalization of both networks, as illustrated in Fig. 8.5c. Overlaying the final MinDE pattern onto the super-resolved images shows that in the case of crosslinking the DNA origami prior to the addition and activation of MinDE fully deprived the system from its transportation ability. Notably, the process of MinDE pattern formation did not seem to be influenced by the presence of a dense and rigid network of DNA origami on the membrane. This is in accordance with previous observations of coupling of MinDE pattern formation across gaps [195, 199].

8.3 Summary and Outlook

We here applied for the first time DNA-PAINT imaging in combination with the reconstitution of a self-assembling protein system. Our aim was to exploit nanometer resolution for visualizing the packing of membrane-bound DNA origami structures by surface-traveling MinDE waves. We were able to successfully perform DNA-PAINT imaging simultaneously to the ongoing ATP-driven reaction of MinDE surface wave formation. However, the tight packing of DNA origami within the minima of static MinDE patterns did not allow to identify individual origami structures and, hence,

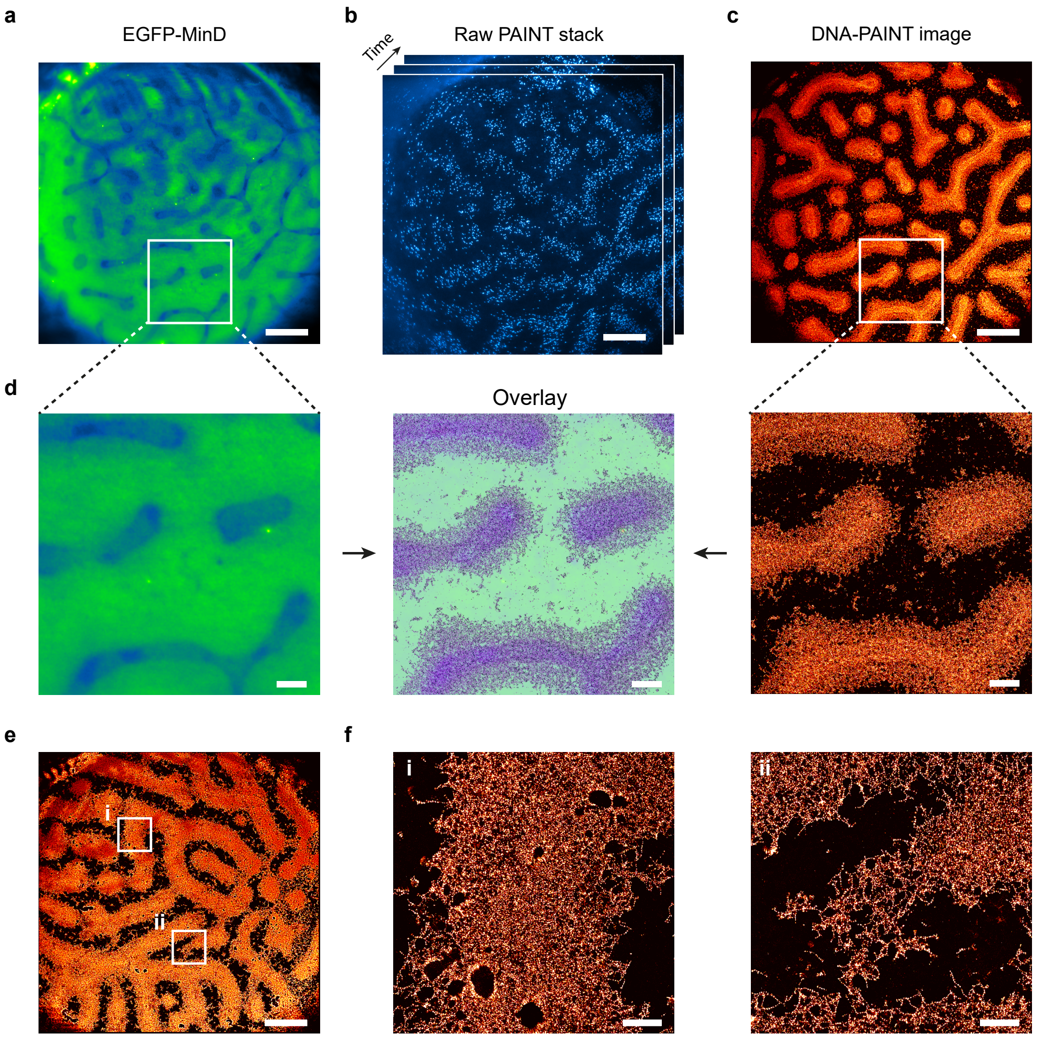

Figure 8.4. DNA-PAINT Imaging of Crosslinked DNA Origami in MinDE Pattern. **a** Stationary MinDE pattern formed on SLB in presence of membrane-anchored and freely-diffusing DNA origami. **b** DNA-PAINT image acquisition after pattern formation and crosslinking of DNA origami exhibiting characteristic SMLM blinking in MinDE minima. Same FOV as in c. **c** Rendered DNA-PAINT image of the same FOV as in a,b. **d** Zoom-ins indicated by white boxes in a,c, including an overlay in the center. **e** DNA-PAINT image from second imaging round after 12 hours. **f** Zoom-ins indicated by white boxes in e. Scale bars: 20 nm in b, 20 µm in (c-e,g), 4 µm in f and 2 µm in h.

higher order packing. Yet, we observed central regions of extremely tight packing and less packed DNA origami towards the periphery, which were covered by MinDE. The origami design of a single line of 5 docking strands turned out as inefficient in this perspective. Repeating the experiments with a flat-structure (i.e., rectangular origami [37]) would provide a larger origami area for positioning a more complex docking strand pattern, possibly allowing a unique identification of each origami. It should be noted that also crosslinking of DNA origami potentially alters the actual spatial arrangement solely produced by the MinDE pattern. Along this direction, it would

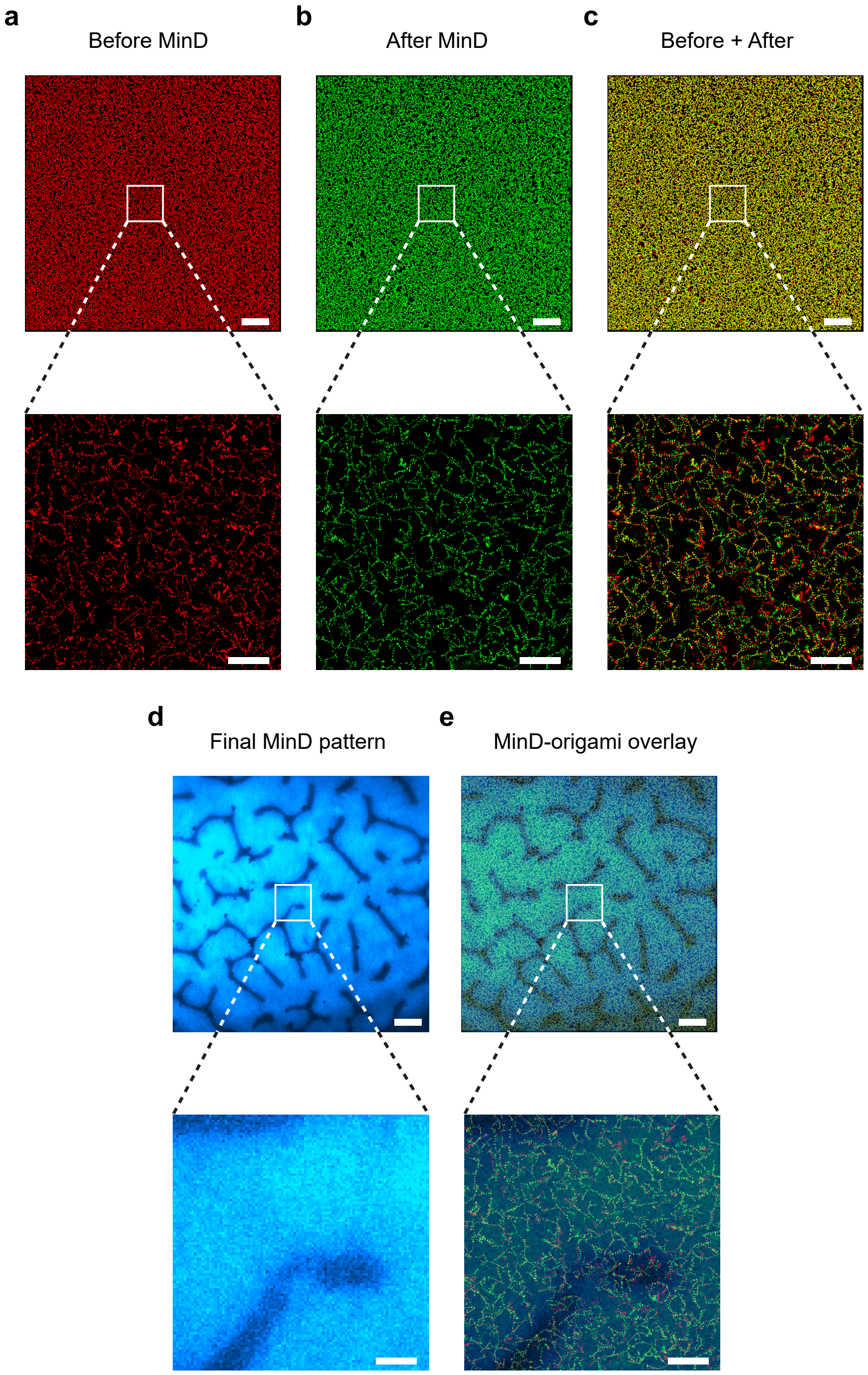
a
Before MinD
b
After MinD
c
Before + After
d
Final MinD pattern
e
MinD-origami overlay

Figure 8.5. Crosslinking DNA Origami Prior to MinDE Pattern Formation. **a** DNA-PAINT image of the crosslinked DNA origami network on a SLB prior to MinDE pattern formation. **b** DNA-PAINT image of the same FOV as in a, but acquired after MinDE pattern formation. **c** Aligned DNA-PAINT images of a and b. **d** Image of the MinDE pattern. Same FOV as in a-c. **e** Overlay of DNA-PAINT images and MinDE pattern. Scale bars, 10 µm in top images and 2 µm in zoom-ins.

be interesting to investigate whether packing can be strong enough to immobilize DNA origami without the need of crosslinking. Furthermore, it might be worth introducing a fraction of unlabeled DNA origami to the sample in order to reduce the density of docking strands in densely-packed regions of DNA origami. The super-resolved images of the crosslinked DNA origami network on a SLB showed that crosslinking was sufficient to force freely-diffusing DNA origami into a rigid network. Subsequent reconstitution of MinDE pattern formation showed that pattern formation was not hindered by the exisiting origami network covering the membrane as potential obstacles, in line with previous results [195, 199]. In addition, we showed that MinDE pattern formation had negligible effects on the structure of the rigid origami network. Overall, these are promising preliminary results, which point towards applications of DNA-PAINT in the context of *in vitro* structural assemblies, e.g., by self-organizing proteins.

9

Future Perspectives

Closing the loop to our initially stated motivation, we developed lbFCS driven by two goals: i) measuring the reaction rates of receptor-ligand binding at the single molecule level and ii) molecular counting of receptor copy numbers in case of multimeric receptor complexes. The results presented within this thesis point towards immediate next steps, which are outlined individually for both branches of lbFCS in the following.

Binding reaction rates. Studying bimolecular interactions at the level of single molecules in a highly parallelized manner is a promising strength of lbFCS. After an initially rather laborious and time-consuming workflow, we optimized sample preparation and acquisition times down to tens of minutes without sacrificing measurement precision. Depending on the requirements with respect to error bounds, even further speed increase is within reach. It will be interesting to explore the limits of lbFCS with respect to fast und slow bimolecular reactions. Within this work, we have shown that lbFCS allows to precisely quantify the effect of temperature and buffer ion composition onto DNA hybridization [97] for a given imager-docking strand design. Virtually any experimental factor influencing DNA hybridization could be monitored using lbFCS. To name a few examples, this could include base pair mismatches, epigenetic modifications or the addition of supplementary substances such as crowding agents. Furthermore, addition of unlabeled strands competing for docking strand binding [164] together with a modified theoretical framework could allow to also measure the reaction rates of the unlabeled species, thereby providing 'label-free' results without potential influences of the dye. These findings will yield valueable insights when applying lbFCS also to study protein-nucleic acid and protein-protein interactions, with one species surface-immobilized and the other species freely-diffusing and fluorescently-labeled. One possible strategy to achieve this would be capturing one of the binding partners on DNA origami as a binding platform. Here, the full strength of lbFCS could come into play when studying heterogeneous receptor-ligand interactions, where individual surface receptors could be assigned to distinct subclasses on the single molecule level. Finally, it might even be possible to study ligand binding interactions to transmembrane proteins of live cells - provided a sufficiently static target, e.g., receptors which are immobilized by an anchor to the cytoskeleton.

Molecular counting. The results presented in Chapters 6 and 7 show that lbFCS can readily be used as a robust quantitative tool for structural *in vitro* studies in combination with DNA-PAINT, e.g., for molecular counting of docking strands on DNA origami structures. However, lbFCS in its current form is laid out to operate in a nanomolar regime of imager concentrations, limiting its applicability to biologically more relevant *in situ* targets such as protein clusters in fixed cells due to high fluorescence background. Decreasing the imager concentrations down to the picomolar range, we were able to make several positive observations: successful imaging solution exchange and DNA-PAINT image alignment, repetitive imager binding to the same targets over hours, a concentration-dependent increase in the number of localizations and a sensible behavior in the lbFCS observables in line with simulations. Nonetheless, decreasing the imager concentration by two orders of magnitude came at the cost of losing the self-calibrating ability of lbFCS. Our next challenge will be to adapt our experimental and analytical strategies to the requirement of lower imager concentrations in order to hopefully retrieve the self-calibration ability of lbFCS in cellular targets. First of all, the decrease in c can be counterbalanced by an increase in k_{on} (see Eq. 2.38 on page 23). We have already demonstrated in Chapter 5 that this can, for instance, be achieved by using higher salt concentrations. Another recent idea is based on concatenating repetitive motives of binding sites to longer docking strands which similarly further enhances k_{on} [101, 167]. Alternatively, the necessity for reducing the imager concentration could potentially be alleviated by using fluorogenic imagers, which have been recently shown to largely reduce fluorescence background of unbound imagers [200]. Finally, in an ongoing study we are currently devising a strategy to make use of additional complementary observables, such as the photon counts, the number of imager binding events, the dark times or the number of localizations, which are currently not considered in lbFCS analysis. Since these additional observables depend solely on the global unknowns of a measurement (k_{on}, k_{off}, N), a closed analytical solution taking all observables into account can potentially be found. Under the reasonable assumption that a measurement must make sense in all of these observables, potentially even a single measurement at the highest possible imager concentration is sufficient for rate determination and molecular counting. Due to this depth of possible routes to go, we are confident to recover the self-calibrating property also in fixed cellular targets and - after careful benchmarking using well-characterized targets - apply lbFCS as a quantitative tool to unresolved structural questions in biology.

Part IV

Appendix

A.1 Appendix to Chapter 7

This section provides the experimental details regarding lbFCS experiments in combination with imager exchange, targeted at DNA origami and fixed U2OS samples. The used docking strand and imager sequences were 'Pm2', the same as in Chapter 6.

A.1.1 Sample Preparation and Imaging Conditions

The experimental data presented in Chapter 8 was acquired using two samples (s1 and s2). The following description includes the imaging protocol for several sequential acquisitions on the same sample. The imaging parameters are listed in Table A.1.

SAMPLE s1

$N = 1$ and $N = 12$ orgami were prepared and purified as described under Supplementary Methods in Chapter 6. DNA origami were diluted 1:200 and mixed at an approximate ratio of 1:1. Mixed DNA origami were surface-immobilized in an open chamber of an Ibidi μ-Slide via BSA-biotin and streptavidin, as described in Chapter 6. The total volume of BSA-biotin solution, streptavidin solution and mixed DNA origami solution in the individual incubation steps was each 200 μl. For washing, as much of the solution as possible was removed from the chamber using a pipette, before washing with 2× 200 μl of buffer A/B. After origami incubation and washing, imager solution at a given concentration was added to the chamber before imaging. In total, six measurements was performed in the order: 5 nM, 10 nM, 20 nM, 5 nM, 10 nM, 20 nM. Between each imaging round, the chamber was washed 3× with 200 μl of buffer B, while remaining mounted on the microscope (waiting time for each washing step: 1 min). Each image acquisition was started after adding the new imaging solution (waiting 3 min for equilibration) and moving to a new FOV.

SAMPLE s2

Nanobody-docking strand conjugation and preparation of fixed U2OS-CRISPR-Nup96-mEGFP cells labeled for DNA-PAINT imaging was performed by Kimberly Cramer, Sebastian Strauss and Bianca Sperl, as described in [167]. Fixed cellular samples were prepared in the open chamber of an open Ibidi μ-Slide. As described for s1, exchange steps were performed by removing as much of the solution from the chamber was possible using a pipette. 200 μl of imager solution at a given concentration was used for each round of imaging and in total four imaging rounds were performed in the order: 100 pM, 200 pM, 50 pM, 500 pM. The imaging buffer contained the oxygen scavenging system pyranose oxidase catalase in combination with the triplet state quencher trolox (POCT, as described in Chapter 3). Between each imaging round, the chamber was carefully washed with 3×200 μl of buffer POCT, while remaining mounted on the microscope (waiting time for each washing step: 2 min). Each image acquisition was started after adding the new imaging solution (waiting 5 min for equilibration) at the same FOV.

Table A.1. Imaging Parameters for Data Sets in Chapter 7. All fluorescence microscopy data was recorded with our custom TIRF microscope (see Chapter 4). The sCMOS camera (2048×2048 pixels, pixel size: 6.5 μm) was operated with the open source acquisition software μManager [201] at 2×2 binning. The exposure time was set to 200 ms, the read out rate to 200 MHz and the dynamic range to 16 bit. If not stated otherwise, the 561 nm laser was used for excitation.

Fig.	**Sample**	**Imager c (nM)**	**Buffer**	**Irradiance (W/cm^2)**	**Frames**	**FOV (px^2)**
7.8b,c	s1	5, 10, 20	B	10	6×4,500	700×700
7.9	s1	5, 10, 20	B	10	6×4,500	700×700
7.10c	s2	0.5	POCT	500	36,000	700×700
7.11b	s2	0.1	POCT	5 (488)	1	700×700
7.11c,d,e	s2	0.05, 0.1, 0.2	POCT	10	3×18,000	700×700
7.12	s2	0.05, 0.1, 0.2	POCT	10	3×18,000	700×700

A.1.2 Filtering and Counting DNA origami Exchange Series

Automatically detected localization clusters in the six DNA-PAINT images included both $N = 1$ and $N = 12$ DNA origami. Preliminary filterting was performed manually, disregarding localization clusters fulfilling the following parameters (T/2 denotes half of the measured frames):

- abs(mean(frame)-/T/2) / T/2 > 0.2
- std(frame) < 0.7 median(std(frame))

Subsequantly, localization clusters for each data set were split according to the number of localizations. Localization clusters fulfilling the following parameters were assigned to the $N = 1$ origami species:

- 5 nM: nlocs < 900
- 10 nM: nlocs < 1,800
- 20 nM: nlocs < 3,150

  The remaining localization clusters were assigned to the $N = 12$ origami species. Subsequently, filtering as decribed in Supplementary Fig. 3 in Chapter 6 was performed.

  Counting of docking strands was performed using the 'fit' method (described in Chapter 6) and the 'direct' method, as derived in Chapter 7 on page 153. For the 'direct' method, we calculated N from the four possible combinations of the four measurements at imager concentrations 5 nM and 20 nM. Using the mean of the distribution in τ and the median of the distribution in A of each data set, we obtained ($\langle\tau_{5\,\mathrm{nM}}\rangle$,$A_{5\,\mathrm{nM}}$,$\langle\tau_{20\,\mathrm{nM}}\rangle$,$A_{20\,\mathrm{nM}}$) as calculation input, allowing to directly calculate k_{off}, $\hat{k}_{on,5\,\mathrm{nM}}$ and $\hat{k}_{on,20\,\mathrm{nM}}$. Knowing these parameters, for each localization cluster the value of A could be transformed into N via Eq. 7.9 (page 153). The distributions of counted docking strands per origami displayed in Fig. 7.9 are the sum over the counting results from the calculations of four possible combinations of data sets.

A.1.3 Filtering and Counting Fixed U2OS Cells

The data sets acquired at imager concentrations 50 pM, 100 pM and 200 pM were subject to lbFCS analysis. Filtering was performed manually, removing localization clusters in the data sets fulfilling the following parameters:

- $\tau > 3\times\text{median}(\tau)$
- $\tau < 0.2\times\text{median}(\tau)$
- $A > 6\times\text{median(A)}$

A.2 Appendix to Chapter 8

This section provides the experimental details regarding DNA-PAINT imaging experiments of surface-immobilized and membrane-bound DNA origami in absence or presence of MinDE surface waves. The used docking strand and imager sequences were 'Pm2', the same as in Chapter 6. DNA origami (featuring 5 docking strands) were folded as described in [198]. After folding, DNA origami were purified using PEG precipitation [202].

A.2.1 Sample Preparation and Imaging Conditions

The experimental data presented in Chapter 8 was acquired using three samples (s1-s3). The following description includes the imaging protocol in case of several sequential acquisitions using the same sample. The imaging parameters are listed in Table A.2.

Sample s1

Surface-immobilized DNA origami were prepared at a dilution of 1:200, as described under Supplementary Methods in Chapter 6.

Sample s2

The SLB sample with membrane-bound DNA origami was prepared in an open chamber, as described in [198]. MinDE pattern formation was initiated by adding of MinD, MinE and ATP to the chamber (at conditions forming quasi-stationary patterns [197]), as described in [198]. After 30 min incubation, crosslinking strands were added to immobilize DNA origami. The imaging buffer contained the oxygen scavenging system pyranose oxidase catalase in combination with the triplet state quencher trolox (as described in Chapter 3). Finally, imagers were added to the chamber resulting in an effective imager concentration of 5 nM. Allowing the imager concentration to equilibrate, a single image of the MinDE pattern was acquired using a 488 nm laser line. Subsequently, DNA-PAINT image acquisition was started. A second round of image acquisition was started in the morning of the next day.

Sample s3

The SLB sample with membrane-bound DNA origami was prepared in an open chamber, as described in [198]. Crosslinking strands were added to the chamber in excess to induce 'head-to-tail'-polymerization of DNA origami into a rigid netword (incubation 2 min). The imaging buffer contained the oxygen scavenging system pyranose oxidase catalase in combination with the triplet state quencher trolox (as described in Chapter 3). Next, imagers were added to the chamber resulting in an effective imager concentration of 5 nM. Allowing the imager concentration to equilibrate, a first DNA-PAINT acquisition was started after 3 min. Subsequently, MinDE pattern formation was initiated by adding of MinD, MinE and ATP to the chamber (at conditions forming quasi-stationary patterns [197]), as described in [198]. Incubation time was 30 min. A single image of the MinDE pattern within the same

FOV as before was acquired using a 488 nm laser line. Finally, a second round of DNA-PAINT imaging was acquired, again of the same FOV.

Table A.2. Imaging Parameters for Data Sets in Chapter 8. All fluorescence microscopy data was recorded with our custom TIRF microscope (see Chapter 4). The sCMOS camera (2048×2048 pixels, pixel size: 6.5 μm) was operated with the open source acquisition software μManager [201] at 2×2 binning. The exposure time was set to 200 ms, the read out rate to 200 MHz and the dynamic range to 16 bit. If not stated otherwise, the 561 nm laser was used for excitation.

Fig.	**Sample**	**Imager c (nM)**	**Buffer**	**Irradiance (W/cm^2)**	**Frames**	**FOV (px^2)**
8.3b	s1	2	B	500	9,000	512×512
8.4a	s2	5	POCT	1 (488 nm)	1	1024×1024
8.4b-d	s2	5	POCT	1,000	10,000	1024×1024
8.4e-f	s2	5	POCT	1,000	40,000	1024×1024
8.5a	s3	5	POCT	1,000	20,000	720×720
8.5b	s3	5	POCT	1,000	40,000	720×720
8.5d	s3	5	POCT	1 (488 nm)	1	720×720

List of Figures

1.1 Specificity in Fluorescence Microscopy 4

2.1 Jablonski Diagram 7
2.2 Principle of Single Molecule Localization Microscopy 9
2.3 Principle of TIRF Microscopy 10
2.4 Schematic of a Confocal FCS Setup 12
2.5 Principle of Surface-Integrated FCS 13
2.6 The Structural Basis of DNA Nanotechnology 14
2.7 Principle of DNA-PAINT 16
2.8 Principle of Localization-Based FCS 19

7.1 Generalization of the Concept of lbFCS 141
7.2 Current lbFCS Workflow for Measuring Binding Kinetics 144
7.3 Two-Point lbFCS Concentration Series on 1DS Origami 146
7.4 Temporal Segmentation - Towards Faster Data Acquisition 148
7.5 Temporal Segmentation Results of lbFCS Concentration Series 149
7.6 Faster Acquisition of Two-Point lbFCS Concentration Series 151
7.7 Temporal Segmentation and a New Counting Approach for lbFCS . . . 155
7.8 lbFCS Concentration Series via Imager Exchange 157
7.9 Counting Results of lbFCS via Imager Exchange 158
7.10 Nuclear Pore Complexes as First Cellular lbFCS Targets 161
7.11 Exchange lbFCS Concentration Series on NPCs in Fixed U2OS Cells . . 162
7.12 Results of Exchange lbFCS Concentration Series on Fixed U2OS Cells . 163

8.1 Principle of MinCDE Oscillations *in Vivo* and *in Vitro* 168
8.2 Nonspecific Cargo Positioning *in Vitro* by MinDE 169
8.3 DNA Origami Design 171
8.4 DNA-PAINT Imaging of Crosslinked DNA Origami in MinDE Pattern 173
8.5 Crosslinking DNA Origami Prior to MinDE Pattern Formation 174

List of Tables

7.1 lbFCS Results for Hybridization Rates for 2-Point Concentration Series 145
7.2 lbFCS Results for Hybridization Rates for Shorter Measurement Times 150
7.3 lbFCS Results for Two-Point Concentration Series at Shorter Measurement Times 151

A.1 Imaging Parameters for Data Sets in Chapter 7 182
A.2 Imaging Parameters for Data Sets in Chapter 8 185

List of Abbreviations

1DS	DNA origami labeled with a single docking strand
EMCCD	Electron-Multiplying Charge-Coupled Device
FCCS	Fluorescence Cross-Correlation Spectroscopy
FCS	Fluorescence Correlation Spectroscopy
FISH	Fluorescence In-Situ Hybridization
FOV	field of view
FRAP	Fluorescence Recovery After Photobleaching
FRET	Förster Resonance Energy Transfer
GFP	Green Fluorescent Protein
HILO	Highly Inclined and Laminated Optical Sheet
lbFCS	localization-based Fluorescence Correlation Spectroscopy
mCh	soluble mCherry
MTS	membrane targeting sequence
NPC	Nuclear Pore Complex
NUP	Nucleoporin
PAINT	Points Accumulation for Imaging in Nanoscale Topography
PALM	Photoactivated Localization Microscopy
ROI	Region of Interest
SI-FCS	Surface-Integrated Fluorescence Correlation Spectroscopy
SIM	Structured Illumination Microscopy
SLB	supported lipid bilayer
SMLM	Single-Molecule Localization Microscopy
SOFI	Super-Resolution Optical Fluctuation Microscopy
STED	Stimulated Emission Depletion
STORM	Stochastic Optical Reconstruction Microscopy
TIR-FCS	Total Internal Reflection Fluorescence Correlation Spectroscopy
TIRF	Total Internal Reflection Fluorescence

Bibliography

1. Lichtman, J. W. & Conchello, J. A. Fluorescence microscopy. *Nature Methods* **2,** 910–919. doi:`10.1038/nmeth817` (Dec. 2005) (cit. on p. 3).
2. Heimstädt, O. Das Fluoreszenzmikroskop. *Z. Wiss. Mikrosk.* **28,** 330–337 (1911) (cit. on p. 3).
3. Egger, M. D. & Petran, M. New Reflected-Light Microscope for Viewing Unstained Brain and Ganglion Cells. *Science* **157,** 305 LP –307. doi:`10.1126/science.157.3786.305` (July 1967) (cit. on p. 3).
4. Sheppard, C. J. R. & Wilson, T. The theory of the direct-view confocal microscope. *Journal of Microscopy* **124,** 107–117. doi:`10.1111/j.1365-2818.1981.tb00304.x` (Nov. 1981) (cit. on p. 3).
5. White, J. G., Amos, W. B. & Fordham, M. An evaluation of confocal versus conventional imaging of biological structures by fluorescence light microscopy. *The Journal of cell biology* **105,** 41–48. doi:`10.1083/jcb.105.1.41` (July 1987) (cit. on p. 3).
6. Axelrod, D. Cell-substrate contacts illuminated by total internal reflection fluorescence. *The Journal of Cell Biology* **89,** 141 LP –145 (Apr. 1981) (cit. on pp. 3, 10, 12).
7. Denk, W., Strickler, J. H. & Webb, W. W. Two-photon laser scanning fluorescence microscopy. *Science* **248,** 73 LP –76. doi:`10.1126/science.2321027` (Apr. 1990) (cit. on p. 3).
8. Voie, A., Burns, D. & Spelman, F. Orthogonal-plane fluorescence optical sectioning: Three-dimensional imaging of macroscopic biological specimens. *Journal of Microscopy* **170,** 229–236. doi:`10.1111/j.1365-2818.1993.tb03346.x` (June 1993) (cit. on p. 3).
9. Huisken, J., Swoger, J., Del Bene, F., Wittbrodt, J. & Stelzer, E. H. K. Optical Sectioning Deep Inside Live Embryos by Selective Plane Illumination Microscopy. *Science* **305,** 1007 LP –1009. doi:`10.1126/science.1100035` (Aug. 2004) (cit. on p. 3).
10. Chalfie, M., Tu, Y., Euskirchen, G., Ward, W. W. & Prasher, D. C. Green fluorescent protein as a marker for gene expression. *Science* **263,** 802 LP –805. doi:`10.1126/science.8303295` (Feb. 1994) (cit. on p. 3).
11. Tsien, R. Y. THE GREEN FLUORESCENT PROTEIN. *Annual Review of Biochemistry* **67,** 509–544. doi:`10.1146/annurev.biochem.67.1.509` (June 1998) (cit. on p. 3).
12. Lippincott-Schwartz, J. & Patterson, G. H. Development and Use of Fluorescent Protein Markers in Living Cells. *Science* **300,** 87 LP –91. doi:`10.1126/science.1082520` (Apr. 2003) (cit. on p. 3).

13. Axelrod, D., Koppel, D. E., Schlessinger, J., Elson, E. & Webb, W. W. Mobility measurement by analysis of fluorescence photobleaching recovery kinetics. *Biophysical Journal* **16,** 1055–1069. doi:`10.1016/S0006-3495(76)85755-4` (Sept. 1976) (cit. on p. 3).
14. Koppel, D. E., Axelrod, D., Schlessinger, J., Elson, E. L. & Webb, W. W. Dynamics of fluorescence marker concentration as a probe of mobility. *Biophysical Journal* **16,** 1315–1329. doi:`10.1016/S0006-3495(76)85776-1` (Nov. 1976) (cit. on p. 3).
15. Magde, D., Elson, E. & Webb, W. W. Thermodynamic fluctuations in a reacting system measurement by fluorescence correlation spectroscopy. *Physical Review Letters* **29,** 705–708. doi:`10.1103/PhysRevLett.29.705` (Sept. 1972) (cit. on pp. 3, 11, 142).
16. Rigler, R. & Widengren, J. Ultrasensitive detection of single mol- ecules by fluorescence correlation spectroscopy. *Bioscience* **3,** 180–183 (1990) (cit. on pp. 3, 11).
17. Rigler, R., Mets, U., Widengren, J. & Kask, P. Fluorescence correlation spectroscopy with high count rate and low background: analysis of translational diffusion. *European Biophysics Journal* **22,** 169–175. doi:`10.1007/BF00185777` (Aug. 1993) (cit. on pp. 3, 11).
18. Hell, S. W. & Wichmann, J. Breaking the diffraction resolution limit by stimulated emission: stimulated-emission-depletion fluorescence microscopy. *Optics Letters* **19,** 780–782. doi:`10.1364/OL.19.000780` (1994) (cit. on pp. 3, 8).
19. Klar, T. A., Jakobs, S., Dyba, M., Egner, A. & Hell, S. W. Fluorescence microscopy with diffraction resolution barrier broken by stimulated emission. *Proceedings of the National Academy of Sciences of the United States of America* **97,** 8206–8210. doi:`10.1073/pnas.97.15.8206` (July 2000) (cit. on pp. 3, 8).
20. Rust, M. J., Bates, M. & Zhuang, X. Sub-diffraction-limit imaging by stochastic optical reconstruction microscopy (STORM). *Nature Methods* **3,** 793 (Aug. 2006) (cit. on pp. 3, 8, 9).
21. Betzig, E., Patterson, G. H., Sougrat, R., Lindwasser, O. W., Olenych, S., Bonifacino, J. S., Davidson, M. W., Lippincott-Schwartz, J. & Hess, H. F. Imaging Intracellular Fluorescent Proteins at Nanometer Resolution. *Science* **313,** 1642 LP –1645 (Sept. 2006) (cit. on pp. 3, 8, 9).
22. Seeman, N. C. Nucleic acid junctions and lattices. *Journal of Theoretical Biology* **99,** 237–247. doi:`10.1016/0022-5193(82)90002-9` (Nov. 1982) (cit. on p. 4).
23. Seeman, N. C. & Sleiman, H. F. DNA nanotechnology. *Nature Reviews Materials* **3,** 1–23. doi:`10.1038/natrevmats.2017.68` (Nov. 2017) (cit. on pp. 4, 13).
24. Seeman, N. C. Nanomaterials Based on DNA. *Annual Review of Biochemistry* **79,** 65–87. doi:`10.1146/annurev-biochem-060308-102244` (2010) (cit. on pp. 4, 13–15).
25. Rothemund, P. W. K. Folding DNA to create nanoscale shapes and patterns. *Nature* **440,** 297 (Mar. 2006) (cit. on pp. 5, 15).
26. Douglas, S. M., Dietz, H., Liedl, T., Högberg, B., Graf, F. & Shih, W. M. Self-assembly of DNA into nanoscale three-dimensional shapes. *Nature* **459,** 414–418. doi:`10.1038/nature08016` (May 2009) (cit. on pp. 5, 15).

27. Adleman, L. M. Molecular computation of solutions to combinatorial problems. *Science* **266,** 1021–1024. doi:`10.1126/science.7973651` (Nov. 1994) (cit. on p. 5).
28. Seelig, G., Soloveichik, D., Zhang, D. Y. & Winfree, E. Enzyme-free nucleic acid logic circuits. *Science* **314,** 1585–1588. doi:`10.1126/science.1132493` (Dec. 2006) (cit. on p. 5).
29. Qian, L., Winfree, E. & Bruck, J. Neural network computation with DNA strand displacement cascades. *Nature* **475,** 368–372. doi:`10.1038/nature10262` (July 2011) (cit. on p. 5).
30. Cherry, K. M. & Qian, L. Scaling up molecular pattern recognition with DNA-based winner-take-all neural networks. *Nature* **559,** 370–388. doi:`10.1038/s41586-018-0289-6` (July 2018) (cit. on p. 5).
31. Andersen, E. S., Dong, M., Nielsen, M. M., Jahn, K., Subramani, R., Mamdouh, W., Golas, M. M., Sander, B., Stark, H., Oliveira, C. L., Pedersen, J. S., Birkedal, V., Besenbacher, F., Gothelf, K. V. & Kjems, J. Self-assembly of a nanoscale DNA box with a controllable lid. *Nature* **459,** 73–76. doi:`10.1038/nature07971` (May 2009) (cit. on p. 5).
32. Omabegho, T., Sha, R. & Seeman, N. C. A bipedal DNA brownian motor with coordinated legs. *Science* **324,** 67–71. doi:`10.1126/science.1170336` (Apr. 2009) (cit. on p. 5).
33. Douglas, S. M., Bachelet, I. & Church, G. M. A logic-gated nanorobot for targeted transport of molecular payloads. *Science* **335,** 831–834. doi:`10.1126/science.1214081` (Feb. 2012) (cit. on p. 5).
34. Landegent, J. E., Jansen In De Wal, N., Van Omment, G. J., Baas, F., De Vijlderi, J. J., Van Duijn, P. & Van Der Ploeg, M. Chromosomal localization of a unique gene by non-autoradiographic in situ hybridization. *Nature* **317,** 175–177. doi:`10.1038/317175a0` (1985) (cit. on p. 5).
35. Lawrence, J. B., Singer, R. H. & McNeil, J. A. Interphase and metaphase resolution of different distances within the human dystrophin gene. *Science* **249,** 928–932. doi:`10.1126/science.2203143` (Aug. 1990) (cit. on p. 5).
36. Jungmann, R., Steinhauer, C., Scheible, M., Kuzyk, A., Tinnefeld, P. & Simmel, F. C. Single-Molecule Kinetics and Super-Resolution Microscopy by Fluorescence Imaging of Transient Binding on DNA Origami. *Nano Letters* **10,** 4756–4761. doi:`10.1021/nl103427w` (Nov. 2010) (cit. on pp. 5, 9, 15–17, 143).
37. Schnitzbauer, J., Strauss, M. T., Schlichthaerle, T., Schueder, F. & Jungmann, R. Super-resolution microscopy with DNA-PAINT. *Nature Protocols* **12,** 1198 (May 2017) (cit. on pp. 5, 15–17, 87, 173).
38. Jungmann, R., Avendaño, M. S., Woehrstein, J. B., Dai, M., Shih, W. M. & Yin, P. Multiplexed 3D cellular super-resolution imaging with DNA-PAINT and Exchange-PAINT. *Nature Methods* **11,** 313 (Feb. 2014) (cit. on pp. 5, 15, 156).
39. Jungmann, R., Avendaño, M. S., Dai, M., Woehrstein, J. B., Agasti, S. S., Feiger, Z., Rodal, A. & Yin, P. Quantitative super-resolution imaging with qPAINT. *Nature Methods* **13,** 439 (Mar. 2016) (cit. on pp. 5, 17, 27, 87, 113).

40. Mücksch, J., Blumhardt, P., Strauss, M. T., Petrov, E. P., Jungmann, R. & Schwille, P. Quantifying Reversible Surface Binding via Surface-Integrated Fluorescence Correlation Spectroscopy. *Nano Letters* **18,** 3185–3192. doi:`10.1021/acs.nanolett.8b00875` (May 2018) (cit. on pp. 5, 12, 13, 20, 142, 146, 163).

41. Abbe, E. Beiträge zur Theorie des Mikroskops und der mikroskopischen Wahrnehmung. *Archiv für mikroskopische Anatomie* **9,** 418–440 (Dec. 1873) (cit. on p. 8).

42. Chen Bai, X., McMullan, G. & Scheres, S. H. How cryo-EM is revolutionizing structural biology. *Trends in Biochemical Sciences* **40,** 49–57. doi:`10.1016/j.tibs.2014.10.005` (Jan. 2015) (cit. on p. 8).

43. Baddeley, D. & Bewersdorf, J. Biological Insight from Super-Resolution Microscopy: What We Can Learn from Localization-Based Images. *Annual Review of Biochemistry* **87,** 1–25. doi:`10.1146/annurev-biochem-060815-014801` (June 2018) (cit. on pp. 8, 113, 141).

44. Hell, S. W., Sahl, S. J., Bates, M., Zhuang, X., Heintzmann, R., Booth, M. J., Bewersdorf, J., Shtengel, G., Hess, H., Tinnefeld, P., Honigmann, A., Jakobs, S., Testa, I., Cognet, L., Lounis, B., Ewers, H., Davis, S. J., Eggeling, C., Klenerman, D., Willig, K. I., Vicidomini, G., Castello, M., Diaspro, A. & Cordes, T. The 2015 super-resolution microscopy roadmap. *Journal of Physics D: Applied Physics* **48,** 443001. doi:`10.1088/0022-3727/48/44/443001` (2015) (cit. on p. 8).

45. Huang, B., Bates, M. & Zhuang, X. Super-Resolution Fluorescence Microscopy. *Annual Review of Biochemistry* **78,** 993–1016. doi:`10.1146/annurev.biochem.77.061906.092014` (June 2009) (cit. on pp. 8, 9).

46. Berning, S., Willig, K. I., Steffens, H., Dibaj, P. & Hell, S. W. Nanoscopy in a living mouse brain. *Science* **335,** 551. doi:`10.1126/science.1215369` (Feb. 2012) (cit. on p. 8).

47. Chojnacki, J., Staudt, T., Glass, B., Bingen, P., Engelhardt, J., Anders, M., Schneider, J., Müller, B., Hell, S. W. & Kräusslich, H. G. Maturation-dependent HIV-1 surface protein redistribution revealed by fluorescence nanoscopy. *Science* **338,** 524–528. doi:`10.1126/science.1226359` (Oct. 2012) (cit. on p. 8).

48. Gustafsson, M. G. Surpassing the lateral resolution limit by a factor of two using structured illumination microscopy. *Journal of Microscopy* **198,** 82–87. doi:`10.1046/j.1365-2818.2000.00710.x` (May 2000) (cit. on p. 8).

49. Heintzmann, R. & Cremer, C. G. *Laterally modulated excitation microscopy: improvement of resolution by using a diffraction grating* in *Optical Biopsies and Microscopic Techniques III* (eds Bigio, I. J., Schneckenburger, H., Slavik, J., Svanberg, K. & Viallet, P. M.) **3568** (SPIE, Jan. 1999), 185–196. doi:`10.1117/12.336833` (cit. on p. 8).

50. Demmerle, J., Innocent, C., North, A. J., Ball, G., Müller, M., Miron, E., Matsuda, A., Dobbie, I. M., Markaki, Y. & Schermelleh, L. Strategic and practical guidelines for successful structured illumination microscopy. *Nature Protocols* **12,** 988–1010. doi:`10.1038/nprot.2017.019` (May 2017) (cit. on p. 8).

51. Dertinger, T., Colyer, R., Iyer, G., Weiss, S. & Enderlein, J. Fast, background-free, 3D super-resolution optical fluctuation imaging (SOFI). *Proceedings of the National Academy of Sciences* **106,** 22287 LP –22292. doi:`10.1073/pnas.0907866106` (Dec. 2009) (cit. on p. 8).

52. Balzarotti, F., Eilers, Y., Gwosch, K. C., Gynnå, A. H., Westphal, V., Stefani, F. D., Elf, J. & Hell, S. W. Nanometer resolution imaging and tracking of fluorescent molecules with minimal photon fluxes. *Science* **355,** 606–612. doi:`10.1126/science.aak9913`. arXiv: `1611.03401` (Feb. 2017) (cit. on p. 8).

53. Gwosch, K. C., Pape, J. K., Balzarotti, F., Hoess, P., Ellenberg, J., Ries, J. & Hell, S. W. MINFLUX nanoscopy delivers 3D multicolor nanometer resolution in cells. *Nature Methods* **17,** 217–224. doi:`10.1038/s41592-019-0688-0` (Feb. 2020) (cit. on p. 8).

54. Hess, S. T., Girirajan, T. P. & Mason, M. D. Ultra-high resolution imaging by fluorescence photoactivation localization microscopy. *Biophysical Journal* **91,** 4258–4272. doi:`10.1529/biophysj.106.091116` (2006) (cit. on p. 9).

55. Heilemann, M., Van De Linde, S., Schüttpelz, M., Kasper, R., Seefeldt, B., Mukherjee, A., Tinnefeld, P. & Sauer, M. Subdiffraction-resolution fluorescence imaging with conventional fluorescent probes. *Angewandte Chemie - International Edition* **47,** 6172–6176. doi:`10.1002/anie.200802376` (Aug. 2008) (cit. on p. 9).

56. Sharonov, A. & Hochstrasser, R. M. Wide-field subdiffraction imaging by accumulated binding of diffusing probes. *Proceedings of the National Academy of Sciences* **103,** 18911 LP –18916 (Dec. 2006) (cit. on pp. 9, 15).

57. Tokunaga, M., Imamoto, N. & Sakata-Sogawa, K. Highly inclined thin illumination enables clear single-molecule imaging in cells. *Nature Methods* **5,** 159 (Jan. 2008) (cit. on pp. 10, 152, 160).

58. Ha, T. & Tinnefeld, P. Photophysics of fluorescent probes for single-molecule biophysics and super-resolution imaging. *Annual Review of Physical Chemistry* **63,** 595–617. doi:`10.1146/annurev-physchem-032210-103340` (May 2012) (cit. on p. 11).

59. Manzo, C. & Garcia-Parajo, M. F. A review of progress in single particle tracking: from methods to biophysical insights. *Reports on Progress in Physics* **78,** 124601 (2015) (cit. on p. 11).

60. Miller, H., Zhou, Z., Shepherd, J., Wollman, A. J. & Leake, M. C. Single-molecule techniques in biophysics: A review of the progress in methods and applications. *Reports on Progress in Physics* **81,** 024601. doi:`10.1088/1361-6633/aa8a02` (Feb. 2018) (cit. on p. 11).

61. Haustein, E. & Schwille, P. Fluorescence Correlation Spectroscopy: Novel Variations of an Established Technique. *Annual Review of Biophysics and Biomolecular Structure* **36,** 151–169. doi:`10.1146/annurev.biophys.36.040306.132612` (June 2007) (cit. on p. 11).

62. Petrov, E. P. & Schwille, P. in *Standardization and Quality Assurance in Fluorescence Measurements II* 145–197 (Springer Berlin Heidelberg, Mar. 2008). doi:`10.1007/4243_2008_032` (cit. on p. 11).

63. Webb, W. W. Fluorescence correlation spectroscopy: Genesis, evolution, maturation and prognosis. *Springer Series in Chemical Physics* **65,** 305–330. doi:10.1007/978-3-642-59542-4_14 (2001) (cit. on p. 11).

64. Macháň, R. & Wohland, T. Recent applications of fluorescence correlation spectroscopy in live systems. *FEBS Letters* **588,** 3571–3584. doi:10.1016/j.febslet.2014.03.056 (Oct. 2014) (cit. on p. 11).

65. Weidemann, T., Mücksch, J. & Schwille, P. Fluorescence fluctuation microscopy: A diversified arsenal of methods to investigate molecular dynamics inside cells. *Current Opinion in Structural Biology* **28,** 69–76. doi:10.1016/j.sbi.2014.07.008 (Oct. 2014) (cit. on p. 11).

66. Ries, J. & Schwille, P. Fluorescence correlation spectroscopy. *BioEssays* **34,** 361–368. doi:10.1002/bies.201100111 (May 2012) (cit. on p. 11).

67. Petrášek, Z. & Schwille, P. Fluctuations as a source of information in fluorescence microscopy. *Journal of The Royal Society Interface* **6.** doi:10.1098/rsif.2008.0200.focus (Feb. 2009) (cit. on p. 11).

68. Schwille, P. There and back again: from the origin of life to single molecules. *European Biophysics Journal* **47,** 493–498. doi:10.1007/s00249-018-1295-1 (May 2018) (cit. on p. 11).

69. Eigen, M. & Rigler, R. Sorting single molecules: Application to diagnostics and evolutionary biotechnology. *Proceedings of the National Academy of Sciences* **91,** 5740–5747. doi:10.1073/pnas.91.13.5740 (June 1994) (cit. on pp. 11, 142).

70. Schwille, P., Meyer-Almes, F. J. & Rigler, R. Dual-color fluorescence cross-correlation spectroscopy for multicomponent diffusional analysis in solution. *Biophysical Journal* **72,** 1878–1886. doi:10.1016/s0006-3495(97)78833-7 (Apr. 1997) (cit. on pp. 12, 142).

71. Kettling, U., Koltermann, A., Schwille, P. & Eigen, M. Real-time enzyme kinetics monitored by dual-color fluorescence cross-correlation spectroscopy. *Proceedings of the National Academy of Sciences of the United States of America* **95,** 1416–1420. doi:10.1073/pnas.95.4.1416 (Feb. 1998) (cit. on p. 12).

72. Heinze, K. G., Rarbach, M., Jahnz, M. & Schwille, P. Two-photon fluorescence coincidence analysis: Rapid measurements of enzyme kinetics. *Biophysical Journal* **83,** 1671–1681. doi:10.1016/S0006-3495(02)73935-0 (Sept. 2002) (cit. on p. 12).

73. Kohl, T., Haustein, E. & Schwille, P. Determining protease activity in vivo by fluorescence cross-correlation analysis. *Biophysical Journal* **89,** 2770–2782. doi:10.1529/biophysj.105.061127 (Oct. 2005) (cit. on p. 12).

74. Thompson, N. L., Burghardt, T. P. & Axelrod, D. Measuring surface dynamics of biomolecules by total internal reflection fluorescence with photobleaching recovery or correlation spectroscopy. *Biophysical Journal* **33,** 435–454. doi:10.1016/S0006-3495(81)84905-3 (Mar. 1981) (cit. on pp. 12, 13, 20, 142).

75. Stout, A. L. & Axelrod, D. Evanescent field excitation of fluorescence by epi-illumination microscopy. *Applied Optics* **28,** 5237. doi:10.1364/ao.28.005237 (Dec. 1989) (cit. on p. 12).

76. Axelrod, D. Total internal reflection fluorescence microscopy in cell biology. *Traffic* **2,** 764–774. doi:`10.1034/j.1600-0854.2001.21104.x` (Nov. 2001) (cit. on p. 12).

77. Hassler, K., Anhut, T., Rigler, R., Gösch, M. & Lasser, T. High count rates with total internal reflection fluorescence correlation spectroscopy. *Biophysical Journal* **88,** L01–L03. doi:`10.1529/biophysj.104.053884` (Jan. 2005) (cit. on p. 12).

78. Hassler, K., Rigler, P., Blom, H., Rigler, R., Widengren, J. & Lasser, T. Dynamic disorder in horseradish peroxidase observed with total internal reflection fluorescence correlation spectroscopy. *Optics Express* **15,** 5366. doi:`10.1364/oe.15.005366` (Apr. 2007) (cit. on pp. 12, 142).

79. Ohsugi, Y., Saito, K., Tamura, M. & Kinjo, M. Lateral mobility of membrane-binding proteins in living cells measured by total internal reflection fluorescence correlation spectroscopy. *Biophysical Journal* **91,** 3456–3464. doi:`10.1529/biophysj.105.074625` (Nov. 2006) (cit. on p. 12).

80. Sonesson, A. W., Blom, H., Hassler, K., Elofsson, U. M., Callisen, T. H., Widengren, J. & Brismar, H. Protein-surfactant interactions at hydrophobic interfaces studied with total internal reflection fluorescence correlation spectroscopy (TIR-FCS). *Journal of Colloid and Interface Science* **317,** 449–457. doi:`10.1016/j.jcis.2007.09.089` (Jan. 2008) (cit. on p. 12).

81. Blom, H., Chmyrov, A., Hassler, K., Davis, L. M. & Widengren, J. Triplet-state investigations of fluorescent dyes at dielectric interfaces using total internal reflection fluorescence correlation spectroscopy. *Journal of Physical Chemistry A* **113,** 5554–5566. doi:`10.1021/jp8110088` (May 2009) (cit. on p. 12).

82. Kannan, B., Guo, L., Sudhaharan, T., Ahmed, S., Maruyama, I. & Wohland, T. Spatially resolved total internal reflection fluorescence correlation microscopy using an electron multiplying charge-coupled device camera. *Analytical Chemistry* **79,** 4463–4470. doi:`10.1021/ac0624546` (June 2007) (cit. on pp. 12, 13).

83. Bag, N., Sankaran, J., Paul, A., Kraut, R. S. & Wohland, T. Calibration and Limits of Camera-Based Fluorescence Correlation Spectroscopy: A Supported Lipid Bilayer Study. *ChemPhysChem* **13,** 2784–2794. doi:`10.1002/cphc.201200032` (Aug. 2012) (cit. on p. 13).

84. Brandão, H. B., Sangji, H., Pandžić, E., Bechstedt, S., Brouhard, G. J. & Wiseman, P. W. Measuring ligand-receptor binding kinetics and dynamics using k-space image correlation spectroscopy. *Methods* **66,** 273–282. doi:`10.1016/j.ymeth.2013.07.042` (Mar. 2014) (cit. on p. 13).

85. Ries, J., Petrov, E. P. & Schwille, P. Total internal reflection fluorescence correlation spectroscopy: Effects of lateral diffusion and surface-generated fluorescence. *Biophysical Journal* **95,** 390–399. doi:`10.1529/biophysj.107.126193` (July 2008) (cit. on p. 13).

86. Ouldridge, T. E., Šulc, P., Romano, F., Doye, J. P. & Louis, A. A. DNA hybridization kinetics: Zippering, internal displacement and sequence dependence. *Nucleic Acids Research* **41,** 8886–8895. doi:`10.1093/nar/gkt687` (Oct. 2013) (cit. on pp. 14, 17).

87. Watson, J. D. & Crick, F. H. Molecular structure of nucleic acids: A structure for deoxyribose nucleic acid. *Nature* **171,** 737–738. doi:`10.1038/171737a0` (1953) (cit. on p. 14).

88. Voet, D. & Rich, A. The Crystal Structures of Purines, Pyrimidines and Their Intermolecular Complexes. *Progress in Nucleic Acid Research and Molecular Biology* **10,** 183–265. doi:`10.1016/S0079-6603(08)60565-6` (Jan. 1970) (cit. on p. 14).

89. Levsky, J. M. & Singer, R. H. Fluorescence in situ hybridization: Past, present and future. *Journal of Cell Science* **116,** 2833–2838. doi:`10.1242/jcs.00633` (July 2003) (cit. on p. 15).

90. Moter, A. & Göbel, U. B. Fluorescence in situ hybridization (FISH) for direct visualization of microorganisms. *Journal of Microbiological Methods* **41,** 85–112. doi:`10.1016/S0167-7012(00)00152-4` (July 2000) (cit. on p. 15).

91. Deschout, H., Zanacchi, F. C., Mlodzianoski, M., Diaspro, A., Bewersdorf, J., Hess, S. T. & Braeckmans, K. Precisely and accurately localizing single emitters in fluorescence microscopy. *Nature Methods* **11,** 253 (Feb. 2014) (cit. on p. 15).

92. Schueder, F., Lara-Gutiérrez, J., Beliveau, B. J., Saka, S. K., Sasaki, H. M., Woehrstein, J. B., Strauss, M. T., Grabmayr, H., Yin, P. & Jungmann, R. Multiplexed 3D super-resolution imaging of whole cells using spinning disk confocal microscopy and DNA-PAINT. *Nature Communications* **8,** 2090. doi:`10.1038/s41467-017-02028-8` (2017) (cit. on p. 15).

93. Stehr, F., Stein, J., Schueder, F., Schwille, P. & Jungmann, R. Flat-top TIRF illumination boosts DNA-PAINT imaging and quantification. *Nature Communications* **10,** 1268. doi:`10.1038/s41467-019-09064-6` (2019) (cit. on pp. 15, 16, 60, 87).

94. Steinhauer, C., Jungmann, R., Sobey, T. L., Simmel, F. C. & Tinnefeld, P. DNA Origami as a Nanoscopic Ruler for Super-Resolution Microscopy. *Angewandte Chemie International Edition* **48,** 8870–8873. doi:`10.1002/anie.200903308` (Nov. 2009) (cit. on p. 16).

95. Howorka, S., Movileanu, L., Braha, O. & Bayley, H. Kinetics of duplex formation for individual DNA strands within a single protein nanopore. *Proceedings of the National Academy of Sciences* **98,** 12996 LP –13001. doi:`10.1073/pnas.231434698` (Nov. 2001) (cit. on pp. 17, 143).

96. Dupuis, N. F., Holmstrom, E. D. & Nesbitt, D. J. Single-molecule kinetics reveal cation-promoted DNA duplex formation through ordering of single-stranded helices. *Biophysical journal* **105,** 756–766. doi:`10.1016/j.bpj.2013.05.061` (Aug. 2013) (cit. on p. 17).

97. Stein, J., Stehr, F., Schueler, P., Blumhardt, P., Schueder, F., Mücksch, J., Jungmann, R. & Schwille, P. Toward Absolute Molecular Numbers in DNA-PAINT. *Nano Letters* **19,** 8182–8190. doi:`10.1021/acs.nanolett.9b03546` (Nov. 2019) (cit. on pp. 17–19, 27, 87, 114, 141, 143, 146, 147, 149–151, 155, 156, 158, 159, 177).

98. Wade, O. K., Woehrstein, J. B., Nickels, P. C., Strauss, S., Stehr, F., Stein, J., Schueder, F., Strauss, M. T., Ganji, M., Schnitzbauer, J., Grabmayr, H., Yin, P., Schwille, P. & Jungmann, R. 124-Color Super-resolution Imaging by Engineering DNA-PAINT Blinking Kinetics. *Nano Letters* **19,** 2641–2646. doi:`10.1021/acs.nanolett.9b00508` (Apr. 2019) (cit. on p. 17).

99. Schickinger, M., Zacharias, M. & Dietz, H. Tethered multifluorophore motion reveals equilibrium transition kinetics of single DNA double helices. *Proceedings of the National Academy of Sciences* **115,** E7512 LP –E7521 (Aug. 2018) (cit. on pp. 18, 87).

100. Schueder, F., Stein, J., Stehr, F., Auer, A., Sperl, B., Strauss, M. T., Schwille, P. & Jungmann, R. An order of magnitude faster DNA-PAINT imaging by optimized sequence design and buffer conditions. *Nature Methods* **16,** 1101–1104. doi:`10.1038/s41592-019-0584-7` (Nov. 2019) (cit. on pp. 18, 88).

101. Stein, J., Stehr, F., Bauer, J., Niederauer, C., Jungmann, R., Ganzinger, K. & Schwille, P. Tracking Single Particles for Hours via Continuous DNA-mediated Fluorophore Exchange. *bioRxiv,* 2020.05.17.100354. doi:`10.1101/2020.05.17.100354` (Jan. 2020) (cit. on pp. 18, 178).

102. Zadeh, J. N., Steenberg, C. D., Bois, J. S., Wolfe, B. R., Pierce, M. B., Khan, A. R., Dirks, R. M. & Pierce, N. A. NUPACK: Analysis and design of nucleic acid systems. *Journal of Computational Chemistry* **32,** 170–173. doi:`10.1002/jcc.21596` (Jan. 2011) (cit. on p. 18).

103. Starr, T. E. & Thompson, N. L. Total Internal Reflection with Fluorescence Correlation Spectroscopy: Combined Surface Reaction and Solution Diffusion. *Biophysical Journal* **80,** 1575–1584. doi:`https://doi.org/10.1016/S0006-3495(01)76130-9` (2001) (cit. on p. 20).

104. Blumhardt, P., Stein, J., Mücksch, J., Stehr, F., Bauer, J., Jungmann, R. & Schwille, P. Photo-Induced Depletion of Binding Sites in DNA-PAINT Microscopy. *Molecules* **23,** 3165. doi:`10.3390/molecules23123165` (Nov. 2018) (cit. on p. 28).

105. Nicovich, P. R., Owen, D. M. & Gaus, K. Turning single-molecule localization microscopy into a quantitative bioanalytical tool. *Nature Protocols* **12,** 453 (Feb. 2017) (cit. on pp. 113, 141).

106. Annibale, P., Vanni, S., Scarselli, M., Rothlisberger, U. & Radenovic, A. Quantitative Photo Activated Localization Microscopy: Unraveling the Effects of Photoblinking. *PLOS ONE* **6,** e22678 (July 2011) (cit. on p. 113).

107. Annibale, P., Vanni, S., Scarselli, M., Rothlisberger, U. & Radenovic, A. Identification of clustering artifacts in photoactivated localization microscopy. *Nature Methods* **8,** 527 (June 2011) (cit. on p. 113).

108. Hummer, G., Fricke, F. & Heilemann, M. Model-independent counting of molecules in single-molecule localization microscopy. *Molecular Biology of the Cell* **27,** 3637–3644. doi:`10.1091/mbc.e16-07-0525` (July 2016) (cit. on p. 113).

109. Laplante, C., Huang, F., Tebbs, I. R., Bewersdorf, J. & Pollard, T. D. Molecular organization of cytokinesis nodes and contractile rings by super-resolution fluorescence microscopy of live fission yeast. *Proceedings of the National Academy of Sciences* **113,** E5876 LP –E5885. doi:`10.1073/pnas.1608252113` (Oct. 2016) (cit. on p. 113).

110. Nino, D., Rafiei, N., Wang, Y., Zilman, A. & Milstein, J. N. Molecular Counting with Localization Microscopy: A Bayesian Estimate Based on Fluorophore Statistics. *Biophysical Journal* **112,** 1777–1785. doi:`https://doi.org/10.1016/j.bpj.2017.03.020` (2017) (cit. on p. 113).

111. Golfetto, O., Wakefield, D. L., Cacao, E. E., Avery, K. N., Kenyon, V., Jorand, R., Tobin, S. J., Biswas, S., Gutierrez, J., Clinton, R., Ma, Y., Horne, D. A., Williams, J. C. & Jovanović-Talisman, T. A Platform To Enhance Quantitative Single Molecule Localization Microscopy. *Journal of the American Chemical Society* **140,** 12785–12797. doi:`10.1021/jacs.8b04939` (Oct. 2018) (cit. on p. 113).

112. Coltharp, C., Kessler, R. P. & Xiao, J. Accurate Construction of Photoactivated Localization Microscopy (PALM) Images for Quantitative Measurements. *PLOS ONE* **7,** e51725 (Dec. 2012) (cit. on p. 113).

113. Lee, S.-H., Shin, J. Y., Lee, A. & Bustamante, C. Counting single photoactivatable fluorescent molecules by photoactivated localization microscopy (PALM). *Proceedings of the National Academy of Sciences* **109,** 17436 LP –17441. doi:`10.1073/pnas.1215175109` (Oct. 2012) (cit. on p. 113).

114. Nan, X., Collisson, E. A., Lewis, S., Huang, J., Tamgüney, T. M., Liphardt, J. T., McCormick, F., Gray, J. W. & Chu, S. Single-molecule superresolution imaging allows quantitative analysis of RAF multimer formation and signaling. *Proceedings of the National Academy of Sciences* **110,** 18519 LP –18524. doi:`10.1073/pnas.1318188110` (Nov. 2013) (cit. on p. 113).

115. Puchner, E. M., Walter, J. M., Kasper, R., Huang, B. & Lim, W. A. Counting molecules in single organelles with superresolution microscopy allows tracking of the endosome maturation trajectory. *Proceedings of the National Academy of Sciences* **110,** 16015 LP –16020. doi:`10.1073/pnas.1309676110` (Oct. 2013) (cit. on p. 113).

116. Ehmann, N., van de Linde, S., Alon, A., Ljaschenko, D., Keung, X. Z., Holm, T., Rings, A., DiAntonio, A., Hallermann, S., Ashery, U., Heckmann, M., Sauer, M. & Kittel, R. J. Quantitative super-resolution imaging of Bruchpilot distinguishes active zone states. *Nature Communications* **5,** 4650 (Aug. 2014) (cit. on p. 113).

117. Fricke, F., Beaudouin, J., Eils, R. & Heilemann, M. One, two or three? Probing the stoichiometry of membrane proteins by single-molecule localization microscopy. *Scientific Reports* **5,** 14072 (Sept. 2015) (cit. on p. 113).

118. Ricci, M. A., Manzo, C., García-Parajo, M. F., Lakadamyali, M. & Cosma, M. P. Chromatin Fibers Are Formed by Heterogeneous Groups of Nucleosomes In Vivo. *Cell* **160,** 1145–1158. doi:`https://doi.org/10.1016/j.cell.2015.01.054` (2015) (cit. on p. 113).

119. Rollins, G. C., Shin, J. Y., Bustamante, C. & Pressé, S. Stochastic approach to the molecular counting problem in superresolution microscopy. *Proceedings of the National Academy of Sciences* **112,** E110 LP –E118. doi:`10.1073/pnas.1408071112` (Jan. 2015) (cit. on p. 113).

120. Hage, D. S. Affinity-Based Separation Methods for the Study of Biological Interactions. *Methods* **146,** 1–2. doi:`10.1016/j.ymeth.2018.07.006` (Aug. 2018) (cit. on p. 141).

121. Akkilic, N., Geschwindner, S. & Höök, F. Single-molecule biosensors: Recent advances and applications. *Biosensors and Bioelectronics* **151,** 111944. doi:`10.1016/j.bios.2019.111944` (Mar. 2020) (cit. on pp. 141, 143).

122. Gooding, J. J. & Gaus, K. Single-Molecule Sensors: Challenges and Opportunities for Quantitative Analysis. *Angewandte Chemie - International Edition* **55,** 11354–11366. doi:`10.1002/anie.201600495` (Sept. 2016) (cit. on pp. 141, 143).

123. Zheng, X., Bi, C., Li, Z., Podariu, M. & Hage, D. S. Analytical methods for kinetic studies of biological interactions: A review. *Journal of Pharmaceutical and Biomedical Analysis* **113,** 163–180. doi:`10.1016/j.jpba.2015.01.042` (Sept. 2015) (cit. on p. 141).

124. Hellman, L. M. & Fried, M. G. Electrophoretic mobility shift assay (EMSA) for detecting protein-nucleic acid interactions. *Nature Protocols* **2,** 1849–1861. doi:`10.1038/nprot.2007.249` (Aug. 2007) (cit. on p. 142).

125. Gonzalez, A., Gaines, M., Gallegos, L. Y., Guevara, R. & Gomez, F. A. Thread-paper, and fabric enzyme-linked immunosorbent assays (ELISA). *Methods* **146,** 58–65. doi:`10.1016/j.ymeth.2018.02.008` (Aug. 2018) (cit. on p. 142).

126. Schiel, J. E., Ohnmacht, C. M. & Hage, D. S. Measurement of drug-protein dissociation rates by high-performance affinity chromatography and peak profiling. *Analytical Chemistry* **81,** 4320–4333. doi:`10.1021/ac9000404` (June 2009) (cit. on p. 142).

127. Li, Z. & Hage, D. S. Analysis of stereoselective drug interactions with serum proteins by high-performance affinity chromatography: A historical perspective. *Journal of Pharmaceutical and Biomedical Analysis* **144,** 12–24. doi:`10.1016/j.jpba.2017.01.026` (Sept. 2017) (cit. on p. 142).

128. Thompson, N. L. Surface binding rates of nonfluorescent molecules may be obtained by total internal reflection with fluorescence correlation spectroscopy. *Biophysical Journal* **38,** 327–329. doi:`10.1016/S0006-3495(82)84567-0` (1982) (cit. on p. 142).

129. Thompson, N. L. & Axelrod, D. Immunoglobulin surface-binding kinetics studied by total internal reflection with fluorescence correlation spectroscopy. *Biophysical Journal* **43,** 103–114. doi:`10.1016/S0006-3495(83)84328-8` (July 1983) (cit. on p. 142).

130. Freyer, M. W. & Lewis, E. A. Isothermal Titration Calorimetry: Experimental Design, Data Analysis, and Probing Macromolecule/Ligand Binding and Kinetic Interactions. *Methods in Cell Biology* **84,** 79–113. doi:`10.1016/S0091-679X(07)84004-0` (Jan. 2008) (cit. on p. 142).

131. Braia, M., Loureiro, D., Tubio, G., Lienqueo, M. E. & Romanini, D. Interaction between trypsin and alginate: An ITC and DLS approach to the formation of insoluble complexes. *Colloids and Surfaces B: Biointerfaces* **155,** 507–511. doi:`10.1016/j.colsurfb.2017.04.033` (July 2017) (cit. on p. 142).

132. Li, Z., Wang, Z., Wang, N., Han, X., Yu, W., Wang, R. & Chang, J. Identification of the binding between three fluoronucleoside analogues and fat mass and obesity-associated protein by isothermal titration calorimetry and spectroscopic techniques. *Journal of Pharmaceutical and Biomedical Analysis* **149,** 290–295. doi:`10.1016/j.jpba.2017.11.007` (Feb. 2018) (cit. on p. 142).

133. Petrov, A., Okhonin, V., Berezovski, M. & Krylov, S. N. Kinetic capillary electrophoresis (KCE): A conceptual platform for kinetic homogeneous affinity methods. *Journal of the American Chemical Society* **127,** 17104–17110. doi:`10.1021/ja0562321` (Dec. 2005) (cit. on p. 142).
134. Alhazmi, H. A., Nachbar, M., Albishri, H. M., El-Hady, D. A., Redweik, S., El Deeb, S. & Wätzig, H. A comprehensive platform to investigate protein-metal ion interactions by affinity capillary electrophoresis. *Journal of Pharmaceutical and Biomedical Analysis* **107,** 311–317. doi:`10.1016/j.jpba.2015.01.017` (Mar. 2015) (cit. on p. 142).
135. Gattu, S., Crihfield, C. L., Lu, G., Bwanali, L., Veltri, L. M. & Holland, L. A. Advances in enzyme substrate analysis with capillary electrophoresis. *Methods* **146,** 93–106. doi:`10.1016/j.ymeth.2018.02.005` (Aug. 2018) (cit. on p. 142).
136. Speight, R. E. & Cooper, M. A. A Survey of the 2010 Quartz Crystal Microbalance Literature. *Journal of Molecular Recognition* **25,** 451–473. doi:`10.1002/jmr.2209` (Sept. 2012) (cit. on p. 142).
137. Cheng, C. I., Chang, Y. P. & Chu, Y. H. Biomolecular interactions and tools for their recognition: Focus on the quartz crystal microbalance and its diverse surface chemistries and applications. *Chemical Society Reviews* **41,** 1947–1971. doi:`10.1039/c1cs15168a` (Feb. 2012) (cit. on p. 142).
138. Wienken, C. J., Baaske, P., Rothbauer, U., Braun, D. & Duhr, S. Protein-binding assays in biological liquids using microscale thermophoresis. *Nature Communications* **1,** 1–7. doi:`10.1038/ncomms1093` (Oct. 2010) (cit. on p. 142).
139. Jerabek-Willemsen, M., André, T., Wanner, R., Roth, H. M., Duhr, S., Baaske, P. & Breitsprecher, D. MicroScale Thermophoresis: Interaction analysis and beyond. *Journal of Molecular Structure* **1077,** 101–113. doi:`10.1016/j.molstruc.2014.03.009` (Dec. 2014) (cit. on p. 142).
140. Asmari, M., Ratih, R., Alhazmi, H. A. & El Deeb, S. Thermophoresis for characterizing biomolecular interaction. *Methods* **146,** 107–119. doi:`10.1016/j.ymeth.2018.02.003` (Aug. 2018) (cit. on p. 142).
141. Gomez-Hens, A. & Perez-Bendito, D. The stopped-flow technique in analytical chemistry. *Analytica Chimica Acta* **242,** 147–177. doi:`10.1016/0003-2670(91)87060-K` (Jan. 1991) (cit. on p. 142).
142. Pérez-Bendito, D., Gómez-Hens, A. & Silva, M. *Advances in drug analysis by kinetic methods* in *Journal of Pharmaceutical and Biomedical Analysis* **14** (Elsevier B.V., June 1996), 917–930. doi:`10.1016/0731-7085(95)01673-2` (cit. on p. 142).
143. Ryle, M. J., Padmakumar, R. & Hausinger, R. P. Stopped-flow kinetic analysis of Escherichia coli taurine/α- ketoglutarate dioxygenase: Interactions with α ketoglutarate, taurine, and oxygen. *Biochemistry* **38,** 15278–15286. doi:`10.1021/bi9912746` (Nov. 1999) (cit. on p. 142).
144. Singh, P. SPR Biosensors: Historical Perspectives and Current Challenges. *Sensors and Actuators, B: Chemical* **229,** 110–130. doi:`10.1016/j.snb.2016.01.118` (June 2016) (cit. on p. 142).

145. Myszka, D. G. & Rich, R. L. Implementing surface plasmon resonance biosensors in drug discovery. *Pharmaceutical Science and Technology Today* **3,** 310–317. doi:`10.1016/S1461-5347(00)00288-1` (Sept. 2000) (cit. on p. 142).

146. Hearty, S., Leonard, P. & O'Kennedy, R. in *Methods in Molecular Biology* 411–442 (Humana Press, Totowa, NJ, 2012). doi:`10.1007/978-1-61779-974-7_24` (cit. on p. 142).

147. Ishijima, A. & Yanagida, T. Single molecule nanobioscience. *Trends in Biochemical Sciences* **26,** 438–444. doi:`10.1016/S0968-0004(01)01860-6` (July 2001) (cit. on p. 143).

148. Peterson, E. M. & Harris, J. M. Identification of Individual Immobilized DNA Molecules by Their Hybridization Kinetics Using Single-Molecule Fluorescence Imaging. *Analytical Chemistry* **90,** 5007–5014. doi:`10.1021/acs.analchem.7b04512` (Apr. 2018) (cit. on p. 143).

149. Levene, H. J., Korlach, J., Turner, S. W., Foquet, M., Craighead, H. G. & Webb, W. W. Zero-mode waveguides for single-molecule analysis at high concentrations. *Science* **299,** 682–686. doi:`10.1126/science.1079700` (Jan. 2003) (cit. on p. 143).

150. Zhu, P. & Craighead, H. G. Zero-mode waveguides for single-molecule analysis. *Annual Review of Biophysics* **41,** 269–293. doi:`10.1146/annurev-biophys-050511-102338` (June 2012) (cit. on p. 143).

151. Heucke, S. F., Baumann, F., Acuna, G. P., Severin, P. M., Stahl, S. W., Strackharn, M., Stein, I. H., Altpeter, P., Tinnefeld, P. & Gaub, H. E. Placing individual molecules in the center of nanoapertures. *Nano Letters* **14,** 391–395. doi:`10.1021/nl401517a` (Feb. 2014) (cit. on p. 143).

152. Thakur, A. K. & Movileanu, L. Real-time measurement of protein–protein interactions at single-molecule resolution using a biological nanopore. *Nature Biotechnology* **37,** 96–104. doi:`10.1038/nbt.4316` (Jan. 2019) (cit. on p. 143).

153. Holzmeister, P., Acuna, G. P., Grohmann, D. & Tinnefeld, P. Breaking the concentration limit of optical single-molecule detection. *Chemical Society Reviews* **43,** 1014–1028. doi:`10.1039/c3cs60207a` (Feb. 2014) (cit. on p. 143).

154. Vilfan, I. D., Lipfert, J., Koster, D. A., Lemay, S. G. & Dekker, N. H. in *Handbook of Single-Molecule Biophysics* 371–395 (Springer US, 2009). doi:`10.1007/978-0-387-76497-9_13` (cit. on p. 143).

155. Berghuis, B. A., Köber, M., van Laar, T. & Dekker, N. H. High-throughput, high-force probing of DNA-protein interactions with magnetic tweezers. *Methods* **105,** 90–98. doi:`10.1016/j.ymeth.2016.03.025` (Aug. 2016) (cit. on p. 143).

156. Kriegel, F., Ermann, N. & Lipfert, J. Probing the mechanical properties, conformational changes, and interactions of nucleic acids with magnetic tweezers. *Journal of Structural Biology* **197,** 26–36. doi:`10.1016/j.jsb.2016.06.022` (Jan. 2017) (cit. on p. 143).

157. Katan, A. J. & Dekker, C. High-speed AFM reveals the dynamics of single biomolecules at the nanometer scale. *Cell* **147,** 979–982. doi:`10.1016/j.cell.2011.11.017` (Nov. 2011) (cit. on p. 143).

158. Heath, G. R. & Scheuring, S. High-speed AFM height spectroscopy reveals µs-dynamics of unlabeled biomolecules. *Nature Communications* **9,** 1–11. doi:10.1038/s41467-018-07512-3 (Dec. 2018) (cit. on p. 143).

159. Sumino, A., Sumikama, T., Uchihashi, T. & Oiki, S. High-speed AFM reveals accelerated binding of agitoxin-2 to a K+ channel by induced fit. *Science Advances* **5,** eaax0495. doi:10.1126/sciadv.aax0495 (July 2019) (cit. on p. 143).

160. Elenko, M. P., Szostak, J. W. & Van Oijen, A. M. Single-molecule imaging of an in vitro-evolved RNA aptamer reveals homogeneous ligand binding kinetics. *Journal of the American Chemical Society* **131,** 9866–9867. doi:10.1021/ja901880v (July 2009) (cit. on p. 143).

161. Elenko, M. P., Szostak, J. W. & Van Oijen, A. M. Single-molecule binding experiments on long time scales. *Review of Scientific Instruments* **81,** 083705. doi:10.1063/1.3473936 (Aug. 2010) (cit. on p. 143).

162. Gebhardt, J. C. M., Suter, D. M., Roy, R., Zhao, Z. W., Chapman, A. R., Basu, S., Maniatis, T. & Xie, X. S. Single-molecule imaging of transcription factor binding to DNA in live mammalian cells. *Nature Methods* **10,** 421–426. doi:10.1038/nmeth.2411 (May 2013) (cit. on p. 143).

163. Lu, X., Nicovich, P. R., Gaus, K. & Gooding, J. J. Towards single molecule biosensors using super-resolution fluorescence microscopy. *Biosensors and Bioelectronics* **93,** 1–8. doi:10.1016/j.bios.2016.10.048 (July 2017) (cit. on p. 143).

164. Peterson, E. M., Reece, E. J., Li, W. & Harris, J. M. Super-Resolution Imaging of Competitive Unlabele DNA Hybriization Reveals the Influence of Fluorescent Labels on Duplex Formation an Dissociation Kinetics. *Journal of Physical Chemistry B* **123,** 10746–10756. doi:10.1021/acs.jpcb.9b09736 (Dec. 2019) (cit. on pp. 143, 177).

165. Yang, J. & Pearson, J. E. Origins of concentration dependence of waiting times for single-molecule fluorescence binding. *Journal of Chemical Physics* **136,** 244506. doi:10.1063/1.4729947. arXiv: 1206.0858 (June 2012) (cit. on p. 143).

166. Strauss, M. T., Schueder, F., Haas, D., Nickels, P. C. & Jungmann, R. Quantifying absolute addressability in DNA origami with molecular resolution. *Nature Communications* **9,** 1600. doi:10.1038/s41467-018-04031-z (2018) (cit. on p. 154).

167. Strauss, S. & Jungmann, R. Up to 100-fold speed-up and multiplexing in optimized DNA-PAINT. *Nature Methods,* 1–3. doi:10.1038/s41592-020-0869-x (June 2020) (cit. on pp. 159, 160, 178, 181).

168. Beck, M. & Hurt, E. The nuclear pore complex: Understanding its function through structural insight. *Nature Reviews Molecular Cell Biology* **18,** 73–89. doi:10.1038/nrm.2016.147 (Feb. 2017) (cit. on p. 160).

169. Löschberger, A., van de Linde, S., Dabauvalle, M. C., Rieger, B., Heilemann, M., Krohne, G. & Sauer, M. Super-resolution imaging visualizes the eightfold symmetry of gp210 proteins around the nuclear pore complex and resolves the central channel with nanometer resolution. *Journal of Cell Science* **125,** 570–575. doi:10.1242/jcs.098822 (Feb. 2012) (cit. on p. 160).

170. Szymborska, A., De Marco, A., Daigle, N., Cordes, V. C., Briggs, J. A. & Ellenberg, J. Nuclear pore scaffold structure analyzed by super-resolution microscopy and particle averaging. *Science* **341,** 655–658. doi:`10.1126/science.1240672` (Aug. 2013) (cit. on p. 160).

171. Von Appen, A., Kosinski, J., Sparks, L., Ori, A., DiGuilio, A. L., Vollmer, B., Mackmull, M. T., Banterle, N., Parca, L., Kastritis, P., Buczak, K., Mosalaganti, S., Hagen, W., Andres-Pons, A., Lemke, E. A., Bork, P., Antonin, W., Glavy, J. S., Bui, K. H. & Beck, M. In situ structural analysis of the human nuclear pore complex. *Nature* **526,** 140–143. doi:`10.1038/nature15381` (Oct. 2015) (cit. on p. 160).

172. Lin, D. H., Stuwe, T., Schilbach, S., Rundlet, E. J., Perriches, T., Mobbs, G., Fan, Y., Thierbach, K., Huber, F. M., Collins, L. N., Davenport, A. M., Jeon, Y. E. & Hoelz, A. Architecture of the symmetric core of the nuclear pore. *Science* **352.** doi:`10.1126/science.aaf1015` (Apr. 2016) (cit. on p. 160).

173. Kim, S. J., Fernandez-Martinez, J., Nudelman, I., Shi, Y., Zhang, W., Raveh, B., Herricks, T., Slaughter, B. D., Hogan, J. A., Upla, P., Chemmama, I. E., Pellarin, R., Echeverria, I., Shivaraju, M., Chaudhury, A. S., Wang, J., Williams, R., Unruh, J. R., Greenberg, C. H., Jacobs, E. Y., Yu, Z., De La Cruz, M. J., Mironska, R., Stokes, D. L., Aitchison, J. D., Jarrold, M. F., Gerton, J. L., Ludtke, S. J., Akey, C. W., Chait, B. T., Sali, A. & Rout, M. P. Integrative structure and functional anatomy of a nuclear pore complex. *Nature* **555,** 475–482. doi:`10.1038/nature26003` (Mar. 2018) (cit. on p. 160).

174. Thevathasan, J. V., Kahnwald, M., Cieśliński, K., Hoess, P., Peneti, S. K., Reitberger, M., Heid, D., Kasuba, K. C., Hoerner, S. J., Li, Y., Wu, Y. L., Mund, M., Matti, U., Pereira, P. M., Henriques, R., Nijmeijer, B., Kueblbeck, M., Sabinina, V. J., Ellenberg, J. & Ries, J. Nuclear pores as versatile reference standards for quantitative superresolution microscopy. *Nature Methods* **16,** 1045–1053. doi:`10.1038/s41592-019-0574-9` (Oct. 2019) (cit. on pp. 160, 164).

175. Schlichthaerle, T., Strauss, M. T., Schueder, F., Auer, A., Nijmeijer, B., Kueblbeck, M., Jimenez Sabinina, V., Thevathasan, J. V., Ries, J., Ellenberg, J. & Jungmann, R. Direct Visualization of Single Nuclear Pore Complex Proteins Using Genetically-Encoded Probes for DNA-PAINT. *Angewandte Chemie International Edition* **58,** 13004–13008. doi:`10.1002/anie.201905685` (Sept. 2019) (cit. on pp. 160, 161).

176. Ramm, B., Heermann, T. & Schwille, P. The E. coli MinCDE system in the regulation of protein patterns and gradients. *Cellular and Molecular Life Sciences* **76,** 4245–4273. doi:`10.1007/s00018-019-03218-x` (2019) (cit. on pp. 167, 168, 172).

177. Hu, Z. & Lutkenhaus, J. Topological regulation of cell division in Escherichia coli involves rapid pole to pole oscillation of the division inhibitor MinC under the control of MinD and MinE. *Molecular Microbiology* **34,** 82–90. doi:`10.1046/j.1365-2958.1999.01575.x` (Oct. 1999) (cit. on p. 167).

178. Hu, Z., Mukherjee, A., Pichoff, S. & Lutkenhaus, J. The MinC component of the division site selection system in Escherichia coli interacts with FtsZ to prevent polymerization. *Proceedings of the National Academy of Sciences of the United States*

of America **96,** 14819–14824. doi:10.1073/pnas.96.26.14819 (Dec. 1999) (cit. on p. 167).

179. Shiomi, D. & Margolin, W. The C-terminal domain of MinC inhibits assembly of the Z ring in Escherichia coli. *Journal of Bacteriology* **189,** 236–243. doi:10.1128/JB.00666-06 (Jan. 2007) (cit. on p. 167).
180. Dajkovic, A., Lan, G., Sun, S. X., Wirtz, D. & Lutkenhaus, J. MinC Spatially Controls Bacterial Cytokinesis by Antagonizing the Scaffolding Function of FtsZ. *Current Biology* **18,** 235–244. doi:10.1016/j.cub.2008.01.042 (Feb. 2008) (cit. on p. 167).
181. Adler, H. I., Fisher, W. D., Cohen, A. & Hardigree, A. A. MINIATURE escherichia coli CELLS DEFICIENT IN DNA. *Proceedings of the National Academy of Sciences* **57,** 321–326. doi:10.1073/pnas.57.2.321 (Feb. 1967) (cit. on p. 167).
182. Davie, E., Sydnor, K. & Rothfield, L. I. Genetic basis of minicell formation in Escherichia coli K-12. *Journal of Bacteriology* **158,** 1202–1203. doi:10.1128/jb.158.3.1202-1203.1984 (June 1984) (cit. on p. 167).
183. De Boer, P. A., Crossley, R. E. & Rothfield, L. I. A division inhibitor and a topological specificity factor coded for by the minicell locus determine proper placement of the division septum in E. coli. *Cell* **56,** 641–649. doi:10.1016/0092-8674(89)90586-2 (Feb. 1989) (cit. on p. 167).
184. Raskin, D. M. & de Boer, P. A. J. Rapid pole-to-pole oscillation of a protein required for directing division to the middle of Escherichia coli. *Proceedings of the National Academy of Sciences* **96,** 4971–4976. doi:10.1073/PNAS.96.9.4971 (Apr. 1999) (cit. on p. 167).
185. Loose, M., Fischer-Friedrich, E., Ries, J., Kruse, K. & Schwille, P. Spatial regulators for bacterial cell division self-organize into surface waves in vitro. *Science* **320,** 789–792. doi:10.1126/science.1154413 (May 2008) (cit. on p. 168).
186. Halatek, J., Brauns, F. & Frey, E. Self-organization principles of intracellular pattern formation. *Philosophical Transactions of the Royal Society B: Biological Sciences* **373.** doi:10.1098/rstb.2017.0107. arXiv: 1802.07169 (May 2018) (cit. on p. 168).
187. Wettmann, L. & Kruse, K. The Min-protein oscillations in <i>Escherichia coli</i> : an example of self-organized cellular protein waves. *Philosophical Transactions of the Royal Society B: Biological Sciences* **373,** 20170111. doi:10.1098/rstb.2017.0111 (May 2018) (cit. on p. 168).
188. Frey, E., Halatek, J., Kretschmer, S. & Schwille, P. in *Physics of Biological Membranes* 229–260 (Springer International Publishing, 2018). doi:10.1007/978-3-030-00630-3_10. arXiv: 1801.01365 (cit. on p. 168).
189. Hu, Z., Gogol, E. P. & Lutkenhaus, J. Dynamic assembly of MinD on phospholipid vesicles regulated by ATP and MinE. *Proceedings of the National Academy of Sciences of the United States of America* **99,** 6761–6766. doi:10.1073/pnas.102059099 (May 2002) (cit. on p. 168).

190. Hu, Z. & Lutkenhaus, J. Topological regulation of cell division in E. coli: Spatiotemporal oscillation of MinD requires stimulation of its ATPase by MinE and phospholipid. *Molecular Cell* **7,** 1337–1343. doi:`10.1016/S1097-2765(01)00273-8` (June 2001) (cit. on p. 168).

191. Woldringh, C. L. The role of co-transcriptional translation and protein translocation (transertion) in bacterial chromosome segregation. *Molecular Microbiology* **45,** 17–29. doi:`10.1046/j.1365-2958.2002.02993.x` (July 2002) (cit. on p. 168).

192. Jun, S. & Mulder, B. Entropy-driven spatial organization of highly confined polymers: Lessons for the bacterial chromosome. *Proceedings of the National Academy of Sciences of the United States of America* **103,** 12388–12393. doi:`10.1073/pnas.0605305103` (Aug. 2006) (cit. on p. 168).

193. Di Ventura, B., Knecht, B., Andreas, H., Godinez, W. J., Fritsche, M., Rohr, K., Nickel, W., Heermann, D. W. & Sourjik, V. Chromosome segregation by the Escherichia coli Min system. *Molecular Systems Biology* **9,** 686. doi:`10.1038/msb.2013.44` (Jan. 2013) (cit. on p. 168).

194. Lee, H. L., Chiang, I. C., Liang, S. Y., Lee, D. Y., Chang, G. D., Wang, K. Y., Lin, S. Y. & Shih, Y. L. Quantitative proteomics analysis reveals the Min system of Escherichia coli modulates reversible protein association with the inner membrane. *Molecular and Cellular Proteomics* **15,** 1572–1583. doi:`10.1074/mcp.M115.053603` (May 2016) (cit. on p. 169).

195. Ramm, B., Glock, P., Mücksch, J., Blumhardt, P., García-Soriano, D. A., Heymann, M. & Schwille, P. The MinDE system is a generic spatial cue for membrane protein distribution in vitro. *Nature Communications* **9,** 3942. doi:`10.1038/s41467-018-06310-1` (2018) (cit. on pp. 169, 170, 172, 175).

196. Shih, Y. L., Huang, L. T., Tu, Y. M., Lee, B. F., Bau, Y. C., Hong, C. Y., lin Lee, H., Shih, Y. P., Hsu, M. F., Lu, Z. X., Chen, J. S. & Chao, L. Active Transport of Membrane Components by Self-Organization of the Min Proteins. *Biophysical Journal* **116,** 1469–1482. doi:`10.1016/j.bpj.2019.03.011` (Apr. 2019) (cit. on pp. 169, 170).

197. Glock, P., Ramm, B., Heermann, T., Kretschmer, S., Schweizer, J., Mücksch, J., Alagöz, G. & Schwille, P. Stationary Patterns in a Two-Protein Reaction-Diffusion System. *ACS Synthetic Biology* **8,** 148–157. doi:`10.1021/acssynbio.8b00415` (Jan. 2019) (cit. on pp. 169, 184).

198. Ramm, B., Goychuk, A., Khmelinskaia, A., Blumhardt, P., Ganzinger, K. A., Frey, E. & Schwille, P. ATP driven diffusiophoresis: active cargo transport without motor proteins. *bioRxiv,* 2020.05.01.072744. doi:`10.1101/2020.05.01.072744` (Jan. 2020) (cit. on pp. 169, 170, 184).

199. Schweizer, J., Loose, M., Bonny, M., Kruse, K., Monch, I. & Schwille, P. Geometry sensing by self-organized protein patterns. *Proceedings of the National Academy of Sciences of the United States of America* **109,** 15283–15288. doi:`10.1073/pnas.1206953109` (Sept. 2012) (cit. on pp. 172, 175).

200. Chung, K. K. H., Zhang, Z., Kidd, P., Zhang, Y., Williams, N. D., Rollins, B., Yang, Y., Lin, C., Baddeley, D. & Bewersdorf, J. Fluorogenic probe for fast 3D whole-cell DNA-PAINT. *bioRxiv,* 2020.04.29.066886. doi:`10.1101/2020.04.29.066886` (Jan. 2020) (cit. on p. 178).

201. Edelstein, A. D., Tsuchida, M. A., Amodaj, N., Pinkard, H., Vale, R. D. & Stuurman, N. Advanced methods of microscope control using μManager software. *Journal of Biological Methods; Vol 1, No 2 (2014)* (Nov. 2014) (cit. on pp. 182, 185).

202. Stahl, E., Martin, T. G., Praetorius, F. & Dietz, H. Facile and Scalable Preparation of Pure and Dense DNA Origami Solutions. *Angewandte Chemie International Edition* **53,** 12735–12740. doi:`10.1002/anie.201405991` (Oct. 2014) (cit. on p. 184).

Acknowledgements

Numerous people have accompanied me during the journey of my PhD over the past years. I am deeply indebted to all supporters for their assistance, advice and encouragement making this journey a success.

Prof. Petra Schwille: Petra, first of all, I would like to thank you for making all of this possible, allowing me to join your department for pursuing my PhD. Your philosophy of supervision based on incredible freedom and trust in combination with the established expertise in the lab and, not least, the extraordinary financial possibilities offer an incredible environment for scientific and personal development. I would like to also thank you for always having an open door for discussions of any kind and for the opportunities to represent you at conferences.

Prof. Ralf Jungmann: Ralf, thank you for all your input and advice in many perspectives, but also for making us feel welcome in your lab at all times. There could not have been a better opportunity for learning DNA-PAINT than having the pioneers next door. It was a pleasure working together with you on all our joint projects.

Prof. Joachim Rädler: Thank you for joining my TAC committee, showing great interest in my projects and for making valuable comments during the meetings.

Florian Stehr: Stehrflo, what a lucky coincident it was to start in the lab on the same day as you. We almost instantaneously teamed up and decided to collaborate in joint projects throughout our PhDs. Relying on our complementary skill set and our mutual trust, the most important part of our journey was that besides all hard work we never forgot to take it easy and to maintain the joy in our daily business. I have learned a lot from you and am extremely grateful to have found in you such a close friend.

Julian Bauer and *Patrick Schüler*: Thank you for spending your master projects with us, for your contributions to joint publications and, most importantly, for the fun time you brought to the lab and our little group.

Philipp Blumhardt and *Jonas Mücksch*: Thank you for sharing your honest experiences from the beginning and for your efforts introducing me to the lab. As a very respected physicist duo within the group you left behind high scientific standards and I am very happy that in the end we successfully finished two joint projects.

Florian Schüder: Thank you for sharing all your experimental know-how. Collaborating on nearly every project, we also became friends outside the lab and I enjoyed a lot exchanging thoughts with you regarding science and everything else.

Beatrice Ramm and *Tamara Heermann*: Thank you for many fun and helpful discussions - work and non-work related. Also thank you for sharing your SLB expertise and, Bea, thank you for the joint experiments on the MinDE system.

Kristina Ganzinger and *Christian Niederauer*: Although none of our joint work on single particle tracking has become part of this thesis, I want to thank you for your input and help.

Henri Franquelim: Thank you for your valuable help on any occasion when we had questions regarding DNA origami, lipids or membranes.

Alexander Auer, *Thomas Schlichthärle*, *Maximilian Strauss*, *Kimberly Cramer*, *Sebastian*

Strauss and *Kimbu Wade*: Thank you for always being available for help, for sharing your know-how as well as for your experimental support during our collaborations.

Frank Siedler, *Thomas Weidemann* and *Helge Vogl*: Thank you for your endless efforts in keeping the lab well-running, safe and functioning - and for your positivity in doing so.

Silke Leuze-Bütün: Thank you for your unbeatable administrative support regarding all aspects of the scientific life and for taking great care of the people in the lab.

Sigrid Bauer and *Katharina Nakel*: Thank you for your valuable help regarding chemicals, buffers and DNA origami purification. Siggi, particular thanks to you for looking after our wetlab in the basement.

Jan-Hagen Krohn and *Yusuf Qutbuddin*: Thank you for taking over, I am looking forward to being around watching you kickstart your PhDs. Best of luck!

Finally, a huge thank you to the whole Schwille department for the nice working atmosphere over the past years.

I am very grateful to have been part of the *Graduate School of Quantitative Biosciences Munich* (QBM). The lectures, particularly the Life Science Primer, equipped me with valuable insights regarding molecular biology and biochemistry, which I was able to leverage throughout my PhD. I am also thankful for all the fun memories with the great QBM crowd during our retreats at amazing locations in Venice, at Lake Chiemsee and Lake Starnberg. Besides substantial financial support funding the first half of my PhD, I really appreciated the accessible budget for conferences and workshops. Thanks to the people who have been involved in making QBM a success – in memoriam *Ulrike Gaul*; *Erwin Frey*, *Filiz Civril*, *Markus Hohle*, *Julia Schlehe*, *Mara Kieke*, *Dietmar Martin* and *Mirely Kollmansberger*.

I have also been fortunate to be associated with the *Center for NanoScience* and would like thank *Susanne Hennig* and Claudia Leonhardt for all their efforts in organizing fun, helpful and very interesting scientific events.

Big thanks to *Markus Jobst* for providing the Latex template used for this thesis and to *Florian Stehr*, *Beatrice Ramm*, *Maike Krause*, *Nikolas Eggers*, *Philipp Blumhardt* and *Jan-Hagen Krohn* for proof-reading it.

Besides the invaluable scientific support, I am deeply thankful to all my friends who have accompanied me during the inevitable ups and downs of this endeavour. *Nikolas Eggers*, knowing you since primary school, we ended up starting our PhDs in Munich at the same time. It has truly been (and still is) a pleasure sharing a flat with you.

To my beloved family, my parents *Susanne* and *Eckart*, and my sister *Toni* (with *Svennar*!). The security, love, interest and unconditional support you have provided were the greatest gift, without which I would not have come to this point. Thank you for being role models in so many perspectives.

The last sentences of this book go back to the very beginning of its story. It was in the first week of my PhD, that I met you, *Maike*, and you have accompanied me on this journey ever since. Thank you for all of your endless love, your support and for our deep bond, allowing me to face the challenges of each day after all with a smile. I am deeply grateful to you for always having my back, for taking me as I am and for walking this chapter together with me. I am looking forward to our next one!